DEVELOPMENT OF GUIDELINES TOWARDS AN UNDERSTANDING OF THE STRUCTURE OF THE CATION – STRUCTURE OF THE HYBRID HALOPLUMBATE MATERIAL RELATIONSHIP

A Dissertation
Presented to
The Academic Faculty

by

Marie-Hélène Tremblay

In Partial Fulfillment
of the Requirements for the Degree
Doctor of Philosophy in Chemistry in the
School of Chemistry and Biochemistry

Georgia Institute of Technology
August 2020

DEVELOPMENT OF GUIDELINES TOWARDS AN UNDERSTANDING OF THE STRUCTURE OF THE CATION – STRUCTURE OF THE HYBRID HALOPLUMBATE MATERIAL RELATIONSHIP

Approved by:

Dr. Seth Marder, Advisor
School of Chemistry and Biochemistry
Georgia Institute of Technology

Dr. Elsa Reichmanis
School of Chemical and Biomolecular Engineering
Georgia Institute of Technology

Dr. David Collard
School of Chemistry and Biochemistry
Georgia Institute of Technology

Dr. Jean-Luc Brédas
School of Chemistry and Biochemistry
Georgia Institute of Technology

Dr. Carlos Silva
School of Chemistry and Biochemistry
Georgia Institute of Technology

Date Approved: July 6, 2020

ACKNOWLEDGEMENTS

I would like to extend my deepest gratitude to my advisor Professor Seth Marder. I thank him for giving me tremendous opportunities during my PhD; the summer school, the research visit in Los Alamos National Lab and Oxford and all the collaborations I was involved in! His broad knowledge of material science and chemistry, his thoroughness, and his devotion motivated me to push myself every day. I thank him for being hard on me when I needed an extra push, challenging me to understand my research better and for always encouraging me in my projects! I want to thank him for believing in me and having high expectations for me. His advice on both my research and life have been priceless.

I'm deeply indebted to Dr Stephen Barlow for all his help during my PhD. This thesis would have not been the same without all the discussions that we had together. His immense knowledge, passion and patience forged me into being a much better scientist. I cannot thank him enough for his intellectual rigor and how his influence played a major role in the quality of my work and will continue to affect all projects I will take on in the future

This thesis is the product of multiple fruitful collaborations. I had the pleasure and privilege to work with amazing scientists during my PhD. I know each of them are only beginning their path on an amazing career. First of all, I would like to thank Felix Thouin for being such an amazing collaborator. His patience, devotion to his research and intelligence are values that everybody dreams of in a collaborator. I envy his broad knowledge in physics and I can't thank him enough for being eager to share it with me. I wish to thank Kelly Schutt for being so kind and helpful during my visits at the University of Oxford. Kelly was always ready to help and I value all the time he spent with me optimizing our solar cells. Kelly's motivation and dedication to his research are impressive. It was so enjoyable to work with someone who has such a broad scientific curiosity and is always ready to start new projects. While we only have one paper out yet, I am confident that our collaboration will continue to shine in the future. I would also like to personally thank Sergei Rigin for

his tremendous help with crystal structure characterization and Allyson Boyington for her help with cation synthesis.

I would like to thank all the Marder group members, present and past. In particular, I would like to thank Dr Elena Longhi and Khaled Al Kurdi for helping me throughout my PhD with their friendship, their time and for patiently staying with me at night when I was running late on experiments. I thank Elena for her willingness to meet me everywhere I go, for her career and life advice and for reminding me that I need to chill out a little. Khaled has been such a stress reliever during the last few years. He helped me cope with my personal and professional problems and always had a funny way to do it. I can't thank you enough for the 11PM McDonald runs, for driving me and my fosters around and for being such an incredible friend. I would also like to extend my gratitude to Junxiang Zhang and Yadong Zhang for transposing their passion for organic chemistry to me. Yadong has been so patient and generous of his time (and precursors!) over the last 3 years. I would like to thank Jorge E Rojas Gatjens for so kindly volunteer to read over my thesis. During my time in the Marder group, I had the opportunity to mentor three bright students during my thesis. With their motivation and deep desire to learn, Boqin Zhao, Eleanor Turaski and Griffin Stewart helped me develop multiple projects. I am grateful for each of them and could not have imagined mentoring better students.

My sincere thanks also go to Professor Henry Snaith and Professor Aditya Mohite, who provided me with an opportunity to join their team. I am grateful for all the help I got from the Condensed Matter Physics Department of the University of Oxford, with a special mention to Dr Kelly Schutt, Dr Florian Leroux, Dr Jongchul Lim, Dr Yen-Hung Lin, Jonathan H. Warby and Clare Moloney.

I am also grateful to the following Georgia Tech university staff: Dr Johannes Leisen, Dr Denise Bale, Dr Timothy Parker, David Bostwick, Jenny Eaton, Amy Hartley and Julia Stackhaus. I want to give a special thanks to Dr John Bacsa, who contributed significantly to my understanding of my crystal structures. I am grateful for the shared equipment facility at Georgia Tech: STAMI, NMR and MCF.

I would like to acknowledge all the funding agency that supported my research. I am also grateful for the financial support provided by the Natural Sciences and Engineering Research Council of Canada and the Georgia Tech's School of Chemistry.

I would like to thank the rest of my thesis committee: Prof. David Collard, Prof. Elsa Reichmanis, Prof. Carlos Silva and Prof. Jean-Luc Brédas for their insightful comments and encouragement.

And finally, last but by no means least, I would like to extend my deepest gratitude to my friends and family. I am grateful to my parents and stepparents who were always encouraging me in my crazy projects, for all the rides to and from the airport, for visiting me everywhere I went and for always being there at 2AM when I needed someone to talk to. I am grateful for all my friends for their encouragement during my thesis, in particular Valerie Lavergne for all her love and help during these four years. I want to thank Khaled Al Kurdi, Victor Aladele, Becca Wernette, Jessica Gray and Jamie George who helped me feel like Atlanta was home. To my eternal cheerleader, Julian, thanks for all your support and love during these past 4 years! There is no doubt in my mind that life would have been so much more complex without your relentless encouragements and your own and unique way to make my life easier.

TABLE OF CONTENTS

LIST OF TABLES

LIST OF FIGURES

SUMMARY

Organic-inorganic hybrid haloplumbate materials have attracted ever-increasing interest in the last ten years, initially due to their incorporation in high efficiency solar cells, but increasingly due to their utility in a variety of technological applications (e.g. light emitting diodes, transistors, laser, catalysis). By mixing PbI_2 with an organic cation, one can synthesize 3D, 2D, 1D and 0D perovskite or perovskitoid compounds depending on the cation used. This thesis is concerned with identifying structural factors of the organic cation that influence the observed structures of low-dimensional organic lead-iodide perovskites and perovskitoids. This understanding is necessary to develop design strategies that enable one to predict the structure of the perovskite and perovskitoid based on the organic cation used. As previously suggested, it was found that both the interaction between adjacent cations or between the inorganic layer and the organic cation have structure directing roles in perovskites and perovskitoids. In each class of cations examined, the cation-cation and cation-inorganic layer interactions that determine the structures are discussed. An understanding of how the structure of the cation determines the structure of the hybrid material helps modify materials properties such as stability and optical properties.

The first chapter surveys the structural types adopted by organic iodoplumbates reported in the literature. Following, several studies are described in which 34 crystal structures are determined for families of compounds including 2D perovskites with substituted phenylethylammonium and benzylammonium cations, a corrugated 2D structure using the 4-nitrophenylethylammonium cation, and 1D perovskitoids. The final chapter summarizes the findings of the thesis, and puts them in a broader perspective, comparing them to related

structural relationships among previously reported structures, recapitulates how this thesis has improved our understanding of the cation structure – iodoplumbate structure relationships, and suggests future directions.

CHAPTER 1: INTRODUCTION: STRUCTURES OF LEAD IODIDE PEROVSKITES AND PEROVSKITOIDS

Perovskite is a mineral composed of $CaTiO_3$ and was named after the Russian mineralogist Lev Perovski. The name "perovskite" is, however, also applied to the structure type exemplified by $CaTiO_3$ and to materials that possess this structure type. The perovskite structure consists of MX_6 (M = small metal ion; X = anion; TiO_6 in the case of perovskite itself) octahedra, each vertex of which is shared with a neighboring octahedron to form a cubic, or approximately cubic, three-dimensional (3D) network (with the same connectivity as that found in the structure of ReO_3), with a relatively large cation (Ca^{2+} in the case of perovskite) occupying the cuboctahedral cavities of the structure. The word perovskite has also been applied to other structures that can be regarded as being obtained by "slicing" the perovskite structure, or that contain portions of perovskite-like structures, and that, therefore, also contain sheets or slabs of vertex-sharing octahedra. More recently, materials in which $PbHal_6$ (Hal = halide) octahedra exhibit different connectivity (i.e., edge and/or face sharing, rather than vertex sharing) have also been described as "perovskites", although this usage is, at best, potentially confusing; here, the structures composed of edge- or face-sharing PbI_6 octahedra will be refered to as "perovskitoids", a name that emphasizes that they are distinct from, but related to, lead iodide perovskites *sensu stricto*.

3D and 2D hybrid organic-inorganic perovskites (HOIPs) composed of $MHal_6$ octahedra and relatively large organic cations, have attracted much interest due to their promising properties in a broad variety of optoelectronic devices, including solar cells and light emitting diodes.[1-20] In 3D perovskites, which have the general formula BMX_3, the size of

the B cation is limited by the size of the cuboctahedral cavity in the structure and only the smallest organic cations are able to fit, the most well-known 3D HOIPs being methylammonium lead iodide ($MAPbI_3$). $MAPbI_3$ was first reported as an active layer of solar cells in 2009[1] and, although mixed-cation mixed-halide analogues are now preferred for technological applications, is by far the mostly widely studied 3D lead halide perovskite.[21-25] Use of bulkier organic cations leads to 2D perovskites or 1D perovskites, or to low-dimensional perovskitoids in which octahedra share edges or faces (see Fig. 1). The properties of lead-halide perovskites and perovskitoids materials change dramatically depending on their dimensionality, which in turn is highly influenced by the choice of cation. For example, while 3D lead halide perovskites are bulk semiconductors, lower dimensionalities exhibit stronger quantum confinement; 2D HOIPs can be considered as quantum well structures, 1D HOIPs or perovskitoids as quantum wires, and 0D HOIPs or perovskitoids as quantum dots. This confinement results in much larger exciton-binding energies for low-dimensional structures. In general, the moisture and heat stability of HOIPs increase as the dimensionality decreases.[26, 27] Because the cations used in 1D perovskitoids can be much more complex than those used in 2D HOIPs, it is possible to introduce new properties to those lead-halide materials. These properties can directly result from those of the cation or arise from interactions between the haloplumbate and organic cation portions of the cation.

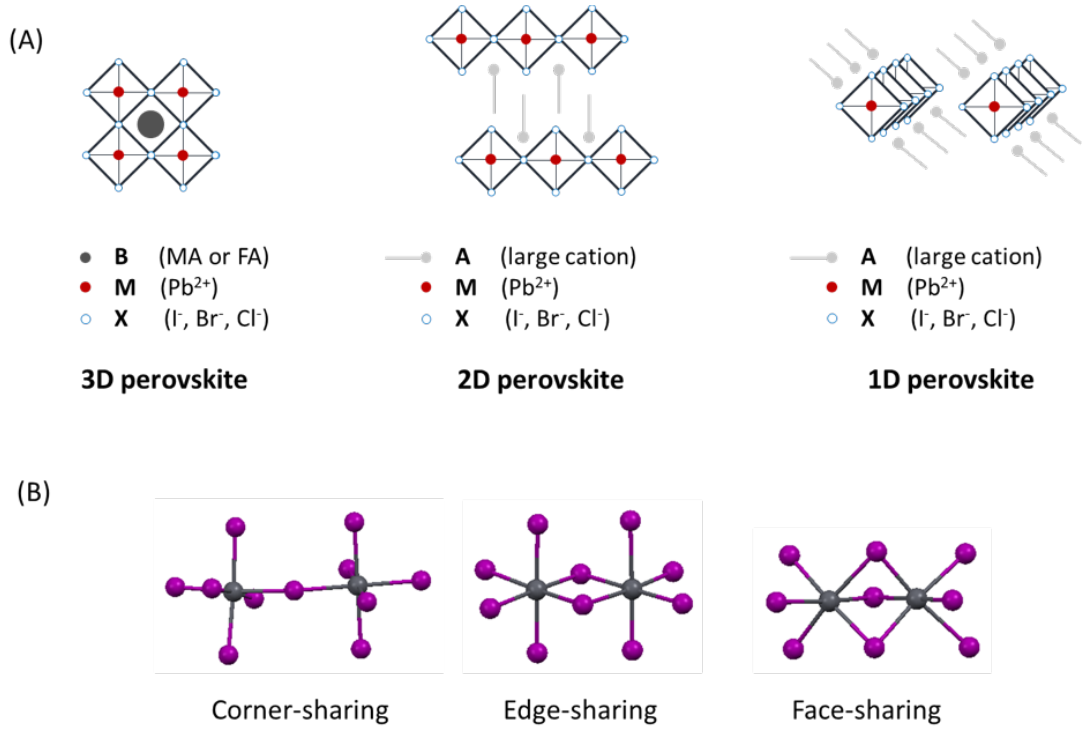

Figure 1.1 Schematic representation of different dimensionality HOIPs (A) and connectivity of iodoplumbate compounds (B).

The structural diversity of the inorganic frameworks found in haloplumbates incorporating organic cations is extraordinary. The various topologies, connectivity, dimensionality, distortion, and orientation possible for $PbHal_6$ octahedra lead to a seemingly infinite variety of structures. In inorganic oxide perovskites, both cations are spherical, whereas in organic-inorganic hybrids, the cations have a wide variety of sizes and shapes and, in many cases, exhibit considerable conformational flexibility; these factors mean it is extremely challenging to predict the final structure of the network. In general, it is unclear which properties of the organic cation are most important in determining the structure of the resulting perovskite/perovskitoid, or how different criteria can be balanced to afford a particular structure type. It is not well understood what structural features of the cation favor the formation of a 2D HOIP, rather than a 1D HOIP or a perovskitoids.

This thesis is concerned with aspects of the structural chemistry of low-dimensional organic lead-iodide perovskites and perovskitoids. Each chapter examines the relationships between the molecular structure of the organic cations used and the crystal structure of resulting iodoplumbates. To put this work in context, this chapter will survey the structure types that have been reported in the literature for organic haloplumbates, primarily focusing of iodoplumbates, since PbI_6-based structures are the most structurally diverse. Since the lead-halide perovskite field was reborn in 2009, following the discovery of the remarkable solar-cell performance of $MAPbI_3$, multiple reviews have discussed those materials and their incorporation in technological devices.[24, 25, 28-34] Moreover, few reviews have reported the structural diversity hybrid lead iodide compounds before 2009.[35-39]

1.1 Survey of Structures

1.1.1 3D HOIPs

As mentioned above, only small organic cations can fit into the 3D cubooctahedral cavity of 3D $BPbHal_3$ HOIPs. Methylammonium (MA) and formamidinium (FA) are the only two well-established organic cations that are reported to date; for B = MA and FA, Hal = Cl, Br, I are reported. $FMAPbBr_3$ (FMA = flluromethylammonium)[40] has also been claimed, but the report does not provide clear evidence for the successful synthesis of this cation or its successful incorporation into a perovskite. Multiple efforts have been made to use other types of cations in 3D HOIPs. A series of nitrogen-based B-site cation for 3D HOIPs have been proposed by Kieshlich *et al.*[41, 42] Some have been incorporated into perovskite precursor solutions to improve the efficiency of mixed-perovskite cells,[43-45] but it is unknown whether, after film processing, these cations fit into the perovskite network or if

they are located at the grain boundaries of the crystals. Among the cations suggested, azetidinium lead iodide ($(CH_2)_3NH_2)PbI_3$ was synthesized, but its crystal structure could not be solved.[46] Other cations that have been proposed to fit in 3D structures including hydroxylammonium,[47] hydrazinium,[48] imidazolium[26, 43] and ethylammonium, all form 1D wires rather than the expected 3D structure. Theoretical investigations have suggested that other small cations, notably aziridinium, could potentially fit into 3D HOIP structures.[49]

1.1.2 2D HOIPs

To obtain lower dimensionality perovskites, one can conceptually slice a cubic 3D perovskite structure along different crystallographic plane. For example, slicing along the (100) plane leads to flat 2D perovskite sheets (with the corresponding organic iodoplumbate materials having the formula A_2PbI_4, where A in a monovalent organic cation), whereas (110) or (111) slicing gives corrugated sheets (also A_2PbI_4), and slicing along (100) and (010) planes leads to a straight wire (A_3PbI_5) (see Fig. 2). Closely related to the 2D layered structures are the so-called quasi-2D perovskites; these compounds contain a mixture of A and B cations and have the general formula $A_2B_{n-1}Pb_nI_{3n+1}$ and a structure in which there are slabs of 3D perovskite that (at least on average) are composed of n layers of PbI_4 sheets; these will be discussed in more detail in section 2.3. Moreover, perovskitoids incorporating face- or edge-sharing octahedra can also be synthesized. While 1D compounds consisting of face- (>50 examples) and edge-sharing octahedra (>5 examples) are quite common (see below), 2D compounds containing purely face- or edge-sharing octahedra are unknown due to geometric restrictions; 2D perovskitoids contain a mixture of different octahedra connectivities.

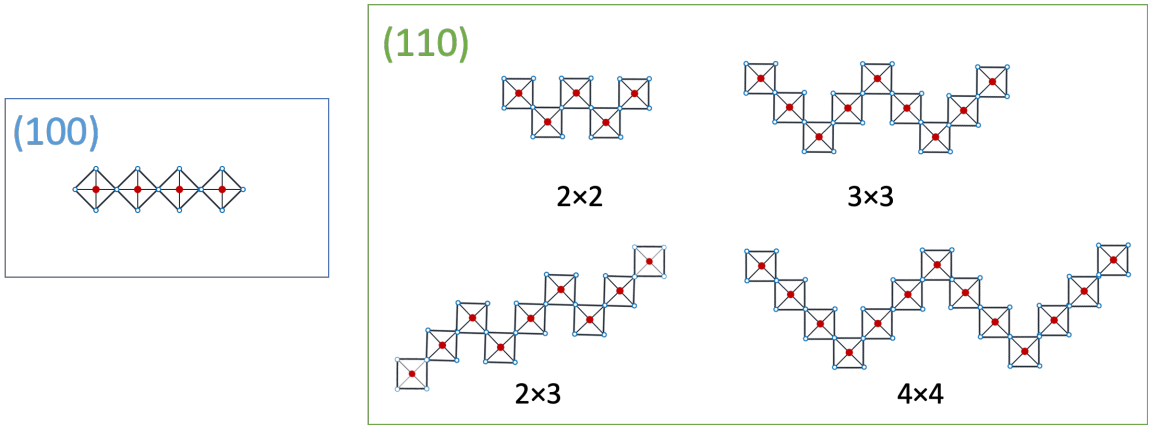

Figure 1.2 Schematic representations of the different type of 2D HOIPs as side views of 1 layer.

2D n = 1 Perovskites with Flat Layers

Single-layer (n = 1) 2D HOIPs have the general formula A_2PbI_4 or $A'PbI_4$ (where A and A' represent organic mono- and dications, respectively). Planar (100)-structures are the most common with more than 70 examples of Pb/I (100)-oriented HOIPs reported in the literature (see Table 1). Flat layered oxide perovskites have been classified into different families, notably the Ruddlesden-Popper (RP) and Dion Jacobson (DJ) structures. The same nomenclature has been used for HOIPs and Chapter 2 suggests a more complete nomenclature.[50, 51] n = 1 RP oxide perovskites have the formula A''_2MO_4 (M = hexacoordinated pentavalent ion, A'' = interlayer univalent cation), while DJ oxides have the general formula $A'''MO_4$ (where A''' is a divalent cation). In RP oxide structures, a bilayer of A'' cations leads to an offset of one layer of MO_6 octahedra from the next by one half of a M-to-M repeat distance in both of the M–O–M directions; this is often referred to as a (½, ½) offset. On the other hand, DJ oxides have a single layer of dications between the inorganic layers and exhibit no offset between successive layers (perfect stacking) or a displacement of (½,0) (i.e., a shift of half a M-to-M repeat distance in one of the two M-

O-M directions). While the cations in oxide perovskite are spheres, those in hybrid perovskite can have different sizes and shapes leading to a lower symmetry of the crystal structure. Moreover, with multiple possible cation-cation and cation-iodide interactions, it is not surprising that HOIPs do not exhibit offsets close to the ideal expectations for oxides with analogous formulae. The offset of the two inorganic layers can be in between 0 and ½, and unsymmetric in both directions.

Even within 2D n = 1 HOIPs there is still variation in the optical properties of the materials that can be important when chosing or designing a material for many of their potential technological applications. Few structural features of these 2D HOIPs have been suggested to be related to optical properties (see Fig. 3). To name a few, the degree of distortion of Pb-I-Pb angles from linearity, the distortion of the octahedra from ideal octahedral geometry, and the distance between adjacent layers.

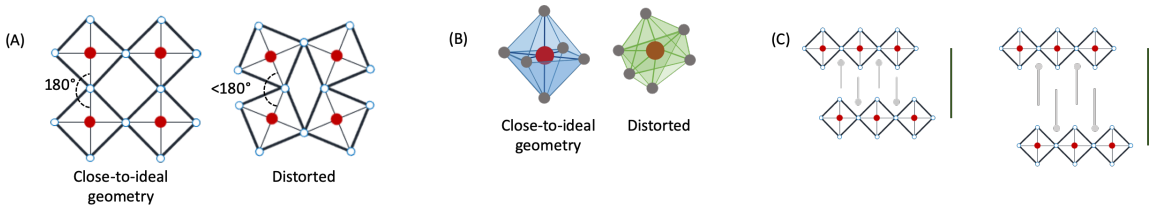

Figure 1.3 Schematic representation few structural indicators that have been suggested to impact the optical properties of the 2D HOIP: the different types of distortion in 2D HOIPs (A-B) and the interlayer distances (C).

The distortion in the lattice, estimated using the M-Hal-M bond angle, is related to the exciton energy of the 2D HOIPs; distorted geometry leads to a blue-shift of the optical gap of the material compared to the close-to-ideal geometry.[16, 52, 53 54] The same trend is observed in 3D HOIPs. Multiple factors influence this bond angle including cation choice, temperature[55 56, 57] and pressure[58, 59]. The distortion within the octahedra itself seems to be

related to the broadness of the photoluminescence of the 2D HOIPs. This has been reviewed elsewhere.[60, 61]

Depending on the charge and size of the cation, the interlayer (inorganic to inorganic) distances will vary. It has been shown that this can influence the optical gap as well due to the quantum well structure of the perovskite; as the inorganic layer come closer to each other, they can start interacting.[62] In some cases, the monocations will form a bilayer, while in some cases, the two layers of cation will be intergenerated, which will affect the interlayer distance. 2D perovskites employing a dication usually have a smaller interlayer distance compare to the analogue structures using the monocation.

Table 1.1 Examples of crystallographically characterized 2D HOIPs (100)-oriented ammonium iodoplumbate compounds, A_2PbI_4 or $A'PbI_4$, reported in the literature.

Compound	Cation	Charge cation	CCDC #	Reference
1	2-Naphthylmethylammonium	1	1542462	[63]
2	2-(Naphthalen-1-yl)ethylammonium	1	1542463	[63]
3	Naphthalene-1,5-diyl diammonium	2	853212	[64]
4	Dodecane-1,12-diyl diammonium	2	853211	[64]
5	Octane-1,8-diyl diammonium	2	853209	[64]
6	Butane-1,4-diyl diammonium	2	853207	[64]
7	Hexane-1,6-diyl diammonium	2	150501	[65]
8	Nonane-1,9-diyl diammonium	2	1869673	[66]
9	*Trans*-Cyclohexane-1,4-diyl bis(methylammonium)	2	781212	[67]
10	*N,N*-Dimethylbenzene-1,4-diammonium	2	1572156	[68]
11	*R*-1-Phenylethylammonium	1	607740	[69]
12	*rac*-1-(4-Chlorophenyl)ethylammonium	1	1885084	[70]
13	3-Chloro-*N*-methylanilinium	1	1883324	[71]
14	2-(2-Fluorophenyl)ethylammonium	1	1890083	-
15	2-(3-Fluorophenyl)ethylammonium	1	1893384	[72]
16	2-(4-Fluorophenyl)ethylammonium	1	1893385	[72]
17	2-(4-Chlorophenyl)ethylammonium	1	-	[73]
18	2-(4-Bromophenyl)ethylammonium	1	-	[73]
19	2-(4-Methylphenyl)ethylammonium	1	-	[73]
20	4-Fluorophenylmethylammonium	1	1819854	[72]
21	4-Chlorophenylmethylammonium	1	249243	[74]
22	4-Bromophenylmethylammonium	1	723486	[75]
23	Phenylmethylammonium	1	1493135	[76]
24	4-(Pyren-1-yl)butylammonium	1	1876191	[77]
25	3-[(Naphthalen-1-yl)oxy]propylammonium	1	1840803	[78]
26	4-[(Pyren-1-yl)oxy]butylammonium	1	1840805	[78]
27	3-[(Pyren-1-yl)oxy]propylammonium	1	1840806	[78]
28	2-[(Pyren-1-yl)oxy]ethylammonium	1	1840802	[78]
29	2-[(Perylen-3-yl)oxy]ethylammonium	1	1840807	[78]
30	4-Bromopyridinium	1	1495869	[78]
31	2-(Ammoniomethyl)pyridinium	2	1838613	[79]
32	1-(2-Ammonioethyl)pyridinium	2	1841680	[80]
33	2-(2-Ammonioethyl)imidazolium (doubly protonated histamine)	2	1841682	[80]
34	Thiophen-2-ylmethylammonium	1	187952	[80]
35	2-(Thiophen-2-ylethyl)ammonium	1	1043214	[81]
36	2-([2,2'-Bithiophen]-5-yl)ethylammonium	1	1861843	[82]

37	2-(4'-Methyl-5'-[7-(3-methylthiophen-2-yl)-2-benzothiophen-4-yl][2,2'-bithiophen]-5-yl)ethylammonium	1	1846392	[82]
38	2-(3‘‘‘,4’-Dimethyl[2,2’:5’,2‘’:5‘’,2‘’‘-quaterthiophen]-5-yl)ethylammonium	1	184391	[82]
39	2,2'-([2,2'-Bithiophene]-5,5'-diyl) bis(ethylammonium)	2	1965305	[83]
40	Benzo[*d*]imidazolium	1	1507154	[84]
41	2,2′-Biimidazolium	2	167103	[85]
42	Benzo[1,2-*d*:4,5-*d′*]diimidazolium	2	1217404	[86]
43	2,2'-Disulfanediyldiethylammonium	2	724583	[87]
44	Cyclopropylammonium	1	609992	[88]
45	Cyclobutylammonium	1	609993	[88]
46	Cyclopentylammonium	1	609994	[88]
47	Cyclohexylammonium	1	1452342	[88]
48	2-Hydroxyethylammonium	1	237189	[88]
49	3-Hydroxypropylammonium	1	746125	[89]
50	3-Iodopropylammonium	1	746127	[89]
51	4-Iodobutylammonium	1	746128	[89]
52	5-Iodopentylammonium	1	746129	[89]
53	6-Iodohexylammonium	1	746130	[89]
54	2-Iodoethyammonium	1	641641	[89]
55	2-Bromoethylammonium	1	641642	[89]
56	2-Chloroethylammonium	1	641644	[89]
57	2-Cyanoethylammonium	1	705087	[89]
58	3-Carboxypropylammonium	1	267398	[90]
59	Isobutylammonium	1	1876240	[91]
60	Butylammonium	1	1268429	[92]
61	Pentylammonium	1	665691	[56]
62	Hexylammonium	1	665694	[56]
63	Heptylammonium	1	805427	[56]
64	Octylammonium	1	805433	[55]
65	Nonylammonium	1	805434	[55]
66	Decylammonium	1	805438	[55]
67	Dodecylammonium	1	692951	[55]
68	Tetradecylammonium	1	692953	[57]
69	Hexadecylammonium	1	692955	[57]
70	Octadecylammonium	1	692957	[57]
71	4-Methylphenylmethylammonium	1	141190	[93]
72	(4-(2-Ammonioethyl)piperazin-1-ium	2	1048275	[94]
73	*N,N*-Dimethylpropane-1,3-diyl diammonium	2	995699	[95]

74	Pent-2-ylammonium	1	1863836	[96]
75	*sec*-Butylammonium	1	1863837	[96]
76	2-Ethylhex-1-ylammonium	1	1863838	[96]
77	Hex-1-ylammonium	1	1863839	[96]
78	4-Ammonio-1-methylpiperidin-1-ium	2	1877264	[96]
79	4,4-Difluorocyclohexylammonium	1	1904976	[97]
80	3-(Ammoniomethyl)piperidin-1-ium	2	1831521	[16]
81	4-(Ammoniomethyl)piperidin-1-ium	2	1831525	[16]
82	3-(Ammoniomethyl)pyridin-1-ium	2	1942543	[98]
83	4-(Ammoniomethyl)pyridin-1-ium	2	1942547	[98]
84	2-([1,1'-Biphenyl]-4-yl)ethylammonium	1	1940831	[99]
85	2-(1-Cyclohexenyl)ethylammonium	1	616101	[100]

1.1.3 n = 1 Corrugated structures

Corrugated layered structures can be regarded as being cut through different crystallographic planes and can have different amplitudes to their "zigzag" patterns (see Fig. 2).[101] Like their planar counterparts they have the general formula A_2PbI_4 or $A'PbI_4$ (where A and A" are mono- and dications, respectively). Multiple (110)-oriented 2D HOIPs have been reported in the last 5 years and Pb/I systems (see Table 2) with 2×2 (110)[102, 103] and 3×3 (110)[36, 37] structures. Although one example of Sn/I 4×4 structure is available in the literature,[104] no Pb/I examples have been reported. While a limited number of corrugated structures are found for iodoplumbates, they seem more common among bromoplumbates.[79, 103, 105-111]

Table 1.2 Examples of corrugated 2D HOIP haloplumbate compounds, A_2PbHal_4 or $A'PbHal_4$, reported in the literature.

Compound	Cation	Cation charge	Thickness	Anion	CCDC #	Reference
86	2,2-(Ethylenedioxy)bis-(ethylammonium)	2	2×2	I, Br, Cl	993477-9	103
87	3-Aminopyrrolidinium	2	2×2	I, Br, Cl	1904555-7	102
88	1-(2-Ammonioethyl)-1H-imidazol-3-ium	2	3×3	I	1841684	80
89	*N*-Methylethan-1,2-diyl diammonium	2	2×2	Br	961379	107
90	1-Ethylpiperazine-1,4-dium	2	2×2	Br	1875165	106
91	3-(3-Ammoniopropyl)imidazolium	2	2×2	Br	283056	108
92	2-(2-Ammonioethyl)isothiouronium	2	2×2	Br	661736	112
93	*N*,*N*-Dimethylethane-1,2-diyl bis(ammonium)	2	3×3	Br	1963064	113

1.1.4 Other 2D HOIP structures

Due to the structural diversity of the lead iodide materials, other classes of materials can be obtained.[114-118] For example, 2D HOIPs incorporating two types of cations or one cation and one neutral molecule in between the inorganic layers can also be synthesized. When two different cations are found in the interlayer space, Kanatzidis and co-workers have referred to these types of structures as "alternating cation in the interlayer space" (ACI); for example $(C(NH_2)_3)(CH_3NH_3)PbI_4$[116] (see Fig. 4A). The ACI perovskites generally adopt a higher crystal symmetry than other 2D perovskites. Quasi-2D examples of ACI structures are also found.[116]

Intercalation of a neutral molecule in the interlayer space has also been reported. A reversible intercalation-deintercalation process was observed by in situ X-ray diffraction measurements using $(C_9H_{19}NH_3)_2PbI_4$ (or $(C_{10}H_{21}NH_3)_2PbI_4$) with weakly interacting organic molecules such as 1-chloronaphthalene and *o*-dichlorobenzene.[119] Using a Sn/I 2D HOIP system, Mitzi *et al.* were able to synthesize single crystals using pentafluorophenylethylammonium or phenylethylammonium cation and an intercalant aryl or perfluoroaryl molecule (see Fig. 4B).[117] van Gompel also showed that organic charge-transfer complexes can self-assembled in the organic layer (see Fig. 4C).[77] Smith *et al.* used a post-synthetic small-molecule intercalation (I_2) to increase the interlayer spacing of $(6\text{-iodohexylammonium})_2PbI_4$ (see Fig. 4D).[118]

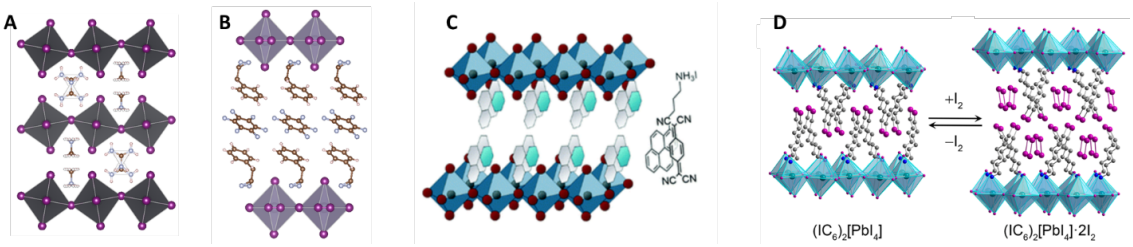

Figure 1.4 (A) Alternating cation, guanidinium and methylammonium, in the interlayer space: $(C(NH_2)_3)(CH_3NH_3)PbI_4$.[116] Intercalation of small molecules in 2D HOIPs. (B) Intercalation of benzene or hexafluorobenzene molecules in $(PEA)_2SnI_4$ perovskite,[117] (C) Intercalation of a tetracyanoquinodimethane in (4-(pyren-1-yl)butylammonium)$_2PbI_4$.[77] (D) Intercalation of I_2 in (6-Iodohexylammonium)$_2PbI_4$.[118]

With the high flexibility of the lead iodide network, other miscellaneous structures can be obtained. A unique staircase-like inorganic network was also reported for $[(H_2en)_7(C_2O_4)_2]Pb_4I_{18}.4H_2O$ (en=ethylendiamine), which is a type of perovskite.[120] (210) structures using 2 A-type cations have been reported recently.[121, 122]

1.1.5 2D n > 1 HOIPs

$A_2B_{n-1}Pb_nI_{3n+1}$ or $A'B_{n-1}Pb_nI_{3n+1}$ (where n > 1, A and B are monocations and A' is a dication) are often referred to as "quasi 2D" perovskites. The B cations occupy cuboctahedral cavities within the 3D-perovskite-like slabs of the structure and thus are restricted to those that can fit in 3D HOIPs (reported to date in quasi-2D structures for B = MA, FA[123]), while the relatively bulky A/A' cations are located between the inorganic slabs in the same way as the A/A' cations of 2D planar perovskites. In principle the inorganic slabs could be either planar or corrugated, in a manner similar to that seen for n = 1 perovskites; however, to date, all examples are planar. Not all A-site cations that form a n=1 2D HOIP can be used to synthesize n>1 analogues. It appears that only cations that induce weak distortions of the Pb-I-Pb bond angle of the inorganic sheet can be used for

multilayered HOIPs (presumably to avoid a mismatch in the demands of the A and B cations on the geometry and alignment of the PbI_6 octahedra), while synthetic practicalities relating the solubility of various starting materials may also limit formation of $n > 1$ materials in some cases.

After their first incorporation in perovskite solar cells, quasi-2D HOIPs have increasingly been a subject of publications due to their higher moisture stability compared to 3D analogues.[15] Phase pure quasi-2D PSCs have subsequently been use in solar cells that have >12% power conversion efficiency, and have since then been incorporated in light emitting diodes.[20] Multiple examples of (100)-oriented structures are presented in the literature (see Table 3 for B = MA examples).[16, 17, 124, 125] It was recently shown that, while ethylammonium (EA) does not form 3D perovskites or an n = 1 2D A_2PbI_4 perovskite, but rather a 1D perovskitoid of formula $EAPbI_3$, it can be used as the B-site cation in quasi-2D perovskites with butylammonium as the A-site cation.[126, 127]

1.1.6 1D HOIPs

1D HOIPs that consist of single wires of vertex-linked octahedra (i.e., true 1D perovskites) have the general formulae A_3PbI_5, $A'_3Pb_2I_{10}$ and $A''PbI_5$ (where A, A', and A" are mono-, di-, and trication, respectively) but are quite rare, with only a few examples reported in the literature, while 1D perovskitoids are somewhat more common. In addition, in several 1D HOIPs the "wires" can be regarded as being formed by vertex sharing between two or more adjacent wires and are, therefore, more like "ribbons" and, by analogy with the pseudo-2D terminology applied to 2D systems with $n > 1$, could be regarded as quasi-1D

systems (n' > 1, where n' is the number of wires that are joined to form the ribbon. The total width of the ribbon will depend on n' value and the zigzag or linear nature of the wire). Three examples of lead-iodide 1D HOIPs are presented here (see Table 4), along with two pseudo 1D lead-bromide examples (see Table 4 and 5) to show the structural diversity possible in these kinds of materials (see Fig. 5).

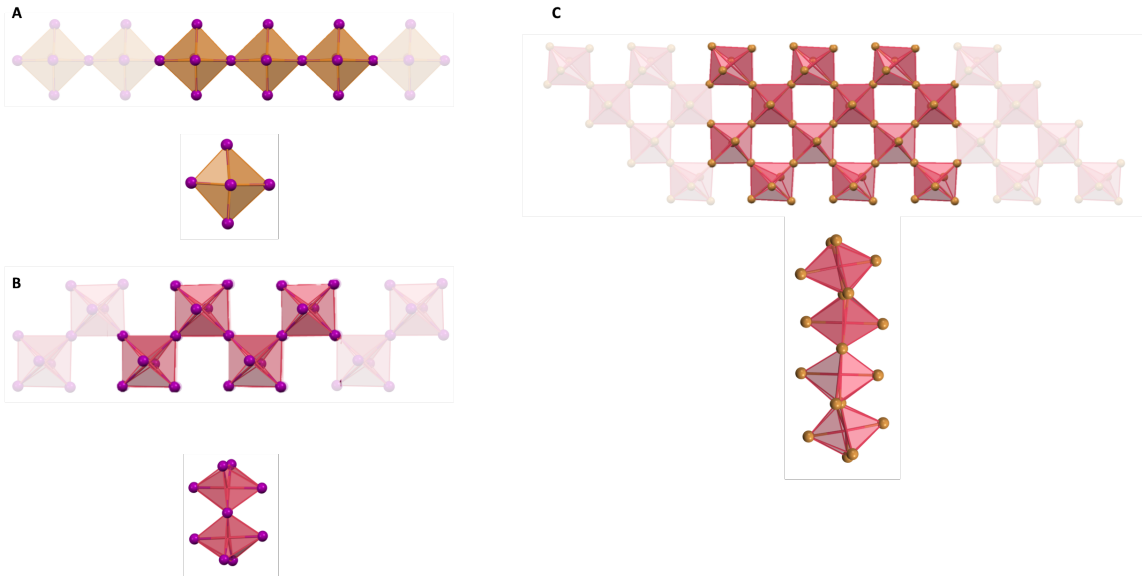

Figure 1.5 Typical octahedra representation of corner-sharing 1D perovskite view perpendicular to the wire long axis (top) and after +90° rotation (bottom). (A) Linear (Iodoformamidinium)$_3$PbI$_5$,[139] (B) zigzag (2-Phenylethylisothiourea)$_3$PbI$_5$.[141] Representation of a pseudo-1D perovskite (C) zigzag, 2 octahedra thick: (Diamminoethane)$_4$Pb$_2$Br$_9$·Br$_3$[110].

There are few different ways to classify 1D and quasi-1D iodoplumbates, both perovskite and perovskitoid, examples. First, the wires can be either linear or zigzag. Second, in some examples, the width of the ribbon differs as mentioned above. Third, they can be classified by the relative position of each wires/ribbons (see Fig. 6). In Chapter 3, structures in which all the wires are related only by translation operations have been designated as "W" structures; multiple examples are found in the literature.[142-145] Other structures have wires related by operation other than translation.

Table 1.3 Examples of crystallographically characterized quasi-2D HOIP iodoplumbate compounds, $A_2(MA)_{n-1}Pb_nI_{3n+1}$ or $A'(MA)_{n-1}Pb_nI_{3n+1}$, reported in the literature with MA = methylammonium.

Compound	Cation	Cation charge	n value	CCDC #	Reference
94	Butylammonium	1	2-4	1478376-8	[17]
95			5	1530117	[128]
96			6-7	1891087-8	[129]
97	2-Phenylethylammonium	1	3	-	[130]
98	Thiophen-2-ylmethylammonium	1	2	187951	[131]
99			3	1834024	-
100	3-Carboxypropylammonium	1	2	267397	[90]
101	3-(Ammoniomethyl)piperidin-1-ium	2	2-4	1831521-4	[16]
102	4-(Ammoniomethyl)piperidin-1-ium	2	2-4	1831525-8	[16]
103	3-(Azaniumylmethyl)pyridin-1-ium	2	2-4	1942544-6	[98]
104	4-(Ammoniomethyl)pyridin-1-ium	2	2-3	1942548-9	[98]
105	Nonane-1,9-diyl ammonium	2	2-4	1869670-1	[66]
106	Octane-1,8-diyl ammonium	2	2-4	1869672, 1869674-5	[66]
107	4-Methylphenylmethylammonium	1	2	141191	[93]
108	Pentylammonium	1	2-5	1904713, 1904717-9	[132]
109	Hexylammonium	1	2-4	1904714-6	[132]
110	4-Fluorophenylmethylammonium	1	2-3	1819860, 1819862	[133]
111	2-Methylpentane-1,5-diyl diammonium	1	2	1964265	[134]
112	Phenylmethylammonium	2	2-3	1876243-4	[91]
113	2-(4-Fluorophenyl)ethylammonium	1	2-3	1483085-6	[135]
114	(*R*)-2-Phenylpropylammonium	1	2	1936623	[136]
115	(*S*)-2-Phenylpropylammonium	1	2	1936624	[136]
116	2-([1,1'-Biphenyl]-4-yl)ethylammonium	1	2	1940830	[99]
117	Propylammonium	1	3-4	1937877, 1937880	[137]

Table 1.4 Examples of crystallographically characterized 1D HOIPs, A_3PbHal_5 or A''$PbHal_5$ (where A mono-cations, A'' tri-cation), available in the literature.

Compound	Cation	Cation charge	Zigzag (Z) or linear (L)	Wire	n' value	CCDC #	Reference
118	1-(2-Ammonioethyl)piperazine-1,4-diium*	3	Z	-	1	-	[138]
119	Iodoformamidinium	1	L	-	1	1307516	[139]
120	2-Methylisothiouronium	1	L	W	1	116583	[140]
121	2-(2-Phenylethyl)isothiouronium	1	Z	W:W'	1	134706	[141]

*Lead bromide-based.

Table 1.5 Examples of crystallographically characterized quasi-1D HOIPs available in the literature.

Compound	Cation	Cation Charge	Zigzag (Z) or linear (L)	Ribbon	n' value	CCDC #	Reference
122 [a]	Ethane-1,2-diyl diammonium*	2	Z	W:W'	2	1850343	[110]

[a] $(A')_4Pb_2Br_9 \cdot (Br)_3$, *Lead bromide-based.

In Chapter 3, the situation of two crystallographically equivalent wires W and W' (where the "middle" wire, W', is related to the "corner" wires, W, by translation and rotation), in which, when viewing along the chain direction, W' falls roughly in the center of four W wires (and vice versa), has been designated as W:W'.[146, 147] In other cases, two crystallographically equivalent wires W' can be in the center of four W wires and is named W:2W'.[148-150] There are also exceptions that do not fall within those categories, and for simplicity, will not be discussed here.[151-153]

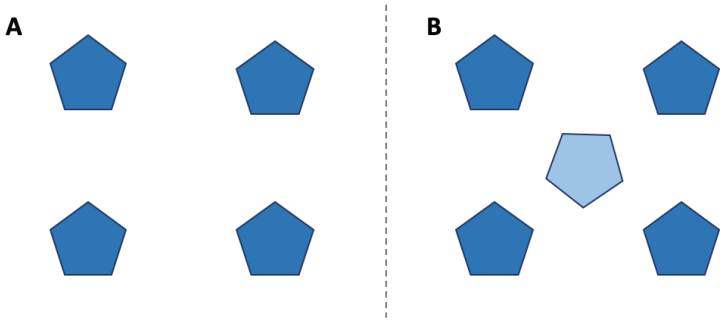

Figure 1.6 Schematic representation of different wire relative position (viewed along the direction of wire propagation): (A) W-structure, (B) W:W'-structure. The dark blue pentagons correspond to the W wires and pale blue ones to the W' wires.

1.1.7 Beyond perovskite materials; 1D perovskitoids

When lead iodide compounds with other types of octahedral connectivity are considered, a seemingly infinite number of combinations become possible. In this section, only hybrid organic-inorganic lead iodide compounds will be considered in which an organic (or metal-organic) cation is used and where the inorganic octahedra are either purely edge-sharing or purely face-sharing. While only ammonium, amidinium, and isothiourea salts have been used in HOIPs, other types of organic cationic species can be incorporated in 1D perovskitoids, including sulfonium,[154] phosphonium,[155, 156] and tropylium ions,[157] as well as protonated amides.[158] Cationic complexes of alkali metals,[153] transition metals[159-164] or

lanthanides[152, 165] with organic ligands have also been incorporated (see Fig.7). As in the case of 1D HOIPs (corner-sharing), edge- and face-sharing iodoplumbate compounds can be 1D wires (1 octahedron thick) or quasi-1D ribbons (>1 octahedron wide).

More than 50 crystal structures of 1D face-sharing iodoplumbate (FSIP) compounds and 8 crystal structures of 1D edge-sharing iodoplumbate (ESIP) have been reported in the literature. Despite this number, our understanding of the relationship between the structure of the A-cation and that of the perovskitoid is poor. Most reports of structures do not address structural relationships in depth. Depending on the structure of the inorganic wire and the cation used, the 1D FSIP compounds can exhibit a wide range of properties that potentially lead to a broad variety of technological applications, for example, as switchable dielectrics,[166-169] ferroelectric materials[149, 170-172] and thermochromic materials.[143, 169]

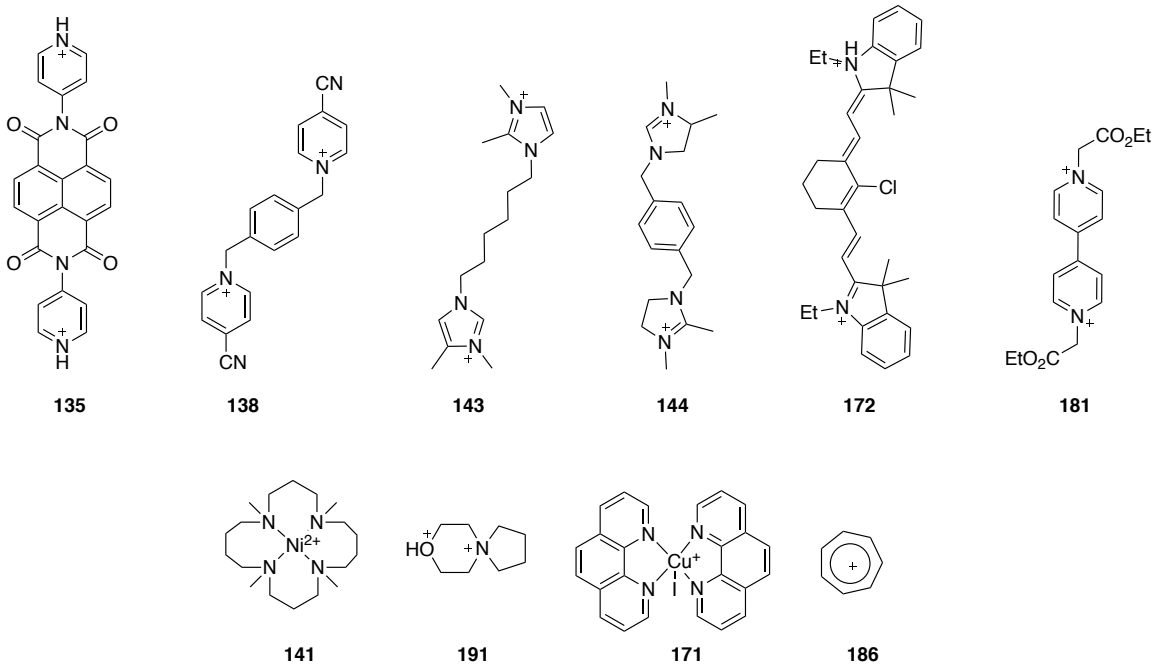

Figure 1.7 Examples of cations incorporated into crystallographically characterized 1D iodoplumbate perovskitoids. (4,4'-Naphthalenediimide-1,8:4,5-bis(dicarboximide)-*N,N'*-diyl dipyridinium)Pb_2I_6 (135)[173], (1,1'-(1,4-Phenylenebis(methylene))bis(4-cyanopyridinium)Pb_2I_6 (138)[174], (1,1'-Hexane-1,6-diyl bis(2,3-dimethylimidazolium)Pb_2I_6 (143)[175], (1,1'-*p*-Xylene-diyl bis(2,3-dimethylimidozolium))Pb_2I_6 (144)[175], (2-(2-(2-Chloro-3-[2-(1-ethyl-3,3-dimethyl-1,3-dihydro-2H-indol-2-ylidene)ethylidene]cyclohex-1-en-1-yl)ethenyl)-1-

ethyl-3,3-dimethyl-3H-indol-1-ium)Pb_2I_6 (172)[176], (1-(2-ethoxy-2-oxoethyl)-1'-((propionyloxy)methyl)-[4,4'-bipyridine]-1,1'-diium)Pb_2I_6 (181)[143], (Ni(1,4,8,11-tetramethyl-1,4,8,11-tetra-azacyclotetradecane))Pb_2I_6 (141),[162] (5-Azonia-8-oxoniaspiro(4.5)decane)Pb_2I_6 (191), (Cu(Iodo-*bis*(1,10-phenanthroline)))PbI_3 (171),[164] (tropylium)PbI_3 (186)[157].

1.1.7.1 Edge-sharing

Eight examples of edge-sharing iodoplumbate (ESIP) compounds are presented here (see Table 6-7, Fig. 8). Single wires of Pb/I with edge-sharing octahedra have not been reported yet, only quasi-1D ribbons. The crystal structure of PbI_2 is similar to the 1D ESIP ribbons with a width of 3. This structure can be seen as 3 parallel wires fused together. In addition, some structures can be described as quasi-1D "cords", where the octahedra are not connected parallel to each other.

1.1.7.2 Face-sharing

Sixty-two examples of face-sharing iodoplumbate (FSIP) compounds are presented here (see Table 8, Fig. 9). Due to geometric constraints, all reported 1D FSIPs compounds have a wire width of 1 octahedron.

1.2 Predicting the structure of HOIPs and Perovskitoids

A series of important factors, including the nature of the organic cation, the charge of the molecule, the halide, the temperature, [55, 57, 198-200] the concentration[201], the solvent,[110, 173, 202-204] the crystallization time,[69, 113] the pressure[205-209] and the relative stoichiometry of the different precursors can significantly affect the structure of the subsequent HOIP or perovskitoid material. A large variety of techniques have been used to synthesize those materials and a few reports detail those findings.[37] These techniques include solvent evaporation, cooling down a saturated solution, solid-state reaction,[210, 211] melt-processing,[212] spray pyrolysis routes[213 214] and solution interface methods.[215]. One can also

produce films by spin-coating, vacuum vapour deposition, and layer-by-layer deposition.[216, 217]

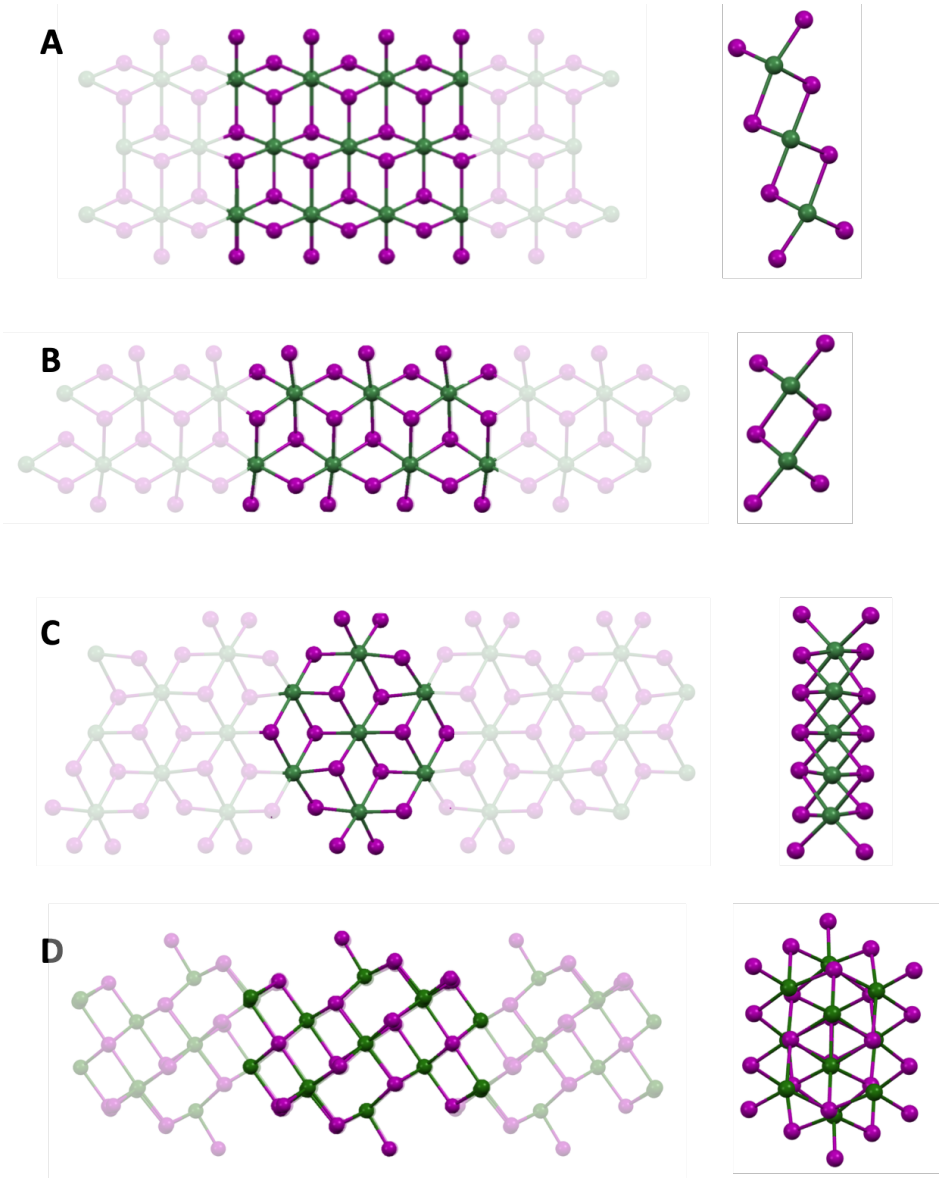

Figure 1.8 Representation of quasi-1D ribbons (A) (methylammonium)$_2$Pb$_3$I$_8$ [59] (n' = 3) and (B) (benzo[*d*]imidazolium)$_2$Pb$_3$I$_8$ [84] (n' = 2) and quasi-1D cords (*N*,*N*,*N*',*N*'-tetraethyl-[1,1'-biphenyl]-4,4'-diyl diammonium)$_2$Pb$_5$I$_{14}$[177] and (*N*,*N*,*N*,*N*',*N*'-pentabutyl-*N*'-propylethan-1,2-diyl diammonium)Pb$_5$I$_9$[153] edge-sharing iodoplumbate perovskitoids. The left image corresponds to the view of the long axis of the wire, the right image is a rotation of the left image, y + 90°.

Table 1.6 Examples of crystallographically characterized quasi-1D ribbons edge-sharing iodoplumbates compounds, $A_2Pb_3I_8$ and $A'Pb_2I_6$, reported in the literature.

Compound	Cation	Cation charge	Wire	n' value	CCDC #	Formula	Reference
123	Methylammonium	1	W:W'	3	1469899	$A_2Pb_3I_8$	[59]
124	Anilinium	1	W:W'	3	1864099	$A_2Pb_3I_8$	[91]
125	1,1''-[1,4-Phenylene-bis(methylene)]bis-4,4'-bipyridinium	2	W:W'	2	1032768	$A'Pb_2I_6$	[178]
126	Benzo[*d*]imidazolium	1	W:W'	2	1507156	$A_2Pb_3I_8$	[84]

Table 1.7 Examples of crystallographically characterized quasi-1D cords edge-sharing iodoplumbates compounds reported in the literature.

Compound	Cation	Cation charge	CCDC #	Formula	Reference
127	*N*,*N*,*N*',*N*'-Tetraethyl-[1,1'-biphenyl]-4,4'-diyl diammonium	2	1573042	$A'_2Pb_5I_{14}$	[177]
128	*N*,*N*,*N*,*N*',*N*'-Pentabutyl-*N*'-propylethan-1,2-diyl diammonium	2	153708	$A'Pb_5I_9$	[153]
129	Phenylammonium	1	1549803	$A_4Pb_5I_{14}$	[179]
130	1,1'-Diethyl-[4,4'-bipyridine]-1,1'-diium	2	1828828	$A'Pb_2I_6$	[180]

Table 1.8 Examples of 1D face-sharing iodoplumbate, $APbI_3$ or $A'Pb_2I_6$, compounds available in the literature.

Compound	Cation	Cation charge	Wire	CCDC #	Reference
131	Pyridinium	2	W:W'	-	[181]
132	Tetramethylammonium	1	W	1500676	[168]
133		1	W	1123333	[182]
134	1-Methylpiperidinium	1	W:W'	1577163	[167]
135 [c]	4,4'-Naphthalenediimide-1,8:4,5-bis(dicarboximide)-*N,N'*-diyl dipyridinium	2	W	1024096	[173]
136	*N,N'*-Dipropyl-4,4'-bipyridinium	2	W	765931	[174]
137	*N*-Ethyl-4-cyanopyridium	1	W	776895	[174]
138 [c]	1,1'-(1,4-Phenylenebis(methylene))bis(4-cyanopyridinium	2	-	776899	[174]
139	Morpholinium	2	W:W'	757317	[183]
140	Trimethylsulfonium	1	W:W'	1547867	[154]
141 [c]	(1,4,8,11-Tetramethyl-1,4,8,11-tetra-azacyclotetradecane)-nickel(II)	2	W	1868901	[162]
142	1,1'-Dimethyl-4,4'-bipyridinium	2	-	114129	[184]
143 [c]	1,1'-Hexane-1,6-diyl bis(2,3-dimethylimidazolium)	2	W:W'	900606	[175]
144 [c]	1,1'-*p*-Xylene-diyl bis(2,3-dimethylimidozolium)	2	W:W'	1015245	[175]
145	*N*-Methylpyrrolidinium	1	W	1400319	[158]
146	Imidazolium	1	W:2W'	1822500	[185]
147	Triethylpropylammonium	1	W:W'	1535129	[169]
148	Iodo-*N,N,N*-trimethylmethanammonium	1	W	1869657	[171]
149	1-(3-Cyanphenylmethylideneamino)pyridinium	1	W:3W'	780405	[149]
150	Octakis(*N,N*-dimethylformamide)-terbium(III)	3	W	856440	[165]
151	Octakis(*N,N*-dimethylformamide)-yttrium(III)	3	W	707166	[152]
152	1,1'-Dimethyl-2,2'-bipyridinium	2	W	1502217	[186]
153	1-Ethylpyridinium	1	-	1524688	[187]
154	Triphenyl(n-butyl)phosphonium	1	W:2W'	1590177	-
155	Triphenyl(ethyl)phosphonium	1	W	1590186	-
156	1,1'-Dimethyl-4,4'-(ethane-1,2-diyl)dipyridinium	2	W:W'	834146	[188]
157	4,4'-Propane-1,3-diylbis(1-methylpiperidin-1-ium)	2	-	958061	[189]
158	1,1'-Butane-1,4-diylbis(3-methylimidazolium)	2	W	871217	[190]
159	1,1'-Diethyl-2,2'-bipyridin-1-ium	2	-	1048276	[94]
160	Nonakis(μ^2-*N,N*-Dimethylformamide)-pentakis(*N,N*-dimethylformamide)-tetra-sodium	4	-	153706	[153]
161	*N,N'*-Dihydroethyl-4,4'-bipyridinium	2	W	1828826	[180]
162	*N,N'*-Bis(2-carboxyethyl)-4,4'-bipyridinium	2	W:W'	1828823	[180]
163	Tetramethylammonium	1	W	1123333	[182]
164	Isopropyl(triphenyl)phosphonium	1	W:W'	1853250	-
165	1-Phenylethylammonium	1	W:W'	607736	[69]

166	Hydroxylammonium	1	W	1894399	[47]
167	4-Carbanoyl-1-methylpyridinium	1	W:W’	219758	[191]
168	Tetra-*n*-butylammonium	1	W	612444	[192]
169	Pyridinium	1	W:W’	1169102	[193]
170	Methylammonium[a]	1	W:W’	998856	[145]
171 [c]	Iodo-*bis*(1,10-phenanthroline)-copper(II)	1	W:W’	879986	-
172 [c]	2-(2-(2-Chloro-3-[2-(1-ethyl-3,3-dimethyl-1,3-dihydro-2H-indol-2-ylidene)ethylidene]cyclohex-1-en-1-yl)ethenyl)-1-ethyl-3,3-dimethyl-3H-indol-1-ium [b]	1	W:W’	1537685	[176]
173	Protonated *N,N*-Dimethylacetamide	1	W:W’	1400321	[158]
174	Trimethylammonium	2	W:3W’	1400323	[158]
175	Dimethylammonium	1	W	1400324	[158]
176	5-carboxypentylammonium	1	W	1400322	[158]
177	Methylammonium, 2,5,8,11-Tetraoxadodecane	1	W	1447264	[147]
178	Methylammonium, 2,2'-Oxydiethanol	1	W:W’	1447265	[147]
179	Methylammonium, 2-(2-(2-Methoxyethoxy)ethoxy)ethan-1-ol	1	W	1447266	[147]
180	1-Ethyl-4-aminopyridinium	1	W	1523553	[144]
181 [c]	1-(2-ethoxy-2-oxoethyl)-1'-((propionyloxy)methyl)-[4,4'-bipyridine]-1,1'-diium [b]	2	W	1504241	[143]
182	1,1'-Dimethyl-4,4'-(ethene-1,2-diyl)dipyridinium	2	W:W’	1526831	[194]
183	4,4'-(Propane-1,3-diyl)di(piperidin-1-ium)	2	W:W’	1844581	[146]
184	Ethane-1,2,-diyldiammonium	1	W	1012805	[142]
185	Ethylammonium	1	-	966419	-
186 [c]	Tropylium	1	W	1047834	[157]
187	1-(4-Fluorophenylmethylideneamino)pyridinium	1	W:W’	780411	[149]
188	*N,N,N′,N′*-Tetramethyl-10H-phenothiazine-3,7-diamine	1	W:W’	790923	[195]
189	4,4'-Ethane-1,2-diyldipyridinium	2	W:W’	1432456	[150]
190	[1,1'-Biphenyl]-4,4'-bis(aminium)	1	W	1902819	[196]
191 [c]	5-Azonia-8-oxoniaspiro(4.5)decane	2	-	722539	-
192	Triethyl(*n*-propyl)ammonium	1	W:W’	1535129	[169]
193	Tetra-*n*-butylammonium	1	W	994586	[197]

Also contains [a] Triethyleneglycol, [b] DMF. [c] See structure in Fig. 7

Due to the lability of the Pb-I bond, multiple different structures can be obtained from the same system; kinetics as well as thermodynamics play a role. As seen above, different iodoplumbate compounds can be isolated using the same cation. This adds another difficulty to the prediction of the relationship between the cation and structure of the perovskite/perovskitoid. In addition, depending on the reaction conditions, it is possible to obtain:

- Different dimensionalities.[84, 179] Benzimidazolium with Pb/I has been isolated in its 2D HOIP ((benzimidazolium)PbI_4) or 1D perovskitoid ((benzimidazolium)PbI_3) form.
- Different octahedra connectivity. Five different crystal structures were obtained using the same NDI-based cation. Both the inorganic and organic component could organize differently depending on the crystallization conditions.
- Planar or corrugated structures. Over 3 weeks in solution, the structure of (*N*,*N*-dimethylethane-1,2-diyl bis(ammonium))$PbBr_4$ transformed from a planar 100-HOIP to a corrugated 110-HOIP.[113]

Rational approaches for control of HOIP structure would be helpful to design materials with specific properties. Due to the high flexibility of Pb-I networks, it is somewhat difficult to predict the dimensionality of perovskite/perovskitoid when choosing a particular cation. Thus far, only a few such guidelines have emerged:

- Only the very smallest cations – predominantly MA and FA – can produce a 3D structure and even then, non-3D structures can be obtained under certain conditions;

- Tertiary and quaternary ammonium increase the chance of obtaining a 1D perovskitoid (exception 40-42[84-86]);
- Cations with head groups other than NH hydrogen bond donor will afford 1D perovskitoids (exceptions are yet to be found);
- Large cations that can engage in multiple cations-cation interactions provide, in most cases, 1D perovskitoids (see discussion below).

That being said, new synthesis techniques could afford other products since that would affect the crystallization pathway. Other than these very general guidelines, a few pointers can be used to try to rationalize the design of the perovskite/perovskitoid, as discussed in the following sections.

1.3 General overview and organization of the thesis

In this thesis, the family of low dimensional lead halide perovskite and perovskitoid materials is expended by reporting a total of 34 new crystal structures. By carefully choosing the cation used with lead and iodide ions, new systems are designed and relationships developed for several classes of cations between the structure of the cation and that of the hybrid organic inorganic lead iodide material.

In Chapter 2, the influence of halogen substituents on hybrid halide iodoplumbate material is studied. In Chapter 2.1, the structures of a family of 2D hybrid structures, (4-Y-$C_6H_4CH_2NH_3)_2PbI_4$, where Y = F, Cl, Br, I), which consist of single ⟨100⟩-terminated perovskite sheets separated by *p*-halobenzylammonium cations, are reported. The offset of the inorganic layers is quantified to allow the structures of hybrid organic inorganic

perovskite to be consistently related to the Dion-Jacobson (DJ) and Ruddlesden-Popper (RP) classifications used for metal oxide perovskite.

In Chapter 2.2, it is shown that the Pb−I−Pb bond angle, which was previously demonstrated to be correlated to the exciton energy, can be tuned by changing the width of the cation in a series of 2D A_2PbI_4 HOIPs. The exciton band energy could be varied over ca. 100 meV, at least within a limited series of A_2PbI_4 compounds where A is a 2-(3,5-disubstitutedphenyl)ethylammonium or 2-(3-substitutedphenyl)ethylammonium ion and where the substituents are H, F, Cl, Br, or Me. Seven new crystal structures are presented here.

In Chapter 3, a rationale is reported for how to choose $R(CH_2)_nNH_3^+$ cations (R = aryl, substituted cyclohexyl; n = 1, 2) to favor the formation of face-sharing hybrid organic-inorganic iodoplumbate compounds, $[R(CH_2)_nNH_3]PbI_3$, in which the inorganic portion consists of 1D wires of face-sharing PbI_6 octahedra (1D FSIPs). Specifically, 1D FSIP formation is favored when hydrogen bonding is possible between the ammonium moiety of one cation and a hydrogen-bond acceptor substituent of the same or another cation. 11 new examples of FSIP compounds and a total of 16 new hybrid organic-inorganic haloplumbate crystal structures are reported. The 1D FSIP structures are categorized according to the arrangement of neighboring wires.

Chapter 4 reports the first synthesis and characterization of a 3x3 corrugated 2D lead iodide hybrid organic inorganic perovskite. This structure was obtained by using the 4-nitrophenylethylammonium (4NPEA) cation. The halogen bonding between the nitro group and the perovskite sheet allows linking the two inorganic perovskite sheets together,

without using a bifunctional cation. This new material exhibits a broad photoluminescence emission, adding another member to the class of two-dimensional white-light emitting hybrid organic inorganic perovskites. A relationship between the ^{207}Pb NMR resonances and the distortion of the octahedra is presented.

In Chapter 5, the crystallization from solutions containing 2,2'-[naphthalene-1,8:4,5-bis(dicarboximide)-*N,N'*-diyl]-bis(ethylammonium) diiodide ((NDIC2)I_2) and PbI_2 is reported. Eight different materials are obtained, either by variation of crystallization conditions or by subsequent thermal or solvent-induced transformations. Crystal structures have been determined for five materials. The optical and electrical properties of these materials are studied.

Chapter 6 discusses the significance of key findings of Chapters 2-5. The chapter focuses on how structural modification of the organic cation can be used to tune the structure of the inorganic portion of the structure. Where possible, guidelines to help predict the structure of the resulting low dimensional networks will be illustrated, along with suggestions for future work to further establish the scope and limitations of these guidelines, or to obtain new structure types.

The Appendix describes four projects involving the incorporation of cross-linkable hole- and electron-transport materials into perovskite solar cells.

CHAPTER 2: INFLUENCE OF HALOGEN SUBSTITUENTS ON HYBRID HALIDE IODOPLUMBATE MATERIAL

2.1 Structures of $(4\text{-Y-}C_6H_4CH_2NH_3)_2PbI_4$ {Y = H, F, Cl, Br, I}: tuning of hybrid organic inorganic perovskite structures from Ruddlesden-Popper to Dion-Jacobson limits

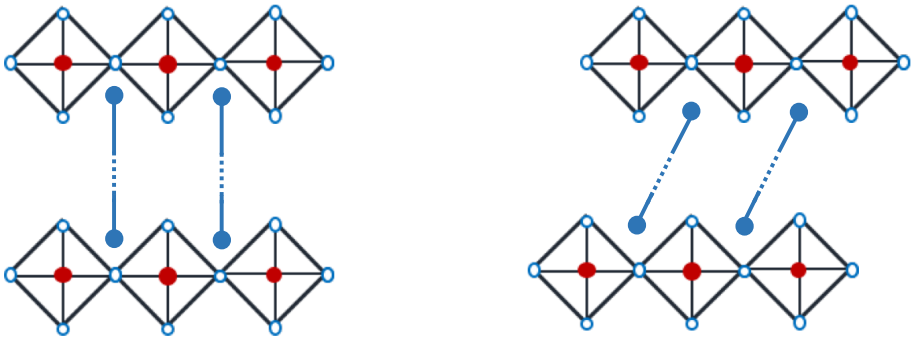

Eclipsed
Near-Dion-Jacobson

Staggered
Near-Ruddlesden-Popper

This project was accomplished with the collaboration of John Bacsa, Boqin Zhao, Stephen Barlow. John Bacsa, from the Crystallography Lab of Emory University, performed the single crystal X-ray diffraction experiments. The single crystals were grown with the help of Boqin Zhao. Stephen Barlow helped with the data analysis and he helped to write the manuscript. The content of this chapter was published in Chemistry of Materials in August 2019 (DOI: 10.1021/acs.chemmater.9b01564). All authors contributed to the redaction of the manuscript. This work was supported by NSERC (ES. D. Scholarship for MHT) and the AFOSR (FA9550-18-1-0499).

2.1.1 Introduction

3D hybrid organic-inorganic perovskites (HOIPs), $BPbX_3$ (B = small organic cation; X = halide), have attracted much interest as they have already shown promising properties in a broad variety of optoelectronic devices.[1-3, 5-8, 218] 2D HOIPs in which each planar ("(100)-oriented") layer of corner-sharing PbX_6 octahedra is separated by a layer of larger organic mono- or dications (A or A' respectively), resulting in compositions of formula A_2PbX_4 or $A'PbX_4$, (along with so-called "quasi-2D" structures of formula $A_2B_{n-1}Pb_nX_{3n+1}$ or $A'B_{n-1}Pb_nX_{3n+1}$) have also been examined as electroactive layers in solar cells[9-18] and light-emitting diodes,[19, 20] and show higher stability then their 3D analogues, coupled with modest performance. Many other aspects of these materials have also been investigated.[219-225] The choice of the A cation or A' dication strongly influences the final structure of the HOIP. Multiple examples of cation-cation interactions (steric[95, 115, 226], aromatic-aromatic[105], van der Waals[227], hydrogen bonding[95, 228, 229]) or cation-halide interactions (hydrogen bonding[230,231,] halogen bonding,[52] nitro-halide interaction[105]) have been reported in materials of this type and presumably help direct the structure.

Layered oxide perovskites have been classified into different families, notably the Ruddlesden-Popper (RP) and Dion Jacobson (DJ) structures.[50, 51] n = 1 RP perovskites have the formula $A"_2MO_4$ (M = hexacoordinated ion, A" = interlayer metal ion). Repulsion between the two layers of A" cations present between each layer of MO_6 octahedra leads to an offset of one layer of MO_6 octahedra from the next by one half of a M-to-M repeat distance in both of the M–O–M directions; this is often referred to as a (½,½) offset. On the other hand, DJ oxides exhibit perfect stacking with no offset between successive layers (0,0), or a displacement of (½,0) (i.e., a shift of half a M-to-M repeat distance in one of the

two M-O-M directions). This can be attributed to the single layer of ions between each layer of octahedra found in these structures; the general formula is A'''MO_4.

Despite the very different interlayer ion sizes and shapes used in HOIPs, their structures have often been classified in a similar way; i.e., as either as RP or DJ structures. A large number of HOIPs incorporating organic monocations – the formulae of which parallel those of RP oxides – have staggered, RP-like structures (although others have been described as "RP", apparently without consideration of the stacking motif). This can be rationalized if one assumes the organic monocation consists of a charge-bearing head group (usually ammonium group) that interacts with the inorganic layer (electrostatically and/or through hydrogen bonding) and a relatively rigid tail perpendicular to the layer; staggering the layers allows the most efficient packing of the tail groups. On the other hand a dication in which two head groups are separated by a rigid bridge would be expected to hold adjacent inorganic layers in registry with one another (Figure 1). Indeed, several HOIPs with A'PbX_4 formulae that parallel those of n = 1 DJ oxides, have been found to exhibit offsets typical of that class. However, the organic A and A' mono- and dications used in HOIPs do *not* generally have rigid tails or bridges held perpendicular to the layers; in view of their irregular shapes and/or conformational flexibility, and the wealth of possible cation-cation and cation-inorganic interactions possible, it is perhaps surprising that so many examples of HOIPs appear to exhibit offsets close to the ideal expectations for oxides with analogous formulae.

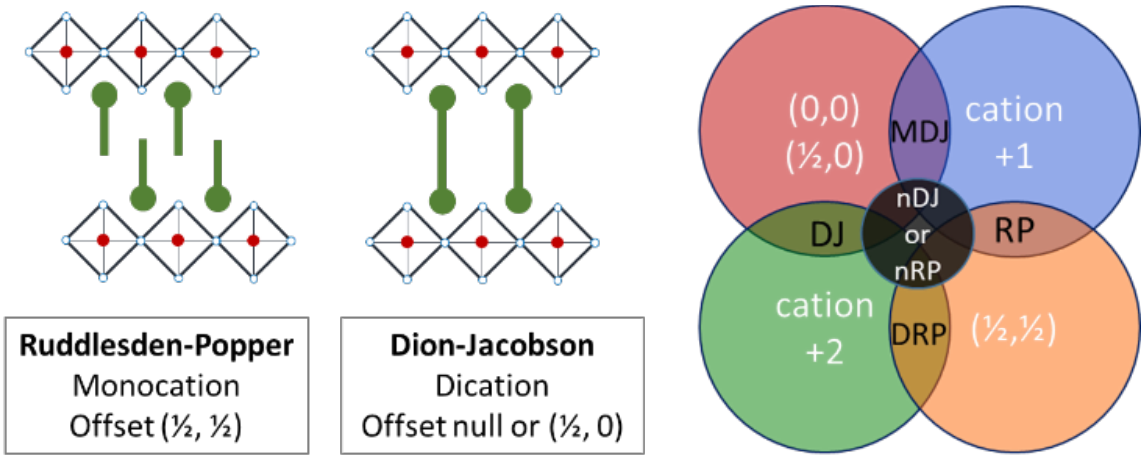

Figure 2.1. Left: Schematic representation of a Ruddlesden-Popper and a Dion-Jacobson n = 1 layered HOIP. Right: Schematic representation of the different possibilities when mixing different offset and different cations. MDJ = monocation-DJ; DRP for dication-RP; nDJ = near-DJ (x<¼, y<¼); nRP = near-RP (x>¼, y>¼).

Here, the structures of a family of 2D HOIPs, (Y-PMA)$_2$PbI$_4$ (Y-PMA = 4-Y-C$_6$H$_4$CH$_2$NH$_3$; Y = H, F, Cl, Br, I) are reported. Despite the presence of A-site monocations, and, therefore, RP-like formulae, adjacent layers of the F, Cl, and Br examples more closely approach DJ-type stacking; this class of compounds is described, in which the chemical formula of a RP perovskite is combined with DJ-like stacking, as monocationic-near-DJ (MnDJ) structures. In contrast, the Y = I analogue has a near RP-structure. Several structures from the literature are classified in a similar manner. In addition, a description of the cation-inorganic and cation-cation interactions in the crystals, the distortions found in the inorganic layers, and the optical and stability characteristics of the materials is presented.

2.1.2 Experimental Procedures

Synthesis.

General synthesis of bulk crystals. PbI_2 (1 eq) was dissolved in HI (57 wt% aqueous solution) and stirred at 100 °C for 2 min. A solution of Y-PMA (2 eq) in HI and MeOH was added to the hot PbI_2 solution and the resultant mixture was stirred at 130 °C for 2 min. The solution was then allowed to crystallize at room temperature for 12 h. The solids were filtered and dried under high vacuum.

Bis(phenylmethylammonium) tetraiodoplumbate ($(PMA)_2PbI_4$). PbI_2 (129 mg, 0.28 mmol) in HI (1 mL). PMA (238 mg, 2.23 mmol) in HI (1 mL) and MeOH (0.2 mL) gave dark orange crystals (90 mg, 35%). Anal. Calcd. for $(C_7H_9N)_2PbI_4$: C, 18.06%; H, 2.17%; N, 3.01%. Found: C, 18.01%; H 1.98%; N, 3.00%.

Bis(4-fluorophenylmethylammonium) tetraiodoplumbate ($(F\text{-}PMA)_2PbI_4$). PbI_2 (131 mg, 0.28 mmol) in HI (1 mL). F-PMA (65 mg, 0.52 mmol) in HI (1 mL) and MeOH (0.8 mL) gave dark orange crystals (82 mg, 30%). Anal. Calcd. for $(C_7H_9NF)_2PbI_4$: C, 17.39%; H, 1.88%; N, 2.90%. Found: C, 17.34%; H 1.75%; N, 2.96%.

Bis(4-chlorophenylmethylammonium) tetraiodoplumbate ($(Cl\text{-}PMA)_2PbI_4$): PbI_2 (124 mg, 0.28 mmol) in HI (2 mL). Cl-PMA (78 mg, 0.55 mmol) in HI (2 mL) and MeOH (1.2 mL) gave orange crystals (96 mg, 29%). Anal. Calcd. for $(C_7H_9NCl)_2PbI_4$: C, 16.81%; H, 1.81%; N, 2.80%. Found: C, 16.80%; H 1.67%; N, 2.82%.

Bis(4-bromophenylmethylammonium) tetraiodoplumbate ($(Br\text{-}PMA)_2PbI_4$): PbI_2 (127 mg, 0.28 mmol) in HI (2 mL). PMA (103 mg, 0.55 mmol) in HI (2 mL) and MeOH

(1.2 mL) gave orange crystals (135 mg, 55%). Anal. Calcd. for $(C_7H_9NBr)_2PbI_4$: C, 15.44%; H, 1.67%; N, 2.57%. Found: C, 15.42%; H 1.57%; N, 2.59%.

Bis(4-iodophenylmethylammonium) tetraiodoplumbate ($(I\text{-}PMA)_2PbI_4$): PbI_2 (202 mg, 0.45 mmol) in HI (4 mL). I-PMA (197 mg, 0.73 mmol) in HI (0.3 mL) and MeOH (4 mL) gave orange crystals (302 mg, 44%). Anal. Calcd. for $(C_7H_9NI)_2PbI_4$: C, 14.21%; H, 1.53%; N, 2.37%. Found: C, 14.46%; H 1.54%; N, 2.38%.

General synthesis of single crystals. A solution of PbI_2 in HI (1 mL of a 25 mg mL^{-1} solution) was added to a vial. 2 mL of MeOH was added on top. Y-PMA was dissolved in a minimum of MeOH and added in the vial slowly. Orange crystals started appearing at the interface between the HI and MeOH after 24 h.

Thin films. A solution made by dissolving $(Y\text{-}PMA)_2PbI_4$ crystals (10 mg) in DMF (100 μL) was spincoated at 4000 rpm for 45 s onto a clean glass or sapphire substrate, pre-cleaned using UV-ozone, in a N_2-filled glovebox. The film was annealed for 30 min at 100 °C.

Stability. The thermal stability of the HOIPs was examined by thermogravimetric analyses (TGA), under nitrogen atmosphere on a Pyris 1 TGA (PerkinElmer) at a heating rate of 5 °C min^{-1}. Data are shown in Figure S17.

Single-crystal X-ray diffraction. Suitable crystals were selected from the reaction mixtures obtained using the general procedure above and were mounted on a loop with paratone oil on a XtaLAB Synergy-S, Dualflex, HyPix diffractometer. The crystals were cooled at the temperature indicated in Table S1 during data collection. The crystals of (Cl-

PMA)2PbI4) undergo an interesting phase transition on cooling with loss of crystallinity below 215 K. Therefore, the crystal was cooled to 225 K during the data collection. Using Olex2,[1] the structure was solved with the ShelXT[2] structure solution program using Intrinsic Phasing and refined with the ShelXL[3] refinement package using least squares minimization. Details of the crystals, data collection, and data refinements are summarized in Table S1. Simulated powder patterns were calculated by Mercury software[4] using the CIF from the single-crystal X-ray experiment.

Powder X-ray diffraction (PXRD). PXRD patterns were acquired on a Panalytical XPert PRO Alpha-1 XRD Diffractometer using Cu K X-ray tube radiation at a voltage of 45 kV and 40 mA, with an incident beam Johannsson monochromator and an X'Celerator solid-state detector. The diffraction pattern was scanned over the angular range of 3-40° with a step size of 0.016°, at room temperature.

Table 2.1 Single-crystal data and structure refinement data.

	$(F\text{-}PMA)_2PbI_4$ **$C_{14}H_{18}F_2N_2PbI_4$**	$(Cl\text{-}PMA)_2PbI_4$ **$C_{14}H_{18}Cl_2N_2PbI_4$**	$(Br\text{-}PMA)_2PbI_4$ **$C_{14}H_{18}Br_2N_2PbI_4$**	$(I\text{-}PMA)_2PbI_4$ **$C_{14}H_{18}I_2N_2PbI_4$**
Formula weight (g mol^{-1})	967.09	999.99	1088.91	1182.89
Temperature (K)	106(6)	225.00(10)	104.0(8)	100.00(10)
Crystal system	monoclinic	monoclinic	monoclinic	monoclinic
Space group	$P2_1/n$	$P2_1$	$P2_1$	$P2_1/c$
a (Å)	8.69555(15)	8.63101(11)	8.60610(10)	16.9722(2)
b (Å)	9.24417(16)	8.95452(10)	8.91160(10)	8.87790(12)
c (Å)	27.5255(6)	15.8648(2)	15.8703(2)	8.67966(11)
β (°)	97.6029(19)	95.9401(13)	95.1410(10)	103.3561(14)
Volume ($Å^3$)	2193.13(7)	1219.55(3)	1212.26(2)	1272.46(3)
Z	4	2	2	2
Z'	1	1	1	0.5
ρ_{calc} (g cm^{-3})	2.929	2.723	2.983	3.087
μ mm^{-1})	13.339	12.199	15.348	13.909
F(000)	1712	880	960	1032
Crystal size (mm^3)	0.26×0.17×0.03	0.364 × 0.165 × 0.04	0.30×0.21×0.04	0.35×0.30×0.13
Radiation	MoKα (λ = 0.71073)	MoKα (λ = 0.71073)	MoKα (λ = 0.71073)	MoKα (λ = 0.71073)
2Θ range for data collection (°)	4.652 to 76.134	4.744 to 75.728	4.752 to 75.964	4.934 to 72.614
Index ranges	$-14 \le h \le 14$, $-15 \le k \le 15$, $-46 \le l \le 46$	$-14 \le h \le 14$, $-15 \le k \le 15$, $-27 \le l \le 27$	$-14 \le h \le 14$, $-15 \le k \le 15$, $-26 \le l \le 26$	$-28 \le h \le 27$, $-14 \le k \le 14$, $-14 \le l \le 14$
Reflections collected	60876	39072	34298	35845
Independent reflections	11438 [R_{int} = 0.0430, R_{sigma} = 0.0304]	12381 [R_{int} = 0.0349, R_{sigma} = 0.0401]	12266 [R_{int} = 0.0325, R_{sigma} = 0.0347]	5770 [R_{int} = 0.0526, R_{sigma} = 0.0289]
Data/restraints/parameters	9751/80/210	12381/1/211	11554/1/212	5437/0/108
Goodness-of-fit on F^2	1.065	0.984	1.013	1.045
Final R indexes [$I>=2\sigma(I)$]	R_1 = 0.0313, wR_2 = 0.0602	R_1 = 0.0396, wR_2 = 0.0873	R_1 = 0.0242, wR_2 = 0.0514	R_1 = 0.0237, wR_2 = 0.0517
Final R indexes [all data]	R_1 = 0.0413, wR_2 = 0.0626	R_1 = 0.0538, wR_2 = 0.0919	R_1 = 0.0267, wR_2 = 0.0519	R_1 = 0.0265, wR_2 = 0.0526
Largest diff. peak/hole (e $Å^{-3}$)	2.574/-2.163	2.21/-1.24	1.142/-1.309	1.989/-2.477

2.1.3 Results and Discussion

The HOIPs were synthesized using a 1:2 ratio of PbI_2 and Y-PMA iodide (where Y = F, Cl, Br, I) in a mixture of methanol and hydroiodic acid. Crystallization afforded the 2D HOIPs as bright to dark orange plates. The crystals were analyzed directly to obtain their single-crystal structures (see Figure 2, Table 1) or filtered, ground, and analyzed by powder X-ray diffraction (PXRD). The structures are compared to the previously reported structure of their Y = H analogue.[232] The single-crystal structural data was acquired at 100 K, except in the case of $(Cl\text{-}PMA)_2PbI_4$, where this was precluded by a phase transition at *ca*. 175 K and where a temperature of 225 K was used instead.

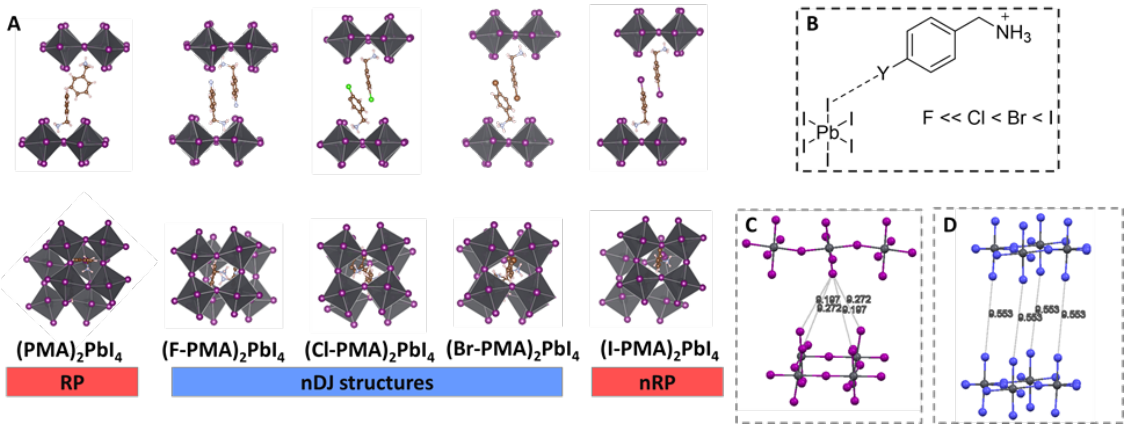

Figure 2.2 (A) Crystal structures of $(Y\text{-}PMA)_2PbI_4$ (data for Y = H taken from ref. [232]). Top: side view parallel to the inorganic layers (along the short axis). Bottom: view along an axis perpendicular to the inorganic planes. (B) Schematic representation of the halogen bonding between the iodine of the inorganic sheet and the cation. (C) and (D) Representations of the inorganic sheets for $(PMA)_2PbI_4$ and $(Br\text{-}PMA)_2PbI_4$ respectively (cations are removed for clarity.

In each case, the PXRD of the powder and the film corresponds to the simulated PXRD from the crystal (see Figure 3). Small peaks were often obtained at low angle next to the (00l) peaks. This minor impurity did not affect the elemental analysis of the products. The

impurity might have the same chemical formula as the crystal, but with different cation arrangement.

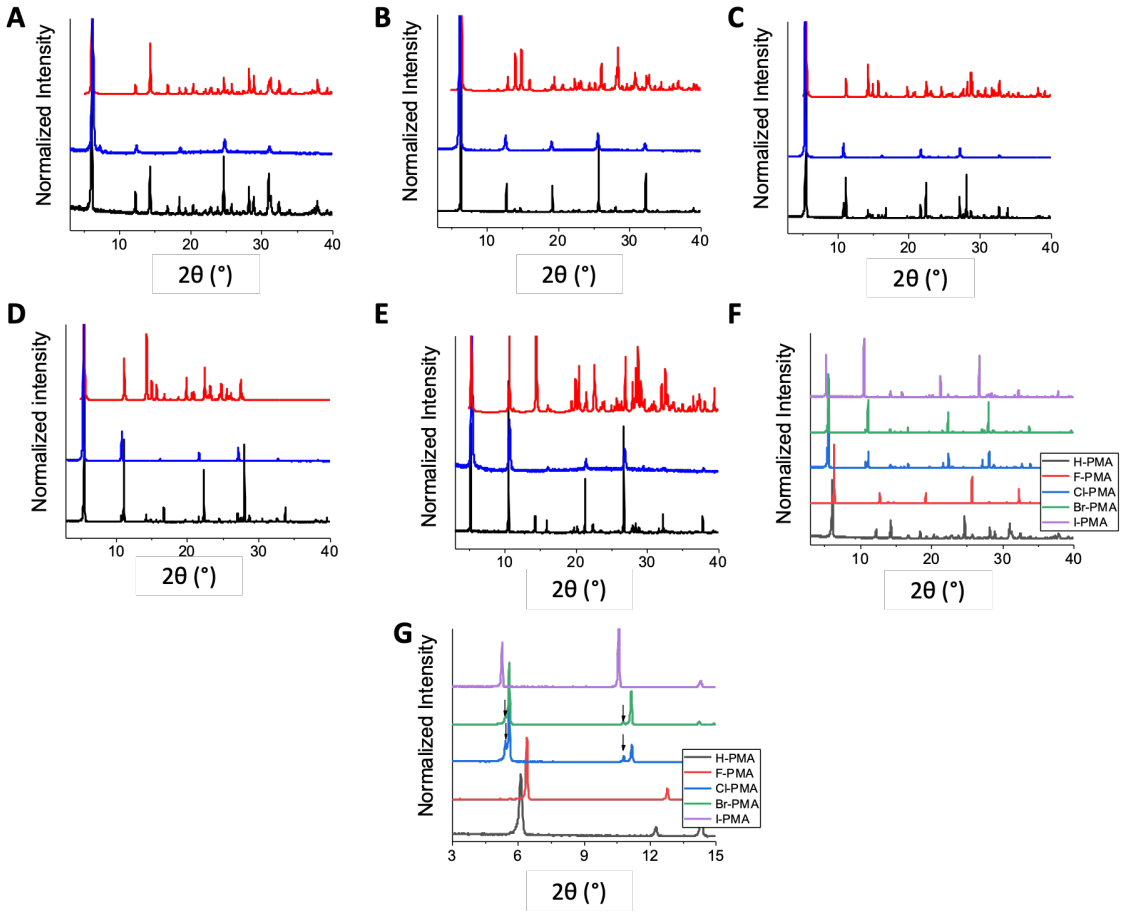

Figure 2.3 Comparison of the powder X-ray diffraction patterns for (A) $(PMA)_2PbI_4$, (B) $(F\text{-}PMA)_2PbI_4$, (C) $(Cl\text{-}PMA)_2PbI_4$, (D) $(Br\text{-}PMA)_2PbI_4$ and (E) $(I\text{-}PMA)_2PbI_4$ powder (red) and film (blue) with a pattern calculated (black) using the single-crystal data. Comparison of the powder pattern of each HOIPs from 3-40 ° (F) and from 3-15 ° (G) to show the impurity peaks (black arrow) of $(Cl\text{-}PMA)_2PbI_4$ and $(Br\text{-}PMA)_2PbI_4$.

All the crystals were stable in the presence of the solution from which they were grown over several days, except those based on Cl-PMA, which decomposed on a timescale of *ca*. 48 h. Films of the HOIPs were obtained through spin-coating onto glass substrates from dimethylformamide. All reflections seen in the Bragg-geometry PXRD patterns of the films can be indexed as (00*l*) reflections, corresponding to the layer stacking direction and indicating a strong preferential growth in the (001) plane to form plate-like crystallites, that

then lie parallel to the substrate. This is consistent with numerous previous studies of n = 1 RP and DJ systems indicating that the orientation of the layers parallel to the substrate is strongly favored over the perpendicular one.[17] The films were used to study the stability of the materials. Ambient stability in the dark of the films were tested and analyzed using PXRD (see Figure 4).

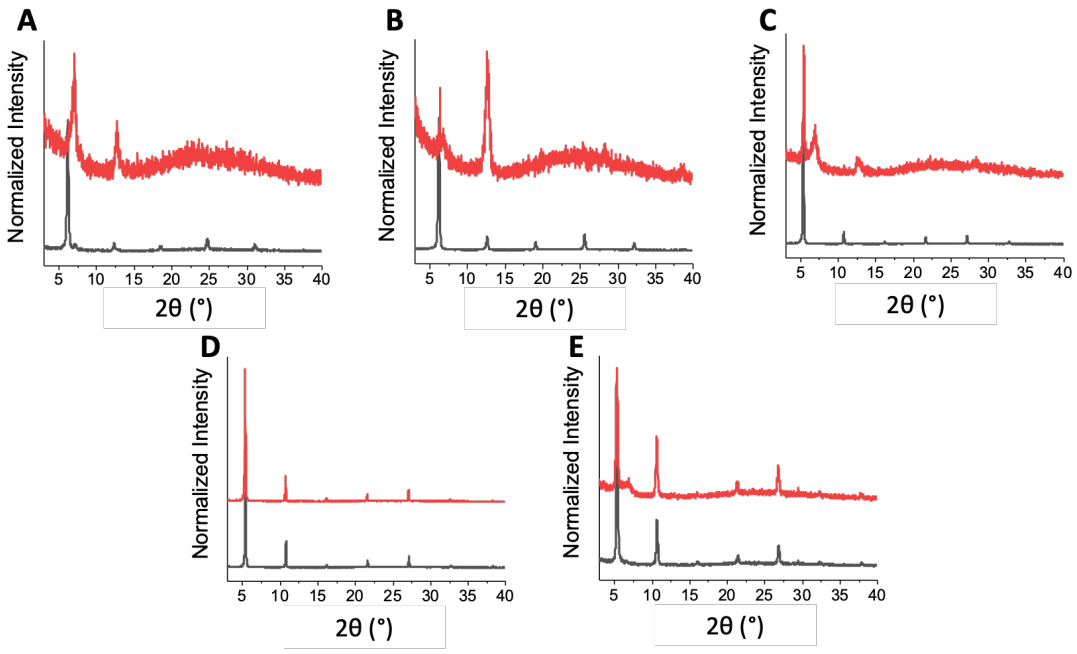

Figure 2.4 PXRD of the films made with the different (Y-PMA)$_2$PbI$_4$ derivatives as initially prepared (black) and after 7 days (red) under ambient conditions in the dark: (A) Y = H, (B) Y = F, (C) Y = Cl, (D) Y = Br, and (E) Y = I.

After 1 week under ambient conditions (*ca*. 50% humidity, *ca*. 20 °C) in the dark, PbI$_2$ peaks were prominent and the HOIP Bragg peaks almost disappeared for films of the Y = H, F, and Cl derivatives. On the other hand, the Br- and I-analogues were unchanged, showing an increased stability for these two compounds, perhaps due to halogen-bonding interactions (*vide infra*) between the heavier halogens and the iodide ions.[233] This may be

related to a slight increase in hydrophobicity, as measured by the water contact angle, in the order Y = F < Cl < Br < I (see Figure 5).

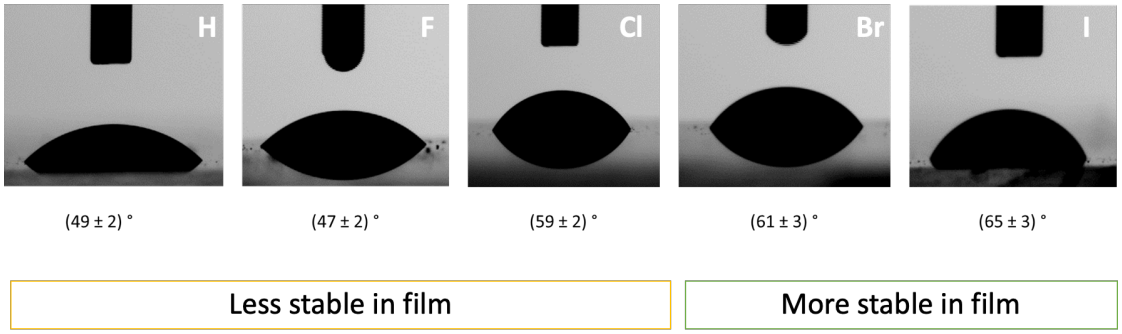

Figure 2.5 Contact angle measurement of water on (Y-PMA)$_2$PbI$_4$ films on glass.

In the previously reported structure of (PMA)$_2$PbI$_4$, in which the Y= H unsusbtituted phenylmethylammonium (benzylammonium) cation is employed, a RP structure, with perfectly ($^1/_2$,$^1/_2$) offset layers is obtained. In the present structures where the *para* position of the phenyl ring is substituted with F, Cl or Br, the layers more closely approach DJ-type stacking (MnDJ), while the I-PMA derivative again has RP-like layer offsets (nRP). In Figure 6, we have quantified the offsets of adjacent inorganic layers as (*x*,*y*) where these coordinates correspond to the mean translation of the offsets of the Pb atoms in one plane relative to that in the next along the two Pb-I-Pb direction (which do not necessarily correspond to the crystallographic axes), expressed as fractions of the Pb–I-Pb repeat distances. Offset data for several previously reported structures are plotted, along with those for the present (Y-PMA)$_2$PbI$_4$ structures. In addition to (PMA)$_2$PbI$_4$, the monocation (*p*-tolylmethylammonium)$_2$PbI$_4$ (1),[131] (thien-2-ylmethylammonium)$_2$PbI$_4$ (2),[131] (cyclopropylammonium)$_2$PbI$_4$ (3),[88] have an "ideal" RP offset of (½,½). (PEA)$_2$PbI$_4$ (4, PEA = phenylethylammonium)[63] deviates significantly from the ideal with an offset of (0.37,037) and so can be regarded as nRP. Two previously reported dication structures, (naphthalene-1,5-diyl ammonium)PbI$_4$ (5)[64] and (4-(ammoniomethyl)piperidinium)PbI$_4$

(6)[16] are "ideal" DJ structures with translations of precisely (0,0). Another reported dication structure, (4-(2-ammonioethyl)-1H-imidazolium)$PbBr_4$ (7),[234] is close to the ($^1/_2$,0) DJ limit, with a translation of (0.42,0), so is best described as having "near-DJ" (nDJ) stacking. Another dication structure, (3-(ammoniomethyl)piperidinium)PbI_4 (8),[16] deviates more significantly from the "ideal" DJ values, but its translation of (0.18,0.18) is still closer to one of the ideal DJ values than the RP limit, and can, therefore, also be regarded as nDJ. Figure 6 shows that the offset for (F-PMA)$_2PbI_4$ is not particularly close to any of the ideal values; however, it is closest to the ($^1/_2$,0) DJ limit and so is best considered a nDJ structure. (Y-PMA)$_2PbI_4$ (Y = Cl, Br) are also nDJ structures, but more closely approach the (0,0) than the ($^1/_2$,0) extreme and exhibit offsets similar to that seen for (3-(ammoniomethyl)piperidinium)PbI_4. Given that (Y-PMA)$_2PbI_4$ (Y = F, Cl, Br) incorporate organic monocations, resulting in a RP-like formula, but DJ-like layer offsets, we classify these materials as monocationic near-DJ, MnDJ, structures. A search of the literature revealed several 2D HOIPs that can also be classified as MnDJ structures, although the DJ-like aspects of their structures were not commented upon in the original publications. The offsets calculated for the structures of (2-hydroxyethylammonium)$_2PbI_4$ (9),[89] (octylammonium)$_2PbI_4$ (10),[55] and (3-bromopyridinium)$_2PbI_4$ (11),[235] are shown in Figure 6. One example of a *perfect* MDJ was found: (5-iodopentylammonium)$_2PbI_4$ (12).[89] Finally, the translation seen for (I-PMA)$_2PbI_4$ is close to, but falls a little short of, the ideal RP value of ($^1/_2$,$^1/_2$) and this structure can, therefore, be classified as near-RP (nRP). Again, our search of the literature revealed several 2D HOIPs that can be classified as nRP structures, such as (2-cyanoethylammonium)$_2PbI_4$ (13)[38] and (pentylammonium)$_2PbI_4$ (14)[200].

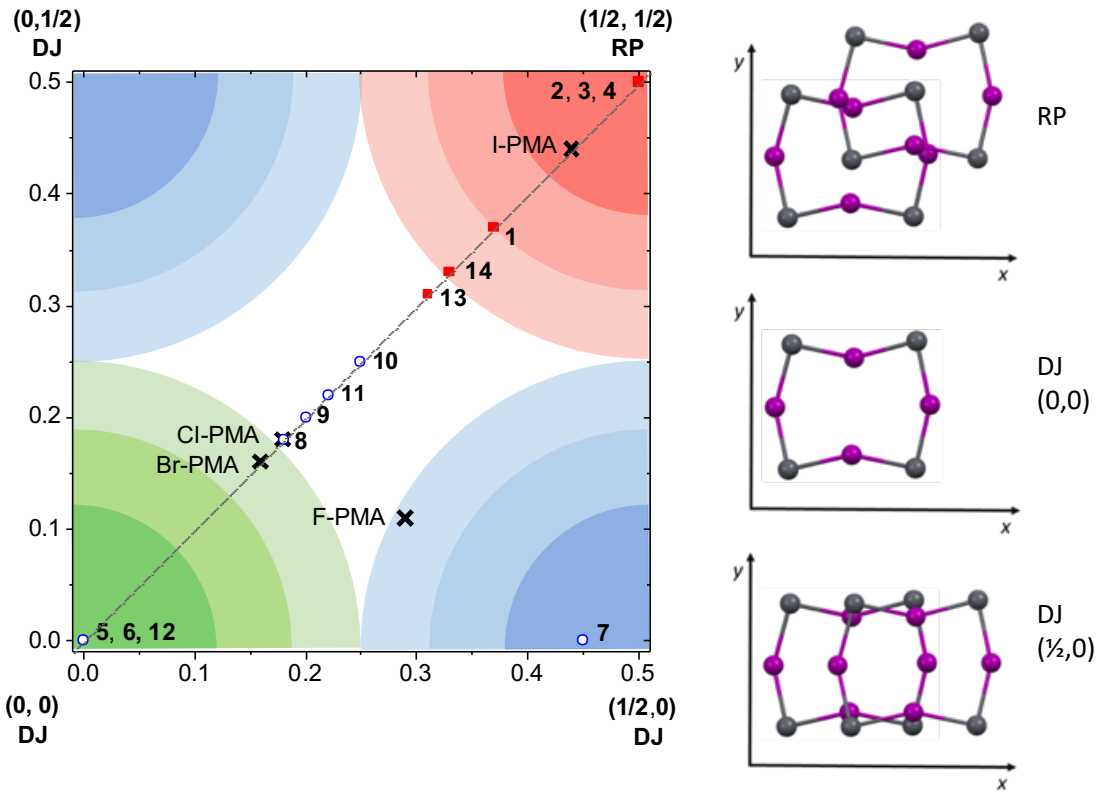

Figure 2.6 Left: Quantification of the offset of the two inorganic layers on the x and y-axes for some literature A_2PbX_4 and A'PbX_4 HOIPs, and for the $(Y\text{-}PMA)_2PbI_4$ HOIPs for which structures are reported in this work. The diagonal line indicates cases where x = y. The "×'s" represent the new structures from this report, the blue circles represent structures with DJ or nDJ stacking, and the red squares represent structures with RP or nRP stacking. Right: schematic showing that offsets of ($^1/_2$,$^1/_2$) are found for ideal Ruddlesden-Popper and (0,0) or ($^1/_2$,0) ideal Dion-Jacobson structures (purple = halide ions; gray = lead ions).

For the four $(Y\text{-}PMA)_2PbI_4$ compounds presented in this work, along with the previously reported structure of $(PMA)_2PbI_4$[232] and in common with the structure of many other 2D HOIPs, there is hydrogen bonding between the inorganic iodide ions and the ammonium groups. While the "head" of each cation, the ammonium moiety, is directed towards the inorganic sheet, the orientation of the tail is governed by the balance of "tail-tail" and, in some cases, "tail-inorganic" interactions possible. "Tail-inorganic" interactions for A_2PbX_4 HOIPs are relatively scarce; indeed, in many such structures, such as those of $(Y\text{-}PEA)_2PbI_4$ (Y-PEA = 2-(4-halophenyl)ethylammonium; Y = F, Cl, Br),[236] which contain A cations differing from the Y-PMA cations used in this work only in the presence of an

extra CH_2 group, the organic cations are arranged in bilayers between successive inorganic layers, and, thus, do not form head-to-tail bridges between the PbI_4 sheets. In the present series, however, there are hydrogen bonds from the NH_3^+ group of the cation to one PbI_4 sheet and a close approach (see Table 2) between the organic halo-substituent, Y, of the same cation and an iodide ion of the next PbI_4 sheets; in some cases, this approach may reflect a halogen bonding interaction in which Y is the halogen-bond donor (Lewis acid) and I^- the acceptor (Lewis base). In the case of $(PMA)_2PbI_4$, the H···I distance exceeds the sum of the van der Waals radii (from refs. [237] and [238]) and so likely does not represent a significant interaction.

Table 2.2 Selected Distances and Angles in the Crystal Structures of $(Y\text{-}PMA)_2PbI_4$.

Y	I···Y distance (Å)	Sum of Y and I VdW radii[a] (Å)	I···Y-C_4 angle (°)	Interlayer I···I distance (Å)
H[b]	3.488	3.07	140.78	9.197
F	3.478, 3.954	3.45	118.7, 157.2	7.777
Cl	4.039, 3.933	3.73	146.41, 164.49	9.546
Br	3.894, 3.805	3.83	150.67, 164.49	9.553
I	3.931	3.96	168.2	10.771

[a]Van der Waals radii for halogens and hydrogen from refs. [237] and [238], respectively. [b]Ref. [232].

In the case of $(F\text{-}PMA)_2PbI_4$ one of two inequivalent Y···I distances is close to the sum of van der Waals radii, but the corresponding C-F···I angle is far from the ideal 180° expected for a halogen bond. In this case, a hydrogen bonding interaction between the fluorine atom and the NH_3^+ of a neighboring cation may be responsible for the close F···I approach. In the case of $(Cl\text{-}PMA)_2PbI_4$, the Cl···I distances are both somewhat larger than the sum of the van der Waals radii, and both C–Cl···I interactions are more linear than the short contact

seen for Y = F, with the shortest of the two being the more linear. For $(Br\text{-}PMA)_2PbI_4$ and $(I\text{-}PMA)_2PbI_4$ the Y···I contacts are similar to or shorter than van der Waals contacts. The C–Br···I angles are similar to the C–Cl···I angles, while the C–I···I interaction in the most linear of any of the C–Y···I interactions seen here. The tendency towards shorter (relative to van der Waals radii) and more linear interactions seen for the heavier halogens is consistent with the strength of C– Y bonds as halogen bond donors, which increases in the order F < Cl < Br < I (see Figure 7).[239]

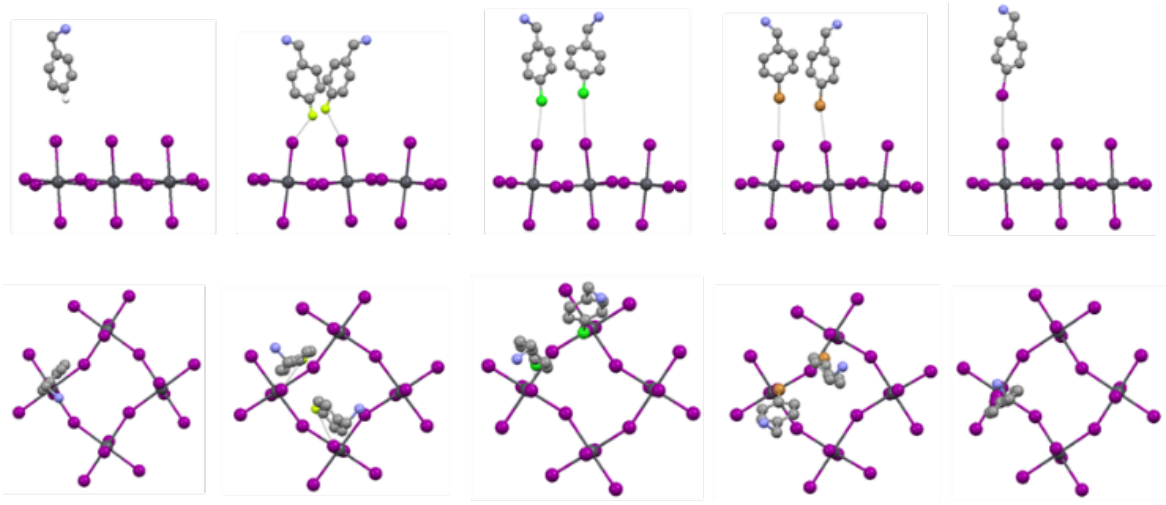

Figure 2.7 Representation of the possible close Y···I approaches between the halo substituent of the organic cation and the inorganic sheet of $(Y\text{-}PMA)_2PbI_4$ (from left to right, Y = H, F, Cl, Br, and I). Note that for Y = F, Cl, Br there are two inequivalent cations in the asymmetric unit, whereas there is only one for Y = H, I.

Figure 8 shows a related observation. For 2D HOIPs incorporating increasingly large cations of similar structure, a linear trend is often observed between the interlayer stacking distance and molecular volume of the cation (see black squares for the alkylammonium series in Figure 8). In the present series, the trend is not observed (see red circles in Figure 9); in particular the Cl- and Br-PMA derivatives show very similar interlayer spacings, despite an increase in cation volume of 7.7 $cm^3\ mol^{-1}$. This can be attributed to the counterbalancing of the increased molecular volume by stronger halogen-bonding in the

Br-PMA derivative, which results in Br···I contacts that are shorter than the Cl···I distances.

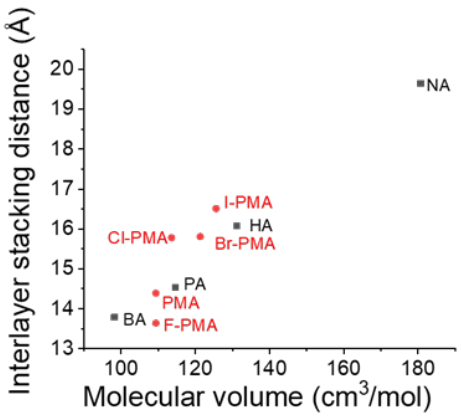

Figure 2.8 Relationship between the interlayer stacking distance and the molar volume for alkylammonium HOIPs (black squares) and for (Y-PMA)$_2$PbI$_4$ derivatives (red circles). The interlayer stacking distance is extracted from the reported crystal structure of BA (butylammonium),[240] PA (pentylammonium),[200] HA (hexylammonium),[200] and NA (nonylammomium).[55]

However, despite the evidence for halogen bonding in some of these structures, (Br-PMA)$_2$PbI$_4$ and (I-PMA)$_2$PbI$_4$, in which the strongest halogen bonding is both suggested by the crystallographic data and expected based on theoretical considerations, exhibit quite different structures, notably exhibiting nDJ and nRP offsets, respectively. In contrast, (Cl-PMA)$_2$PbI$_4$ and (Br-PMA)$_2$PbI$_4$ adopt similar packing and nDJ translations, despite their different halogen-bonding strengths. Thus, although halogen bonding allows the Y-PMA monocations to act as interlayer bridges, potentially affecting the stacking of the inorganic layers, the conformational flexibility of the cations, combined with the other cation-cation interactions present, steric hindrance, and the various distortions of the PbI$_4$ layers that can take place, means that halogen bonding is not the only factor. Interestingly, while the present series shows an evolution from RP to MnDJ to nRP with increasing halogen size potential halogen-bonding strength, a series of $(CH_3(CH_2)_{m-1}NH_3)_2PbI_4$ structures[55, 200, 240,

[241] with m = 4-10, 12, 14, 16, 18 (the m = 2 and 3 cations lead to compounds containing 1D chains of face-sharing octahedra of formula $APbI_3$,, rather than 2D HOIPs [242, 243]) shows a similar evolution from ideal RP (m = 4) to near-ideal MnDJ (m = 6) and back to ideal RP (m = 10+) with increasing alkyl chain length and increasing alkyl-alkyl van der Waals interaction (see Figure S7). Even in the (Y-PEA)$_2$PbI$_4$ series (Y = H, F, Cl, Br),[63,236] where there is a bilayer of organic cations, but in which the cation:cation interaction strength likely increases with the halogen polarizability, the deviation from ideal RP stacking increases from Y = H to F, with ideal RP stacking for Y = Cl, Br (Figure S7).

Cation-cation interactions and contacts in the (Y-PMA)$_2$PbI$_4$ structures are shown in Figure 10. As noted above, C–Y···H hydrogen bonding is present in some structures. Another interesting feature is the presence of π–π interactions between F-PMA cations; this is a rare interaction for HOIPs, with only few examples in the literature.[105] The distortions in the inorganic portion of the structures are discussed in the following section.

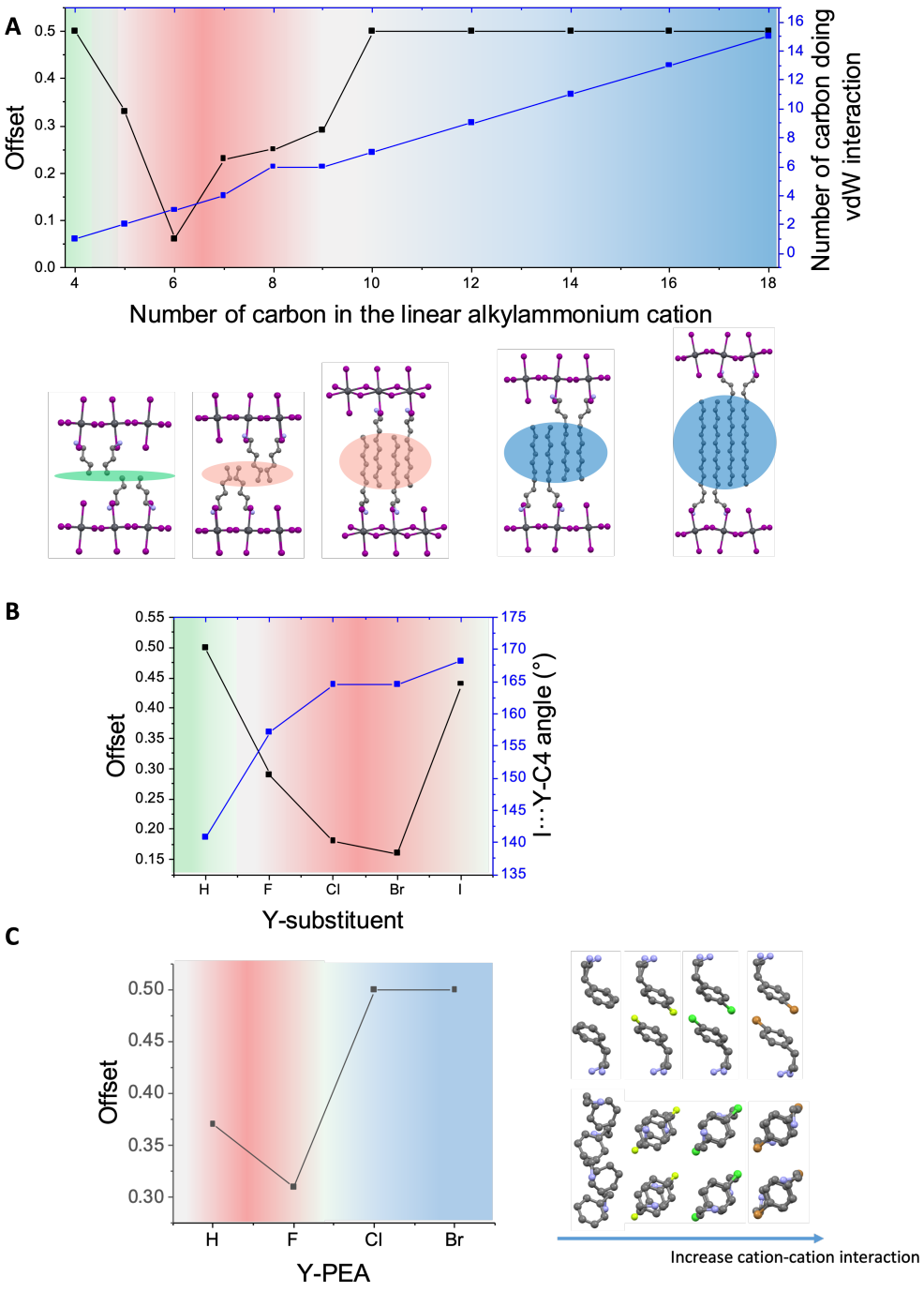

Figure 2.9 Comparison of the evolution in offset as function of cation-cation or cation-inorganic interaction for (A) $(RNH_3)_2PbI_4$ (R = alkyl, crystal data from refs. [55, 57, 92, 244]), (B) the $(Y\text{-}PMA)_2PbI_4$ series (crystal data for Y = H from ref. [232]) presented in this work, (C) $(Y\text{-}PEA)_2PbI_4$ derivatives (crystal data from refs. [63] and [73]). In all the structures considered, except that of $(F\text{-}PMA)_2PbI_4$, for which the largest of the two offsets is plotted, x- and y-offsets are equal. The right-hand portion of (C) shows increased aryl…aryl interactions with halogen size in the $(Y\text{-}PEA)_2PbI_4$ derivatives (the distance from centroid of one aryl to the plane of its neighbor increase from 3.494 to 3.576 to 3.625 Å from Y = F through Br, but, as shown, the overlap increases).

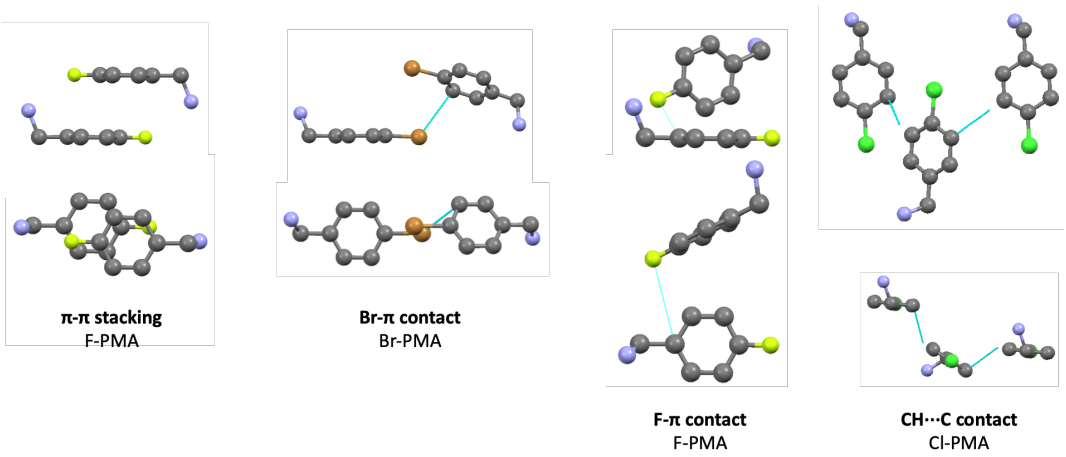

Figure 2.10 Cation-cation interactions present in the different analogues $(Y\text{-}PMA)_2PbI_4$ (Y = F, Cl, Br, I).

Various distortions have been found in the PbX_4 layers of HOIPs and, in various series of compounds, have been correlated with optical properties. One important structural parameter that can be used to describe HOIPs is the Pb-I-Pb angle (see Figure 11A and Table 3), where larger Pb-I-Pb angles represent less distortion; smaller distortions have been correlated with lower exciton energy for both RP and DJ perovskites.[31] In the series presented here, these distortions are fairly large, and fall into a relative narrow range of 150-160°. The Br-PMA compound has the smallest Pb-I-Pb angle (151°), while its F- and H-analogue have the largest (ca. 158°). The ammonium penetration past the peripheral iodine is also related to the Pb-I-Pb angle.[63] As mentioned before, the $(Cl\text{-}PMA)_2PbI_4$ and $(Br\text{-}PMA)_2PbI_4$ structures are less symmetric than the Y = H, I analogues, perhaps due to the asymmetrical ammonium penetration (see Figure 11B). $(F\text{-}PMA)_2PbI_4$ is also slightly asymmetrical. Due to the large penetration on one side, the octahedra tilt away from one another on that side, which results in a tilt towards one another on the opposite face of the PbI_4 layer, allowing only a small penetration of the other ammonium. In this series, as the

ammonium penetration is increased (taking, where relevant, the largest of the two values), the Pb-I-Pb angle is reduced, showing more distortion.

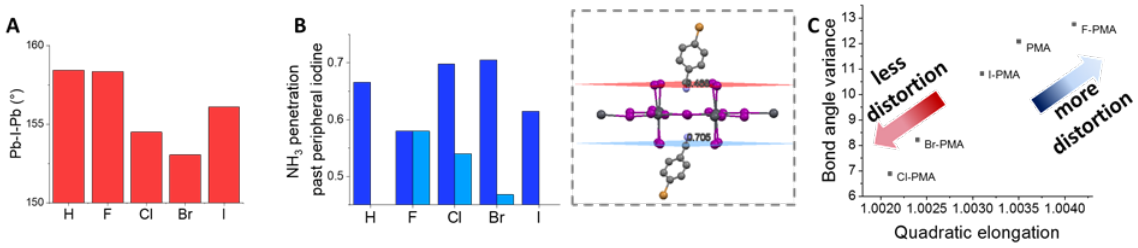

Figure 2.11 Comparisons of the Pb-I-Pb angles (A) and the ammonium penetration past the peripheral iodine (B) for $(Y\text{-}PMA)_2PbI_4$ (where, Y = H, F, Cl, Br, I). The ammonium penetration is the distance between the nitrogen of the ammonium and the plane made by the four iodine of the octahedron. Due to the crystallographic symmetry of the crystal structures, there are two values for the Cl and Br compounds. (C) Relationship between the bond angle variance and the quadratic elongation.

Table 0.3 Distortion Parameters for the PbI_4 Layers in the Crystal Structures of $(Y\text{-}PMA)_2PbI_4$.[a]

Y	Pb–I–Pb / °	r(Pb–I)av. / Å	λ_{oct}	σ^2_{oct} / (°)^2
H[b]	158.43	3.2082	1.0035	12.0819
F	158.00, 158.69	3.2090	1.0041	12.7554
Cl	153.91, 155.07	3.1907	1.0021	6.8871
Br	151.34, 154.75	3.1868	1.0024	8.2175
I	156.11	3.1840	1.0031	10.8138

[a]Calculated using VESTA.[245] [b]Ref. [232].

The distortion of the geometry of the PbI_6 octahedra from regularity has also been discussed in the literature and correlated with optical properties. This distortion can be gauged through the quadratic elongation (λ_{oct}) or the bond angle variance (σ^2_{oct}):[246]

$$\lambda_{oct} = \frac{1}{6}\sum_{i=1}^{6}\left(\frac{d_i}{d_0}\right)^2 \quad \text{Eq. 1}$$

$$\sigma^2_{oct} = \frac{1}{11}\sum_{i=1}^{12}(\alpha_i - 90)^2 \quad \text{Eq. 2}$$

where d_i is the Pb–I bond length, d_0 is the center-to-vertex distance of a regular polyhedron of the same volume, and α_i is the I-Pb-I angle. In the present series there is good correlation between the two measures of distortion (Figure 11C), consistent with that seen for most other haloplumbate HOIPs.[247] However, the distortions are all relatively small and there is no obvious trend with the identity of Y (see Table 3 and Figure 11C).

The photophysical properties of the HOIP films and powders were investigated by diffuse reflectance UV−vis spectroscopy and steady-state photoluminescence (PL)[248] spectroscopy (see Figure 12 and Table 4).

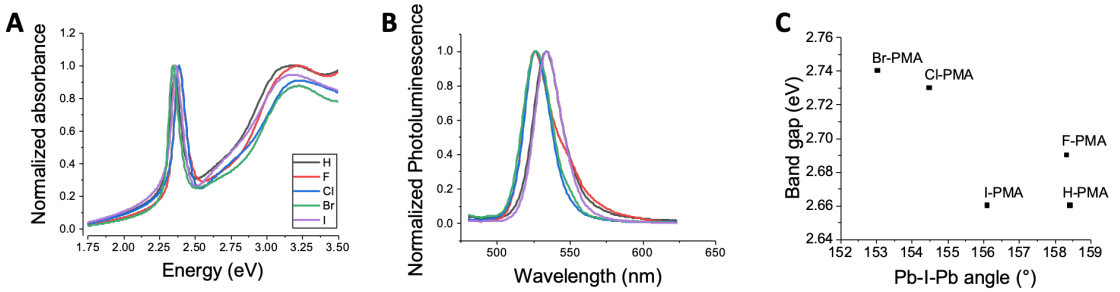

Figure 2.12 (A) Absorption and (B) photoluminescence spectra of the HOIP films. (C) Relationship between the band gap and the average of the Pb-I-Pb angle.

Table 2.4 Optical Properties of $(Y\text{-}PMA)_2PbI_4$ Films.

Y	E_g / eV	E_{ex} / eV	PL / eV	color
H	2.66	2.29	2.32	dark orange
F	2.69	2.33	2.36	dark orange
Cl	2.73	2.33	2.36	pale orange
Br	2.74	2.28	2.36	pale orange
I	2.66	2.29	2.32	dark orange

The exciton energy, E_{ex}, is estimated by extrapolating the low-energy edge of the low-energy discrete peak in the UV-visible spectra to the energy axis, while the bandgap, E_g, is estimated by extrapolating the edge of the higher energy feature to the energy axis. Overall, there is relatively little variation in the energies in the present series. As shown in Figure 7C, values of E_g (but not of E_{ex} or the PL) correlate fairly well with the Pb-I-Pb angle over

the series, a relation that has previously been suggested;[31] the deviations from this relation may be due to the competing effects of other structural features, but it should be emphasized that the ranges of Pb-I-Pb angles and E_g values are both relatively small compared to those seen in ref. [31]. Regardless, the Cl-PMA and Br-PMA derivatives, which exhibit the smallest (most distorted) Pb–I–Pb angles of this series *do* exhibit the highest values of E_g. The values of E_g also show some correlation with λ_{oct} and σ^2_{oct} (Figure 13). The PL spectrum for $(F\text{-}PMA)_2PbI_4$ is the broadest one among those collected (Figure 7B), following the expected trend where the structure with the most distorted octahedra, as measured by the quadratic elongation, has a larger full-width at half maximum (FWHM).

It is worth noting that some DJ A'PbI_4 structures have been previously found to exhibit lower band gaps than typical RP HOIPs. However, this is attributed to closer I···I interlayer distances (arising from relatively small bridging dications) and to less distorted inorganic frameworks, rather than being a direct consequence of the different stacking motifs.[16] In the present series, the *largest* band gaps are found for the MnDJ structures (Y = F, Cl, Br). However, the interlayer distances in the present MnDJ structures are much greater than those in previously studied DJ examples (and, as shown in Figure 5, there is no clear pattern in this distance between (n)RP and MnDJ structure types), and are likely sufficiently large to preclude the layer-layer interactions thought to be responsible for the red-shift of previous DJ examples. In addition, two of the MnDJ structures (Y = Cl, Br) exhibit the most distorted Pb–I–Pb angles and least distorted octahedra, while the other nDJ structure (Y = F) has the least distorted Pb–I–Pb angles and most distorted octahedra.

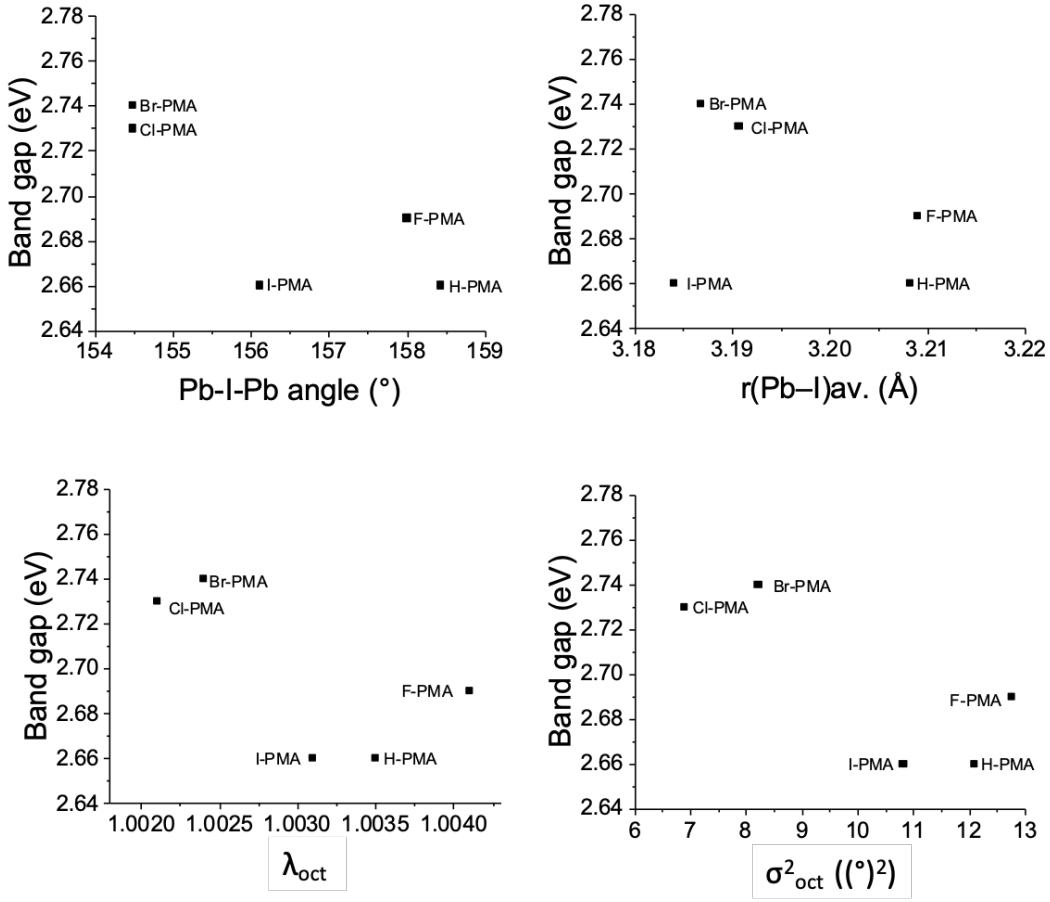

Figure 2.13 Variation of E_g with various structural parameters for $(Y\text{-}PMA)_2PbI_4$.

2.1.4 Conclusion

In summary, the structures, optical properties, film formation and stability data of a series of A_2PbI_4 HOIPs employing Y-PMA cations, where Y = F, Cl, Br and I, are reported and compared to those of their Y = H analogue. Short contacts are seen between the halo substituents of the cations and the iodides of the inorganic sheets; in particular, the Y···I distances and C–Y···I geometries seen for Y = Br and I are suggestive of halogen bonding. Moreover, we have quantified the DJ- vs. RP-like nature of 2D HOIPs according to the

offsets of subsequent inorganic layers; this may prove useful in classifying other HOIPs. We classify the Y = F, Cl and Br derivatives as "MnDJ" on the basis that they include organic monocations, but exhibit stacking of the inorganic layers that is closer to that found in DJ perovskites than in RP perovskites. For the X = I example, a more RP-like stacking is found. Examination of literature crystal structures reveals some similar behavior in other series, suggesting that the trends in thestacking motif can perhaps be correlated with those in the strength of organic-inorganic or organic-organic interactions. Based on the stacking obtained for a given cation it may even be possible to engineer stronger or weaker interactions in order to obtain whichever stacking pattern is desired. Further systematic structural studies of A_2PbX_4 HOIPs containing families of closely related cations will be required to validate or refute this idea.

The distortions of the inorganic layers in the $(Y\text{-}PMA)_2PbI_4$ series have also been examined; in particular, when the ammonium penetration is increased, the Pb-I-Pb angle is reduced, showing more distortion in the plane of the sheet. Further understanding of the role of cation-cation and cation-inorganic sheet interactions may help engineer new HOIPs; the findings presented here underscore the importance of increasing the library of HOIP structures, in particular of MnDJ structures, available in order to attempt to understand the factors determining their structural characteristics. The optical properties of the series show relative minor variations, consistent with the large interlayer spacings and highly distorted Pb-I-Pb angles found in each case.

2.2 Exciton-band tuning induced by the width of the cation in 2D lead iodide perovskite hybrids

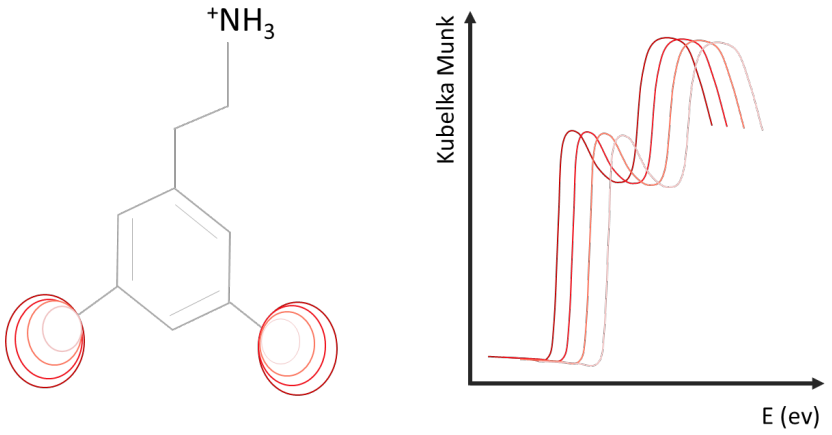

This project was accomplished with the collaboration of John Bacsa, Stephen Barlow and Seth Marder. John Bacsa, from the Crystallography Lab of Emory University, performed the single crystal X-ray diffraction experiments. Stephen Barlow helped with the data analysis and he helped to write the manuscript. Khaled Al Kurdi is acknowledged for his help with thermal measurements. Ningxin Jiang, Dr. Alexander Steiner and Tom Pickel are acknowledged for help with crystal measurement. The content of this chapter was published in Materials Chemistry Frontiers in May 2020 (DOI: 10.1039/D0QM00118J). All authors contributed to the redaction of the manuscript. This work was supported by NSERC (ES. D. Scholarship for MHT) and the AFOSR (FA9550-18-1-0499).

2.2.1 Introduction

Recently, two-dimensional (2D) hybrid organic inorganic perovskites (HOIP) have been used as the active layer for solar cells[9-18] and light emitting diodes.[19, 20] Compared with their 3D counterparts (such as $MAPbI_3$, where MA = methylammonium), they can offer superior stability and a much wider structural diversity, since the cation size is not limited by the interstitial volume of the lattice 3D lead iodide lattice. The optical properties of the perovskite can be tuned by different methods, for example, by changing the connectivity of the octahedra[179] or the halide[249-251] used. The optical characteristics of these materials are particularly relevant to solar-cell and light-emitting diode applications. Previous work, both computational[252, 253] and experimental,[254] on 3D lead iodide structures showed a relationship between the M−X−M (M = metal, X = halide) bond angles and the onset of the optical absorption of the material.[255] On increasing the size of the cation ($Cs^+ < MA^+ < FA^+$, where MA = methylammonium and FA = formamidinium), the Pb−I−Pb angle decreases due to more distortion of the network of PbI_6 octahedra, resulting in poorer Pb-Hal orbital overlap and an increased band gap.[256, 257] In 2D HOIPs, there is considerably more pronounced excitonic character than in the 3D counterparts. However, trends in the exciton energy often closely follow those in the band gap, Moreover, in some instances, the exciton energy has been found to also be correlated with the Pb−I−Pb angle.[31]

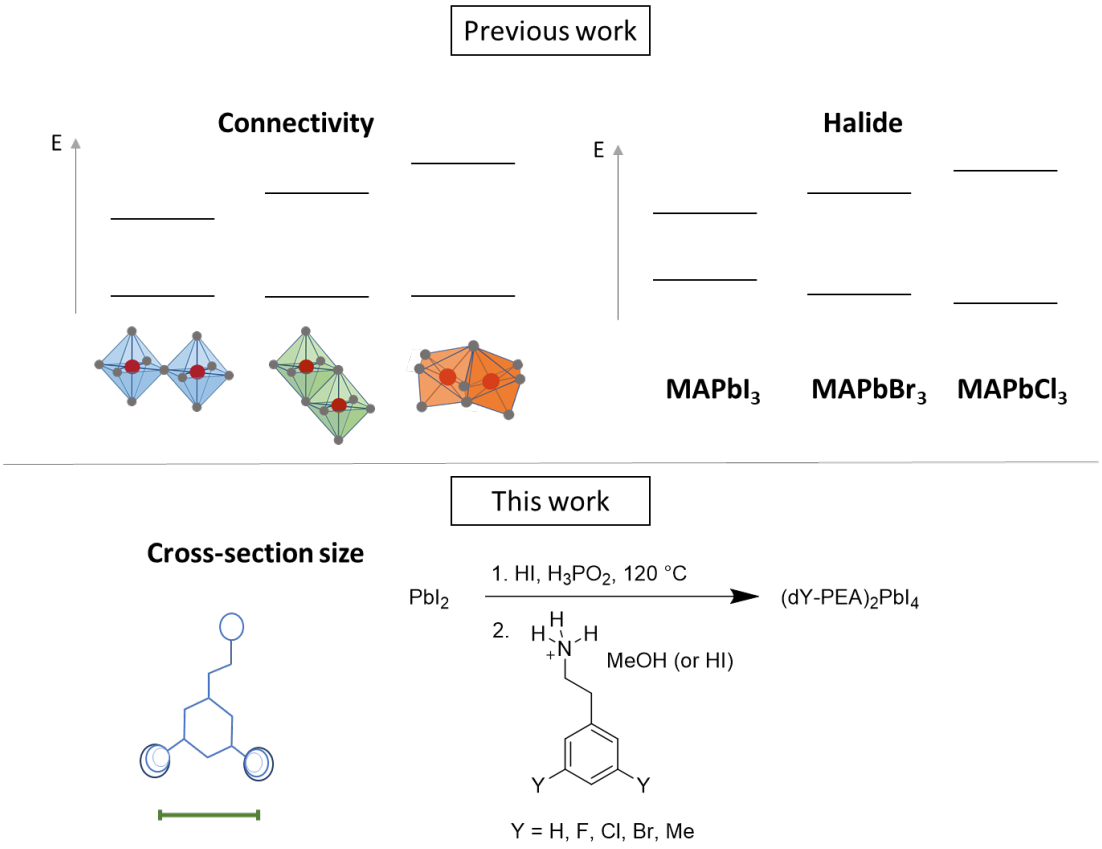

Figure 2.14 Top. Approaches to tuning the band energies of HOIPs. Trends in both excitonic and interband transitions of 2D and 3D HOIPs correlate well with the energy separation between valence and conduction bands within a series. Bottom. Approach presented here, where the width (atom-atom distance) of the cation is varied.

Knowing that the Pb−I−Pb angle correlates with the properties of the material, we were interested to probe whether the width of 2-arylethylammonium cations (defined as the distance between *meta* and *meta'* substituents) was related to this bond angle. We report the synthesis and crystal growth of a series of 2D perovskites where the aryl group have different *widths*; the *meta* substituents on phenylethylammonium (PEA) are systematically changed in the series $(dY\text{-}PEA)_2PbI_4$ where Y = H, F, Cl, Br and Me (Figure 1). We describe the structural and optical properties of these materials and compare them to those of other A_2PbI_4 species reported in the literature.

2.2.2 Experimental Procedures

Synthesis.

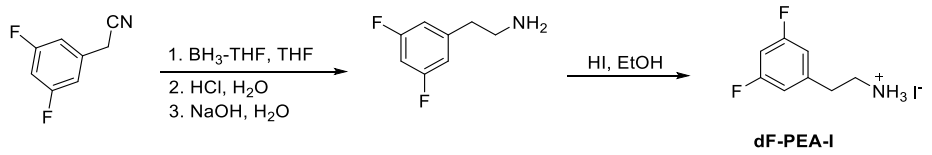

dF-PEA-I

1,3-Difluorophenylethylammonium iodide (dF-PEA-I): To a solution of 1,3-difluorophenylacetonitrile (1.5 g, 10 mmol) in THF (5 mL) was added BH_3•THF (25 mL of a 1 M solution in THF, 26 mmol) at room temperature was slowly added over 10 min under nitrogen. The mixture was heated under reflux and the reaction was followed by TLC. After 3 h, the reaction mixture was cooled in an ice bath and distilled water (20 mL) was added cautiously; this was followed by addition of concentrated aqueous hydrochloric acid (20 mL) over a period of 5 min. The mixture was brought up to reflux for 1 h and was then cooled in an ice bath and poured into water (20 mL) and brought to pH 12 with a 40% aqueous sodium hydroxide solution and extracted with dichloromethane (3 × 25 mL). The combined organic extracts were dried over sodium sulfate and then filtered; the solvent was removed using a rotary evaporator, while keeping the solution below 40 °C, to yield a colorless oil. The crude oil was dissolved in ethanol (2 mL) and cooled down to 0 °C. Hydroiodic acid (57 wt% aqueous solution) was added and the mixture was stirred for 1 h at 0 °C. The solid was filtered and washed with diethyl ether to yield dF-PEA-I as a white powder (1.4 g, 49%). ^{1}H NMR (DMSO-d_6, 500 MHz): 7.09 (td, J = 9.6, 4.8 Hz, 1H), 7.06 – 7.02 (m, 2H), 3.11 (t, J = 7.6 Hz, 2H), 2.90 (t, J = 7.6 Hz, 2H) ^{13}C{^{1}H} NMR (DMSO-d_6, 125 MHz): δ 163.78, 142.18, 112.64, 102.71, 39.73, 32.91. HRMS-ESI (*m/z*): calcd for

$C_8H_{10}NF_2$ $(M–I)^+$, 158.0772; found, 158.0776. Anal. Calcd for $C_8H_{10}NF_2I$: C, 33.71; H, 3.54; N, 4.91. Found: C, 33.96; H, 3.56; N, 4.90.

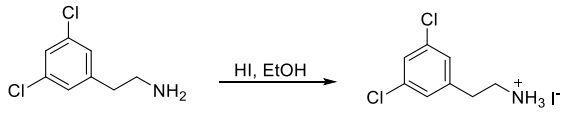

dCl-PEA-I

1,3-Dichlorophenylethylammonium iodide (dCl-PEA-I): 1,3-dichlorophenylethylamine (1 g, 5.26 mmol) was dissolved in ethanol (2 mL) and cooled down to 0 °C. Hydroiodic acid (57 wt% aqueous solution) was added and the mixture was stirred for 1 h at 0 °C. The solid was filtered and washed with diethyl ether to yield dCl-PEA-I as a white powder (1.3 g, 78%). 1H NMR (DMSO-d6, 500 MHz): δ 7.75 (br, 3H), 7.51 (s, 1H), 7.39 (s, 2H), 2.37 (br, 2H), 2.88 (t, J = 7.5 Hz, 2H). 13C{1H} NMR (DMSO-d6, 125 MHz): δ 141.99, 134.51, 128.27, 126.97, 32.65. HRMS-ESI (m/z): calcd for C8H10NCl2 (M–I)+, 190.0182; found, 190.0185. Anal. Calcd for $C_8H_{10}NCl_2I$: C, 30.22; H, 3.17; N, 4.41. Found: C, 30.51; H, 3.10; N, 4.23.

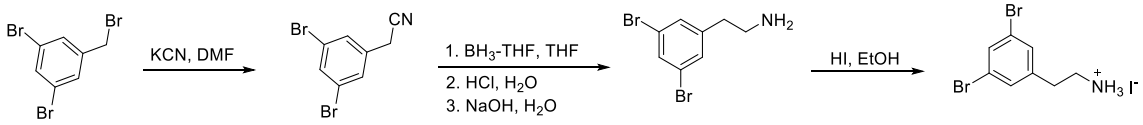

dBr-PACN dBr-PEA-I

2-(3,5-dibromophenyl)acetonitrile (dBr-PACN): To a stirred solution of 3,5-Dibromobenzyl bromide (4 g, 12 mmol) in a mixture of EtOH (63 mL) and H_2O (16 mL) was added NaCN (0.73 g, 15 mmol). The mixture was stirred under reflux until completion of the reaction. Then the EtOH was removed under reduced pressure and the residue was extracted with EtOAc, dried over Na_2SO_4 and filtered. The filtrate was evaporated under

reduced pressure and the resulting residue was purified by flash column chromatography (1:9 Ethyl acetate/Hexanes) to obtain a white powder (2.49 g, 76%). ^{1}H NMR ($CDCl_3$, 500 MHz): 7.68 (s, 1H), 7.47 (s, 2H), 3.75 (s, 2H). $^{13}C\{^{1}H\}$ NMR ($CDCl_3$, 125 MHz): δ 134.1, 133.4, 129.8, 123.7, 116.5, 22.9. HRMS-ESI (m/z): calcd for $C_8H_5NBr_2$ $(M+H)^+$, 272.8783; found, 272.8784. Anal. Calcd for $C_8H_5NBr_2$: C, 34.95; H, 1.83; N, 5.09. Found: C, 35.13; H, 1.67; N, 4.98.

2-(3,5-dibromophenyl)ethan-1-amine (dBr-PEA-I): 2-(3,5-dibromophenyl)acetonitrile (1.0 g, 3.63 mmol) in anhydrous tetrahydrofuran (2 mL) was added to 1M solution of BH_3-THF (9 mL, 9.1 mmol) over 10 min at room temperature. Following the addition, the mixture was heated under reflux and under argon. The reaction was cooled, water was added and the mixture was extracted with dichloromethane. The organic layer was washed with brine (4.5 mL), dried over sodium sulfate and evaporated at reduced pressure to yield transparent oil (1.02g, 100%). The product was used without further purification. HI solution (0.91 mL, 5 mmol) was added dropwise to a cold (0 °C), stirred solution of 2-(3,5-dibromophenyl)ethan-1-amine (1.02 g, 3.7 mmol) in ethanol (0.6 mL). The solution was stirred for 30 minutes and the solvent was evaporated. The resulting solids were filtered through paper and washed repeatedly with diethyl ether to afford a yellow powder. The product was precipitated in ether from ethanol to afford a white powder (0.79 g, 53%). ^{1}H NMR (DMSO-d6, 500 MHz): δ 7.75 (t, J=1.8Hz, 1H), 7.73 (br, 3H), 7.55 (d, J=1.8Hz, 2H), 3.10 (q, J=7.0 Hz, 2H), 2.86 (t, J=7.5Hz, 2H). $^{13}C\{^{1}H\}$ NMR (DMSO-d_6, 125 MHz): δ 142.6, 132.3, 131.5, 123.0, 32.6. HRMS-ESI (m/z): calcd for $C_8H_{10}NBr_2$ $(M+H)^+$, 277.9175; found, 277.9175. Anal. Calcd for $C_8H_{10}NBr_2I$: C, 23.62; H, 2.48; N, 3.44. Found: C, 23.48; H, 2.66; N, 3.30.

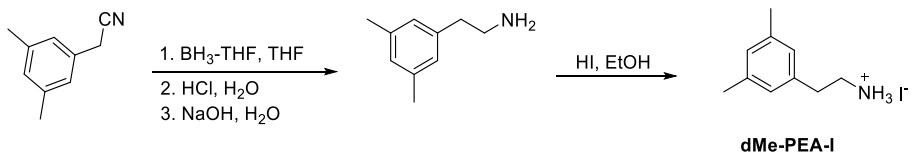

dMe-PEA-I

1,3-Dimethylphenylethylammonium iodide (dMe-PEA-I): To a solution of 1,3-dimethylphenylacetonitrile (1.7 g, 12 mmol) in THF (5 mL) was added BH_3•THF (25 mL of a 1 M solution in THF, 30 mmol) at room temperature was slowly added over 10 min under nitrogen. The mixture was heated under reflux and the reaction was followed by TLC. After 3 h, the reaction mixture was cooled in an ice bath and distilled water (20 mL) was added cautiously; this was followed by addition of concentrated aqueous hydrochloric acid (20 mL) over a period of 5 min. The mixture was brought up to reflux for 1 h and was then cooled in an ice bath and poured into water (20 mL) and brought to pH 12 with a 40% aqueous sodium hydroxide solution and extracted with dichloromethane (3 × 25 mL). The combined organic extracts were dried over sodium sulfate and then filtered; the solvent was removed using a rotary evaporator, while keeping the solution below 40 °C, to yield a colorless oil. The crude oil was dissolved in ethanol (2 mL) and cooled down to 0 °C. Hydroiodic acid (57 wt% aqueous solution) was added and the mixture was stirred for 1 h at 0 °C. The solid was filtered and washed with diethyl ether to yield dMe-PEA-I as a white powder (0.7 g, 22%). ^{1}H NMR (DMSO-d_6, 500 MHz): δ 7.74 (br, 3H), 6.89 (s, 1H), 6.86 (s, 2H), 3.02 (t, J = 7.9 Hz, 2H), 2.77 (t, J = 7.9 Hz, 2H), 2.25 (s, 6H). 13C{1H} NMR (DMSO-d6, 125 MHz): δ 138.03, 137.43, 128.63, 126.87, 40.45, 33.36, 21.36. HRMS-ESI (m/z): calcd for $C_{10}H_{16}N$ (M–I)+, 150.1274; found, 150.1277. Anal. Calcd for $C_{10}H_{16}NI$: C, 43.34; H, 5.82; N, 5.05. Found: C, 43.22; H, 5.95; N, 4.94.

General synthesis of bulk crystals. PbI_2 (1 eq) was dissolved in HI (57 wt% aqueous solution) and stirred at 100 °C for 2 min. A solution of dY-PEA-I (2 eq) in HI and MeOH was added to the hot PbI_2 solution and the resultant mixture was stirred at 130 °C for 2 min. The solution was then allowed to crystallize at room temperature for 12 h. The solids were filtered and dried under high vacuum.

Bis(3,5-difluorophenylethylammonium) tetraiodoplumbate ((dF-PEA)2PbI4). PbI_2 (510 mg, 0.1 mmol) in HI (10 mL). dF-PEA-I (580 mg, 0.2 mmol) in MeOH (10 mL) gave pale orange crystals (560 mg, 54%). Anal. Calcd. for (C8H10NF2)2PbI4: C, 18.64%; H, 1.96%; N, 2.72%. Found: C, 18.80%; H 1.85%; N, 2.76%.

Bis(3,5-dichlorophenylethylammonium) tetraiodoplumbate ($(dCl\text{-}PEA)_2PbI_4$). PbI_2 (50 mg, 0.1 mmol) in HI (4 mL). dCl-PEA-I (68 mg, 0.2 mmol) in HI (4 mL) and MeOH (2 mL) gave dark orange crystals (90 mg, 81%). Anal. Calcd. for $(C_8H_{10}NCl_2)_2PbI_4$: C, 17.52%; H, 1.84%; N, 2.55%. Found: C, 17.56%; H 1.71%; N, 2.50%.

Bis(3,5-dibromophenylethylammonium) tetraiodoplumbate ($(dBr\text{-}PEA)_2PbI_4$). PbI_2 (46 mg, 0.1 mmol) in HI (0.5 mL). dBr-PEA-I (64 mg, 0.2 mmol) in MeOH (2.5 mL) gave dark orange crystals (68 mg, 53%). Anal. Calcd. for $(C_8H_{10}NBr_2)_2PbI_4$: C, 15.08%; H, 1.58%; N, 2.20%. Found: C, 15.36%; H 1.55%; N, 2.22%.

Bis(3,5-dimethylphenylethylammonium) tetraiodoplumbate ($(dMe\text{-}PEA)_2PbI_4$). PbI_2 (46 mg, 0.1 mmol) in HI (0.5 mL). dMe-PEA-I (94 mg, 0.2 mmol) in MeOH (2 mL) gave dark orange crystals (68 mg, 64%). Anal. Calcd. for $(C_9H_{16}N)_2PbI_4$: C, 21.79%; H, 3.25%; N, 2.83%. Found: C, 21.87%; H 2.71%; N, 2.56%.

Bis(3-chlorophenylethylammonium) tetraiodoplumbate ($(3Cl\text{-}PEA)_2PbI_4$). PbI_2 (460 mg, 1 mmol) in HI (10 mL). 3Cl-PEA (310 mg, 2 mmol) in HI (0.2 mL) and MeOH (5 mL) gave orange crystals (706 mg, 69%). Anal. Calcd. for $(C_8H_{11}NCl)_2PbI_4$: C, 18.69%; H, 2.16%; N, 2.72%. Found: C, 18.84%; H 2.00%; N, 2.72%.

Bis(3-bromophenylethylammonium) tetraiodoplumbate ($(3Br\text{-}PEA)_2PbI_4$). PbI_2 (461 mg, 1 mmol) in HI (10 mL). 3Br-PEA (400 mg, 2 mmol) in HI (0.2 mL) and MeOH (2.5 mL) gave orange crystals (685 mg, 66%).

Bis(3-methylphenylethylammonium) tetraiodoplumbate ($(3Me\text{-}PEA)_2PbI_4$). PbI_2 (460 mg, 1 mmol) in HI (10 mL). 3Me-PEA (270 mg, 2 mmol) in HI (0.2 mL) and MeOH (5 mL) gave orange crystals (620 mg, 63%). Anal. Calcd. for $(C_9H_{14}N)_2PbI_4$: C, 21.90%; H, 2.86%; N, 2.84%. Found: C, 22.03%; H 2.88%; N, 2.87%.

General synthesis of single crystals. A solution of PbI_2 in HI (1 mL of a 25 mg mL^{-1} solution) was added to a vial. 2 mL of MeOH was added on top. The cation was dissolved in a minimum of MeOH and added in the vial slowly. Crystals started appearing at the interface between the HI and MeOH after 24 h.

Thermal gravimetric analysis (TGA). TGA was performed using Mettler Toledo Instrument (TGA/ DSC 3+ Star e system) with a scan rate set to 10 ^oC min^{-1}, under a nitrogen gas flow of 80 mL min^{-1}.

Absorbance. Absorbance and diffuse reflectance were measured on a Cary 5000 UV-vis/NIR.

Photoluminescence. Photoluminescence were measured on a Horiba FL3-2i Fluorometer with an excitation at 350 nm.

Powder X-ray diffraction (PXRD). PXRD patterns were acquired on a Panalytical XPert PRO Alpha-1 XRD Diffractometer using Cu K X-ray tube radiation at a voltage of 45 kV and 40 mA, with an incident beam Johannsson monochromator and an X'Celerator solid-state detector. The diffraction pattern was scanned over the angular range of 3-40° with a step size of 0.016°, at room temperature.

Single-crystal X-ray diffraction. Suitable crystals were selected from the reaction mixtures obtained using the general procedure above and were mounted on a loop with paratone oil on a XtaLAB Synergy-S, Dualflex, HyPix diffractometer. The crystals were cooled at the temperature indicated in Table S1 during data collection. Using Olex2,[258] the structure was solved with the ShelXT[259] structure solution program using Intrinsic Phasing and refined with the ShelXL[260] refinement package using least squares minimization. Details of the crystals, data collection, and data refinements are summarized in Tables S1 and S2, while data may be obtained in CIF format from the Cambridge Crystallographic Data Center (www.ccdc.cam.ac.uk); the deposition numbers for the structures are CCDC 1986784-1986789 and 1987208. Simulated powder patterns were calculated by Mercury software[4] using the CIF from the single-crystal X-ray experiment.

Table 2.5 Single-crystal data and structure refinement data.

	$(dF\text{-}PEA)_2PbI_4$ $\mathbf{C_{32}H_{41}F_8N_4Pb_2I_8}$	$(dCl\text{-}PEA)_2PbI_4$ $\mathbf{C_{16}H_{20}Cl_4N_2PbI_4}$	$(dBr\text{-}PEA)_2PbI_4$ $\mathbf{C_{16}H_{20}Br_4N_2PbI_4}$	$(dMe\text{-}PEA)_2PbI_4$ $\mathbf{C_{10}H_{16}NPbI_4}$
Formula weight (g mol^{-1})	2063.27	1096.93	1274.77	1015.26
Temperature (K)	109(4)	106(2)	106(9)	100(2)
Crystal system	triclinic	monoclinic	monoclinic	monoclinic
Space group	$P\bar{1}$ (2)	$P2_1/c$ (14)	$P2_1/c$ (14)	$P2_1/c$ (14)
a (Å)	12.21680(19)	18.0323(4)	18.1147(7)	18.0933(15)
b (Å)	12.27147(16)	8.64280(10)	8.7853(3)	8.7451(7)
c (Å)	16.8535(3)	8.8430(2)	8.8694(3)	8.9006(7)
α (°)	100.4107(13)	90	90	90
β (°)	95.9(10)	100.226(2)	95.314(4)	98.823(3)
γ (°)	90.0024(12)	90	90	90
Volume ($Å^3$)	2471(4)	1356.29(5)	1403.42(9)	1391.66(19)
Z	2	2	2	2
Z'	1	0.5	0.5	0.5
ρ_{calc} (g cm^{-3})	2.773	2.686	3.012	2.423
μ (mm^{-1})	11.858	11.173	16.088	10.524
F(000)	1842.0	984	1128	920
Crystal size (mm^3)	0.195 × 0.107 × 0.073	0.539 × 0.191 × 0.063	0.30×0.16×0.02	0.213×0.182×0.147
Radiation	MoKα (λ = 0.71073)	MoKα (λ = 0.71073)	MoKα (λ = 0.71073)	MoKα (λ = 0.71073)
2Θ range for data collection (°)	3.35 to 66.28 (0.65 Å)	4.59 to 72.63 (0.60 Å)	4.52 to 51.35 (0.82 Å)	4.56 to 76.15 (0.58 Å)
Index ranges	-18 ≤ h ≤ 18 -18 ≤ k ≤ 18 -25 ≤ l ≤ 25	-30 ≤ h ≤ 30 -14 ≤ k ≤ 14 -14 ≤ l ≤ 14	-21 ≤ h ≤ 21 -10 ≤ k ≤ 10 -10 ≤ l ≤ 10	-30 ≤ h ≤ 30 -15 ≤ k ≤ 14 -14 ≤ l ≤ 15
Reflections collected	66819	41439	16074	43561
Independent reflections	18736 R_{int} = 0.0480 R_{sigma} = 0.0430	6585 R_{int} = 0.1089 R_{sigma} = 0.0572	4218 R_{int} = 0.0584 R_{sigma} = 0.0734	7239 R_{int} = 0.0454 R_{sigma} = 0.0239
Data/restraints/parameters	18736/328/528	6585/0/125	4218/69/126	7239/63/173
Goodness-of-fit on F^2	1.031	1.00	1.063	1.116
Final *R* indexes [I>=2σ(I)]	R_1 = 0.0326 wR_2 = 0.0782	R_1 = 0.0556 wR_2 = 0.1416	R_1 = 0.0654 wR_2 = 0.1835	R_1 = 0.0202 wR_2 = 0.0459
Final *R* indexes [all data]	R_1 = 0.0450 wR_2 = 0.0819	R_1 = 0.0657 wR_2 = 0.1472	R_1 = 0.0690 wR_2 = 0.1880	R_1 = 0.0223 wR_2 = 0.0464
Largest diff. peak/hole (e $Å^{-3}$)	2.29/-3.04	10.94/-3.98	5.38/-1.91	1.76/-1.12

Table 2.6 Single-crystal data and structure refinement data.

	(3Cl-PEA)$_2$PbI$_4$ **$C_{32}H_{44}Cl_4N_4Pb_2I_8$**	(3Br-PEA)$_2$PbI$_4$ **$C_{32}H_{44}Br_4N_4Pb_2I_8$**	(3Me-PEA)$_2$PbI$_4$ **$C_{18}H_{28}N_2PbI_4$**
Formula weight (g mol^{-1})	2056.09	1116.96	988.16
Temperature (K)	99.9(5)	100(2)	104(7)
Crystal system	Monoclinic	Triclinic	Triclinic
Space group	Cc (9)	$P1$ (1)	$P\bar{1}$ (2)
a (Å)	34.0099(5)	8.65320(10)	12.32860(10)
b (Å)	8.54985(11)	8.65570(10)	19.0688(2)
c (Å)	8.82458(12)	17.9336(2)	24.3751(2)
α (°)	90	86.6110(10)	67.7520(10)
β (°)	94.8655(14)	79.4250(10)	89.9860(10)
γ (°)	90	89.7100(10)	80.6850(10)
Volume (Å^3)	2556.76(6)	1318.07(3)	5222.14(9)
Z	2	2	8
Z'	0.5	2	4
ρ_{calc} (g cm^{-3})	2.671	2.814	2.514
μ (mm^{-1})	11.645	14.120	11.205
F(000)	1840	992	3555
Crystal size (mm^3)	0.324×0.19×0.092	0.219×0.181×0.07	0.347×0.119×0.084
Radiation	MoKα (λ = 0.71073)	MoKα (λ = 0.71073)	MoKα (λ = 0.71073)
2Θ range for data collection (°)	4.808 to 72.630(0.60 Å)	4.71 to 62.96 (0.68 Å)	2.35 to 56.56 (0.75 Å)
Index ranges	-56 ≤ h ≤ 56 -14 ≤ k ≤ 14 -14 ≤ l ≤ 14	-12 ≤ h ≤ 12 -12 ≤ k ≤ 12 -23 ≤ l ≤ 26	-16 ≤ h ≤ 16 -25 ≤ k ≤ 25 -31 ≤ l ≤ 32
Reflections collected	42345	24825	69618
Independent reflections	12144	11923 R_{int} = 0.0306 R_{sigma} = 0.0372	25770 R_{int} = 0.0784 R_{sigma} = 0.0774
Data/restraints/parameters	12144/162/240	15453/387/459	25770/924/958
Goodness-of-fit on F^2	1.032	1.169	1.023
Final R indexes [I>=2σ(I)]	R_1 = 0.0291 wR_2 = 0.0708	R_1 = 0.0391 wR_2 = 0.1106	R_1 = 0.0434 wR_2 = 0.1097
Final R indexes [all data]	R_1 = 0.0307 wR_2 = 0.0714	R_1 = 0.0426 wR_2 = 0.1146	R_1 = 0.0504 wR_2 = 0.1144
Largest diff. peak/hole (e Å^{-3})	1.57/-1.86	2.11/-3.06	2.37/-1.89

2.2.3 Results and Discussion

We investigated the structure and optical characteristics of lead iodide HOIPs with aromatic cations of increasing width. The width, defined here as the Y···Y distance, is incrementally enlarged by adding substituents at the 3,5-position of the PEA ring. The synthesis of the different cations is presented in the Experimental Section. The HOIPs were crystallized as pale to dark orange plates from a 1:2 solution of PbI_2 and A^+I^- in HI/MeOH (see Figure 2 and Experimental Section for detailed synthesis). We abbreviate these HOIPs as PEA (2-phenylethylammonium), dF-PEA (2-(3,5-difluorophenyl)ethylammonium), dCl-PEA (2-(3,5-dichlorophenyl)ethylammonium), dBr-PEA (2-(3,5-dibromophenyl)ethylammonium), and dMe-PEA (2-(3,5-dimethylphenyl)ethylammonium).

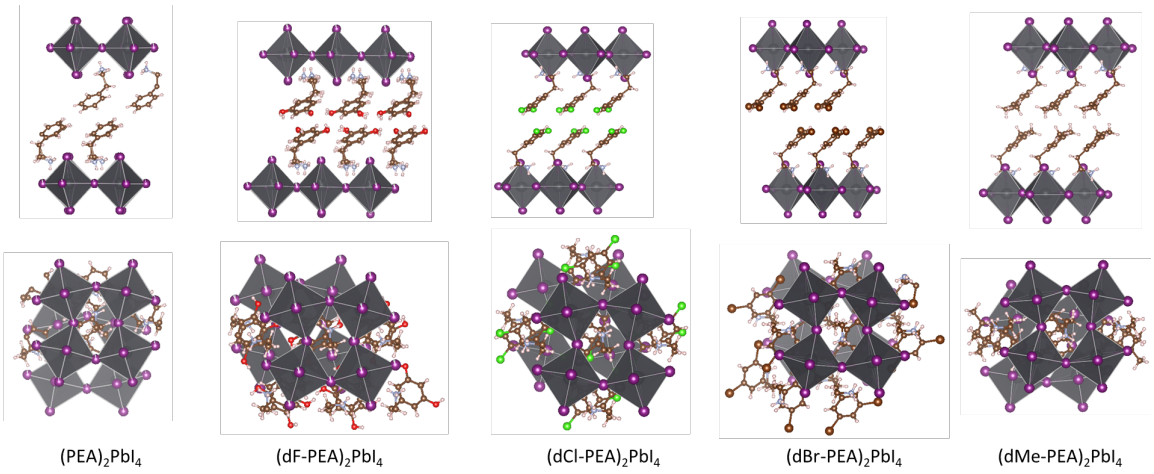

Figure 2.15 Crystal structure of $(dY\text{-}PEA)_2PbI_4$, Y = H, F, Cl, Br, Me, viewed along the plane of the inorganic sheet and after + 90° rotation around the long in-layer axis. The structure of $(PEA)_2PbI_4$ is taken from the literature.[63]

Of course, the increase of halogen atom size also results in an increase in polarizability, whereas dMe-PEA has approximately the same width as dBr-PEA, but is anticipated to be less polarizable. The purity of the crystals was assessed by elemental analysis and powder

XRD; in each case, XRD patterns for powder samples were consistent with the corresponding single-crystal structures (see Figure 3). In all cases, we obtained PbI_4^{2-} layers of corner-sharing octahedra separated by bilayers of the organic cations. In all compounds, there is hydrogen bonding between the iodides and the ammonium groups, which is typical for A_2PbI_4 HOIP structures. Based on the offset of successive inorganic layers, we can categorize dF-PEA, PEA, dCl-PEA and dMe-PEA as near-Ruddlesden-Popper structure and dBr-PEA as monocation-near-Dion-Jacobson structures (see offset in Table S3).[261]

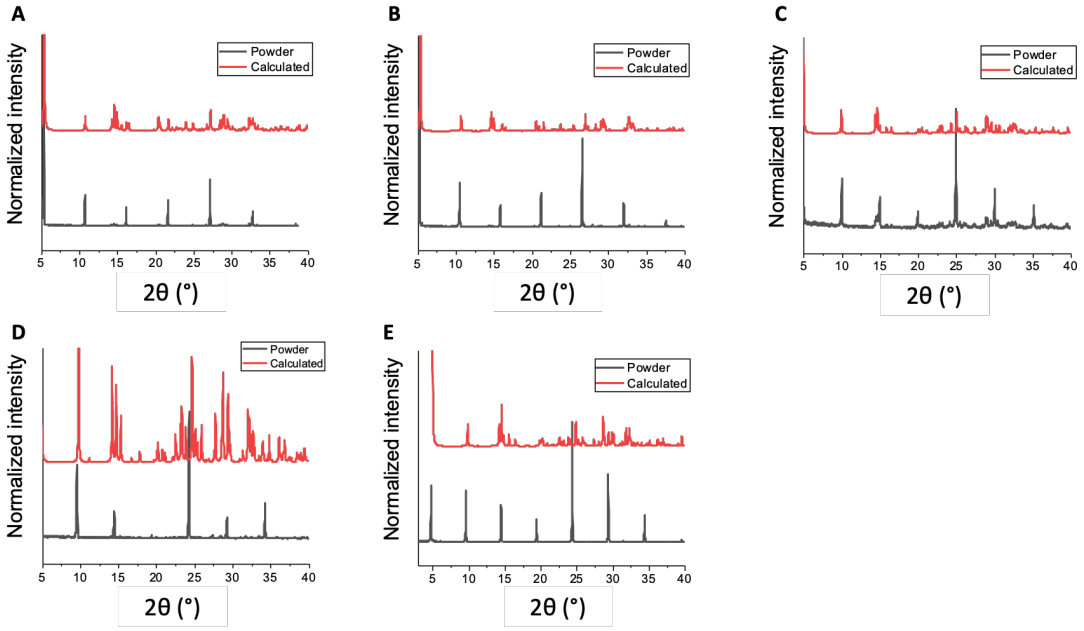

Figure 2.16 Comparison of the powder X-ray diffraction patterns for (A) $(dF\text{-}PEA)_2PbI_4$, (B) $(PEA)_2PbI_4$, (C) $(dCl\text{-}PEA)_2PbI_4$ and (D) $(dBr\text{-}PEA)_2PbI_4$ and $(dMe\text{-}PEA)_2PbI_4$ powder (gray) with a pattern calculated (red) using the single-crystal data.

Thermogravimetric analysis of the four HOIPs based on 2-(3,5-disubstitutedphenyl)ethylammonium ions (see Fig. S2, ESI) shows two distinct weight losses: one begins at ca. 230 °C, while our reference $(PEA)_2PbI_4$ starts exhibiting weight loss at 200 °C.[12] This initial weight lost is likely due to the organic cation decomposition

and loss, while the second period of weight loss is presumably due to the sublimation of the lead iodide.

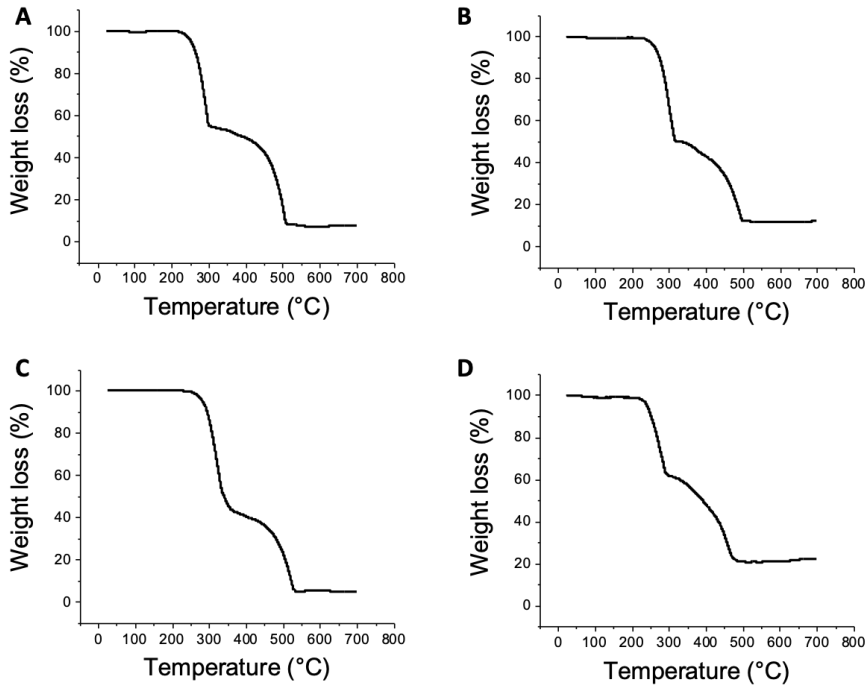

Figure 2.17 Thermogravimetric analysis of (A) $(dF\text{-}PEA)_2PbI_4$, (B) $(dCl\text{-}PEA)_2PbI_4$, (C) $(dBr\text{-}PEA)_2PbI_4$ and (D) $(dMe\text{-}PEA)_2PbI_4$ from 25 to 700 °C (5 °C min^{-1}). Weight loss for these two HOIPs begins at ca. 280 °C. This initial weight lost is likely due to the organic cation decomposition and loss, while the second period of weight loss is presumably due to the sublimation of the lead halide.

Multiple cation-cation interactions can be found in these HOIPs single crystals. For dF-PEA and dCl-PEA, the benzene rings from the two different organic layers are found to lay on top of each other. The distance between the centroid of one benzene to the plane made by another benzene is 3.343 Å for Y = F and 3.508 Å for Y = Cl, which could arise from a dipole-dipole interaction between the two cations (see Figure 5A). In the case of dBr-PEA, there is a close approach between the bromine atoms from the two layers. This may be due to a Br···Br van der Waals interaction (see Figure 5B). A close approach between the methyl groups is also seen for dMe-PEA.

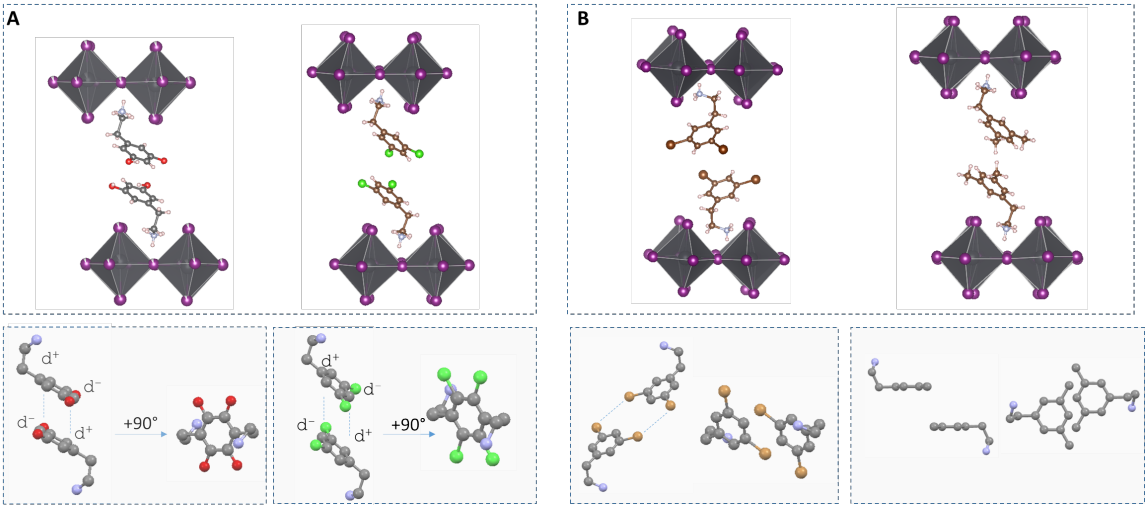

Figure 2.18 Top. Partial crystal structure showing only two or three cations per four octahedra. Bottom. Cations showing the close approaches attributed to (A) dipole-dipole interaction $(dY\text{-}PEA)_2PbI_4$, where Y = F, Cl and (B) van der Waals interaction between Br···Br in $(dBr\text{-}PEA)_2PbI_4$ (Br-Br distance 4.15 Å) and $(dMe\text{-}PEA)_2PbI_4$ (C-C distance 3.94 Å).

All compounds exhibited narrow linewidths for the photoluminescence feature characteristic of free exciton emission (Figure 6).

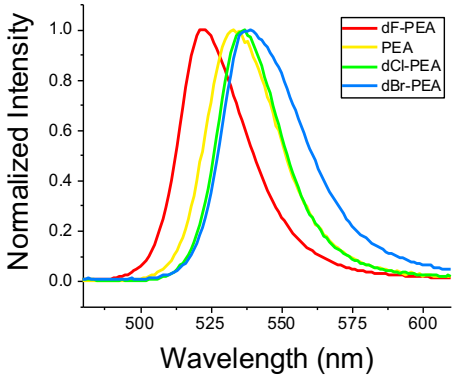

Figure 2.19 PL spectra of the different analogues $(dY\text{-}PEA)_2PbI_4$ (Y= F, H, Cl, Br) powder (excitation wavelength 400 nm).

Figure 7A shows the Kubelka-Munk transformation of the diffuse reflectance of the different HOIP powders and indicate the presence of two distinct bands. The energy of the high-energy peak is assigned to the exciton band energy (see Fig. 7A). As expected, there

is a linear relationship between the Pb−I−Pb angle and the exciton energy; the exciton band is red shifted by ca. 100 meV from dBr-PEA to dF-PEA (see Fig. 7B).[31] There is also a linear trend between the Pb−I−Pb angle and the width of the cation (see Fig. 7C). What emerges, based on these 5 compounds, is that, even if the reference compound (PEA, smallest cross-section size) does not follow the trend, we are able to show that the width of the cation is a *fair* indicator of the Pb−I−Pb of the HOIPs.

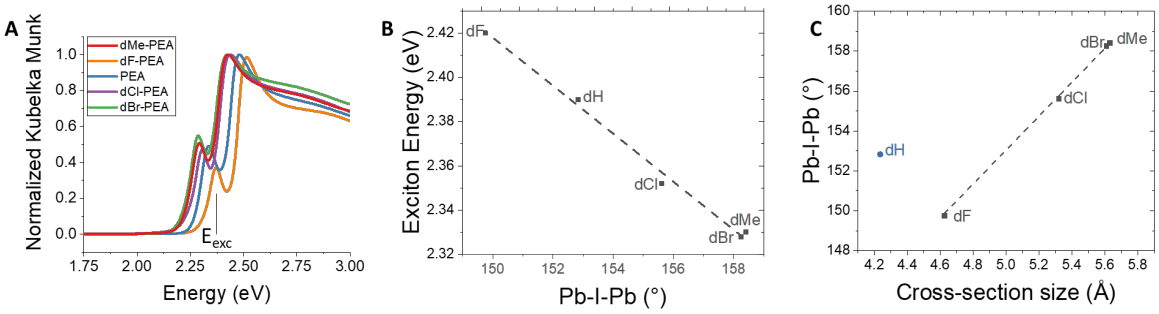

Figure 2.20 (A) Normalized Kubelka-Munk transform of diffuse reflectance data for the different HOIPs powders (with exciton energy, E_{exc}, indicated for the example of $(dF\text{-}PEA)_2PbI_4$). (B) Relationship between the exciton energy and the Pb−I−Pb angle. (C) Relationship between the Pb−I−Pb bond angle and the width (Y-Y distance calculated from the MM2-minimized geometry of the cation in Chem3D) (dH is excluded from the fit). The width of dMe-PEA is calculated as the average of the three longest H-H distances of the methyl.

In order to establish whether this trend holds true for cations other than 3,5-disubstituted PEAs, we extended the study to other families of cations (see Fig. 8). First, we synthesized *meta*-substituted phenylethylammonium-based HOIPs (3Y-PEA, where Y = Cl, Br, Me) and determined the structures. Again, the Pb−I−Pb bond angle is linearly proportional to the width. Moreover, data for three compounds fit the same linear plot between the exciton energy and the Pb−I−Pb bond angle as the dY-PEA derivatives discussd above (see Fig. 8B).

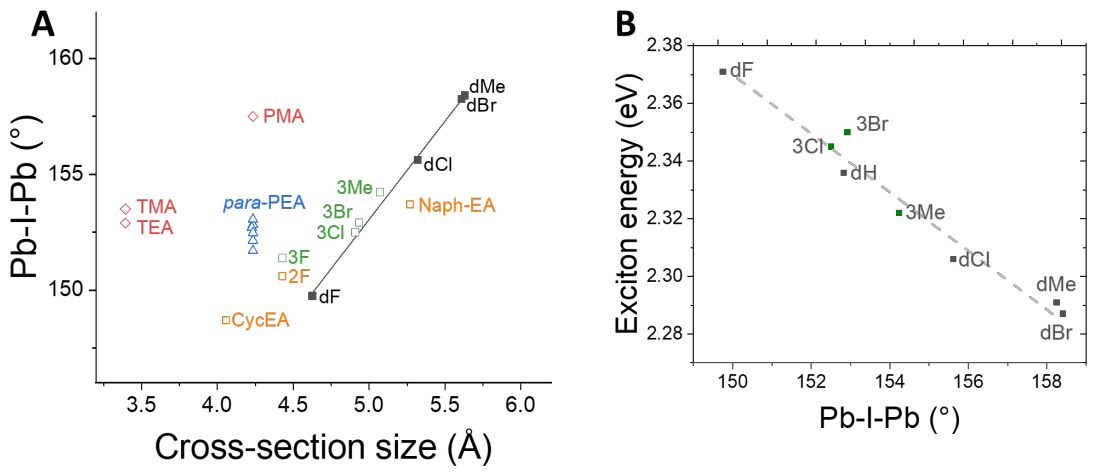

Figure 2.21 Relationship between the Pb−I−Pb bond angle and the cross-section sizes (Y-Y distance calculated from the MM2-minimized geometry in Chem3D). The Pb−I−Pb bond angle of 2F-PEA, 3F-PEA, 4F-PEA, 4Cl-PEA, 4Br-PEA, 4Ph-PEA, TMA, TEA, NEA, CycEA, PMA were calculated using the reported crystallographic data. The red diamonds are compounds that don't follow the hypothesis. The blue (*para*-PEA), black (dY-PEA), green (3Y-PEA) and yellow (others) compounds represent different families of compounds and follow the hypothesis.

We then examined additional structures available from literature reports. *para*-Substituted phenylethylammonium-based perovskites (in which the cross-section size is constant) have similar Pb−I−Pb bond angles (A_2PbI_4 where A = PEA 152.9°,[63] 4F-PEA 151.5°,[73] 4Cl-PEA 152.48°,[73] 4Br-PEA 152.15°,[73] 4Ph-PEA 153.1°,[99] 4Cl-Ph-$CH(CH_3)NH_3$ 152.7°[70]), reinforcing the hypothesis that cross-section size is an important factor in determining the Pb−I−Pb bond angle, although the data points for these derivatives do not fall on the same line as the disubstituted and *meta*-substituted derivatives. A_2PbI_4 perovskites for A = TMA[131] and TEA[81] cations (TMA = 2-(2-thienyl)methylammonium, TEA = 2-(2-thienyl)ethylammonium), which have the same cross-section size but different alkyl length, have similar Pb−I−Pb bond angles to one another, but larger than one would expect based on the trend in the disubstituted and *meta*-substituted compounds. On the other hand, Pb−I−Pb angle and cross-section size data for A_2PbI_4 perovskites based on several other cations including 2-(naphth-2-yl)ethylammonium (NEA),[63] 2-(1-

cyclohexenyl)ethylammonium (CycEA),[100] 2-fluorophenylethylammonium (2F-PEA)[262] and 2-(3-fluorophenyl)ethylammonium (3F-PEA)[72] do lie close to the line defined by the $(dY\text{-}PEA)_2PbI_4$ derivatives (and other $(3Y\text{-}PEA)_2PbI_4$ derivatives) reported here.

There are cases of families of 2D A_2PbI_4 structures reported in which the cross-section and Pb−I−Pb angle do not linearly correlate: (1) when the two layer of cations interpenetrate one another, instead of being separated in two sheets (*para*-substituted PMAs);[261] (2) when the 2D structure is not planar, but corrugated instead (as in the case of A = 2-(4-nitrophenyl)ethylammonium);[105] and (3) when the core of the cation is much larger than that of 2-(phenyl)ethylammonium (pyrene and perylene derivatives).[78-37]

2.2.4 Conclusion

We report a total of 7 new 2D HOIPs containing 1,3-disubstituted-phenylethylammonium cations, dY-PEA (Y = F, Cl, Br, Me) and 3-substituted-phenylethylammonium cations, 3Y-PEA (Y = Cl, Br, Me). We were able to demonstrate that, at least for some limited series of compounds, the width of the cation influences the distortion of the inorganic sheet through Pb−I−Pb bond angle variation, which leads to a variation of the exciton energy. There is unlikely to be a universal indicator; multiple factors must be taken into account, but it brings us closer to developing an understanding between the structure of the organic cation and the structure of the corresponding 2D HOIP. The deviations observed from the proposed relation may afford insight into other descriptors that could be looked at in the future.

CHAPTER 3: CATION ENGINEERING TO OBTAIN 1D FACE-SHARING IODOPLUMBATE PEROVSKITE-LIKE COMPOUNDS

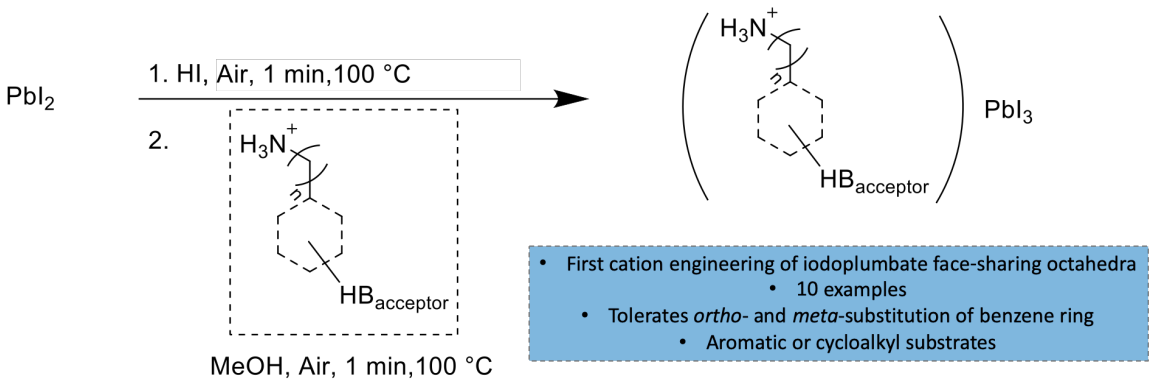

This project was accomplished with the collaboration of Allyson Boyington, Sergei Rigin, Jie Jiang, John Bacsa, Khaled Al Kurdi, Ruth Pachter, Tatiana V. Timofeeva, Nathan Jui, Stephen Barlow and Seth R. Marder. Allyson Boyington, in the group of Nathan Jui, from the Department of Chemistry and Winship Cancer Institute, Emory University, synthesized most of the cations. Sergei Rigin, in the group of Tatiana V. Timofeeva, from New Mexico Highlands University, and John Bacsa, from the Crystallography Lab of Emory University, performed the single crystal X-ray diffraction experiments. Jie Jiang, in the group of Ruth Pachter, from the Air Force Research Laboratory, performed all the theoretical calculations. John Bacsa, from the Crystallography Lab of Emory University, performed the single crystal X-ray diffraction experiments. Khaled Al Kurdi helped with the thermal experiments and helped with the data analysis. Stephen Barlow helped with the data analysis and he helped to write the manuscript. The content of this chapter is unpublished. This work was supported by NSERC (ES. D. Scholarships for MHT), the AFOSR

(FA9550-18-1-0499), the NSF (via ECCS-1608095 and through the PREM program via DMR-1523611)

3.1 Introduction

Organic-metal-halide perovskites and related structures (perovskitoids), particularly those based on lead(II) and iodide, have attracted considerable recent attention. They exhibit a remarkable combination of facile solution processibility with optical and electronic properties more characteristic of inorganic semiconductors, along with considerable structural diversity and, therefore, tunability of these optical and electronic characteristics. In turn, these properties have led to studies aimed at various applications; in particular, 3D examples have been used in highly efficient solar cells,[9-18] but other possibilities include light-emitting diodes and field-effect transistor lasers.[19, 20] Despite their high performance, the low moisture and heat stability of these materials preclude their commercialization. This has driven the interest in lower-dimensional hybrid perovskites and perovskitoids that, in addition to higher stability, offer structural versatility, prompting their use as active components in a wide range of optoelectronic applications.

The crystal structures of hybrid iodoplumbate perovskites and perovskitoids consist of an inorganic portion consisting of catenated PbI_6 octahedra bearing an overall negative charge and positively charged organic cations. The optical and electrical properties are primarily determined by the basic connectivity (2D vs. 1D etc, vertex- vs. edge- vs. face-sharing octahedra) and subtle structural details (e.g., octahedral distortions) of the lead iodide part, which, in turn, are dictated by the properties of the organic cation, including its steric characteristics, geometry, charge, charge-bearing group(s), and its ability to engage in non-covalent interactions with other cations or with the inorganic portions.

Many hybrid iodoplumbates have been synthesized and structurally characterized; for example, more than one hundred different organic cations have been successfully incorporated into 2D hybrid iodoplumbates. However, it is not well understood what structural features of the cation favor the formation of a 2D structure, and what features favor lower dimensional (1D or 0D) material. Development of reliable guidelines relating the cation's structure to the formation of different classes of low-dimensional hybrid perovskite and perovskitoid materials, would be highly desirable and would enable engineering materials with specific structures and properties.

1D perovskites, in the strict sense, consist of chains of vertex-sharing octahedra but haloplumbate examples, A_3PbHal_5 (A = organic cation, Hal = halogen), are relatively rare. On the other hand, reports of perovskitoid, where there are chains of octahedra sharing faces instead of vertices, which is refer to here as 1D face-sharing iodoplumbates (FSIPs), $APbI_3$, are somewhat more numerous.

Compared with 3D and 2D perovskites, where the cation is generally an ammonium ion or another protonated nitrogen, a much wider range of cations, including sulfonium,[154] phosphonium,[155, 156] tropylium,[157] and protonated amide[158] ions, can also be used in 1D FSIPs. In addition to using small simple cations, much complex cations can be incorporated in the 1D structures, such as large chromophores,[143, 173, 175, 176, 180, 184] alkali metal,[153] transition-metal complexes,[159-163] and lanthanide complexes.[152, 165]

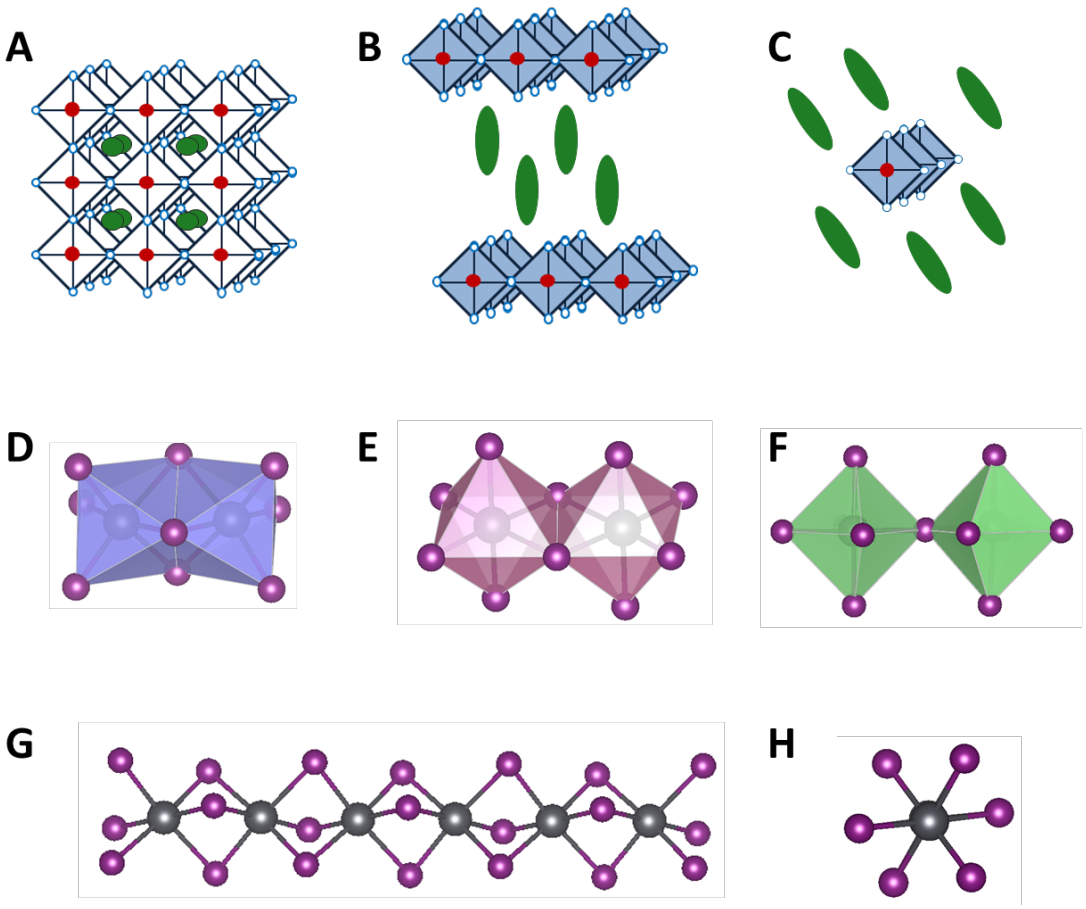

Figure 3.1 Structural variation in perovskites and perovskitoids. Top: schematic structures of (A) 3D, (B) 2D and (C) 1D perovskites. Center: different connectivities of octahedra: (D) face-sharing, (E) edge-sharing, and (F) vertex-sharing. Bottom: representation of a 1D face-sharing wire where the wire propagation is in the axis (G) parallel or (H) perpendicular to the page.

While 2D perovskite can be considered as quantum well structures, the structure of 1D inorganic−organic hybrid metal halides can be regarded as nanoarrays of parallel quantum wires isolated by organic components,[263] which leads to stronger quantum confinement.[264] Depending on the cation used, 1D FSIPs can have a wide range of optical and electronic properties. Aspects studied include their visible light absorption,[157] high dielectric constant,[265] high photo-conductivity,[266, 267] luminescence,[149] and their use as potential photo or thermochromic,[143, 169] photocatalytic,[268] switchable dielectric,[166-169] hybrid ferroelectrics,[149, 170-172] magnetic,[165] and third-order nonlinear optical (NLO)[183] materials.

In many cases, 1D $APbI_3$ perovskitoids have higher conductivity compared to their 2D perovskite analogues.[269, 270] While the optical properties of 3D and 2D Pb/I perovskites can only be tuned to rather limited extent (~150 meV in each case), the optical properties of 1D $APbI_3$ perovskitoids can be varied to a larger extent due to the large variety of cation that can be incorporated. For 1D $APbI_3$, either the optical property arises from the cation itself, for example, by using of a cyanine heptamethine cation that imparts near-IR absorption property, [10] or from interactions between the cation and the haloplumbate portion of the compound, for example by using a naphthalene diimide that can engage in charge transfer interactions with the iodide of the haloplumbate.[173, 271] In most cases, $APbI_3$ 1D FSIPs photoluminescence (PL) have a large Stokes shift (~1.2 eV) and broad PL width that suggests strong exciton -interaction.[272] PL emission is thought to arise from self-trapped exciton recombination, a characteristic of systems with easily deformable lattice;[273] in contrast, there are only few 2D examples with broadband photoluminescence.

In most cases, 1D $APbI_3$ have increased moisture and heat stability compare to 2D and 3D perovskites,[26, 27] with some examples even stable to immersion in water.[94] This stability has led to the recent use of 1D $APbI_3$ compounds to protect three-dimensional (3D) perovskite films.[274] They have been shown to prevent iodide ion migration from the 3D perovskite film, be a robust barrier against environmental degradation, and mitigate charge-carrier recombination.[275-277]

To date there exists no reliable general strategy for ensuring formation of 1D FSIPs, beyond the use of bulky cations lacking hydrogen-bond donor groups. Although it has been recognized that synthetic conditions affect the crystal structure obtained, no guidelines for using primary ammonium-based cations to engineer the structure have been proposed

yet.[235, 278, 279] Here, the first example of how the choice of different ammonium cations of the general type $R(CH_2)_nNH_3^+$ (R = aryl, substituted cyclohexyl; n = 1, 2) can be used to engineer 1D FSIP crystals (Fig. 2) is reported. Within a series of cations the formation of 1D FSIPs can be correlated with cases with cation-cation hydrogen bonding interactions – either between neighboring cations or within a cation – are possible. Specifically, seven new crystals using hydrogen-bond acceptor (HBA) groups on the *ortho*- or *meta*-positions of a 2-phenylethylammonium (PEA) cation were obtained. On the other hand, the corresponding methyl-substituted PEA (which doesn't hydrogen bond) analogues afford 2D perovskites. The approach is further expended to examples of 2-(napthyl)ethylammonium (NEA), phenylmethylammonium (PMA), and cyclohexylmethyl ammonium (CycMA) cations. The crystal structures of the new materials and their optical properties are discussed. A detailed description of the relative arrangement of the 1D wires in the 1D FSIP structures is presented here, as well as a comparation to other examples found in the literature.

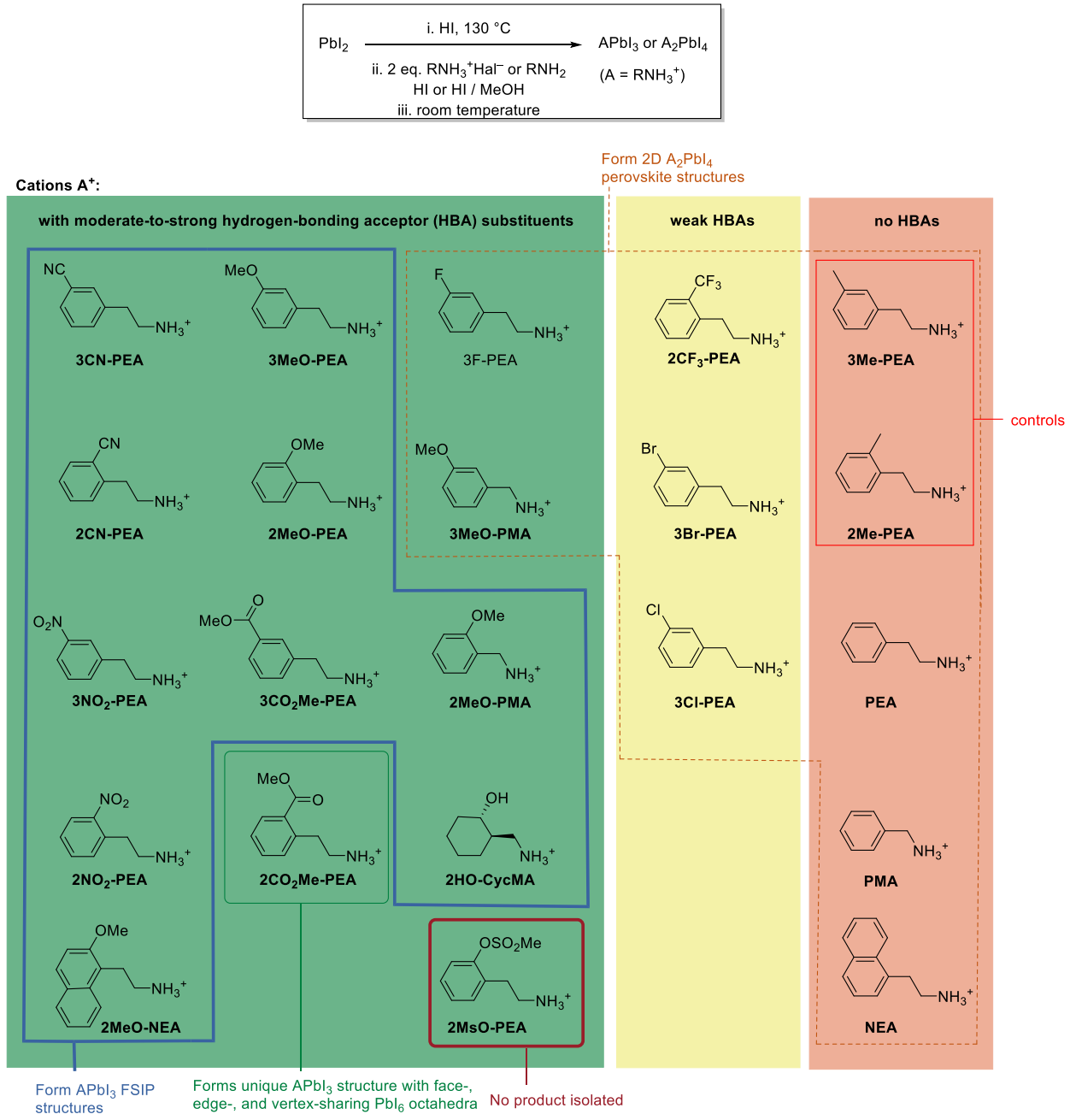

Figure 3.2 Top: general synthesis of hybrid organic-inorganic materials used in this work. Bottom: structures of cations employed, and structure types obtained. The use of cations in bold in HIPC synthesis has not previously been reported, while HIPCs derived from 3F-PEA,[280] 3Cl-PEA, 3Br-PEA, PMA[76] and NEA[63] are reported in the literature.

3.2 Experimental Procedures

Synthesis of 2-Arylethylammonium Salts

All reactions were set up on the bench top and conducted under argon atmosphere while subjected to irradiation from blue LEDs. Silica gel chromatography was carried out using Siliaflash® P60 silica gel obtained from Silicycle. Photoredox catalyst *N*-phenylphenothiazine[281] and *tert*-butylvinyl carbamate[282] were prepared according to literature procedures. Other chemicals were purchased and used as received unless stated otherwise. DMSO was distilled over CaH_2 and degassed by sonication under vacuum after adding deionized water (Fisher Scientific) (20:1 DMSO/H_2O) and stored under N_2.

General Procedure

The general procedure for the synthesis of 2-arylethylammonium salts was adapted from the literature procedure for photoredox hydroarylation of vinylamine derivatives.[282] An oven-dried Schlenk flask with a stir bar was sealed with a septa and cooled to room temperature under vacuum. The tube was charged with PTH (5 mol%), sodium formate (3 equiv), haloarene (if solid, 1 equiv), and *tert*-butylvinyl carbamate (2.5 equiv). The atmosphere was exchanged by applying vacuum and backfilling with N_2 three times. Under N_2 atmosphere, the tube was charged with haloarene (if liquid, 1 equiv) and cyclohexanethiol (5 mol%); separately degassed 20:1 DMSO:H_2O (to give a 0.1 M solution of haloarene) was then added via syringe. The resulting mixture was stirred for 16 hours under irradiation with two blue LED lamps (PARsource PowerPAR LED Bulb-Blue 15 Watt available at www.1000bulbs.com). The reaction was quenched with saturated aqueous sodium bicarbonate solution (100 mL) and extracted with ethyl acetate (3 x 100

mL). The organic extracts were combined, dried over magnesium sulfate, filtered, and concentrated by rotary evaporation. The crude residue was purified by flash column chromatography using the indicated solvent mixture to afford the boc-protected compound which was carried forward to deprotection. The boc-protected compound was stirred overnight in 25% TFA/DCM. The reaction mixture was concentrated by rotary evaporation, azeotroped with toluene (this process was conducted a total of three times), and the residue was reconstituted in diethyl ether. If the TFA salt precipitated under these conditions, it was collected by filtration on a Buchner funnel to give the title compound. If the solid salt was not obtained, cold methanolic HCl (~5-10 mL) was added dropwise to the mixture in ether was added dropwise to give the HCl salt of the amine. The mixture was then concentrated by rotary evaporation and diethyl ether was added to aid in salt formation. The HCl salt was collected by filtration on a Buchner funnel.

2-(2-(Methylsulfonyl)oxy)phenylethylammonium chloride, 2MsO-PEA-Cl. Following the general procedure, the reaction of 2-iodophenyl methanesulfonate (0.447 g, 1.5 mmol, 1 equiv), *tert*-butyl vinylcarbamate (0.536 g, 3.75 mmol, 2.5 equiv), PTH (20 mg, 0.075 mmol, 5 mol%), sodium formate (0.306 g, 4.5 mmol, 3 equiv), and cyclohexanethiol (9 μL, 0.075 mmol, 5 mol%) provided the boc-protected product after purification by silica gel chromatography (5:95 to 30:70 EtOAc:hexanes). The purified product was then stirred overnight in 25% TFA/DCM (12 mL). The reaction mixture was concentrated by rotary evaporation and azeotroped with toluene. Diethyl ether was added, followed by cold methanolic HCl. The mixture was concentrated by rotary evaporation and reconstituted in diethyl ether to yield a light orange crystalline solid which was collected by filtration (0.265 g, 70% yield). ^{1}H NMR (500 MHz, methanol-d_4) δ 7.52–7.26 (m, 4H), 3.43–3.18 (m, 2H),

3.11 (dd, J = 9.4, 6.0 Hz, 2H). $^{13}C\{^{1}H\}$ NMR (126 MHz, methanol-d_4) δ 147.63, 130.96, 130.07, 128.64, 127.48, 122.43, 48.11, 47.94, 47.77, 47.60, 47.43, 47.26, 47.09, 39.29, 37.26, 27.78. HRMS (ESI) m/z: [M^+-Cl] calcd. for $C_9H_{14}NO_3S$, 216.0689. Found, 216.0374.

2-(2-(Methoxycarbonyl)phenyl)ethylammonium chloride, 2MeOC(O)-PEA-Cl. Following the general procedure, the reaction of methyl 2-chlorobenzoate (0.215 g, 1.50 mmol, 1 equiv), *tert*-butyl vinylcarbamate (0.536 g, 3.75 mmol, 2.5 equiv), PTH (21.0 mg, 0.075 mmol, 5 mol%), sodium formate (0.306 g, 4.50 mmol, 3 equiv), and cyclohexanethiol (9 μL, 0.075 mmol, 5 mol%) provided the boc-protected compound after purification by silica gel chromatography (10:90 to 20:80 EtOAc:hexanes). The purified compound was then stirred overnight in 25% TFA/DCM (12 mL). The reaction was concentrated by rotary evaporation and azeotroped with toluene. Diethyl ether was added followed by cold methanolic HCl. The mixture was concentrated by rotary evaporation and reconstituted in diethyl ether to yield an off-white crystalline solid, which was collected by filtration (0.288 g, 89% yield). The physical properties and spectral data match those reported. ^{1}H NMR (500 MHz, methanol-d_4) δ 7.99 (d, J = 7.7 Hz, 1H), 7.57 (t, J = 7.6 Hz, 1H), 7.46 – 7.36 (m, 2H), 3.92 (s, 3H), 3.43 – 3.15 (m, 4H). ^{13}C NMR (126 MHz, Methanol-d_4) δ 167.58, 138.32, 132.56, 131.42, 130.82, 129.48, 127.24, 51.33, 48.09, 47.92, 47.75, 47.58, 47.41, 47.24, 47.07, 40.55, 32.02. HRMS (ESI) *m/z*: [M^+-Cl] calcd. for $C_{10}H_{14}NO_2$, 180.1019. Found, 180.0689.

2-(2-Cyanophenyl)ethylammonium chloride, 2NC-PEA-Cl.[283] Following the general procedure, the reaction of 2-chlorobenzonitrile (1.1 g, 8 mmol, 1 equiv), *tert*-butyl vinylcarbamate (2.86 g, 20 mmol, 2.5 equiv), PTH (110 mg, 0.40 mmol, 5 mol%), sodium

formate (1.6 g, 24 mmol, 3 equiv), and cyclohexanethiol (49 μL, 0.4 mmol, 5 mol%) provided the boc-protected compound after purification by silica gel chromatography (5:95 to 30:70 EtOAc:hexanes). The purified product was then stirred overnight in 25% TFA/DCM (30 mL). The reaction was concentrated by rotary evaporation and azeotroped with toluene. Diethyl ether was added followed by cold methanolic HCl. The mixture was concentrated by rotary evaporation and reconstituted in diethyl ether to yield a white crystalline solid which was collected by filtration (0.834 g, 57% yield).

2-(2-Methylphenyl)ethylammonium trifluoroacetate, 2Me-PEA-CF_3CO_2. Following general procedure A, the reaction of 2-iodotoluene (0.127 mL, 1.00 mmol, 1 equiv), *tert*-butyl vinylcarbamate (0.358 g, 2.5 mmol, 2.5 equiv), PTH (13.5 mg, 0.05 mmol, 5 mol%), sodium formate (0.204 g, 3.00 mmol, 3 equiv), and cyclohexanethiol (6 μL, 0.05 mmol, 5 mol%) provided the boc-protected product after purification by silica gel chromatography (5:95 to 20:80 EtOAc:hexanes). The purified product was then stirred overnight in 25% TFA/DCM (8 mL). The reaction was concentrated by rotary evaporation and azeotroped with toluene. Diethyl ether was added to provide a white crystalline solid which was collected by filtration (0.165 g, 71% yield). The spectral data match those reported.[284]

2-(3-Methylphenyl)ethylammonium trifluoroacetate, 3Me-PEA-CF_3CO_2. Following the general procedure, the reaction of 3-iodotoluene (0.128 mL, 1.00 mmol, 1 equiv), *tert*-butyl vinylcarbamate (0.358 g, 2.5 mmol, 2.5 equiv), PTH (13.5 mg, 0.05 mmol, 5 mol%), sodium formate (0.204 g, 3.00 mmol, 3 equiv), and cyclohexanethiol (6 μL, 0.05 mmol, 5 mol%) provided the boc-protected product after purification by silica gel chromatography (5:95 to 20:80 EtOAc:hexanes). The purified product was then stirred overnight in 25% TFA/DCM (8 mL). The reaction was concentrated by rotary evaporation and azeotroped

with toluene. Diethyl ether was added to provide a white crystalline solid which was collected by filtration (0.154 g, 66% yield). The physical properties and spectral data match the reported values.[285]

2-(3-Cyanophenyl)ethylammonium chloride, 3NC-PEA-Cl. Following the general procedure, the reaction of 3-iodobenzonitrile (0.343 g, 1.5 mmol, 1 equiv), *tert*-butyl vinylcarbamate 0.536 g, 3.75 mmol, 2.5 equiv), PTH (21 mg, 0.075 mmol, 5 mol%), sodium formate (0.306 g, 4.5 mmol, 3 equiv), and cyclohexanethiol (9 μL, 0.075 mmol, 5 mol%) provided the boc-protected after purification by silica gel chromatography (5:95 to 30:70 EtOAc:hexanes). The purified product was then stirred overnight in 25% TFA/DCM (12 mL). The reaction was concentrated by rotary evaporation and azeotroped with toluene. Diethyl ether was added followed by cold methanolic HCl. The mixture was concentrated by rotary evaporation and reconstituted in diethyl ether to yield a white crystalline solid which was collected by filtration (0.202 g, 74% yield). The spectral data match those reported.[286]

2-(2-(Methoxycarbonyl)phenyl)ethylammonium chloride, 2MeOC(O)-PEA-Cl. Following the general procedure, the reaction of methyl-3-iodobenzoate (0.393 g, 1.50 mmol, 1 equiv), *tert*-butyl vinylcarbamate (0.536 g, 3.75 mmol, 2.5 equiv), PTH (21 mg, 0.075 mmol, 5 mol%), sodium formate (0.306 g, 4.50 mmol, 3 equiv), and cyclohexanethiol (9 μL, 0.075 mmol, 5 mol%) provided the boc-protected product after purification by silica gel chromatography (5:95 to 30:70 EtOAc:hexanes). The purified product was then stirred overnight in 25% TFA/DCM (8 mL). The reaction was concentrated by rotary evaporation and azeotroped with toluene. Diethyl ether was added followed by cold methanolic HCl. The mixture was concentrated by rotary evaporation and

reconstituted in diethyl ether to yield a white crystalline solid which was collected by filtration (0.255 g, 79% yield). The spectral data match those reported.[287]

Synthesis of hybrid organic-inorganic A_nPbI_{n+2} compounds

General procedure for bulk crystals/powder synthesis: PbI_2 (1 eq.) was dissolved in HI (57 wt% aqueous solution) and stirred at 130 °C for 2 min. A solution of a salt of the cation (2 eq.) in HI (or HI and MeOH) was added and the resultant mixture was stirred at 130 °C for 2 min. The solution was then allowed to crystallize at room temperature for 24 h. The solids were filtered and dried under high vacuum.

2-(3-Cyanophenyl)ethylammonium triiodoplumbate ((3CN-PEA)PbI_3): Beige crystals (36 mg, 56%) from 46 mg (0.1 mmol) PbI_2 in 250 µL HI solution and 37 mg (0.2 mmol) 3CN-PEA-Cl in 500 µL HI. Anal. Calcd. for $(C_9H_{11}N_2)PbI_3$: C, 14.71%; H, 1.51%; N, 3.81%. Found: C, 14.93%; H 1.46%; N, 3.88%.

2-(2-Cyanophenyl)ethylammonium triiodoplumbate ((2CN-PEA)PbI_3): Beige crystals (41 mg, 64%) from 46 mg (0.1 mmol) PbI_2 in 250 µL HI solution and 36 mg (0.2 mmol) 3CN-PEA-Cl in500 µL HI. Anal. Calcd. for $(C_9H_{11}N_2)PbI_3$: C, 14.71%; H, 1.51%; N, 3.81%. Found: C, 14.92%; H 1.50%; N, 3.81%.

2-(3-Nitrophenylethylammonium triiodoplumbate ((3NO_2-PEA)PbI_3): Beige crystals (51 mg, 68%) from 46 mg (0.1 mmol) PbI_2 in 250 µL HI solution and 58 mg (0.2 mmol) 3NO_2-PEA-I in 500 µL HI. Anal. Calcd. for $(C_8H_{11}N_2O_2)PbI_3$: C, 12.73%; H, 1.47%; N, 3.71%. Found: C, 12.91%; H 1.32%; N, 3.55%.

2-(2-Nitrophenyl)ethylammonium triiodoplumbate ($(2NO_2\text{-PEA})PbI_3$): Beige crystals (50 mg, 67%) from 46 mg (0.1 mmol) PbI_2 in 250 µL HI solution and 58 mg (0.2 mmol) $2NO_2$-PEA-I (58 mg, 0.2 mmol) in 500 µL HI. Anal. Calcd. for $(C_8H_{11}N_2O_2)PbI_3$: C, 12.73%; H, 1.47%; N, 3.71%. Found: C, 12.70%; H 1.43%; N, 3.58%.

2-(3-Methoxyphenyl)ethylammonium triiodoplumbate ($(3MeO\text{-PEA})PbI_3$): Yellow powder (60 mg, 77%) from 92 mg (0.2 mmol) PbI_2 in 2 mL HI solution and 64 mg (0.4 mmol) 3MeO-PEA-I in 200 µL HI and 2mL MeOH. Anal. Calcd. for $(C_9H_{14}NO)PbI_3$: C, 14.61%; H, 1.91%; N, 1.89%. Found: C, 14.79%; H 1.96%; N, 1.80%.

2-(2-Methoxyphenyl)ethylammonium triiodoplumbate ($(2MeO\text{-PEA})PbI_3$): Beige crystals (180 mg, 67%) from 224 mg (0.5 mmol) PbI_2 in 5 mL HI solution and 312 mg (1 mmol) 2MeO-PEA-I in 500 µL HI and 2 mL MeOH (2 mL). Anal. Calcd. for $(C_9H_{14}NO)PbI_3$: C, 14.61%; H, 1.91%; N, 1.89%. Found: C, 14.72%; H 1.93%; N, 1.86%.

2-(3-(Methoxycarbonyl)phenyl)ethylammonium triiodoplumbate ($(3CO_2Me\text{-PEA})PbI_3$): Yellow powder (45 mg, 49%) from 46 mg (0.1 mmol) PbI_2 in 250 µL HI solution and 43 mg (0.1 mmol) $3CO_2$Me-PEA-Cl in 250 µL HI and 250 µL MeOH. Anal. Calcd. for $(C_{10}H_{14}NO_2)PbI_3$: C, 15.64%; H, 1.74%; N, 1.82%. Found: C, 15.90%; H 1.74%; N, 1.80%.

2-(2-(Methoxycarbonyl)phenyl)ethylammonium triiodoplumbate ($(2CO_2Me\text{-PEA})PbI_3$): Yellow powder (45 mg, 49%) from 46 mg (0.1 mmol) PbI_2 in 200 µL HI solution and 47 mg (0.2 mmol) $2CO_2$Me-PEA-Cl in 200 µL HI and 200 µL MeOH. Anal. Calcd. for $(C_{10}H_{14}NO_2)PbI_3$: C, 15.64%; H, 1.74%; N, 1.82%. Found: C, 12.68%; H 1.37%;

N, 1.44%. Satisfactory elemental analysis could not be obtained; $(2CO_2Me\text{-}PEA)PbI_3$ seems unstable over 2 days.

3-Methoxybenzylammonium tetraiodoplumbate ($(3MeO\text{-}PMA)_2PbI_4$): Yellow powder (28 mg, 34%) from 46 mg (0.1 mmol) PbI_2 in 200 µL HI solution and 30 mg (0.2 mmol) 3MeO-PMA in 200 µL HI. Anal. Calcd. for $(C_8H_{11}NO)_2PbI_4$: C, 19.39%; H, 2.44%; N, 2.83%. Found: C, 19.59%; H 2.20%; N, 2.82%.

2-Methoxybenzylammonium triiodoplumbate ($(2MeO\text{-}PMA)PbI_3$): Yellow powder (15 mg, 18%) from 46 mg (0.1 mmol) PbI_2 200 µL in HI solution and 28 mg (0.2 mmol) 2MeO-PMA in 200 µL HI. Anal. Calcd. for $(C_8H_{11}NO)PbI_3$: C, 13.23%; H, 1.67%; N, 1.93%. Found: C, 15.34%; H 1.81%; N, 2.13%. Satisfactory elemental analysis could not be obtained; $(2MeO\text{-}PMA)PbI_3$ seems unstable over 2 days.

2-(2-Methoxynaphthalen-1-yl)ethylammonium triiodoplumbate ($(2MeO\text{-}NEA)PbI_3$): Yellow powder (73 mg, 47%) from 100 mg (0.2 mmol) PbI_2 in 400 µL HI solution and stirred at 130 °C 50 mg (0.4 mmol) MeO-NEA-Cl in 400 µL HI and 200 µL MeOH. Anal. Calcd. for $(C_{10}H_{14}NO_2)PbI_3$: C, 15.64%; H, 1.74%; N, 1.82%. Found: C, 15.90%; H 1.74%; N, 1.80%.

(trans-2-Hydroxycyclohexyl)methylammonium triiodoplumbate ($(2HO\text{-}CycMA)PbI_3$): Yellow powder (133 mg, 90%) from 100 mg (0.2 mmol) PbI_2 in 200 µL HI solution and 40 mg (0.4 mmol) 2HO-CycMA-Cl in 200 µL HI. Anal. Calcd. for $(C_{10}H_{14}NO_2)PbI_3$: C, 11.71%; H, 2.25%; N, 1.95%. Found: C, 11.85%; H 2.07%; N, 1.99%.

2-(3-Methylphenyl)ethylammonium tetraiodoplumbate ($(3Me\text{-}PEA)_2PbI_4$): Orange powder (180 mg, 67%) from 46 mg (0.1 mmol) PbI_2 in 200 mL HI solution and 28 mg (0.2 mmol) 3Me-PEA-CO_2CF_3 in 200 μL HI and 200 μL MeOH. Anal. Calcd. for $(C_9H_{14}N)_2PbI_4$: C, 21.90%; H, 2.86%; N, 2.84%. Found: C, 21.68%; H 2.71%; N, 2.78%.

2-(2-Methylphenyl)ethylammonium tetraiodoplumbate ($(2Me\text{-}PEA)_2PbI_4$): Yellow powder (13 mg, 16%) from 47 mg (0.1 mmol) PbI_2 in 200 μL HI and 34 mg (0.2 mmol) 2Me-PEA-CO_2CF_3 in 200 μL HI and 200 μL MeOH. Anal. Calcd. for $(C_9H_{14}N)_2PbI_4$: C, 21.90%; H, 2.86%; N, 2.84%. Found: C, 21.72%; H 2.70%; N, 2.78%.

2-(2-Trifluoromethylphenyl)ethylammonium tetraiodoplumbate ($(2CF_3\text{-}PEA)_2PbI_4$): Yellow powder (13 mg, 16%) from 47 mg (0.1 mmol) PbI_2 in 200 μL HI and 34 mg (0.2 mmol) 2CF_3-PEA in 200 μL HI and 200 μL MeOH. Anal. Calcd. for $(C_9H_{14}N)_2PbI_4$: C, 21.90%; H, 2.86%; N, 2.84%. Found: C, 21.72%; H 2.70%; N, 2.78%.

General procedure for single crystal growth: 1 mL of a solution of PbI_2 in HI (100 mg mL^{-1}) was added to a test tube and 2 mL of MeOH was layered on top. The cation iodide salt was prepared from mixing the corresponding amine or cationic salt (5 eq.) in a minimum of MeOH, to which two drops of HI were added. This solution was slowly layered on top of the MeOH layer. The solution was then allowed to crystallize at room temperature for 24-72h.

Thin Films FSIP. A solution made by dissolving FSIP crystals (10 mg) in DMF (100 μL) was spincoated at 4000 rpm for 45 s onto a clean UV-ozoned glass in a N_2-filled glovebox. The films were annealed for 30 min at 100 °C.

UV−Vis Absorption Spectroscopy. Absorbance spectra were measured with a Cary 5000 UV−vis/NIR spectrometer.

Fluorescence Spectroscopy. Fluorescence spectra were measured with a Horiba Jobin Yvon Fluorolog 3-2i spectrometer.

Thermogravimetric analyses (TGA). TGA were measured under nitrogen atmosphere on a Pyris 1 TGA (PerkinElmer) at a heating rate of 15 °C min^{-1} from 50-700 °C.

DFT Calculations. DFT calculations were carried out with the Vienna ab initio simulation package VASP 5.4.[288, 289] The Kohn-Sham equations are solved using a plane wave basis set with an energy cutoff of 550 eV, and the projector augmented-wave (PAW) potential was applied.[289] A 4×3×2 k-point sampling was used for (2CN-PEA)PbI_3 1D perovskite, which has lattice constants of 8.019, 11.322, and 16.831 Å. The same k-point density was used for other 1D perovskites studied. Structures were optimized using the PBE functional[290] with the zero damping D3 correction of Grimme,[291] as inclusion of London dispersion in the functional for treating organic-inorganic halide perovskites has been recently emphasized.[292] The experimentally determined structures were used as initial structures. Geometries were fully relaxed regarding lattice parameters and interatomic distances until forces were less than 0.01 eV $Å^{-1}$. To correct for the underestimation in band gap predictions using the PBE functional, the range-separated HSE06 functional[293, 294] was employed in the electronic structure calculations. Spin-orbit coupling (SOC) was included in all cases.[295]

Powder X-ray diffraction (PXRD). The PXRD patterns were acquired on a Panalytical XPert PRO Alpha-1 XRD Diffractometer using Cu K X-ray tube radiation at a voltage of

45 kV and 40 mA, with an incident beam Johannsson monochromator and an X'Celerator solid-state detector. The diffraction pattern was scanned over the angular range of 3-40° with a step size of 0.016°, at room temperature.

Single-crystal X-ray diffraction. Suitable crystals were selected from the reaction mixtures obtained using the general procedure above and were mounted on a loop with paratone oil on a XtaLAB Synergy-S, Dualflex, HyPix diffractometer or a Bruker SMART APEX II CCD diffractometer, with a radiation MoK_α (λ=0.71073 Å). The crystals were cooled at the temperature indicated in Table 1-2 during data collection. Using Olex2,[258] the structure was solved with the ShelXT[259] structure solution program using Intrinsic Phasing and refined with the ShelXL[260] refinement package using least squares minimization. Details of the crystals, data collection, and data refinements are summarized in Table 1-2. Simulated powder patterns were calculated by Mercury software using the CIF from the single-crystal X-ray experiment.

Table 3.1 Single-crystal data and structure refinement data.

	(3NO$_2$-PEA)PbI$_3$	**(2NO$_2$-PEA)PbI$_3$**	**(3CN-PEA)PbI$_3$**	**(2CN-PEA)PbI$_3$**
Empirical formula	$C_8H_{11}I_3N_2O_2Pb$	$C_8H_{11}I_3N_2O_2Pb$	$C_9H_{11}I_3N_2Pb$	$C_{18}H_{22}I_6N_4Pb_2$
Formula weight	755.09	755.119	735.131	1470.263
Temperature (K)	100(2)	99.9(7)	100(1)	100.06(17)
Crystal system	triclinic	triclinic	monoclinic	monoclinic
Space group	$P\bar{1}$ (2)	$P\bar{1}$ (2)	$P2_1/c$ (14)	Pc (7)
***a* (Å)**	8.27410(10)	7.9883(2)	12.1311(5)	8.00842(14)
***b* (Å)**	13.6422(3)	8.6265(3)	7.8491(3)	11.2667(2)
***c* (Å)**	29.2523(6)	11.9146(3)	16.7251(7)	16.8951(3)
***α* (°)**	80.590(2)	94.240(2)	90	90
***β* (°)**	83.3020(10)	97.580(2)	105.038(5)	90.1149(16)
***γ* (°)**	72.462(2)	103.126(3)	90	90
Volume (Å^3)	3098.09(11)	788.00(4)	1537.99(11)	1524.42(5)
Z	8	2	4	2
ρ_{calc} (g cm^{-3})	3.238	3.182	3.175	3.203
μ (mm^{-1})	16.860	16.574	16.970	17.121
F(000)	2640	648.765	1257.477	1265.119
Crystal size (mm^3)	0.095×0.063×0.062	0.255×0.176×0.051	0.203×0.096×0.057	0.247×0.151×0.086
2Θ range for data collection (°)	3.16 to 62.00 (0.69 Å)	4.88 to 72.64 (0.60 Å)	3.48 to 72.64 (0.60 Å)	3.62 to 58.26 (0.73 Å)
Index ranges	$-11 \le h \le 11$, $-19 \le k \le 19$, $-42 \le l \le 42$	$-13 \le h \le 13$ $-14 \le k \le 14$ $-19 \le l \le 19$	$-20 \le h \le 20$, $-12 \le k \le 13$, $-27 \le l \le 28$	$-13 \le h \le 12$, $-19 \le k \le 19$, $-28 \le l \le 28$
Reflections collected	19107	34230	24800	46422
Independent reflections	19107 R_{int} = 0.0692 R_{sigma} = 0.0338	7619 R_{int} = 0.0516 R_{sigma} = 0.0356	7327 R_{int} = 0.0669 R_{sigma} = 0.0620	7765 R_{int} = 0.0749 R_{sigma} = 0.0707
Data/restraints/parameters	19107/538/633	7619/197/294	7327/59/290	7765/146/475
Goodness-of-fit on F^2	1.095	1.0574	1.0127	1.0316
Final *R* indexes [I>=2σ(I)]	R_1 = 0.0588 wR_2 = 0.1531	R_1 = 0.0372 wR_2 = 0.0832	R_1 = 0.0382 wR_2 = 0.0837	R_1 = 0.0455 wR_2 = 0.1198
Final *R* indexes [all data]	R_1 = 0.0634 wR_2 = 0.1573	R_1 = 0.0471 wR_2 = 0.0865	R_1 = 0.0511 wR_2 = 0.0884	R_1 = 0.0470 wR_2 = 0.1210
Largest diff. peak/hole / e Å^{-3}	5.77/-4.94	3.84/-2.10	3.26/-2.10	3.01/-2.11

Table 3.2 Single-crystal data and structure refinement data.

	(3Me-PEA)$_2$PbI$_4$	**(2CO$_2$Me-PEA)PbI$_3$**	**(3MeO-PMA)$_2$PbI$_4$**	**(2MeO-PMA)PbI$_3$**
Empirical formula	$C_{18}H_{28}I_4N_2Pb$	$C_{10}H_{14}I_3NO_2Pb$	$C_{16}H_{24}I_4N_2O_2Pb$	$C_8H_{12}I_3NOPb$
Formula weight	988.16	768.158	991.16	726.121
Temperature/K	104(7)	99.9(9)	100(1)	100(1)
Crystal system	triclinic	monoclinic	orthorhombic	orthorhombic
Space group	$P\bar{1}$ (2)	$C2/c$ (15)	$Pnma$ (62)	$Pca2_1$ (29)
***a*/Å**	12.32860(10)	23.6241(3)	8.5626(2)	15.5711(3)
***b*/Å**	19.0688(2)	16.4191(2)	69.6570(17)	12.2858(2)
***c*/Å**	24.3751(2)	8.67466(10)	8.53290(10)	7.86060(14)
***α*/°**	67.7520(10)	90	90	90
***β*/°**	89.9860(10)	96.8023(12)	90	90
***γ*/°**	80.6850(10)	90	90	90
Volume/Å^3	5222.14(9)	3341.10(7)	5089.41(18)	1503.77(5)
Z	8	8	8	4
ρ_{calc}/gcm^3	2.514	3.054	2.587	3.207
μ/mm^{-1}	11.205	15.637	11.494	17.357
F(000)	3555	2659.091	3552	1241.506
Crystal size/mm^3	0.347×0.119×0.084	0.294×0.206×0.04	0.235×0.162×0.027	0.24×0.174×0.126
2Θ range for data collection/°	2.35 to 56.56 (0.75 Å)	4.96 to 68.68 (0.63 Å)	3.51 to 55.50 (0.76 Å)	3.32 to 72.64 (0.60 Å)
Index ranges	$-16 \le h \le 16$ $-25 \le k \le 25$ $-31 \le l \le 32$	$-40 \le h \le 39$ $-28 \le k \le 27$ $-14 \le l \le 13$	$-10 \le h \le 9$ $-88 \le k \le 82$ $-10 \le l \le 10$	$-25 \le h \le 25$ $-20 \le k \le 19$ $-11 \le l \le 13$
Reflections collected	69618	37497	25670	24383
Independent reflections	25770 R_{int} = 0.0784 R_{sigma} = 0.0774	6991 R_{int} = 0.0474 R_{sigma} = 0.0330	5616 R_{int} = 0.0457 R_{sigma} = 0.0353	6538 R_{int} = 0.0440 R_{sigma} = 0.0372
Data/restraints/parameters	25770/924/958	6991/219/383	5616/133/242	6538/178/296
Goodness-of-fit on F^2	1.023	1.0357	1.239	1.0285
Final *R* indexes [$I>=2\sigma(I)$]	R_1 = 0.0434 wR_2 = 0.1097	R_1 = 0.0239 wR_2 = 0.0577	R_1 = 0.0453 wR_2 = 0.0955	R_1 = 0.0267 wR_2 = 0.0658
Final *R* indexes [all data]	R_1 = 0.0504 wR_2 = 0.1144	R_1 = 0.0264 wR_2 = 0.0586	R_1 = 0.0491 wR_2 = 0.0966	R_1 = 0.0312 wR_2 = 0.0671
Largest diff. peak/hole (e Å^{-3})	2.37/-1.89	1.91/-1.59	1.68/-2.94	1.92/-1.12

3.3 Results and Discussion

Engineering 1D FSIP compounds

More than 50 iodoplumbates containing only face-sharing octahedra (FSIPs) can be found in the literature. In many cases, 1D FSIP structures are obtained rather than 2D HOIP structures because the atom(s) on which the cationic charge is formally located is sterically encumbered and, therefore, unable to interact with the inorganic part of the structure. In the structures of two $APbI_3$ FSIPs with A^+ = protonated aminohexanoic acid or two *N,N*-dimethylacetamine molecules bridged by a proton, there are cation-cation (ammonium-to-HBA substituent) hydrogen bonds.[158] To test whether intra- or inter-cation hydrogen bonding between an ammonium group and a HBA is a general approach that favours the formation of FSIPs, we set out to examine a wide variety of structures in which the ammonium cation is based on a six-membered ring (primarily benzene, but also including a naphthalene and a cyclohexane derivative) is 1,2- or 1,3-functionalized with both a methylammonium ($CH_2NH_3^+$) or ethylammonium ($(CH_2)_2NH_3^+$) group and a HBA (CN, NO_2, OMe, CO_2Me), as shown in Fig. 1. In addition, we examined several examples of cations containing substituents with similar steric bulk, but medium, weak, or no HBA character (F, CF_3, OMs [OSO_2Me], Me). Unsubstituted PEA, PMA and NEA are known in the literature and all form 2D HOIPs when synthesized in these conditions. Moreover, *para*-substituted PEA ions, where no intramolecular hydrogen bonding is possible, form 2D structures when the same substituents are used (CN,[1] NO_2,[105] OMe,[296] CO_2Me,[1] Me[73]).

[1] Footnote: The crystal structure is unknown, but the PXRD of $(4CN\text{-}PEA)_2PbI_4$ and $(4CO_2Me\text{-}PEA)_2PbI_4$ characteristic of 2D HOIP structure.

Most of the ammonium salts, or corresponding amines used in our study were available commercially or through literature syntheses. However, to broaden the range examined, several new derivatives (2MsO-PEA-Cl, 3CN-PEA-Cl, 2CN-PEA-Cl, 3CO_2Me-PEA-Cl, 2CO_2Me-PEA-Cl, 3Me-PEA-Cl, 2Me-PEA-Cl) were synthesized according to a recently developed procedure (as described in SI).[282] We used conditions commonly used to synthesize 2D HOIPs, i.e., slow crystallization of mixture of solutions obtained by dissolving PbI_2 in HI and by dissolving the halide salt of the cation (or the corresponding neutral amine) in HI,[12, 16, 105, 106, 113, 125] and investigated the purity and structure of the resulting crystalline materials using single-crystal X-ray diffraction (SC-XRD), powder XRD (PXRD), and elemental analysis. Figure 1 summarizes the cations employed and the structure types obtained.

Of the twelve cations examined that bear moderate-to-strong HBA substituents, ten of the resulting hybrid organic-inorganic structures were found to be 1D APbI_3 FSIPs, i.e., linear PbI_3^- wires composed of face-sharing octahedra separated by layers of organic cations. Of the remaining two structures, 2CO_2Me-PEA forms a highly unusual APbI_3 structure in which there is face-, edge-, and vertex-sharing by the PbI_6 octahedra (see SI for further description and discussion), while 3MeO-PMA forms a A_2PbI_4 2D perovskite. The cation in the 1D (2CN-PEA)PbI_3 crystals in solution could slowly rearrange to form bicyclic 1-amino-3,4-dihydroisoquinolin-2-ium, while the inorganic wires remained mostly unchanged (see Fig. 3). Once dried, the crystals' cation of (2CN-PEA)PbI_3 were not showed to rearrange in the time frame measured (1 month). Post-synthetic transformations of 2D perovskites have been demonstrated before.[297] To the best of our knowledge, this is the first post-synthetic transformation of the cation in 1D FSIP perovskitoids. While the

mechanism is unknown, the formation of 3,4-dihydro-1-isoquinolinamine core in one step from a commercially available compound is significant. Derivatives of this compound are known inhibitor of the human nitric oxide synthases.[298]

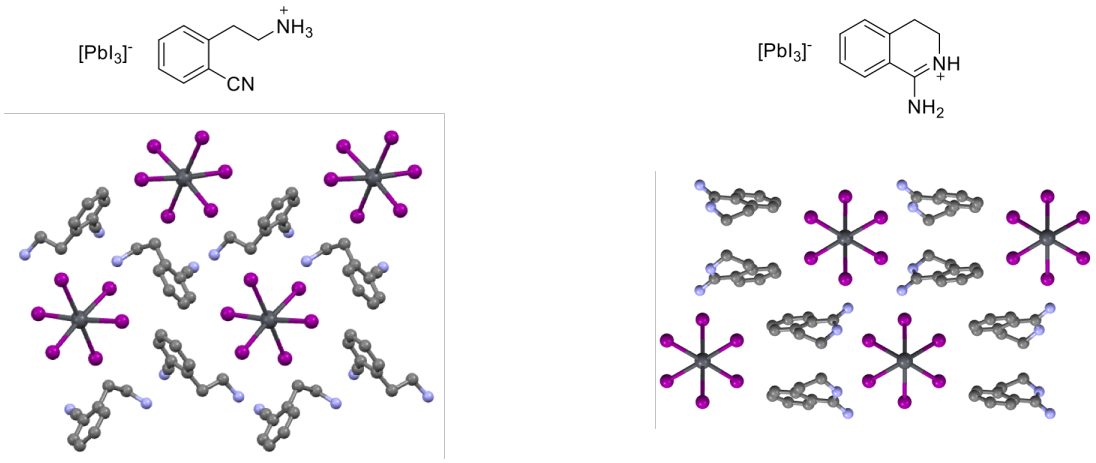

Figure 3.3 Transformation of the cation 2CN-PEA in (2CN-PEA)PbI_3 to a bicyclic 1-amino-3,4-dihydroisoquinolin-2-ium.

In two cases – 2MeO-PEA and 3MeO-PEA – 2D materials (identified as such by their PXRD patterns) could also be obtained instead of 1D FSIPs when higher concentrations of reagents were used. This is not particularly surprising, since other examples in which the structure of hybrid materials depend on the concentration employed have been reported in the literature.[201] Nevertheless, for 2MeO-PEA the thermodynamic product is still apparently the 1D FSIP; 2D $(2MeO\text{-}PEA)_2PbI_4$ was observed to transform to 1D (2MeO-PEA)PbI_3 on standing at room temperature over a timescale of days using the PXRD (presumably with loss of A^+I^-) (see Fig. 4).

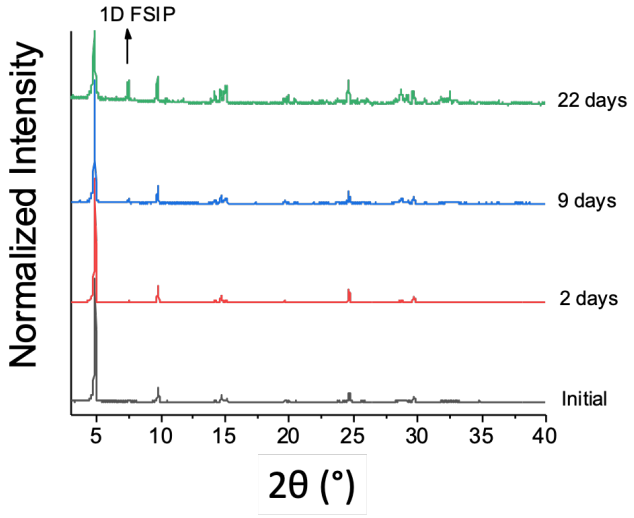

Figure 3.4 PXRD showing the slow conversion of $(2MeO\text{-}PEA)_2PbI_4$ to the more thermodynamically product $(2MeO)PbI_3$ after *x* amount of time.

When the substituents have little or no HBA character, but similar bulk as those described previously, 1D FSIPs are not formed under the same conditions. In the case of 2MsO-PEA, no solid product was formed, while in the case of 3Me-PEA, 2Me-PEA, and $2CF_3$-PEA, 2D A_2PbI_4 structures were obtained. In each of the FSIP structures there is hydrogen bonding between the ammonium moieties and the HBA, either intermolecular and forming chains of hydrogen-bonded organics (see Fig. 5A), intermolecular and forming dimers (Fig. 5B), or intramolecular (see Fig. 5C). We suggest that it is these interactions that promote formation of a 1D structure, rather than a 2D layered perovskite. While $R\text{-}NH_3\cdots I$ close contact are present in certain cases, the intra- or intermolecular H-bonding present between cations prevent the ammonium substituent to penetrate the half-cubooctahedral "pocket" of a 2D HOIP.

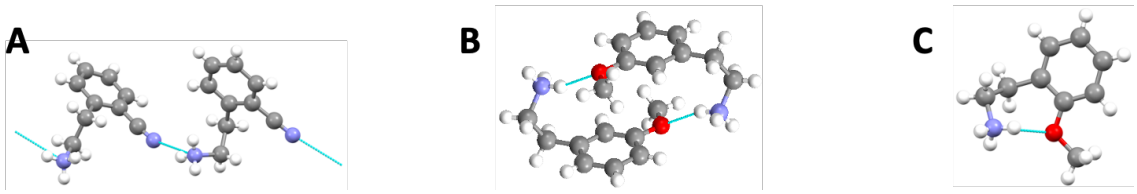

Figure 3.5 Type of hydrogen bonding found in the FSIP: examples of (A) linear, (B) close pair, (C) intramolecular hydrogen bonding taken from the structures of 3CN-PEA, 3MeO-PEA, and 2MeO-PEA, respectively.

Systematic comparison of the 1D FSIP structures

The ten new FSIP structures referred to above, and their comparison to previously reported structures, enables us to further classify these materials into different families based on their structural characteristics. 2D HOIP structures are often classified based on the type of cation used and/or the offset of the inorganic layers from one another as Ruddlesden-Popper or Dion-Jacobson structures. For 1D structure, to the best of our knowledge, no comparable classifications have been suggested in the literature. The geometries of the wires themselves show little variation. However, FSIP structures do fall into several groups, based on the relation between neighboring wires.

In many cases, all the PbI_3 chains are crystallographically equivalent; when viewed along the chain direction these structures from a roughly square, rectangular, or rhombic lattice of chains. We have designated as a W structure type when all the wires are related only by translation operations; multiple examples are found in the literature[142-145] and several structures reported here belong to this class (Fig. 6A; A = 2HO-CycMA, 2MeO-PEA, 3CN-PEA, 3MeO-PEA, $2NO_2$-PEA). Other FSIPs have wires related by operations other than translation. We have designated the situation of two crystallographically equivalent wires W and W' (where the “middle” wire, W', is related to the “corner” wires, W, by translation *and* rotation), in which, when viewing along the chain direction, W’ falls roughly in the

center of four W wires (and vice versa) as W:W' (see Fig. 6B).[146, 147] In other cases, two crystallographically equivalent wires W' can be in the center of four W wires and we have used the label W:2W'.[148-150] Moreover, there are also exceptions that do not fall within these categories.[151-153] For example, $(3NO_2\text{-PEA})PbI_3$ has two crystallographically inequivalent wires in its unit cell and, therefore, cannot be described in the same way as the examples above.

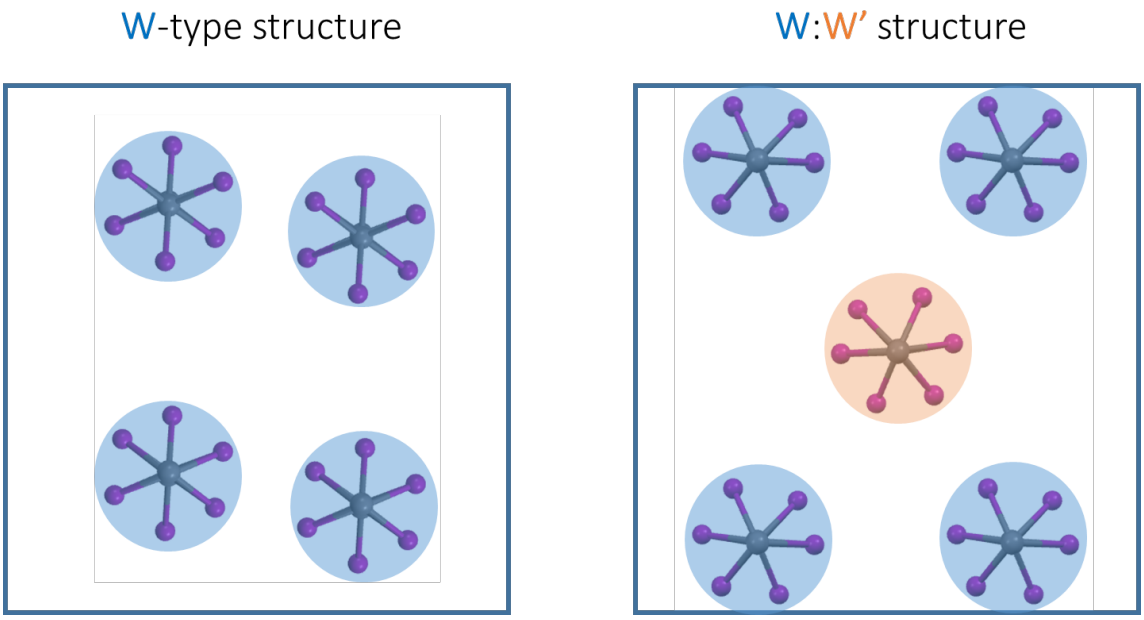

Figure 3.6 Schematic representation of W (left) and W:W' (right) structure of 1D FSIPs. The different color shown for the central chain of the W:W' structure indicates a crystallographically equivalent chain related to the corner ones by translation and rotation.

Relation of FSIP Structure and Exciton energy

The photophysical properties of the HOIP films were investigated by UV−vis spectroscopy (see Fig. 7). The exciton energy, E_{ex}, was in each case estimated using the maximum of the low-energy peak. Overall, there is little variation in the optical properties of the materials examined here. For the W-type structures, all compounds have similar exciton energy (3.26 eV) (see Fig. 7C). However, among the W:W' structures, $(2MeO\text{-NEA})PbI_3$

and (2CN-PEA)PbI_3 have exciton energies at lower energy (3.06 eV) than those of (3CO_2Me-PEA)PbI_3 and (2MeO-PMA)PbI_3 (3.26 eV, see Fig. 7D). Different crystal structure characteristics were examined for possible correlation with this variation in exciton energy. Variation in the inter-chain distance (see Table 3 for Pb_{wire1} to Pb_{wire2} distance) is, at least in principle, expected to affect the quantum-confinement of the exciton within the wire. However, the exciton energy is constant for W-type structures regardless of the closest interwire distances, likely because these distances are sufficiently long that the excitons are well confined in all the structures. Indeed, for the W:W' type structures, (2MeO-NEA)PbI_3 and (2CN-PEA)PbI_3, in which there is a larger interwire distance, the exciton bands are red shifted compared to those of (3CO_2Me-PEA)PbI_3 and (2MeO-PMA)PbI_3 (in which the interchain distance is relatively short), the reverse of what is expected on exciton-confinement grounds.

The distortion of the PbI_6 octahedra from ideal geometry also correlates well with the exciton energy of 3D and 2D perovskites, with the Pb–I–Pb bond angle often being found to be a good indicator of the optical gap. For the 1D wires, we considered that the smallest I–Pb–I angle might be important distortion parameter, since this is largely responsible for the distortion in the wire axis direction. However, there is no clear correlation between the exciton energy and this angle (Table 3).

The one criterion that seems to be related to the exciton energy is the position of the W' wire in the W:W’ structures; the W' wire can either be aligned more-or-less symmetrically in the middle of the four W wires or in a significantly asymmetric way (see Fig. 7E). The two pseudo-centered W:W' structures have an exciton band red-shifted compared to the other two structures. However, more structures are needed to understand the generality of

this observation, and it is not clear to us why this arrangement should afford a red shift. For the W structures, it seems that, in the absence of charge transfer between the inorganic and organic components found where the organic cation is an electron acceptor, the exciton energy is constant regardless of structural modifications. Indeed, other W-type structures where charge transfer was observed have orange to black color.[149, 157, 174, 180]

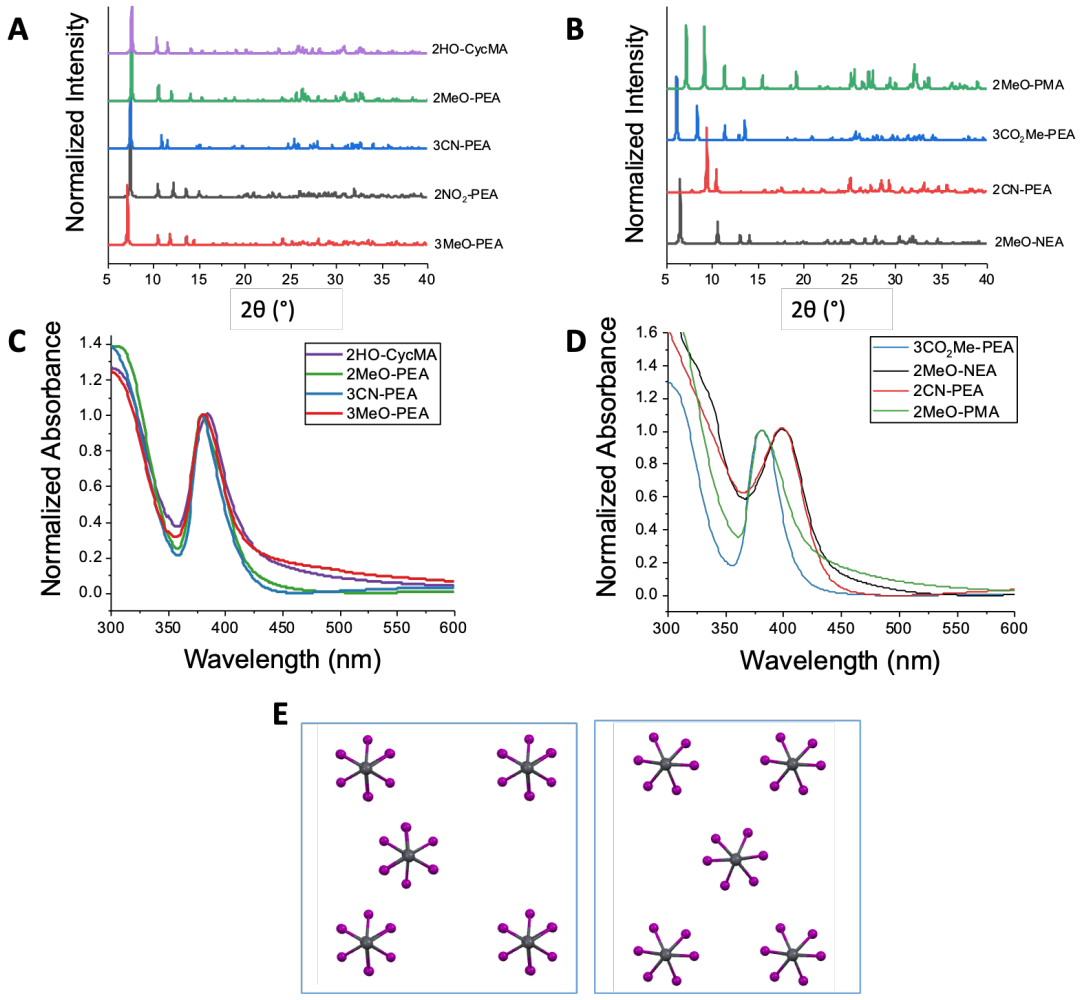

Figure 3.7 PXRD of the 1D FSIP W (A) and W:W' (B) structures. Absorbance of FSIP films on glass: W (C) and W:W' (D) structures. (E) Wire arrangement in W:W' FSIP when the W' wire is unsymmetrically (left, $3CO_2$Me-PEA shown here, 2MeO-PMA is similar) and symmetrically (right, MeO-NEA shown here, 2CN-PEA is similar) located in the middle of the W wires.

Table 3.3 Selected characteristics, distances and angles in the crystal structure of the FSIP compounds.

Cation	Structure type	Wire arrangement in A:B FSIP	Type of hydrogen bonding [a]	$Pb_{wire1}\cdots Pb_{wire2}$ (Å) [b]	I–Pb–I (°) [b]	$E_{exciton}$ (eV)
$3CO_2Me$-PEA	W:W'	unsymmetrical	A	8.5	170.3	3.26
2MeO-PMA		unsymmetrical	C	8.4	177.7	3.26
2CN-PEA		symmetrical	A	9.8	174.5	3.06
2MeO-NEA		symmetrical	C	8.8	174.7	3.06
2HO-CycMA	W	-	C	8.5	180.0	3.26
$2NO_2$-PEA		-	B	8.4	180.0	3.26
3MeO-PEA		-	B	8.4	172.4	3.26
2MeO-PEA		-	C	8.4	172.6	3.26
3CN-PEA		-	A	8.3	171.2	3.26

[a] The type of hydrogen bonding is defined as for Fig. 2 where A = linear, B = close pair and C = intramolecular hydrogen bonding. [b] $Pb_{wire1}\cdots Pb_{wire2}$ and I–Pb–I are calculated using Mercury. $Pb_{wire1}\cdots Pb_{wire2}$ is defined as the shortest Pb_{wire1} to Pb_{wire2} distance. I_1–Pb–I_2 is defined as the smallest of the *trans* angles, where I_1 and I_2 are coordinated to two different Pb atoms.

Weak PL was observed for the W and W:W' 1D FSIP powder (see Fig. 8). The large Stokes shift and the broad PL bandwidth suggests strong exciton lattice interaction in these FSIP crystals.[272] This is consistent with previous findings that PL in 1D FSIPs arises from self-trapped excitons, a characteristic of 1D systems with easily deformable lattice.[273]

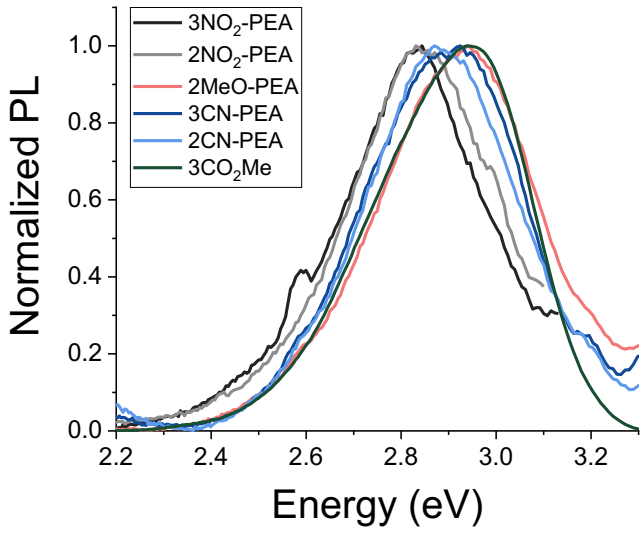

Figure 3.8 Photoluminescence of the 1D FSIP powders using the cations 3CN-PEA, 2CN-PEA, 3MeO-PEA, 2MeO-PEA, $3NO_2$-PEA, $2NO_2$-PEA, 2MeO-NEA, $3CO_2Me$-PEA, 2HO-CycMA, 2MeO-PMA.

To further analyze the consequences of the structural difference between W and W:W' type structures, we investigated one example of each, W structure, 2MeO-PEA, and a W:W' structure, 2CN-PEA, using density functional theory (DFT) calculations, including spin-orbit coupling (SOC). A good agreement between the experimental and the computationally optimized structures was obtained (Table 4), as expected. The band structures and projected density of states (PDOS) were calculated at the HSE06+SOC level of theory. The *k* paths are shown in Figure 9.

For 2CN-PEA, the inorganic 1D wires are oriented along the $Y_2\Gamma$ direction, where the inorganic parts are stacked. Therefore, stronger band dispersions are expected in the Γ-A, E-Z-C_2, and Y_2-Γ segments due to stronger interactions in 1D $[PbI_3]^-$ wire, and weaker dispersions in the Γ-Z-D-B-Γ, A-E, and C_2-Y_2 segments due to weaker van der Waals interactions between the organic cations (see Fig. 10A). For 2MeO-PEA, the inorganic wires run along the Γ-Z direction. Stronger band dispersions are thus shown for the Γ-Z,

D-B, A-E, and C_2-Y_2 segments, and weaker dispersions for the Z-D, B-Γ, and E-Z-C_2 segments (see Fig. 10B). The PDOS for 2CN-PEA indicate strong band hybridization near the bottom of the conduction band, but no hybridization near the top of the valence band (see Fig. 10A, right panel). On the other hand, the PDOS for 2MeO-PEA show strong band hybridization both near the bottom of the conduction bottom and the top of the valence band (see Fig. 10B, right panel). We note that hybridization generally tends to decrease band dispersions in the inorganic framework. The band gap for 2NC-PEA occurs at Γ and has a magnitude of 3.13 eV, and the band gap for 2MeO-PEA occurs at A and has a value of 3.45 eV. These show the same trend as the measured exciton energies of 3.06 eV for 2CN-PEA and 3.26 eV for 2MeO-PEA, respectively.

Table 3.4 Pb-I bond lengths, $\langle\lambda\rangle$, σ^2, I-Pb-I bond angles and shortest Pb_{wire1} to Pb_{wire2} distances.

		Average Pb-I bond length (Å)	**Quadratic elongation ($\langle\lambda\rangle$)** [a]	**I-Pb-I variance (σ^2)** [b]	**I-Pb-I (°)**	**Pb_{wire1}…Pb_{wire2} (Å)**
Exp.	2CN-PEA	3.23	1.0102	34.99	174.5	9.8
	2MeO-PEA	3.22	1.0124	41.74	172.6	8.4
DFT	2CN-PEA	3.26	1.0098	33.48	174.8	9.8
	2MeO-PEA	3.25	1.0122	42.57	173.9	8.5

[a] $\langle\lambda\rangle$ is given by $\langle\lambda\rangle = \frac{1}{n}\sum_{i=1}^{n}\left(\frac{l_i}{l_0}\right)^2$, where l_0 is the center-to-vertex distance of a regular octahedron of the same volume, independent of the effective size of the octahedron. [b] Distortions can be quantified by the octahedron bond length quadratic elongation $\langle\lambda\rangle$ and the bond angle variance (σ^2).[246] The bond angle variance is calculated by $\sigma^2 = \frac{1}{m-1}\sum_{i=1}^{m}(\phi_i - \phi_0)^2$, where m is number of bond angles, ϕ_i the i^{th} bond angle, and ϕ_0 the bond angle for a regular octahedron (90°).

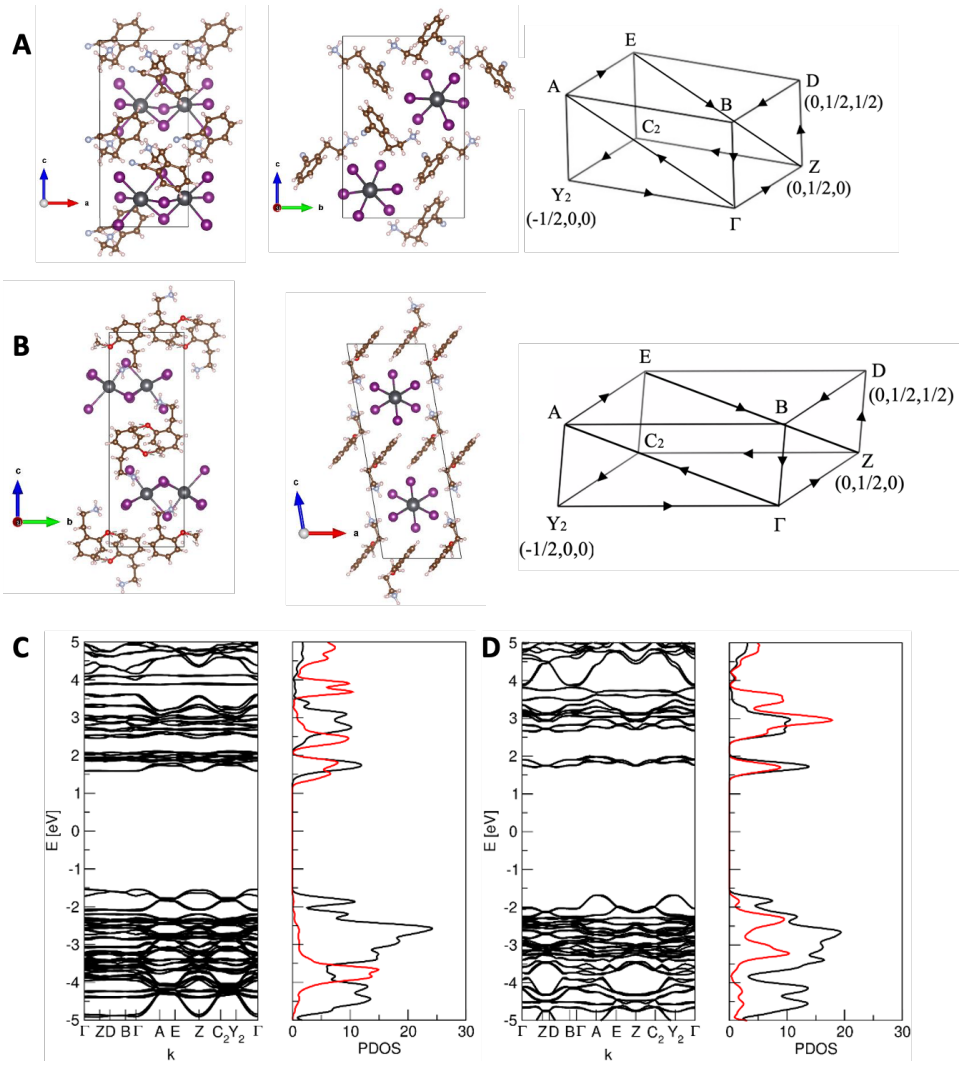

Figure 3.9 Primitive cells (left panels) and k-paths (right panels) in the first Brillouin zone for 2CN-PEA (A) and 2MeO-PEA (B). Band structure (left panel) and PDOS (right panel) (black and red for inorganic and organic components, respectively) for 2CN-PEA (C) and 2MeO-PEA (D).

3.4 Conclusion

This study adds to the understanding of how the structures of hybrid organic iodoplumbate materials can be controlled by interactions within and between the organic cations. Specifically, hybrid lead iodide materials incorporating $R(CH_2)_nNH_3$ (n = 1, 2; R = aryl, substituted cyclohexane) cations show a strong tendency to adopt a FSIP structure where hydrogen bonding interaction between the cation and itself or neighboring cations is

possible. We added 11 examples to the young library of FSIP compounds and a total of 16 new crystal structures. Considering the potential applications of this class of materials, including their use as capping layers to improve the long-term stability of 3D perovskite solar cells, some ability to predict the tendency to form a FSIP rather than a 2D perovskite is significant. Adding more structures to this family of compound could help further understand the optical properties of this class of materials.

CHAPTER 4: $(4NPEA)_2PBI_4$ (4NPEA = 4-NITROPHENYLETHYLAMMONIUM): STRUCTURAL, NMR, AND OPTICAL PROPERTIES OF A 3×3 CORRUGATED 2D HYBRID PEROVSKITE

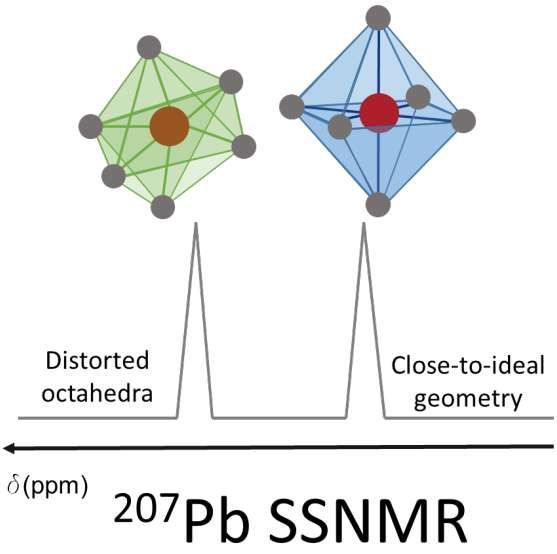

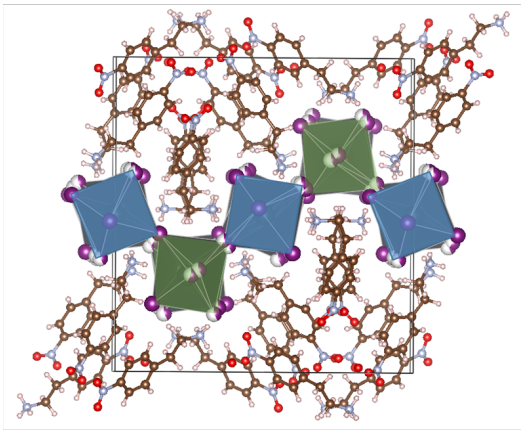

This project was accomplished with the collaboration of Félix Thouin, Johannes Leisen, John Bacsa, Ajay Ram Srimath Kandada, Justin M. Hoffman, Mercouri G. Kanatzidis, Aditya Mohite, Carlos Silva and Stephen Barlow. Felix Thouin, in the group of Carlos Silva, performed all the low temperature optical measurement and helped with the redaction of the manuscript. Johannes Leisen helped with the optimization of pulse sequence for the solid state nuclear-magnetic resonance experiments. John Bacsa, from the Crystallography Lab of Emory University, performed the single crystal X-ray

diffraction experiments. Ajay Ram Srimath Kandada, Justin M. Hoffman (Northwestern University), Mercouri G. Kanatzidis (Northwestern University), Aditya Mohite (Rice University) and Carlos Silva provided useful discussion on 2D perovskite synthesis and characterization. Stephen Barlow helped with the data analysis and he helped to write the manuscript. The content of this chapter was published in Journal of American Chemical Society in March 2019 (DOI: 10.1021/jacs.8b13207). All authors contributed to the redaction of the manuscript. This work was supported by NSERC (ES. D. Scholarships for MHT and FT) and the AFOSR (FA9550-18-1-0499).

4.1 Introduction

The structures and properties of hybrid organic-inorganic perovskites (HOIPs) and related compounds are highly tunable via the metal ions (M), the inorganic anions (X), and the organic cations. The dimensionality and the detailed structure of the inorganic portion are influenced by the organic cations.[39, 106] Metal halide HOIPs can form 0D,[299] 1D,[139, 300] 2D,[16, 63] or 3D[301] networks; small cations, such as $MeNH_3$ (MA) and $CH(NH_2)_2$, lead to 3D HOIPs, while larger cations, such as $BuNH_3$ (BA)[92] or $Ph(CH_2)_2NH_3$ (PEA)[63], afford lower dimensionalities. Further variation can be obtained using *both* small and large cations, allowing the thickness of inorganic slabs in 2D HOIPs to be tuned; such structures are promising for optoelectronic applications due to their superior stability relative to their 3D counterparts.[92, 130, 302, 303] Structures in which MX_6 octahedra share edges or faces, rather than only vertices (true perovskites), afford even more structural diversity.[106, 264, 304, 305]

2D structures can be conceptually obtained from slicing a cubic 3D structure along different crystallographic planes: along (100) affords flat sheets, whereas (110) gives corrugated sheets (Figure 1). Most 2D Pb/I HOIPs are of the (100) type, consisting of $[PbI_6]^{2-}$ octahedra sharing equatorial vertices, leaving two unshared vertices *trans* to one another. In 2×2 (110) HOIPs, for which a few Pb/I examples are known,[103, 107, 108] the unshared vertices are *cis*. $(DMEN)PbBr_4$ (DMEN = $H_3N(CH_2)_3NMe_2H$)[113] was the first 3×3 (110) HOIP, with layers consisting of alternating rows of *cis* and *trans* octahedra.

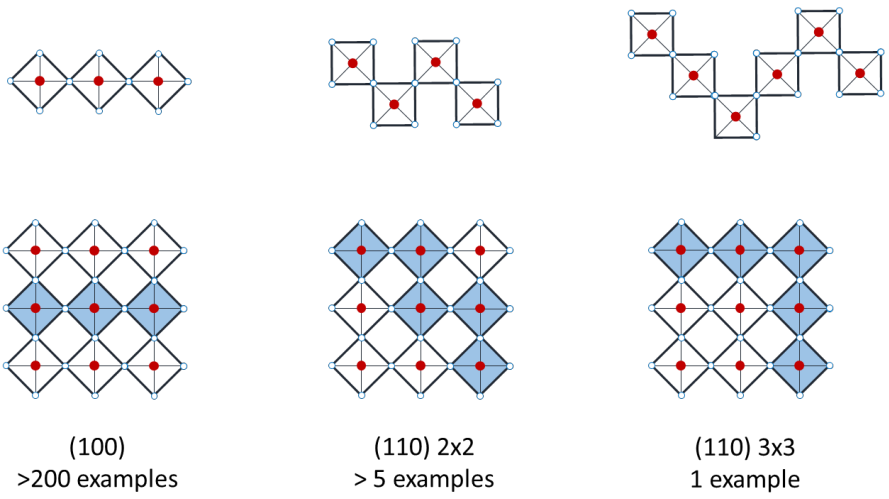

Figure 4.1 Schematic of 2D HOIPs as derived from cuts along crystallographic planes of a cubic 3D perovskite.

While tremendous progress has been made in understanding how the cation affects the structure of 3D and (100) 2D HOIPs, there are many fewer corrugated HOIPs and little knowledge of how they can be controllably synthesized. Here we report (4NPEA)2PbI4, the first Pb/I 3×3 (110) structure and the first corrugated HOIP employing an organic monocation rather than a bridging dication. We describe the 4NPEA···I and 4NPEA···4NPEA interactions in the crystal structure, and relate its NMR and optical properties to the structure. This demonstrates that 2D HOIPs based on cations with different functional groups can exhibit new structures; this is an important step towards rational design of functional 2D HOIPs with predictable structure and properties.

4.2 Experimental Procedures

Synthesis.

4-Nitrophenylethylammonium iodide (4NPEA-I): A solution of 4-nitrophenylacetonitrile (4.5 g, 28 mmol) in THF (15 mL) was cooled to 0 °C. BH_3•THF (77 mL of a 1 M solution in THF, 69 mmol) at room temperature was slowly added to the

cooled solution over 10 min under nitrogen. The mixture was heated under reflux and the reaction was followed by TLC. After 3 h, the reaction mixture was cooled in an ice bath and distilled water (20 mL) was added; this was followed by cautious addition of concentrated aqueous hydrochloric acid (20 mL) over a period of 30 min. The mixture was brought up to reflux for 1 h and was then cooled in an ice bath and poured into water (20 mL). The solution was extracted once with dichloromethane. The aqueous layer was brought to pH 12 with a 40% aqueous sodium hydroxide solution and extracted with dichloromethane (3 × 25 mL). The combined organic extracts were dried over sodium sulfate and then filtered; the solvent was removed using a rotary evaporator, while keeping the solution below 40 °C, to yield a colorless oil. The crude oil was dissolved in ethanol (3 mL) and cooled down to 0 °C. Hydroiodic acid (5 mL of a 57 wt% aqueous solution) was added and the mixture was stirred for 1 h at 0 °C. The solid was filtered and washed with diethyl ether to yield 4NPEA-I as a yellow powder (5.1 g, 62%). ^{1}H NMR (DMSO-d_6, 700 MHz): δ 8.21 (dt, J = 2.5, 8.5 Hz, 2H), 7.79 (br, 3H), 7.57 (d, J = 8.7 Hz, 2H), 3.16-3.01 (m, 2H), 3.00 (d, J = 9.2 Hz, 2H). ^{13}C(^{1}H) NMR (DMSO-d_6, 175 MHz): δ 146.99, 145.91, 130.68, 124.13, 40.36, 33.18. HRMS-ESI (*m/z*): calcd for $C_8H_{11}N_2O_2$ $(M–I)^+$, 167.0815; found, 167.0812.

Bis(4-nitrophenylethylammonium) tetraiodoplumbate ((4NPEA)$_2$PbI$_4$): PbI_2 (230 mg, 0.5 mmol) was dissolved in HI (2.5 mL of a 57 wt% aqueous solution) and H_3PO_2 (1.0 mL of a 50 wt% solution in water) and stirred at 130 °C for 2 min. A solution of 4NPEA-I (294 mg, 1 mmol) in ^{i}PrOH (5 mL) and MeOH (0.5 mL) was added and the resultant mixture was stirred at 130 °C for 2 min. The solution was then allowed to crystallize at room temperature for 24 h. The solids were filtered and dried under high vacuum to yield yellow

crystals (243 mg, 55%). Anal. Calcd. for $(C_8H_{11}N_2O_2)_2PbI_4$: C, 18.32%; H, 2.11%; N, 5.34%. Found: C, 18.35%; H 1.92%; N, 5.15%.

Bis(4-nitrophenylethylammonium) tetrabromoplumbate ($(4NPEA)_2PbBr_4$): MeOH (1 mL) was layered onto a solution of $PbBr_2$ (18 mg, 0.05 mmol) in HBr (1 mL of a 48 wt % aqueous solution) at the bottom of a test tube to form a two-phase bilayer. A solution of 4NPEA-I (29 mg, 1 mmol) in 0.2 mL MeOH (0.5 mL) was added on top of the MeOH layer. After 48 h standing at room temperature, white crystals that had formed between the two layers were filtered and dried under high vacuum (25 mg, 60%). Anal. Calcd. for $(C_8H_{11}N_2O_2)_2PbBr_4$: C, 22.32%; H, 2.58%; N, 6.51%. Found: C, 21.91%; H 2.41%; N, 6.33%.

Thin Films. A solution made by dissolving $(4NPEA)_2PbI_4$ crystals (10 mg) in DMF (100 μL) was spincoated at 4000 rpm for 45 s onto a clean glass or sapphire substrate, pre-cleaned using UV-ozone, in a N_2-filled glovebox. The film was annealed for 30 min at 100 °C.

Temperature-dependent absorption and photoluminescence. The measurements were performed using a Montana Instruments Cryostation closed-cycle cold-finger cryostat. A heated tungsten filament lamp was used to probe the absorption spectra of the film. The third harmonic of a commercial ultrafast laser system (Pharos - Model, Light Conversion, Lithuania) emitting 1030-nm pulses at 100 KHz with a pulse duration of ca. 220 fs was used as an excitation source for the photoluminescence measurements. All spectra were acquired using an Andor Idus CCD coupled to a Shamrock 163 monochromator calibrated with an argon-mercury lamp.

Time-dependent photoluminescence. The measurements were performed using a Montana Instruments Cryostation closed-cycle cold-finger cryostat. The second harmonic of a commercial non-collinear optical parametric amplifier (ORPHEUS-N, Light Conversion, Lithuania) pumped by the second harmonic of an ultrafast laser system (Pharos, Light Conversion, Lithuania) emitting 1030-nm pulses at 600 KHz with a pulse duration of ca. 220 fs was used as an excitation source for the photoluminescence measurements. This produced pulse centered at 400 nm with 20nm of bandwith. Temporal acquisitions were obtained by Time-Correlated Single Photon Counting (TCSPC) using an HydraHarp 400 picosecond histogram generator and a PD-100 single photon avalanche photodetector coupled to a Princeton Instruments 2300i monochromator.

Photoluminescence quantum yield. Solid-state absolute photoluminescence quantum yields were determined with a Quantaurus-QY C11347 spectrometer; samples were excited at 345 nm.

Stability. The thermal stability of the HOIPs was examined by thermogravimetric analyses (TGA), under nitrogen atmosphere on a Pyris 1 TGA (PerkinElmer) at a heating rate of 5 °C min^{-1}. Data are shown in Figure S17. The photostability of $(4NPEA)_2PbI_4$ films was examined by recording the spectrally integrated photoluminescence intensity under continuous exposure from 210 μW of 343 nm light, as shown in Figure S18.

Solid-State Nuclear Magnetic Resonance (SS NMR). The SS NMR measurements were performed on a Bruker Advance III HD 500 operating at a ^{1}H frequency of 500 MHz for the ^{207}Pb NMR and on a Bruker Advance III HD 300 for the ^{13}C SSNMR experiments. HX MAS probes from Bruker were used in both cases. A 3.2 mm MAS rotor was used for the

^{207}Pb NMR while a 4.0 mm MAS rotor was used for the ^{13}C SSNMR. The MAS spinning speed was 12 kHz for the ^{13}C experiments and 23 kHz for the ^{207}Pb experiments. A Hahn-Echo pulse sequence was used for the ^{207}Pb experiments, while the ^{13}C CP-MAS experiments were conducted under standard conditions using a ramped ^{1}H contact pulse. The temperature-dependent ^{13}C SSNMR experiments were conducted using a Bruker BCU II chiller.

Powder X-ray diffraction (PXRD). PXRD patterns were acquired on a Panalytical XPert PRO Alpha-1 XRD Diffractometer using Cu K**α** X-ray tube radiation at a voltage of 45 kV and 40 mA, with an incident beam Johannsson monochromator and an X'Celerator solid-state detector. The diffraction pattern was scanned over the angular range of 3-40° with a step size of 0.016°, at room temperature. PXRD data were compared to simulated powder patterns calculated by Mercury software[306] using the CIFs obtained from the single-crystal X-ray experiments.

Single-crystal X-ray diffraction. A suitable crystal was selected from the reaction mixture and was mounted on a loop with paratone oil on a XtaLAB Synergy, Dualflex, HyPix diffractometer. The crystal was kept at ca. 100 K during data collection. Using OLEX2,[307] the structures were solved with the SHELXT[308] structure solution program using Intrinsic Phasing and refined with the SHELXL[309] refinement package using least squares minimization. Details of the crystals, data collection, and data refinements are summarized in Table 1. Data may be obtained in CIF format from the Cambridge Crystallographic Data Center; the deposition numbers for the structures of $(4NPEA)_2PbI_4$ and $(4NPEA)_2PbBr_4$ are CCDC 1873890 and 1874262, respectively.

Table 4.1 Single-crystal data and structure refinement data.

	$(4NPEA)_2PbI_4$	**$(4NPEA)_2PbBr_4$**
Empirical formula	$C_{16}H_{22}N_4O_4PbI_4$	$C_{16}H_{22}N_4O_4PbBr_4$
Formula weight	1049.16	861.20
Temperature/K	100(2)	110(10)
Crystal system	monoclinic	monoclinic
Space group	$P2_1/c$	$P2_1/c$
a/Å	21.0976(4)	21.2912(5)
b/Å	19.8255(3)	19.4228(4)
c/Å	12.6149(2)	11.7888(3)
β/°	98.2252(17)	97.290(2)
Volume/Å^3	5222.17(16)	4835.70(19)
Z	8	8
ρ_{calc}/gcm^3	2.669	2.366
μ/mm^{-1}	11.218	13.616
F(000)	3776.0	3200.0
Crystal size/mm^3	0.099 × 0.088 × 0.019	0.299 × 0.194 × 0.08
Radiation	MoKα (λ = 0.71073)	MoKα (λ = 0.71073)
2Θ range for data collection/°	3.856 to 59.15	5.292 to 76.122
Index ranges	$-29 \le h \le 29$, $-27 \le k \le 27$, $-17 \le l \le 17$	$-34 \le h \le 36$, $-33 \le k \le 30$, $-18 \le l \le 20$
Reflections collected	90640	84119
Independent reflections	14658 [R_{int} = 0.0476, R_{sigma} = 0.0348]	24781 [R_{int} = 0.0737, R_{sigma} = 0.0603]
Data/restraints/parameters	14658/603/555	24781/0/530
Goodness-of-fit on F^2	1.025	1.030
Final R indexes [I>=2σ(I)]	R_1 = 0.0521, wR_2 = 0.1129	R_1 = 0.0420, wR_2 = 0.0989
Final R indexes [all data]	R_1 = 0.0704, wR_2 = 0.1208	R_1 = 0.0652, wR_2 = 0.1068
Largest diff. peak/hole / e Å^{-3}	3.26/-2.53	3.43/-2.25

4.3 Results and Discussion

$(4NPEA)_2PbI_4$ was crystallized as yellow plates from a solution of 1:2 PbI_2 / 4NPEA-I in HI/MeOH/^{i}PrOH. While $(DMEN)PbBr_4$, the previously reported 3×3 HOIP,[113] required weeks to crystallize, $(4NPEA)_2PbI_4$ could be synthesized in only a few hours. Its purity was assessed by elemental analysis and powder XRD, while single-crystal XRD showed it to be a corrugated 3×3 2D structure (Figure 2). The four inequivalent 4NPEA cations in the asymmetric unit each interact differently with the PbI_4 sheets and the neighboring cations.

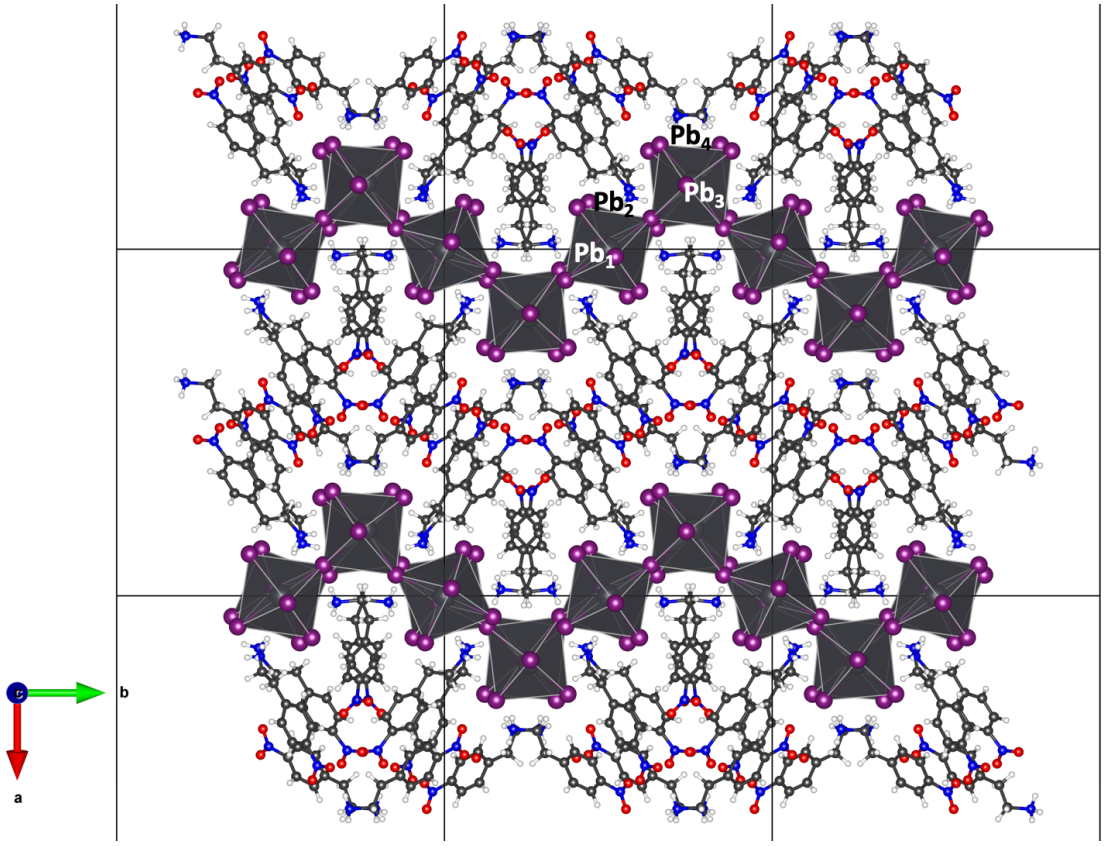

Figure 4.2 Crystal structure of $(4NPEA)_2PbI_4$.

XRD for powder and film samples are consistent with the single-crystal structure (Figure 3).

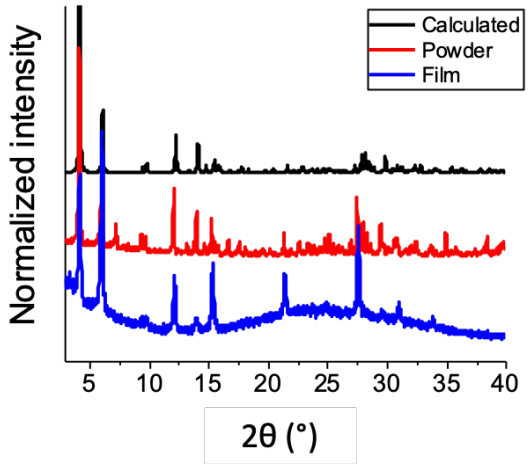

Figure 4.3 Comparison of the powder X-ray diffraction patterns for $(4NPEA)_2PbI_4$ powder (red) and film (blue) with a pattern calculated (black) using the single-crystal data

Based upon the single-crystal XRD data, we dissect the numerous cation-cation and cation-inorganic interactions to better understand the cation's structure directing role. The ammonium moieties hydrogen bond to iodide ions (Figure 4) with N···I contacts ranging from 3.37 to 3.90 Å. For three of the cations, $N_{NH3}\cdots I$ distances are comparable to those in the 100 structure $(PEA)_2PbI_4$ (3.63 Å)[63] and the 2×2 110 structure (EDBE)PbI_4 {EDBE = $NH_3(CH_2)_2O(CH_2)_2O(CH_2)_2NH_3$} (3.63 Å),[103] while for the fourth the distance (3.37 Å) is smaller than the sum of van der Waals radii.

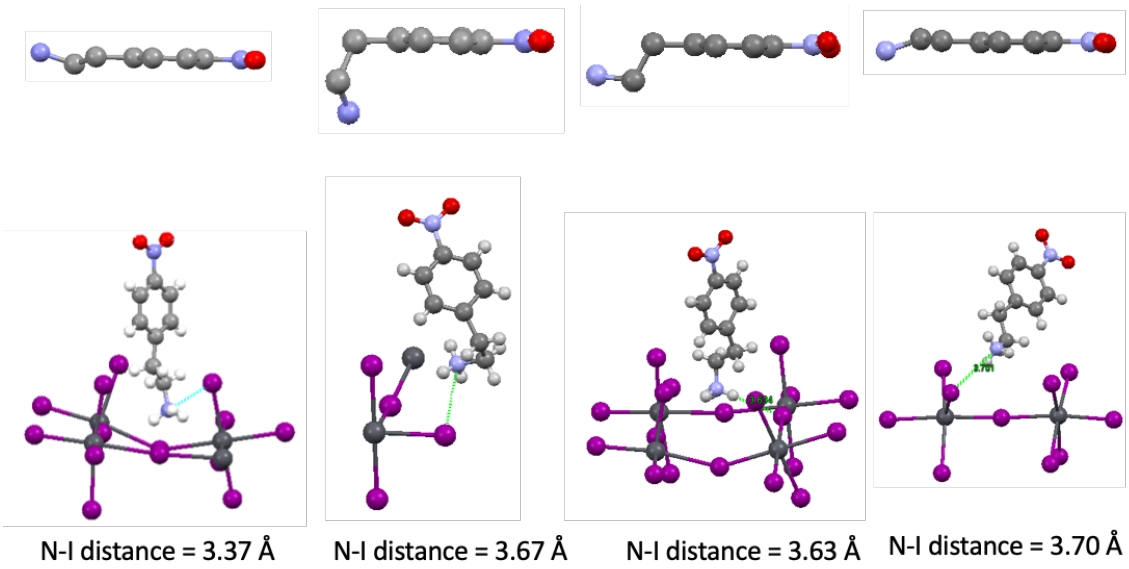

Figure 4.4 Hydrogen bonding between the four different 4NPEA cations and the lead iodide sheet in $(4NPEA)_2PbI_4$.

Nitro groups can interact with each other, with aromatic rings, and with halogens in many modes.[310] $(4NPEA)_2PbI_4$ displays five different intermolecular nitro···nitro interactions attributable to electrostatic attraction between partial positive and negative charges on nitrogen and oxygen atoms, respectively (Figures 5). Perpendicular nitro···nitro interactions (O···O distance of 2.71 Å for the pair of cations in Figure 5A) may help guide the structure, in which the arrangement of cations is very different to the parallel alignment found in typical structures based on derivatives of the PEA cation. Lateral nitro···nitro interactions, where short O···O distances of 2.775, 2.828 and 2.946 Å form a zig-zag structure, may also assist in the formation of the corrugated structure (Figure 5E).

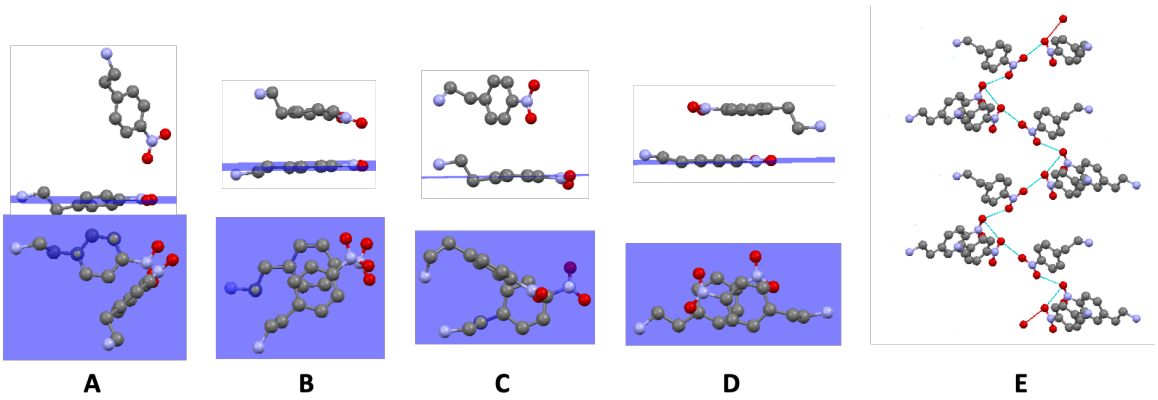

Figure 4.5 Representation of five different modes of interaction involving the nitro group in the crystal structure of $(NPEA)_2PbI_4$. Nitro groups perpendicular (A) and parallel (B) to each other; Nitro group perpendicular (C) and parallel (D) to the benzene ring. Lateral nitro···nitro interactions. The lower views are obtained by an x+90° rotation of the upper views.

Although oligothiophene dications π–stack in Pb/I, Bi/I and Sb/I 2D HOIPs,[38, 311] π–stacking is rare in HOIPs. However, two different π–π stackings (defined here by $R < 4.4$ Å and $\alpha < 45°$, where R is the distance between the plane of one phenyl ring and the centroid of another, and α is the angle between the two phenyl planes) are observed in $(4NPEA)_2PbI_4$ (Figure 6).

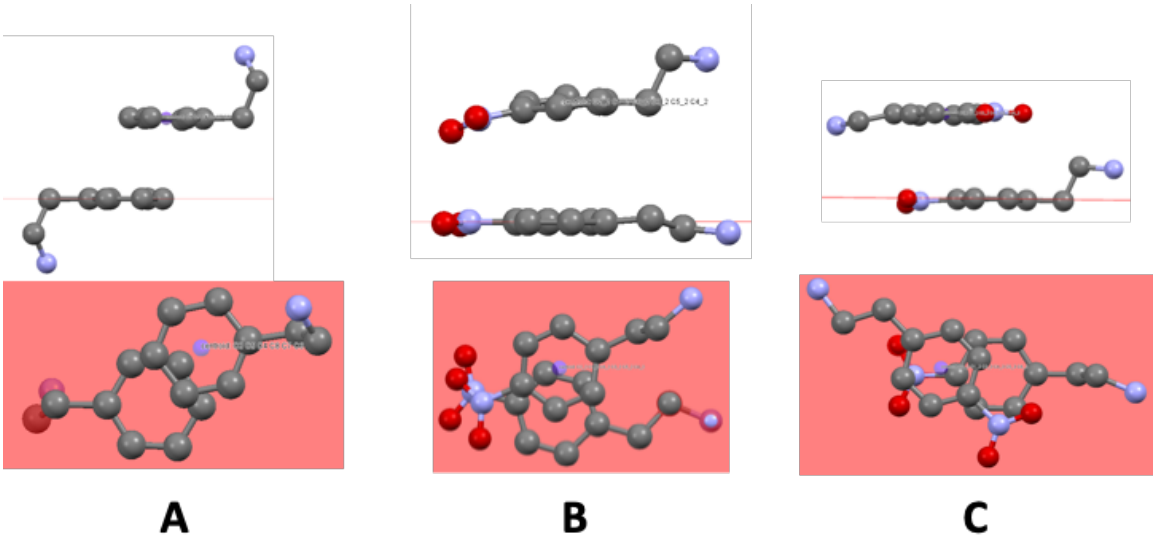

Figure 4.6 π-π stacking interactions between cations in 2D HOIPs: (A) minimal π-overlap between PEA cations seen in the structure of $(PEA)_2PbI_4$,[63] (B) and (C) two π-stacking interactions between pairs of 4NPEA cations in

the structure of $(4PEA)_2PbI_4$, The lower views are obtained by an x+90° rotation of the upper views; the red line/plane represents the plane passing through the aryl groups of one of the cations.

Finally, for one of the four inequivalent cations there is a short contact (3.47 Å) between a nitro oxygen and an iodide (Figure 7) belonging to a *cis*-PbI_6 of one perovskite sheet, while the NH_3 of the same cation interacts with a *trans*-PbI_6 of the neighboring sheet. This nitro group makes a dihedral of 18.4° with the benzene ring, while the corresponding angles for the other three cations are less than 7°. The ability of 4NPEA to bridge the two layers may be significant, since previous corrugated structures involve bridging dications.

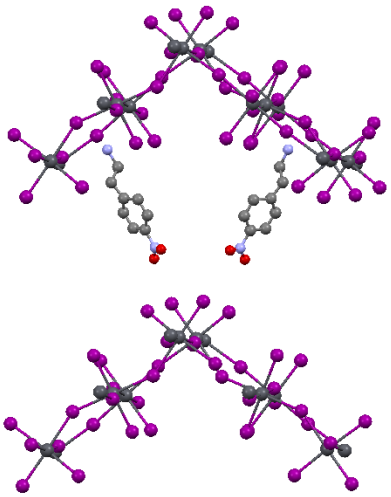

Figure 4.7 NO_2···I interactions between some of the organic cations and the inorganic sheets (other cations omitted).

Thus, the cations may play multiple structure-directing roles. The ammonium moieties anchor and sandwich the inorganic sheets, leading to a 2D structure. The nitro···I interaction may, along with nitro···nitro interactions, provide the driving force for a corrugated structure. Indeed, $(4NPEA)_2PbBr_4$ can be obtained under similar conditions and exhibits an essentially isomorphous structure (see Figure 8, Table 1), but $(4NPEA)_2PbCl_4$ cannot, consistent with both the trend in halide polarizability and halogen-bond donor strength (I > Br >> Cl).

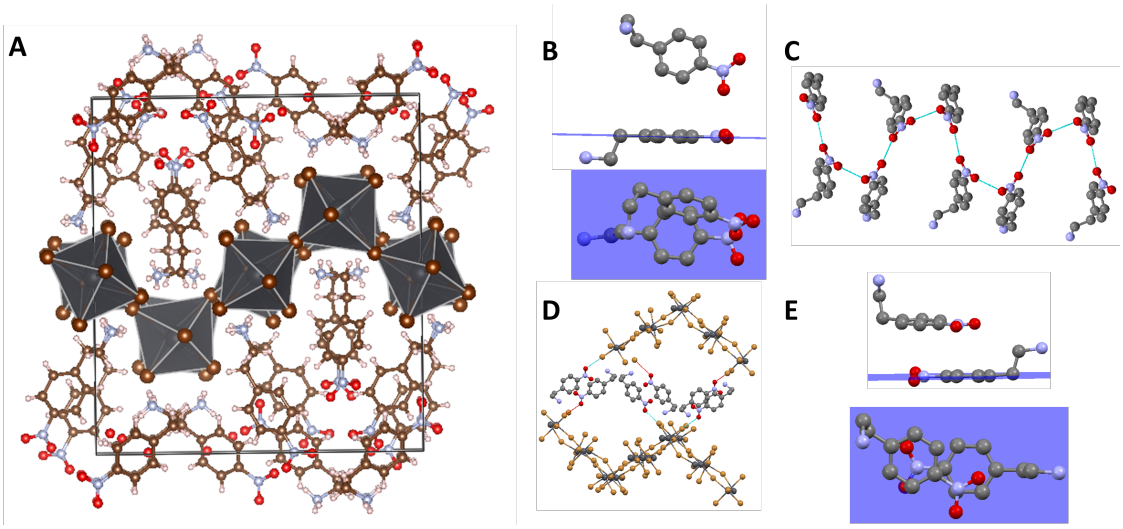

Figure 4.8 (A) Crystal structure of $(4NPEA)_2PbBr_4$. (B) Perpendicular and (C) lateral $O_{NO2}\cdots O_{NO2}$ interaction between two 4NPEA, (D) Representation of the halogen bonding between the inorganic sheet and the organic cation. (E) Representation of the nitro-benzene parallel interaction.

The wealth of non-covalent cation-cation and cation-perovskite interactions in the crystal prompted us to examine the motion of the cation using ^{13}C cross-polarization magic angle spinning (CP/MAS) solid-state (SS) NMR. We reproduced a previous study[312] of $(PEA)_2PbI_4$ showing that $C_{2,6}$ and $C_{3,5}$ linewidths increase with increasing temperature (Figure 9), while those for C_1 and C_4 remain relatively narrow. This has been attributed to flipping of the phenyl ring around its C_2 (C_1-C_4) axis, with the correlation time between rotational jumps (τ_c) at the lowest temperatures being long relative to ω_1^{-1}, where ω_1 is the strength of the rf field (50 kHz here).[313] In contrast, the $C_{2,6}$ and $C_{3,5}$ resonances of $(4NPEA)_2PbI_4$ are relatively broad from 260 to ca. 300 K, but as the temperature is raised to 385 K, become increasingly narrowed, indicating that it falls in the limit where τ_c is short compared to ω_1^{-1}, indicating a lower activation energy of motion, presumably due to less tight packing of the cations.

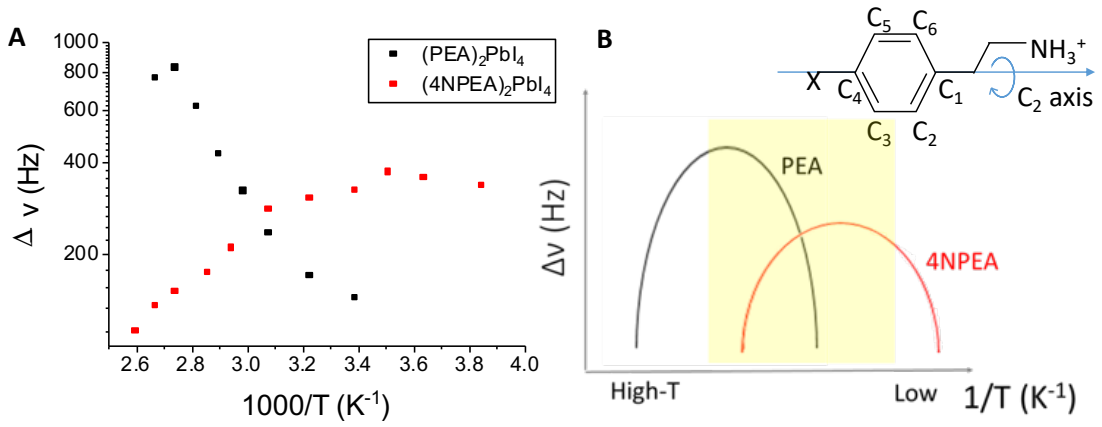

Figure 4.9 (A) Temperature dependence of the linewidth (Δν) of the $C_{2,3}/C_{5,6}$ ^{13}C CP/MAS NMR resonances for $(PEA)_2PbI_4$ and $(4NPEA)_2PbI_4$. (B) Schematic showing how the temperature range used (shaded) accesses different regimes for the two HOIPs. Inset: motion about the C_2 axis of a phenyl ring.

An interesting aspect of Pb/X HOIPs, due in part to its effect on optical properties, is the extent to which PbX_6 octahedra are distorted from ideal geometry; this has been quantified using the octahedral elongation (λ_{oct}) and the octahedral angle variance (σ^2_{oct}):[139, 314]

$$\lambda_{oct} = \frac{1}{6}\sum_{i=1}^{6}\left(\frac{d_i}{d_0}\right)^2 \qquad \text{Eq. 1}$$

$$\sigma^2_{oct} = \frac{1}{11}\sum_{i=1}^{12}(\alpha_i - 90)^2 \qquad \text{Eq. 2}$$

where d_i is the Pb-X bond length, d_0 is the center-to-vertex distance of a regular polyhedron of the same volume, and α_i is the X-Pb-X angle.

In $(4NPEA)_2PbI_4$ there are four inequivalent PbI_6 octahedra; the two with *cis* unshared vertices (Pb4,3 in Figure 2) are significantly distorted, while the two *trans* octahedra (Pb1,2) are near-ideal. A similar, although less pronounced, difference between *cis* and *trans* octahedra is found in the 3×3 corrugated structure of $(DMEN)PbBr_4$.[113] *Cis* octahedra are not necessarily highly distorted; near-ideal geometries are found in the 2×2 corrugated

structure of (API)$PbBr_4$ (API = 3-(3-ammoniopropyl)imidazolium) and in the 3x3 structure of $(4NPEA)_2PbBr_4$ (see Table 1).[108] Figure 10 compares $\boldsymbol{\lambda_{oct}}$ and σ^2_{oct} for $(4NPEA)_2PbI_4$ with values for some other crystallographically characterized Pb/I-based HOIPs. Structural distortion parameters have been calculated using the VESTA software from the published crystallographic data. The λ_{oct} values are similar to those in the *cis* octahedra of other corrugated structures including 3×3 (DMEN)$PbBr_4$[113] and $(4NPEA)_2PbBr_4$, and 2×2 (EDBE)PbI_4[103] and (API)$PbBr_4$ (API = 3-(3-ammoniopropyl)imidazolium).[108] However, σ^2_{oct} values for $(4NPEA)_2PbI_4$ are unusually large and, in contrast to other corrugated structures including that of $(4NPEA)_2PbBr_4$, deviate significantly from a previously suggested[314] linear relationship between σ^2_{oct} and λ_{oct} (Figure 10A).

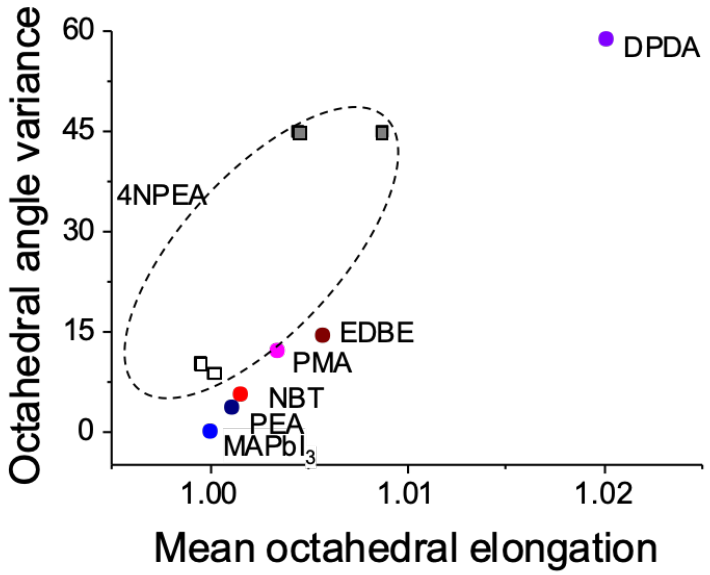

Figure 4.10 (A) λ_{oct} vs σ^2_{oct} for Pb/I HOIPs.

Consistent with the two types of PbI_6 units in the structure of $(4NPEA)_2PbI_4$, two well-separated peaks are seen in its MAS ^{207}Pb SS-NMR spectrum (Figure 11). We also acquired ^{207}Pb spectra for other A_2PbI_4 compounds with varying distortions.

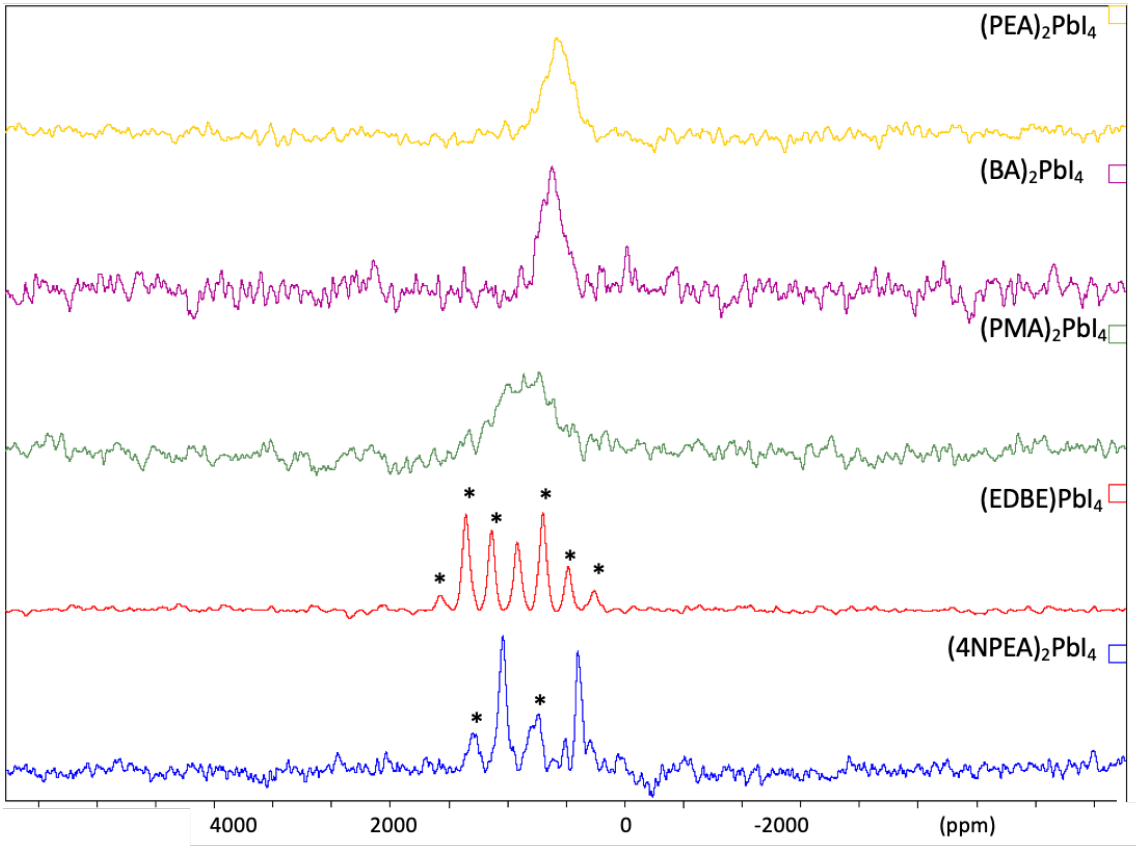

Figure 4.11 ^{207}Pb MAS SS NMR spectra of different $(A)_xPbI_4$. The spinning side bands are indicated with "*".The spinning side bands for $(EDBE)PbI_4$ are more intense than the peak at the isotropic shift because the spinning rate is less than the extent of the anisotropic NMR interactions.[315] $(EDBE)_2PbI_4$,[103] $(PMA)_2PbI_4$ (PMA = $PhCH_2NH_3$),[63] $(PEA)_2PbI_4$,[63] and $(BA)_2PbI_4$[92] were synthesized according to the literature. The structural distortions were taken from crystallographic data in the same publications using the VESTA software. Figure 4A also includes distortion parameters from additional structures: $MAPbI_3$[316] and (DPDA)PbI_4 (DPDA = *p*-$NH_3(C_6H_4)NMe_2H$).[68] Spectra were referenced using $Pb(NO_3)_2$ at 298 K using the equation $\delta(^{207}Pb) = 0.70T - 3712.8$.[317]

^{207}Pb spectra for other A_2PbI_4 compounds with varying distortions in their crystal structures reveal a linear relationship between chemical shift, $\delta(^{207}Pb)$, and λ_{oct} (Figure 10B):

$$\lambda_{oct} = 1.31 \times 10^{-5} \cdot \delta\left(^{207}\mathrm{Pb}\right) + 0.987 \qquad \text{Eq. 3}$$

indicating $\delta(^{207}Pb)$ may be a useful probe of octahedral distortion where crystallographic data are unavailable. Data for $(4NPEA)_2PbI_4$ also fit this relationship, allowing the peak at

ca. 900 ppm to be assigned to the near-ideal *trans* octahedra and that at ca. 1500 ppm to the distorted *cis* octahedra.

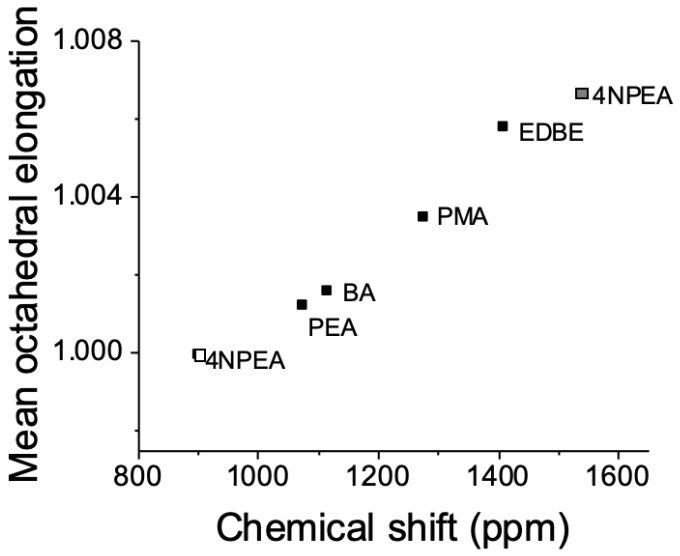

Figure 4.12 Relationship between λ_{oct} and $\delta(^{207}Pb)$ for A_2PbI_4 HOIPs. See Figure 11 for cation definitions and references for structures.

The distortion in the structure also affects the UV-vis. absorption and photoluminescence (PL) properties of $(4NPEA)_2PbI_4$ films (Figure 13). Consistent with other 2D HOIPs, the absorption spectrum for $(4NPEA)_2PbI_4$ shows a continuum-like feature extending into the UV and a sub-bandgap exciton-like feature (Figure 13A). As the temperature is decreased the exciton peak energy (2.56 eV) remains constant and the absorption cross-section slightly decreases, while fine structure becomes discernable. The temperature independence of the peak position is similar to that seen for corrugated 2×2 $(EDBE)_2PbI_4$,[318] which also contains highly distorted octahedra, whereas (100) $(PEA)_2PbI_4$,[319] with more regular octahedra, exhibits increasingly red-shifted exciton bands. Shoulders at low-temperature suggest three peaks separated by ca. 35 meV, as observed for other 2D Pb/I HOIPs including $(EDBE)PbI_4$,[318] $(PEA)_2PbI_4$,[319] and $(BA)_2PbI_4$.[318] The lack of a distinct

band edge, even at low temperature, is another way in which $(4NPEA)_2PbI_4$ resembles $(EDBE)PbI_4$ and differs from Ruddlesden-Popper Pb/I perovskites, which do exhibit a clear edge. A possible explanation is that the highly distorted octahedra in both corrugated structures may increase the density of defects, probably lead and/or iodide vacancies, leading to a long absorption tail extending into the bandgap.

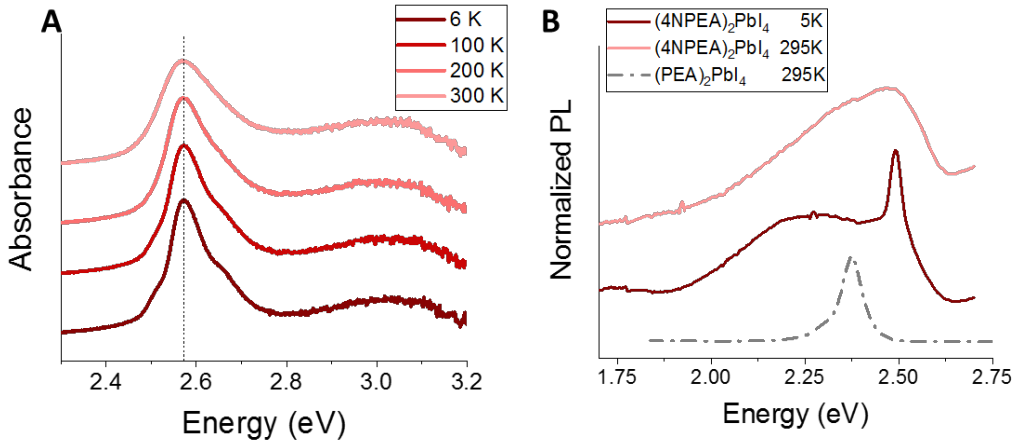

Figure 4.13 (A) Absorption spectra of $(4NPEA)_2PbI_4$ films. (B) PL spectra of a $(4NPEA)_2PbI_4$ film at 5 K and 295 K and a $(PEA)_2PbI_4$ film at 295 K.

Upon photoexcitation at 343 nm within the carrier continuum, the PL of polycrystalline $(4NPEA)_2PbI_4$ is broad (1.8-2.6 eV) (Figure 13B). At 295 K, this emission peaks at 2.4 eV, with a FWHM of 440 meV, a Stokes shift of 200 meV, and a quantum yield of (0.4±0.1)% (comparable to other 2D Pb/I HOIPs[13]). PL lifetimes are ca. 4 ns and do not change appreciably with emission wavelength (Figure 14A-B). In contrast, the PL of (100) HOIPs, such as $(PEA)_2PbI_4$, attributed to radiative emission from free excitons, is typically narrow, exhibits fine structure and smaller Stokes shifts, and resembles a mirror image of the exciton absorption band. Broad strongly Stokes-shifted emissions *are* typical of (110) HOIPs, and have been hypothesized to arise from both free and self-trapped excitons,[320, 321] the latter arising from strong electron/hole-lattice coupling. The linear dependence of

the broadband emission of $(4NPEA)_2PbI_4$ on excitation power over two orders of magnitude is consistent with this mechanism, rather than with extrinsic defect emission (Figure 14C). The low-temperature PL of a $(4NPEA)_2PbI_4$ film exhibits an additional sharp feature at 2.49 eV, which vanishes above 30K and is easily saturated by increasing the excitation power (Figure 14D). This behavior is typical of defect bound emission.[321, 322] Moreover, this sharp feature was not observed uniformly across the film (and unobservable for some films), suggesting an inhomogenous spatial distribution of defects (Figure 14E).

4.4 Conclusion

In summary, $(4NPEA)_2PbI_4$ is the first 3×3 Pb/I HOIP and the first corrugated HOIP to contain organic monocations. A wide range of cation-cation and cation-iodide interactions are present; further understanding of these interactions may help engineer new HOIPs. These interactions do not hinder cation motion, which is more rapid than that in $(PEA)_2PbI_4$. The structure contains both near-regular and highly distorted PbI_6 octahedra, resulting in two distinct ^{207}Pb NMR resonances; indeed, we find $\delta(^{207}Pb)$ correlates with the distortion from the octahedra. The optical properties of $(4NPEA)_2PbI_4$ resemble those of other HOIPs containing highly distorted octahedra, rather than those with more regular octahedra.

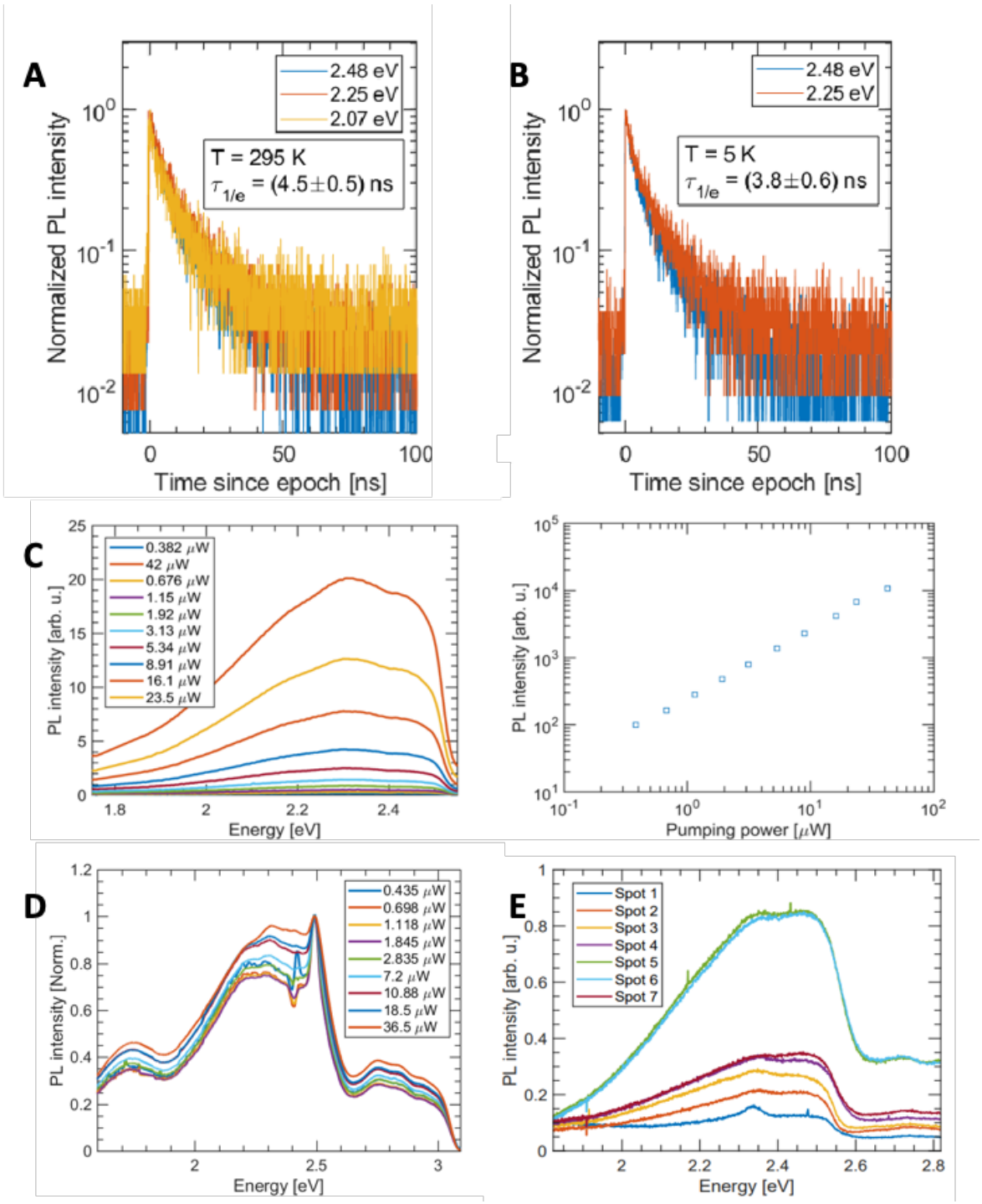

Figure 4.14 Time resolved photoluminescence at (A) 295K and (B) 5 K for $(4NPEA)_2PbI_4$ films for different emission energies. The PL lifetimes are taken to be the time required for the signal to drop to 1/e of its maximal value. The uncertainties on the lifetimes arise from shot noise in the signal. (C) Relationship between the 295 K photoluminescence intensity for a $(4NPEA)_2PbI_4$ film and the power of the laser. (D) Emission spectra for a $(4NPEA)_2PbI_4$ film at 5 K at different optical excitation power. (E) Photoluminescence of $(4NPEA)_2PbI_4$ films when excited with 700 nW of 343nm light at various spots on the sample. The heterogeneity of the film manifests itself through the position-dependent intensity and lineshape of the PL.

CHAPTER 5: STRUCTURAL DIVERSITY IN 2,2'-[NAPHTHALENE-1,8:4,5-BIS(DICARBOXIMIDE)-*N*,*N*'-DIYL]-BIS(ETHYLAMMONIUM) IODOPLUMBATES

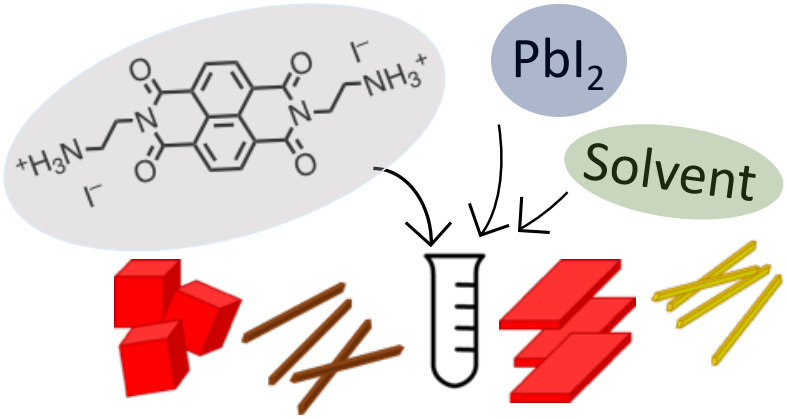

This project was accomplished with the collaboration of Andrew M. Zeidell, Sergei Rigin, Colin Tyznik, John Bacsa, Yadong Zhang, Khaled Al Kurdi, Oana D. Jurchescu, Tatiana V. Timofeeva and Stephen Barlow. Andrew M. Zeidell and Colin Tyznik, in the group of Oana D. Jurchescu, from Wake Forest University, performed the conductivity measurements. Sergei Rigin, in the group of Tatiana V. Timofeeva, from New Mexico Highlands University, and John Bacsa, from the Crystallography Lab of Emory University, performed the single crystal X-ray diffraction experiments. Yadong Zhang provided the organic compounds. Khaled Al Kurdi helped with the thermal experiments. Stephen Barlow helped with the data analysis and he helped to write the manuscript. The content of this chapter was published in Chemistry of Materials in August 2019 (DOI: 10.1021/acs.chemmater.9b01564). This work was supported by NSERC (ES. D. Scholarship for MHT) and the AFOSR (FA9550-18-1-0499). All authors contributed to

the redaction of the manuscript. This work was supported by NSERC (ES. D. Scholarship for MHT), the AFOSR (via award FA9550-18-1-0499), the NSF (via ECCS-1608095 and through the PREM program via DMR-1523611).

5.1 Introduction

A wide range of organic-inorganic hybrid iodoplumbate(II) compounds (HIPC) with 3-, 2-, 1- or 0-dimensional structures have been synthesized and studied.[323-330] The organic cation used in HIPCs has a key role as a structure-directing agent.[331] The smallest cations – methylammonium and formamidinium – form 3D networks with the perovskite structure, i.e. based on corner sharing between PbI_6 octahedra, while somewhat larger (phenylethylammonium, butylammonium) cations instead form 2D perovskite structures, often with $RNH_3\cdots I$ hydrogen bonding. Still larger cations, including many examples without hydrogen-bond donors, form 1D HIPCs. Face- and/or edge-sharing between PbI_6 octahedra, rather than the corner sharing characteristic of perovskites, are frequently found in 1D HIPCs, and also in some examples of 2D HIPCs with larger cations; such structures are, accordingly, sometimes referred to as "perovskitoids".

An attractive feature of 1D, and to a lesser extent, 2D perovskitoids, is that they can incorporate a much greater diversity of cations than 2D and 3D perovskites, opening the possibility of introducing new properties to the HIPC. These properties can directly result from those of the cation; for example, use of a cyanine heptamethine cation imparts near-IR absorption and emission properties,[10] while paramagnetism has been imparted by the use of tetrathiafulvalene radical cation[11] or $Tb(DMF)_8^{3+}$ (DMF = *N,N*-dimethylformamide).[12] Other properties arise from interactions between the haloplumbate and organic cation portions of the cation. Thus, the use of electron acceptors such as viologen dications[13-15] and the tropylium cation[16] lead to haloplumbate-to-cation

panchromatic visible absorption, which in the case of viologens has been found to be associated with photoconductivity,[15] and thermochromism.[14]

The electron-accepting and electron-transporting naphthalene diimide (NDI) moiety has been incorporated into a number of HIPCs. The first example was reported by Liu *et al.* and incorporated a di(pyridinium)-substituted NDI dication, $\mathbf{I}^{2+}$ (Figure 1);[204, 332] the reaction of the corresponding neutral di(pyridyl) NDI (**II**, Figure 1), PbI_2, and HI in *N*-methyl-2-pyrrolidone (NMP) gave $[(\mathbf{I})Pb_2I_6]\cdot H_2O\cdot NMP$, which has a 1D structure consisting of chains of face-sharing PbI_6 octahedra. A similar reaction in DMF gave $[(\mathbf{II})PbI_2]$, in which the pyridine nitrogen atoms of neutral **II** are coordinated to lead: PbI_4N_2 octahedra share their iodide edge to form chains, while **II** molecules act as bridges between adjacent chains.[204] An alkylated ammonium-NDI monocation ($\mathbf{III}^{+}$, Figure 1) has been incorporated into a 2D HIPC in which corrugated iodoplumbate sheets consist of both corner- and edge-sharing octahedra.[333] All three of these NDI-iodoplumbates showed absorption spanning the visible part of the spectrum.

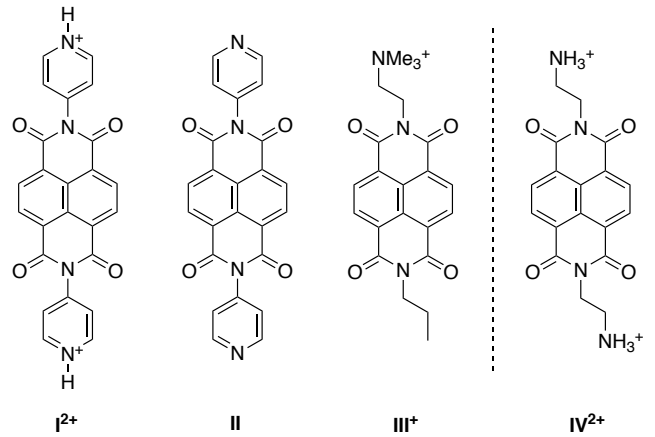

Figure 5.1 Left: NDI derivatives previously incorporated into the HIPCs $[(\mathbf{I})Pb_2I_6]\cdot H_2O\cdot NMP$, $[(\mathbf{II})PbI_2]$, and $[(\mathbf{III})_4Pb_3I_{10}]$. Right: NDI dication ($\mathbf{IV}^{2+}$, $NDIC2^{2+}$) used in this work.

The possibility of using different types of NDI-based species in HIPCs was explored. In particular, the previously examined species possess either rigidly oriented hydrogen bond donors ($\mathbf{I}^{2+}$) or no hydrogen-bond donors (**II** and $\mathbf{III}^{+}$). In this study, a NDIs linked to ammonium hydrogen-bond donors through flexible linkers is studied. 2,2'-[naphthalene-1,8:4,5-bis(dicarboximide)-*N,N*'-diyl]-bis(ethylammonium) dication ($\mathbf{IV}^{2+}$, $NDIC2^{2+}$, Figure 1) is selected as the simplest example of such a dication. Here it is reported that a diverse range of structures can be obtained from the $(NDIC2)I_2/PbI_2$ system, depending on the reaction conditions and subsequent thermal or solvent treatments. The structural, thermal stability, electronic, and optical properties of these compounds are discussed.

5.2 Experimental Section

(NDIC2)I_2. 2,2'-[Naphthalene-1,8:4,5-bis(dicarboximide)-*N,N*'-diyl]-bis(ethylammonium) bis(trifluoroacetate)[334, 335] (5.8 g, 10 mmol**)** was stirred in HI (30 mL of a 50% aqueous solution) at room temperature for 24 h. The solids were collected by filtration, washed with water, and dried under vacuum to yield a yellow powder (5.9 g, 97%), which elemental analysis suggest contains a small quantity of additional HI. Anal. Calcd for $C_{18}H_{18}N_4O_4I_2$ [(NDIC2)I_2]: C, 35.55; H, 2.98; N, 9.21. Anal. Calcd for $C_{18}H_{18.17}N_2O_4I_{2.17}$ [(NDIC2)$I_2 \cdot {}^1/_6$HI] C, 34.34; H, 2.91; N, 8.90. Found C 34.05, H 2.74, N 8.81. ^{1}H NMR (400 MHz, DMF-d_7): δ 8.6 (s, 4H), 8.4 (s, br, 6H), 4.5 (t, J = 6 Hz, 4H), 3.5 (s, 4H). ^{13}C{^{1}H} NMR (100 MHz, DMF-d_7): δ 162.60, 130.62, 126.95, 126.74, 38.65, 38.27. HRMS (ESI) calcd for $C_{18}H_{17}O_4N_4$ ($M^+ - HI_2$): 353.1244, found: 353.1236.

General perovskitoid synthesis. All syntheses were carried out in air at room temperature.

[(NDIC2)$_2$Pb$_5$I$_{14}$(DMF)$_2$]·4DMF (1). PbI_2 (15.0 mg, 0.03 mmol) and (NDIC2)I_2 (36.1 mg, 0.06 mmol) were dissolved in DMF (3 mL). A portion (0.5 mL) of this solution was placed in a 2 mL vial, which was placed in a 20 mL vial containing CH_2Cl_2 (5 mL), the larger vial being then capped. After 4 d, red crystalline product (< 1 mg), including the crystal used for structure determination, was obtained at the bottom of the small vial. Alternatively, PbI_2 (120 mg, 0.22 mmol) and (NDIC2)I_2 (218 mg, 0.36 mmol) were dissolved in DMF (12 mL). A portion of this solution (6 mL) was added to a 20 mL vial and layered with EtOH (14 mL). After 48 h, the resulting solids were collected using vacuum filtration to yield dark red crystals (120 mg, 70%). Anal. Calcd for $C_{54}H_{78}I_{14}N_{14}O_{14}Pb_5$: C, 16.38; H, 1.99; N, 4.95. Found: C, 16.79; H, 1.99; N, 4.95.

[(NDIC$_2$)$_3$Pb$_5$I$_{16}$]·6NMP (2). PbI_2 (5.2 mg, 0.01 mmol) and (NDIC2)I_2 (11.8 mg, 0.02 mmol) solution were dissolved in NMP (1 mL); a portion (0.5 mL) of this solution was placed in a 2 mL vial, which was placed in a 20 mL vial containing CH_2Cl_2 (5 mL), the larger vial being then capped. After 5 d, the red product crystallized (< 1 mg) at the bottom of the small vial.

[(NDIC$_2$)Pb$_4$I$_{10}$]·4DMF (3). PbI_2 (15.0 mg, 0.03 mmol) and (NDIC2)I_2 (36.1 mg, 0.06 mmol) were dissolved in DMF (3 mL). A portion (0.5 mL) of this solution was to a 2 mL vial, which was placed in a 20 mL vial containing 5 mL of EtOH, the larger vial being then capped. After 30 d, a yellow product crystallized (< 1 mg) at the bottom of the small vial.

[(NDIC$_2$)Pb$_2$I$_6$]·4NMP (4). PbI_2 (10.0 mg, 0.02 mmol) and (NDIC2)I_2 (24 mg, 0.04 mmol) were dissolved in NMP (2 mL). A portion (0.5 mL) of this solution was placed in a 2 mL vial and layered with EtOH (1 mL). After 10 d, red product crystallized (< 1 mg) at the bottom of the vial.

[(NDIC2)Pb$_2$I$_6$]·2H$_2$O (5). Compound **1** (50 mg, 0.013 mmol) was added to water (1 mL). After 24 h, the brown powder (32 mg) was filtered and dried under vacuum. This material contained crystals of **5**, but powder XRD indicated a mixture with **6**, the approximate molar ratio of these two compounds was estimated as ca. 3:2 from elemental analysis. Anal. Calcd for $C_{18}H_{20.4}I_{8.4}N_4O_{5.2}Pb_{3.2}$ (3:2 **5**/**6** mixture): C, 10.27; H, 0.98; N, 2.66; I, 50.64. Found: C, 10.37; H, 0.90; N, 2.63; I, 49.29.

[(NDIC2)Pb$_5$I$_{12}$] (6). Compound **1** (50 mg, 0.013 mmol) was added to water (1 mL). After 50 d, the brown powder (9 mg, 20%) was filtered and dried under vacuum. Anal. Calcd for

$C_{18}H_{18}I_{12}N_4O_4Pb_5$: C, 7.42; H, 0.62; N, 1.92; I, 52.27. Found: C, 7.79; H, 0.60; N, 1.88; I, 50.38.

[(NDIC2)Pb_2I_6] (7). Compound **1** (17 mg) was added to MeCN (1 mL); after 24 h, the brown powder was filtered and dried under vacuum. Alternatively, **1** (16 mg) was added to THF (1 mL); after 24 h, the brown powder was filtered and dried under vacuum. Alternatively, **1** (20 mg) was heated at 150 °C for 20 min to obtain the same brown powder. Anal. Calcd for $C_{18}H_{18}I_6N_4O_4Pb_2$: C, 14.13; H, 1.19; N, 3.66; I, 49.76. Found: C, 13.47; H, 1.09; N, 3.54; I, 49.58.

[(NDIC2)Pb_3I_8]·MeCN (8). Compound **1** (100 mg, 0.025 mmol) was added to MeCN (3 mL). After 14 d, the solution was filtered and dried under vacuum to yield a brown powder (32 mg, 40%). Anal. Calcd for $C_{19}H_{19}I_8N_5O_4Pb_3$: C, 11.31; H, 0.95; N, 3.47; I, 50.30. Found: C, 11.82; H, 0.92; N, 2.93; I, 49.69.

Characterization.

PXRD patterns were acquired on a Panalytical XPert PRO Alpha-1 XRD Diffractometer using Cu Kα X-ray tube radiation at a voltage of 45 kV and 40 mA, with an incident beam Johannsson monochromator and an X'Celerator solid-state detector. The diffraction pattern was scanned over the angular range of 3-40° with a step size of 0.016°, at room temperature. PXRD data were compared to simulated powder patterns calculated by Mercury software[306] using the CIFs obtained from the single-crystal X-ray experiments.

Differential scanning calorimetry (DSC) and thermogravimetric analysis (TGA) were performed using Mettler Toledo Instrument (TGA/DSC 3+ Star e system) at 10 °C min^{-1},

under nitrogen flow (80 mL min^{-1}). Diffuse reflectance spectra were measured on a Cary 5000 UV-vis-NIR instrument.

Electrical measurements were performed in the dark on single crystals of **1** in a nitrogen atmosphere using an Agilent 4155C semiconductor parameter analyzer. Ag epoxy contacts (Chemtronics CW2400) were painted by hand, and the contact separation and width were measured for each sample based on the optical images acquired using an Olympus BH-2 optical microscope. Over ten crystals were measured and the results were consistent. The thickness of crystals was measured with a Neiko 01407A caliper. The photocurrent response was evaluated for the same crystals. For these measurements, a 0.8 mW broadband fiber-coupled LED source (Thorlabs, MBB1F1) was used as the light source, and the measurements were taken under nitrogen for several different light intensities, while sweeping the voltage from 0 to 5 V.

Crystals for single-crystal X-ray measurements were mounted on a loop with paratone oil on a XtaLAB Synergy-S Dualflex HyPix diffractometer (**1**, **3-5**) or a Bruker SMART APEX II CCD diffractometer (**2**). The crystals were cooled during data collection. Using OLEX2,[307] the structures were solved with the SHELXT[308] structure solution program using Intrinsic Phasing and refined with the SHELXL[309] refinement package using least squares minimization. Further details are given in Table 1. Data may be obtained in CIF format from the Cambridge Crystallographic Data Center; the deposition numbers for the structures of **1-5** are CCDC 1977725-1977729, respectively.

The structure of **3** was refined as a 2-component twin. The diffraction intensity data suffered from problems related to the quality of the crystals. The fine yellow crystals grew

as very thin needles. The needles are only a few microns thick, were flexible and therefore only a few thousand molecules thick in one direction. The needles bend when prodded and they peel away from each other forming thinner needles. It is reasonable to assume that the crystals grow preferentially along the needle axis and that the crystal forces between the donors and acceptors operating perpendicular to the needle axis are very weak. The quality of the diffraction data was consistent with a very short *a*-axis (the needle direction, stronger diffraction) and a long *c*-axis (perpendicular to the needle axis). The diffraction was very weak and showed considerable splitting along the c-axis corresponding to the growth morphology, twinning and disorder.

4 was obtained as dark red needles. The needle axis corresponding to the [100] lattice vector. Precession Images show that the lattice planes orthogonal to the *b*-axis are highly ordered but those along the direct lattice vector are partially disordered and that that these red needles crystallize with dislocation or stacking faults. The repeat distance of this disorder appears to have a divisor of two. This type of disorder has been studied in wurtzite crystals.[336] We did not see evidence for doubling the *b*-axis. The organic molecules are held together by a mixture of H bonds and π-π stacking interactions. There are three hydrogen-bonds for each NH_3 group. During the preliminary refinements, the data gave very large residual electron densities in the portions of the crystal lattice where the organic groups are (*i.e.* in the large regions of the crystal structure between the (Pb_2I_6) chains). The size of the peaks was roughly eight electrons per $Å^3$, about the size of an oxygen atom. Therefore, it does not make sense that these correspond to partially occupied organic groups. The mechanism of the formation of the disorder is not obvious but closer inspection of the size and shape of the electron densities showed secondary (Pb_2I_6) chains

following the same direction as the primary chains, but displaced by *b*/2. Thus the crystal structure is a disordered (but not a composite structure) with alternating 1D chains and the disorder is a displacement of the entire structure by 1/2**b* along the [100] lattice vector. The second component makes up about 5% of the overall structure. Although the heavy Pb and I show up very strongly, the disorder of the lighter organic groups could not be modelled.

Crystals of **5** were found to be twinned.

Table 5.1 Single-crystal data and structure refinement data

	1	2	3
Empirical formula	$[(C_{18}H_{18}N_4O_4)_2Pb_5I_{14}(C_3H_7NO)_2]\cdot 4(C_3H_7NO)$	$[(C_{18}H_{18}N_4O_4)_3Pb_5I_{16}]\cdot 6(C_5H_9NO)$	$[(C_{18}H_{18}N_4O_4)Pb_4I_{10}]\cdot 4(C_3H_7NO)$
FW	3951.85	4724.23	2744.50
***T* / K**	100(2)	150	100(1)
Crystal system	Triclinic	Triclinic	Monoclinic
Space group	$P\bar{1}$	$P\bar{1}$	$P2_1/c$
***a* / Å**	11.26264(8)	13.940(2)	4.56680(19)
***b* / Å**	11.86182(8)	14.785(3)	20.2158(6)
***c* / Å**	17.57847(11)	16.220(3)	32.1154(8)
***α* / °**	95.2668(5)	112.512(3)	90
***β* / °**	95.7774(5)	99.122(3)	90.096(3)
***γ* / °**	94.3397(6)	94.423(3)	90
***V* / Å^3**	2318.05(3)	3014.1(9)	2964.94(16)
Z	1	1	2
***ρ* / g cm^{-3}**	2.837	2.603	3.074
***μ* / mm^{-1}**	13.767	11.119	62.918
***F*(000)**	1764	2140	2400
Crystal size / mm^3	0.32 × 0.17 × 0.17	0.415 × 0.181 × 0.123	0.38 × 0.04 × 0.04
Radiation (λ / nm)	MoKα (0.71073)	MoKα (0.71073)	CuKα (1.54184)
2*θ* range data coll. / °	3.460–76.14	3.016–50.00	5.504–130.132
Index ranges	$-19 \le h \le 19$, $-20 \le k \le 20$, $-30 \le l \le 30$	$-16 \le h \le 16$, $-17 \le k \le 17$, $-19 \le l \le 19$	$-5 \le h \le 5$, $-24 \le k \le 23$, $-37 \le l \le 36$
Reflections collected	113900	84423	14653
Independent reflections	24056 [Rint = 0.0451]	10598 [R_{int} = 0.2358]	4803 [R_{int} = 0.0609]
Data/ restraints / param.	24056 / 0 / 466	10598 /0 / 565	4803 / 165 / 277
GOF on F^2	1.086	0.997	1.049
Final R_1, wR_2 [$I \ge 2\sigma(I)$]	0.0253, 0.0555	0.0532, 0.1254	0.0612, 0.1574
Final R_1, wR_2 [all data]	0.0299, 0.0565	0.0909, 0.1424	0.0701, 0.1633
Largest peak, hole / e Å^{-3}	2.293, –1.522	1.69, –2.72	2.767, -1.491

Table 5.2 Single-crystal data and structure refinement data

	4	5
Empirical formula	$[(C_{18}H_{18}N_4O_4)Pb_2I_6]\cdot 4(C_5H_9NO)$	$[(C_{18}H_{18}N_4O_4)Pb_2I_6]\cdot 2H_2O$
FW	1926.69	1566.17
***T* / K**	101(2)	100.00(10)
Crystal system	Triclinic	Monoclinic
Space group	$P\bar{1}$	$P2_1/n$
***a* / Å**	8.00200(10)	14.3259(6)
***b* / Å**	14.2273(4)	8.0619(3)
***c* / Å**	23.9584(7)	14.5420(7)
***α* / °**	101.158(2)	90
***β* / °**	92.6467(19)	107.170(5)
***γ* / °**	94.1063(17)	90
***V* / Å^3**	2664.33(12)	1604.68(12)
Z	2	2
***ρ* / g cm^{-3}**	2.402	3.241
***μ* / mm^{-1}**	9.839	16.287
***F*(000)**	1768	1376
Crystal size / mm^3	0.313 × 0.059 × 0.029	0.11 × 0.05 × 0.04
Radiation (λ / nm)	MoKα (0.71073)	MoKα (0.71073)
2*θ* range data coll. / °	3.094–49.426	3.506–54.966
Index ranges	$-9 \le h \le 9$, $-16 \le k \le 16$, $-26 \le l \le 28$	$-18 \le h \le 18$, $-10 \le k \le 10$, $-18 \le l \le 18$
Reflections collected	32253	15286
Independent reflections	9043 [R_{int} = 0.0403]	3671 [R_{int} = 0.0412]
Data/ restraints / param.	9043 / 651 / 609	3671 / 165 / 202
GOF on F^2	1.084	1.101
Final R_1, wR_2 [$I \ge 2\sigma(I)$]	0.0524, 0.1185	0.0501, 0.1334
Final R_1, wR_2 [all data]	0.0627, 0.1226	0.0564, 0.1409
Largest peak, hole / e Å^{-3}	2.491, –2.365	2.588, –2.593

5.3 Results and Discussion

Synthesis of HIPCs from (NDIC2)I_2 and PbI_2. We investigated the reaction of (NDIC2)I_2 and PbI_2 in either NMP or DMF, these being the only two common solvents in which both components have sufficient solubility, followed by different crystallization conditions. To limit the number of variables in our experiments, we kept a constant initial molar starting (NDIC2)I_2 / PbI_2 ratio of 2:1, and conducted all initial HIPC syntheses under air at room temperature. This approach resulted in four HIPCs of general formula $(NDIC2)_xPb_yI_{2(x+y)}S_z$ (S = DMF, NMP) (**1-4**, Figure 2), one of which (**1**) was obtained in good yield, while the other three were obtained as only a few crystals and were not obtained in larger quantities on scaling up the reaction. Each of these four HIPCs was characterized by single-crystal X-ray diffraction (SCXRD). Additional HIPCs (**5-8**) were obtained by subsequent treatment of these initially formed materials (again, as shown in Figure 2), and are discussed in more detail below.

The formation of a large number of different materials emphasizes the great structural diversity achievable in organic haloplumbates. In the present study, the cation and cation:Pb reactant ratio are always the same, yet multiple structures are still obtained. The different reagent concentrations and crystallization times strongly affect the crystal formation. This has been noticed in other systems; for example, the planar (DMEN)$PbBr_4$ (DMEN = 2-(dimethylamino)ethylamine) transform to the 3×3 corrugated structure over time.[337] Moreover, as in some previous studies,[204, 332, 338] the specific solvent also strongly affects the crystallization; indeed, as discussed below, **1-5** and **8** all incorporate solvent.

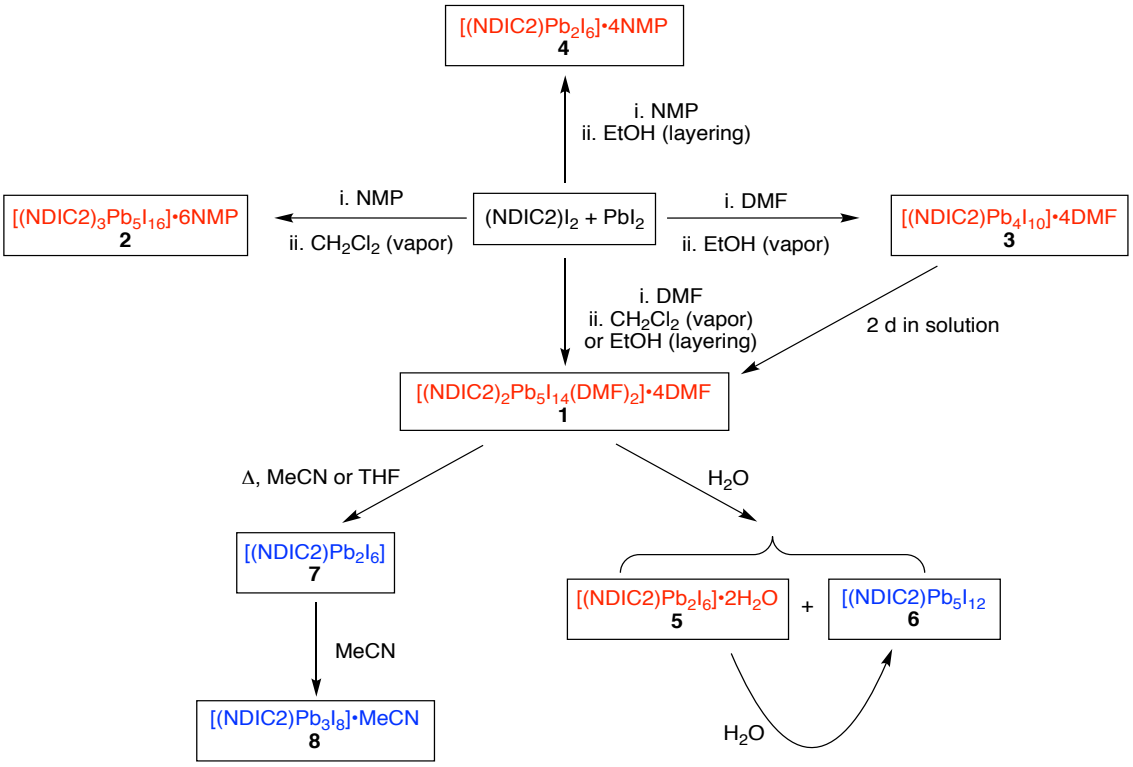

Figure 5.2 Synthesis of the HIPCs obtained in this work. The formulae shown in red were established through single-crystal structure determinations, while those shown in in blue were deduced based on elemental analysis and PXRD. For simplicity, the equations are not balanced; in principle, each reaction can be balanced by loss of either PbI_2 or $(NDIC2)I_2$, in addition to loss or gain of solvent molecules.

Synthesis and Structure of $[(NDIC2)_2Pb_5I_{14}(DMF)_2]\cdot 4DMF$ (1). HIPC **1** was crystallized as red blocks by slow diffusion of ethanol into a DMF solution of $(NDIC2)I_2$ and PbI_2 over 3 days. In addition to determination of its structure using SCXRD (discussed in more detail below), elemental analysis (EA), solution ^1H NMR spectroscopy and powder X-ray diffraction (PXRD) (Figure 3A) were used to confirm the purity and uniformity of **1**. HIPC **1** is stable in ambient conditions (for at least four months, see Figure 3B). TGA (Figure 3C-D) suggests four distinct regimes of weight loss, with weight changes consistent with successive loss of DMF, HI, and the neutral diamine, followed by final sublimation of PbI_2. An endotherm peak is seen by DSC at ca. 175 °C (Figure 3E-F) and may also be associated with loss of DMF.[339]

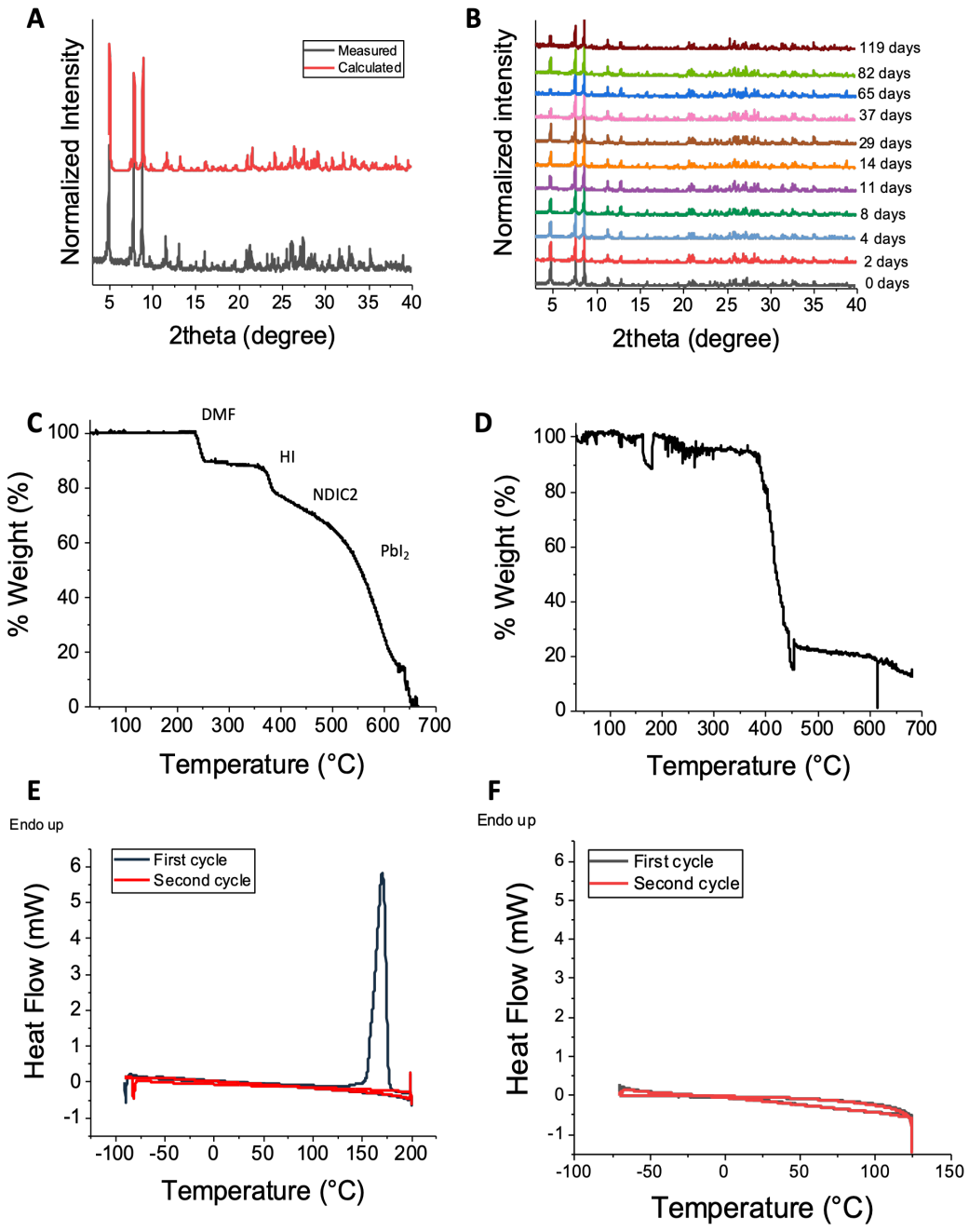

Figure 5.3 (A) Comparison of the powder X-ray diffraction patterns for **1** powder (black) with a pattern calculated (red) using the single-crystal data. (B) Ambient atmosphere stability in the dark of **1** studied by PXRD over time. Thermogravimetric analysis of (C) **1** and (D) $(NDIC2)I_2$ from 25 to 700 °C (5 °C min^{-1}). Weight loss for **1** starts at ca. 240 °C, likely due to the DMF solvent loss (theoretical loss 10%, experimental loss 11%), while the second phase of weight loss is consistent with loss of 4 equivalents of HI (theoretical loss 13%, experimental loss 12%). Around 400-500 °C, there is a poorly defined region of mass loss that might be due to the loss of the diamine (theoretical loss 18%, experimental loss ca. 17%), while the remaining mass loss is attributed to sublimation of PbI_2 (theoretical loss ca. 58%, experimental loss 60%). Differential scanning calorimetry (plotted with endothermic up) of **1** from (E) –90 to 200 °C and (F) –75 to 125 °C.

The crystal structure (Figure 4) reveals a 1D material consisting of: zigzag wires of formula $[Pb_5I_{14}(DMF)_2^{4-}]_n$, in which DMF molecules are coordinated through oxygen to some of the Pb centers; $NDIC2^{2+}$ dications that bridge adjacent wires; and additional uncoordinated DMF molecules.

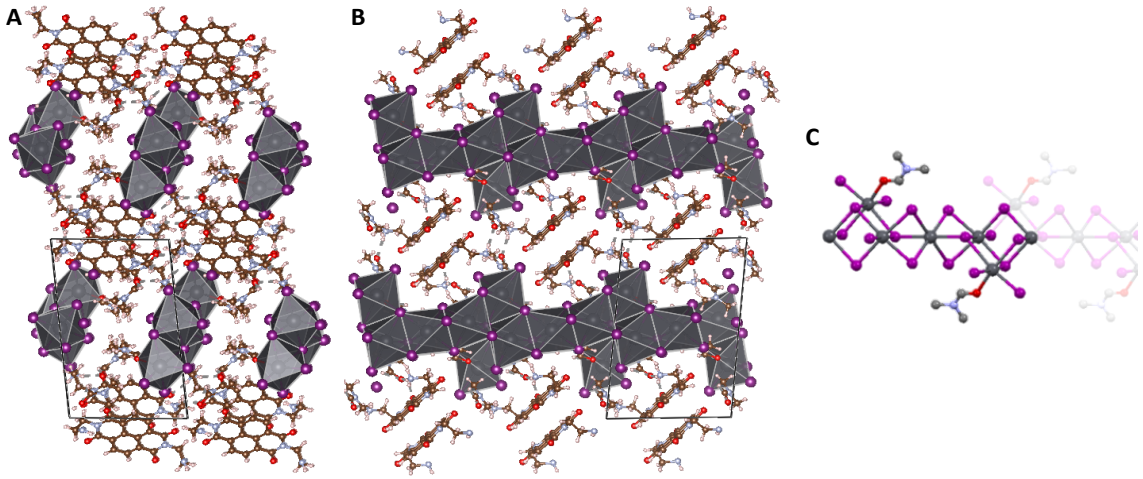

Figure 5.4 (A, B) Two views of the crystal structure of **1**, $[(NDIC2)_2Pb_5I_{14}(DMF)_2]\cdot 4DMF$. (C) Detail showing a $[Pb_5I_{14}(DMF)_2]^{4-}$ chain (NDIC2 and non-coordinated DMF not shown).

The wires contain three crystallographically distinct lead environments – two types of PbI_6 octahedra and $PbI_5(DMF)$ octahedra – in a 1:2:2 ratio. $PbI_5(DMF)$ octahedra have previously been reported in the structures of $[(Pr_3NC_2H_4NPr_3)Pb_6I_{14}(DMF)_2]\cdot 4DMF$, $[(Ph_4P)_4Pb_{15}I_{34}(DMF)_6]$, and $[PbI_2(DMF)]$.[340-342] Other solvent molecules, such as dimethyl sulfoxide (DMSO), have also been found to replace iodide ions in the coordination sphere of Pb.[342-344] In the present structure, the main chain is defined by the two types of PbI_6 octahedra, with the $PbI_5(DMF)$ octahedra fused to the sides of the chains. The first of the two types of PbI_6 octahedra shares two of its faces with PbI_6 octahedra of the second type, while two of its vertices are also shared with two $PbI_5(DMF)$ units. Each PbI_6 octahedron of the second type each share a face with one of the first type, an edge

with another PbI_6 of the second type, another edge with a PbI_5(DMF) unit, and a corner with another PbI_5(DMF) unit. Each PbI_5(DMF) moiety shares two adjacent edges with PbI_6 units of the second type, with one of those edge iodides being further shared with a PbI_6 of the first type.

The ammonium moieties of the NDIC2 dication each form hydrogen bonds to iodide ions in the wires (see Figure 5). The N···I distances (3.649(2)-3.955(2) Å) are similar to those in 2D HOIPs (e.g. 3.63 Å for $(PEA)_2PbI_4$ (PEA = 2-phenylethylammonium)). In addition, there are a variety of close NDIC2···NDIC2 and NDIC2···DMF contacts. One of the two ammonium moieties in each dication is bridged to the corresponding group on a neighboring cation through hydrogen-bonding with two DMF molecules; the oxygen atom of each DMF molecule being hydrogen-bonded to both NH_3 groups (see Figure 5) with N···O distances of 2.773(3)-2.780(3) Å. The other ammonium group of each dication is hydrogen bonded to the oxygen atom of a single non-bridging DMF molecule with an N···O distance of 2.756(3) Å. The NDIC2 dications also form π-stacked dimers with an interplanar distance of 3.31701(2) Å and an offset between the two molecules of around half a benzene ring (see Figure 5), the π-stacking involving a different neighbor to that with which there is a DMF bridge. π-Stacking[34] is a common feature of both small-molecule NDI derivatives in the solid state[35-37] and of π-conjugated species incorporated in HIPCs,[15,38-40] including the NDI moieties of (**II**)PbI_2[18] and (**III**)$_4Pb_3I_{10}$.[19]

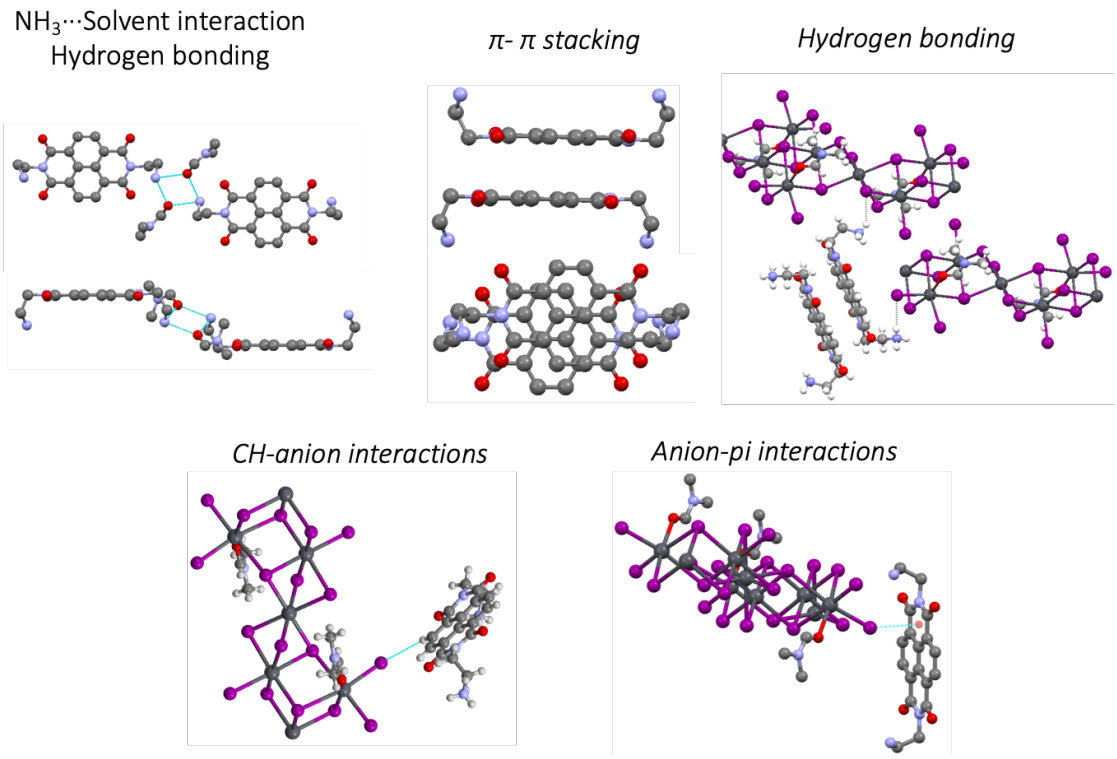

Figure 5.5 Cation-cation and cation-inorganic interactions present in **1**.

Synthesis and Structure of $[(NDIC_2)_3Pb_5I_{16}]\cdot 6NMP$ (2). Red plate-like crystals of HIPC **2** were obtained following slow vapor diffusion of dichloromethane into an NMP solution of (NDIC2)I_2 and PbI_2 over 3 days. SCXRD (Figure 6) revealed that this material contains iodoplumbate clusters, isolated from each other by NDIC2 dications and NMP solvent molecules. Compounds, such as this, in which there is finite metal-halide catenation, rather than formation of infinite 1D chains, 2D sheets, or 3D frameworks are often described as 0D perovskite-like materials;[41,42] however, only a few such 0D iodoplumbates have been reported.[43-50] The present structure is particularly unusual, however, in that the clusters are linked to one another by NDIC2 dications acting as bridging ligands in the coordination

sphere of Pb, rather than by hydrogen-bonding or Van der Waals forces, and so could also arguably be described as a 1D structure.

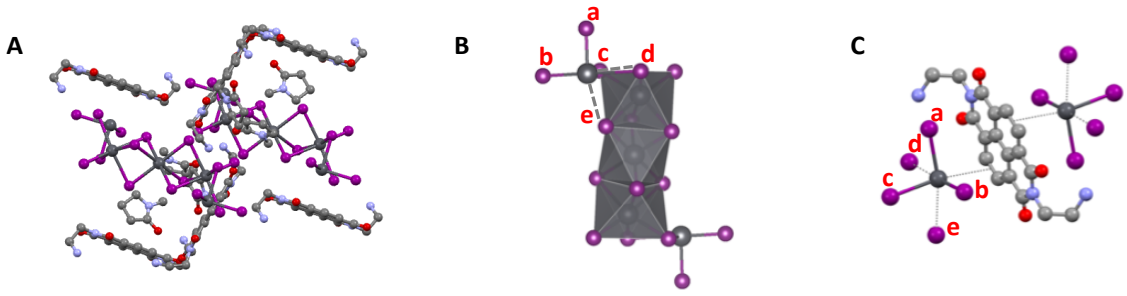

Figure 5.6 (A) Crystal structure of **2**, $[(NDIC_2)_3Pb_5I_{16}]\cdot 6NMP$. (B) Detail showing the structure of the inorganic $Pb_5I_{16}^{6-}$ "0D" clusters consisting of a linear chain of three face-sharing PbI_6 octahedra and two terminal distorted Pb environments characterized by 3 short Pb—I bonds (to iodides a-c) and two very long bonds (to d and e). (C) Detail showing how NDIC2 molecules in the structure serve as η^2:η^2 ligands bridging the inorganic clusters and complete the octahedral coordination of the terminal Pb centers of the clusters.

The core of each cluster in **2** consists of a linear Pb_3I_{12} moiety formed by face-sharing between three octahedra (Figure 6B), similar to that seen in the structure of $[(H_3N(CH_2)_7NH_3)_4Pb_3I_{12}(I)_2]$.[51] To each end of this core is attached a highly distorted Pb coordination polyhedron in which there are three short Pb—I bonds (2.9766(12)-3.0099(13) Å; one to an iodide of the Pb_3I_{12} core and two to terminal unshared iodides), two much longer Pb···I distances (3.7446(12) and 3.6416(13) Å, with iodides of the core), and a NDIC2···Pb contact (discussed in more detail below). Taking into account only the three short bonds, the lead appears to be coordinated in a trigonal pyramidal fashion, but considering also the two more distant iodides and the NDIC2 contact, the coordination can be regarded as a highly distorted octahedron. The two long Pb···I distances are much longer than the typical Pb—I bond lengths in perovskites and perovskite-like materials: typical ranges are 3.125-3.196 Å,[52] 3.137-3.278 Å,[64, 345, 346] and 3.002-3.458 Å.[347-349] for 3D, 2D,

and 1D materials, respectively, with bonds to terminal unshared iodides being shorter than those to shared iodides.

There are two independent types of NDIC2 dication present in a 1:2 ratio in the structure of **2**. The first of these closely approaches two Pb centers in separate clusters. These close approaches can be regarded as η^2-coordination of one of the aromatic rings of the NDIC2 dication to a Pb center; C—Pb distances are 3.614(16)-3.712(16) Å, with a distance of 3.592(12) Å between the centroid of the C—C bond in question and the metal centers (Figure 6C). Thus the dication acts as an η^2:η^2 bridging ligand that stitches the iodoplumbate clusters into chains. Although a number of Pb^{II}-arene π-complexes have previously been reported,[58] the arene is usually coordinated in an axial (η^6) fashion, and examples with η^2-arenes are rare.[350, 351]

As in the structure of **1**, the structure also exhibits NDIC2···(solvent) hydrogen bonding and NDIC2···NDIC2 π-stacking (Figure 7). Each ammonium group on the Pb-coordinated NDIC2 dications is bridged to corresponding groups in neighboring cations through a hydrogen-bonding interaction with two NMP molecules; the oxygen atom of each NMP molecule being hydrogen-bonded to both NH_3 groups. Thus, these molecules form hydrogen-bonded chains. The NDIC2 molecules that are not coordinated to Pb exhibit a similar hydrogen-bonding pattern to the NDIC2 groups of **1**: one NH_3 group is bridged by two NMP groups to another dication, while the other NH_3 is hydrogen-bound to one terminal NMP molecule. Each uncoordinated NDIC2 molecule also forms a π-dimer with a neighboring molecule (not that to which it is connected via hydrogen-bonding), while those coordinated to Pb are not engaged in π-stacking.

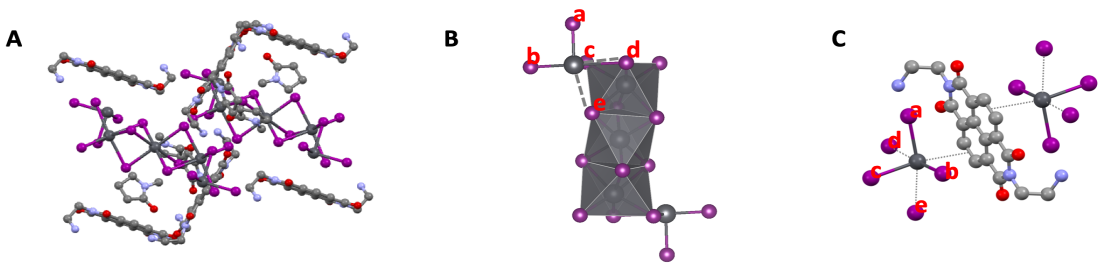

Figure 5.7 Cation-cation and cation-inorganic interactions present in **2**.

Synthesis and Structure of [(NDIC$_2$)Pb$_4$I$_{10}$]·4DMF (3). A third iodoplumbate compound, **3**, was obtained as yellow crystals by slow vapor diffusion of ethanol in a DMF solution containing PbI_2 and (NDIC2)I_2 (Figure 8). HIPC **3** is unstable both in solvents and in ambient conditions and is readily converted to **1**. It structure consists of highly distorted octahedra assembled into 1D ribbons. The ribbons consist of four parallel chains of edge-sharing octahedra fused together. In addition to sharing two edges with octahedra in its own chain, each octahedron in one of the peripheral chains also shares two edges with octahedra in one of the two central chains. Each octahedron in a center chain shares six edges in total: two in-chain, two with octahedra in the peripheral chain, and two with octahedra in the other central chain (Figure 8C). A large range of Pb—I bond lengths (2.9893(13)–3.5168(12) Å, the longest of which are shown as dotted lines in Figure 8A), is present in the structure. These ribbons are surrounded by DMF molecules and NDIC2 dications.

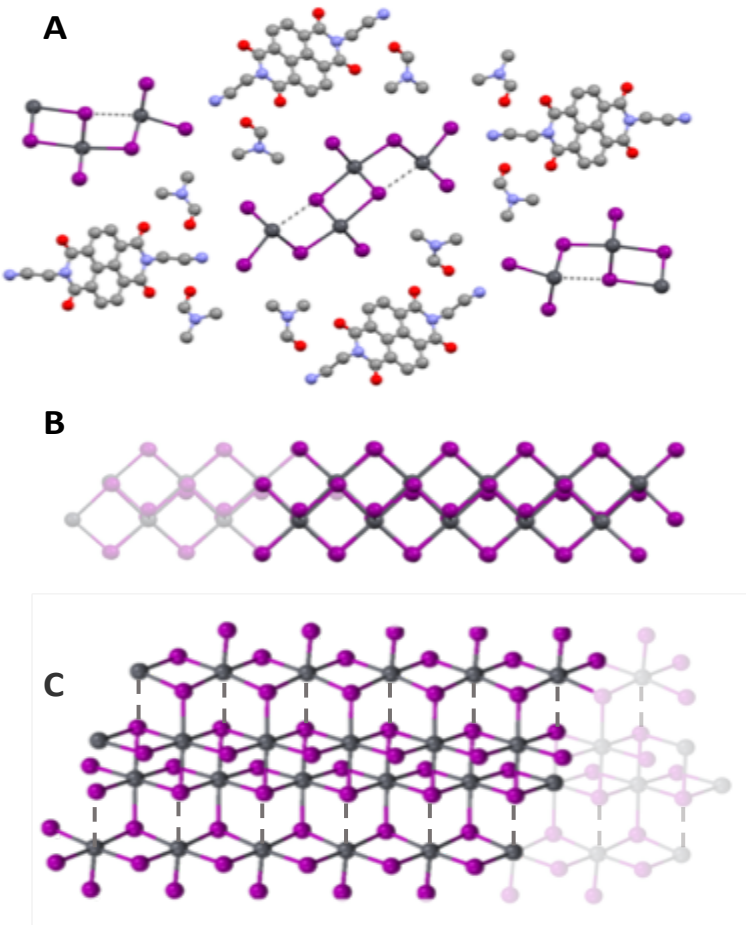

Figure 5.8 (A) Crystal structure of **3**, $[(NDIC_2)Pb_4I_{10}]\cdot 4DMF$, viewed along the direction of the inorganic ribbons. (B, C) "Side" and "top" views of the inorganic ribbons.

In contrast to what is seen in the structure of **1** and **2**, the NDIC2 dications in **3** form polymeric π-stacks (Figure 9), rather than π-dimers. The ammonium groups of the NDIC2 cations each hydrogen bond to an iodide, so that the π-stacked NDIC2 dications bridge adjacent ribbons, and to the oxygen atoms of two DMF molecules. Compared to what is seen in the structures of **1** and **2**, however, the π-conjugated cores of the NDIC2 dications are located further from the inorganic portions of the structure, which is consistent with the yellow, rather than red, coloration (see discussion of optical properties below).

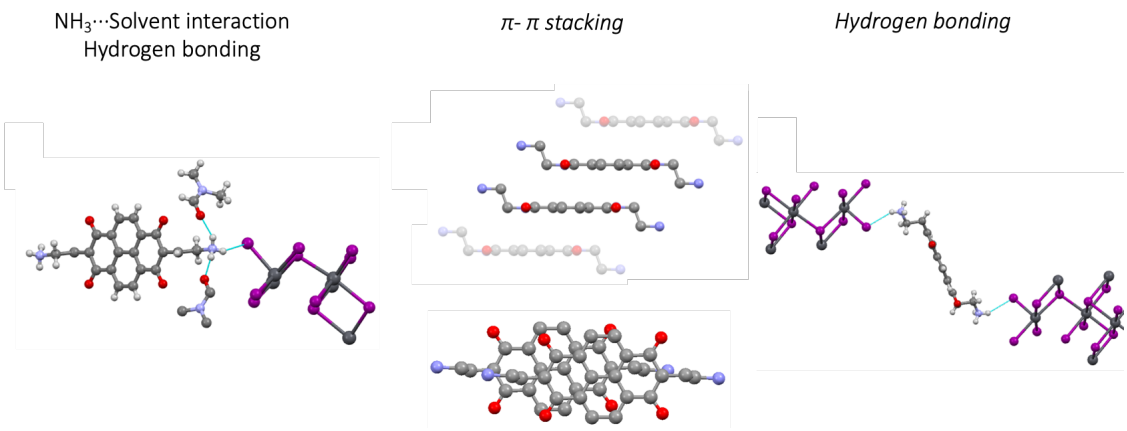

Figure 5.9 Cation-cation and cation-inorganic interactions present in **3**.

Synthesis and Structure of [(NDIC$_2$)Pb$_2$I$_6$]·4NMP (4). **4** was synthesized by slow diffusion of ethanol in a solution of NMP containing (NDIC2)I_2 and PbI_2. The inorganic portion of the structure is simple relative to that of **1-3**, consisting of linear 1D wires of *trans*-face-sharing octahedra, similar to those reported in several other 1D HIPC structures (see Figure 10A).[332, 352-356] One of ammonium groups in each NDIC2 dication is hydrogen-bonded to the oxygen atoms of three NMP molecules, while the other forms hydrogen bonds to one NMP and two iodide ions. Aromatic CH···I contacts are also present. Although the conjugated cores of adjacent NDIC2 dications exhibit an interplanar distance of 3.190(12) Å, there is little overlap between the π-faces (see Figure 10C).

Transformations Between HIPC Structures. Structural transformations have been observed in several lead halide networks. Here we examine, in turn, the transformations of HIPC **1** by: firstly, exposure to water; secondly, exposure to organic solvent; and, finally, heating.

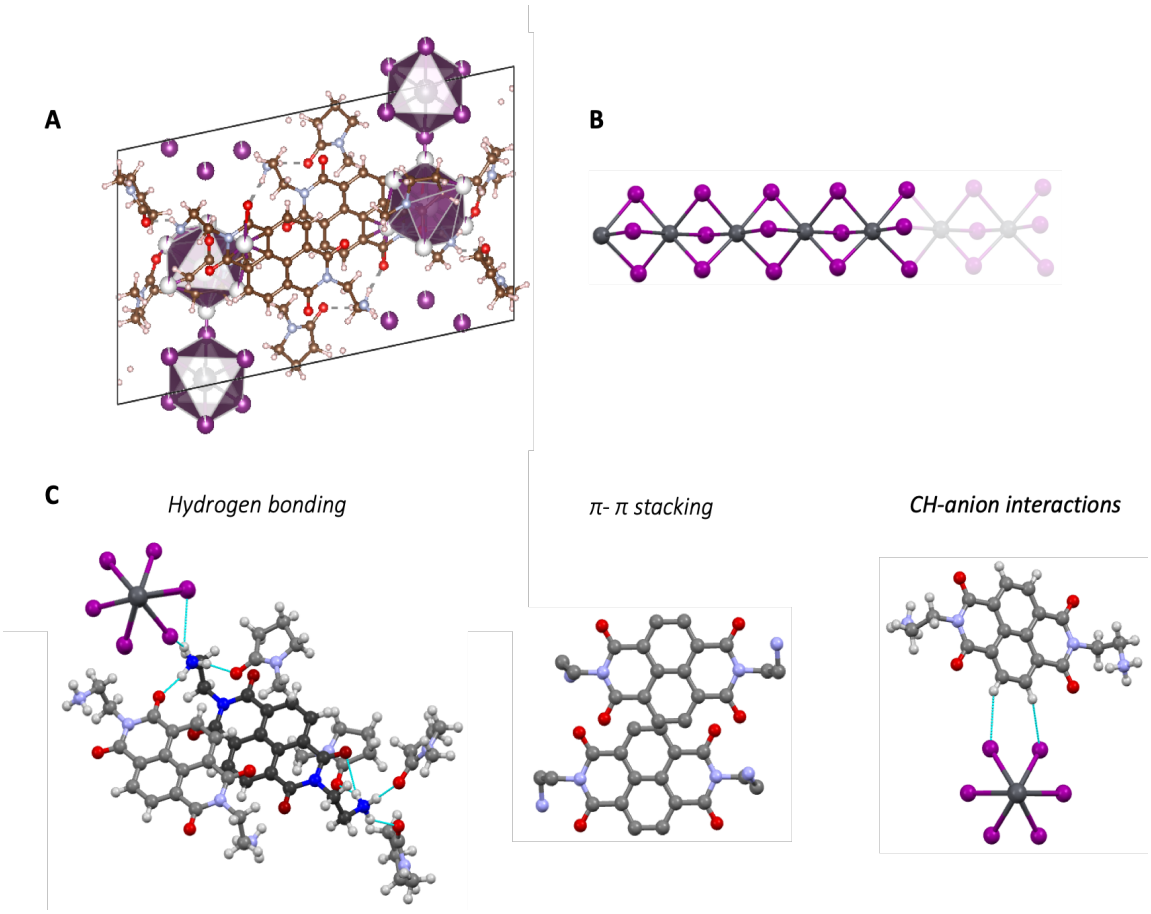

Figure 5.10 (A) Crystal structure of **4**, $[(NDIC_2)Pb_2I_6]\cdot 4NMP$, viewed along the direction of the inorganic chains. (B) View of the inorganic chain. (C) Cation-cation and cation-inorganic interactions present in **4**.

Upon immersion in water, most hybrid organic inorganic lead iodide compounds are known to decompose to PbI2 or Pb(OH)H.[62] For example, crystals of the 2D HOIP $(PEA)_2PbI_4$ decompose to PbI_2 immediately upon addition of water. However, in the case of **1**, immersion in water for 24 h resulted in formation of a brown powder (Figure 11A). SCXRD revealed a crystal picked from this material to have the composition $(NDIC_2)Pb_2I_6\bullet 2H_2O$ and to consist of 1D wires of *trans*-face-sharing octahedra; this material is designated **5** (see below). However, PXRD and elemental analysis indicated another component, which we label **6** and for which we were unable to obtain suitable

crystals for SCXRD, to be present. The **5**/**6** mixture is reasonably stable under ambient conditions (Figure 11B), but is found to be transformed to PXRD-pure **6** on further exposure to water (Figure 11C).

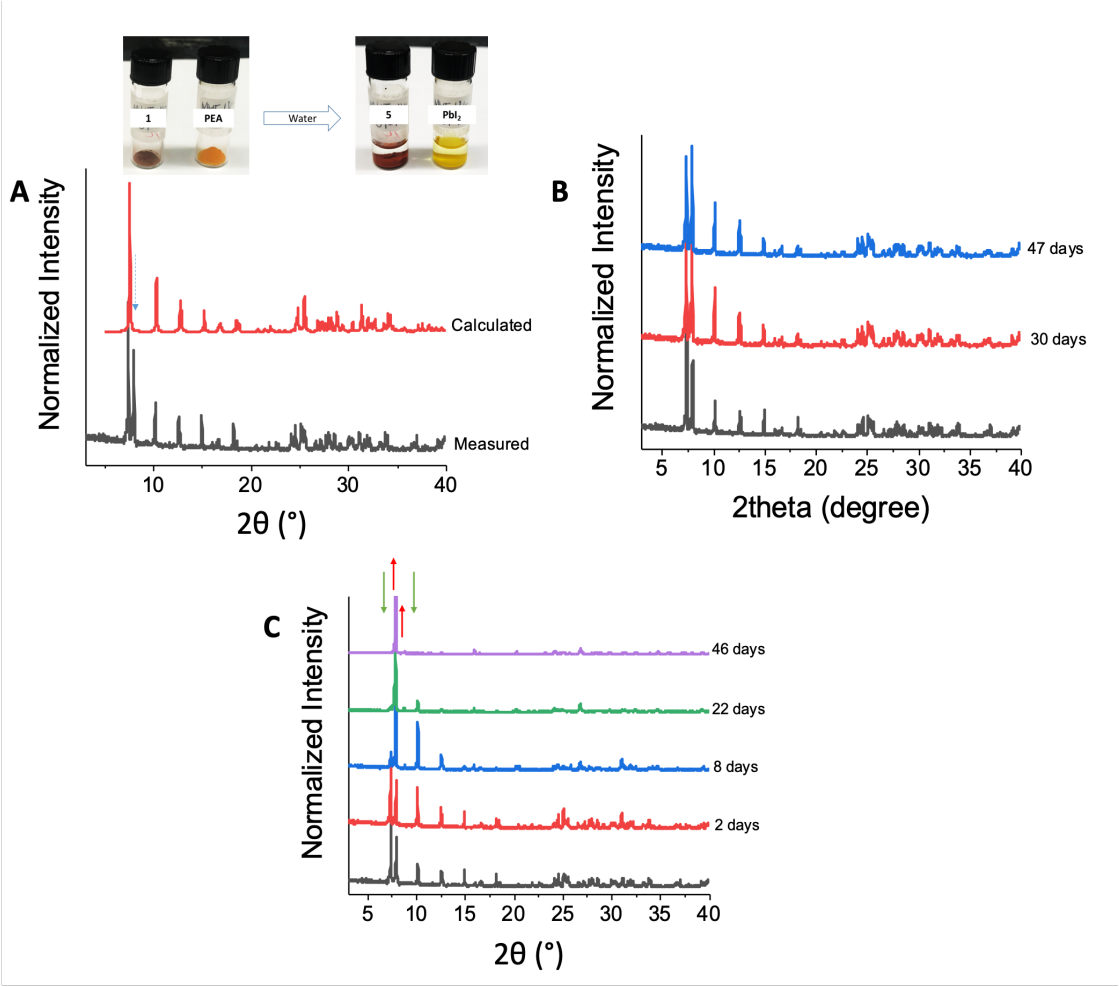

Figure 5.11 (A) Comparison of PXRD measured for the initially formed precipitate obtained from treatment of **1** with water to that calculated based on the single-crystal structure of **5**; the dotted arrow indicates the most prominent peak attributable to **6**. Photographs showing the effects of water on **1** and $(PEA)_2PbI_4$. (B) (B) Ambient atmosphere stability in the dark of the initially obtained **5**/**6** mixture studied by PXRD. (C) PXRD data showing transformation of the initially formed **5**/**6** mixture to **6** over 46 days in water.

DSC of **6** shows no endotherm corresponding to solvent loss, whereas **5** shows an endotherm at ca. 100 °C (Figure 12), and EA (assuming that the HIPC **6** evident in PXRD is the only material present) is consistent with an empirical formula of $(NDIC_2)Pb_5I_{12}$,

which in turn implies **5** and **6** are formed in a ca. 2:3 ratio in the initially formed brown precipitate (again, assuming no additional non-crystalline materials are present). The transformation of both **1** to the **5**/**6** mixture and of **5**/**6** to pure **6** requires loss of (NDIC2)I_2 (or another NDIC2-rich material), while DMF is also lost in the first of these reactions. A material with similar stoichiometry to **6** – [$(PPh_4)_2Pb_5I_{12}$] – has previously been reported and contains ladder-like structures consisting of two pairs chains of face-sharing octahedra that are bridged to one another by additional face-sharing octahedra.[341] Indeed, the PXRD patterns for **6** and [$(PPh_4)_2Pb_5I_{12}$] are similar, although our failure to grow single crystals of **6** prevents confirmation of any structural similarity.

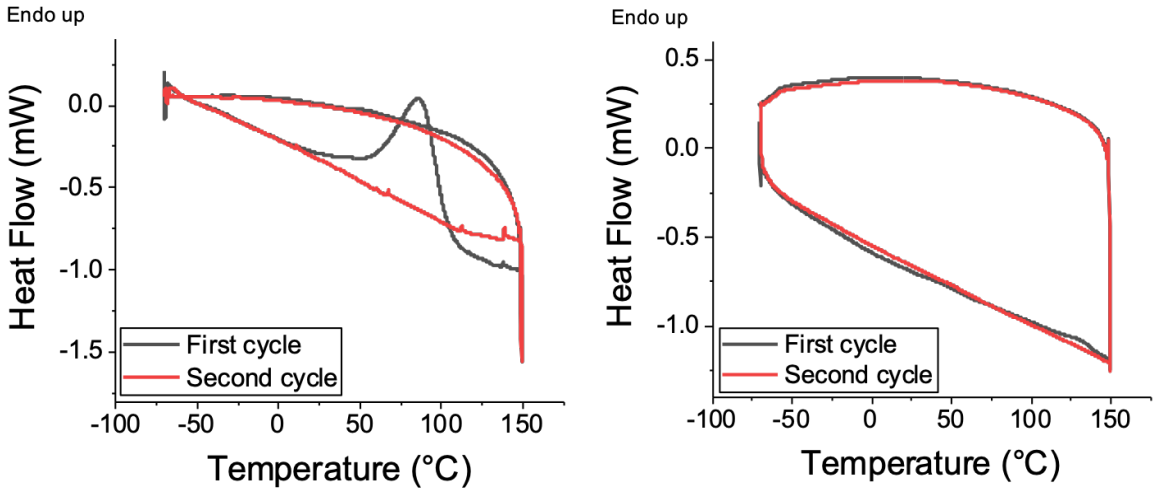

Figure 5.12 Differential scanning calorimetry (plotted with endothermic up) for (left) **5** and (right) **6**.

We also examined the stability of **1** crystal to various organic solvents. Crystals were stable in toluene, and dissolved in DMSO, with [$PbI_2(DMSO)_2$][342] crystallizing after three days. Acetonitrile or tetrahydrofuran, however, led the transformation of **1** to **7**, with the change being more rapid in the former solvent (1 day vs 5 days) (Figure 13). These two solvents have been incorporated into several other haloplumbate structure;[174, 357, 358] however,

solution NMR spectroscopy following redissolution of **7** in d_6-DMSO indicates only trace amounts of solvent relative to NDIC2^{2+}. Furthermore, comparison of the PXRD pattern of **7** to that of **5** suggests a similar structure, but reduced interwire distances, again consistent with a solvent-free crystal. EA suggests a formula for **7** of [(NDIC$_2$)Pb$_2$I$_6$], also consistent with this PXRD data.

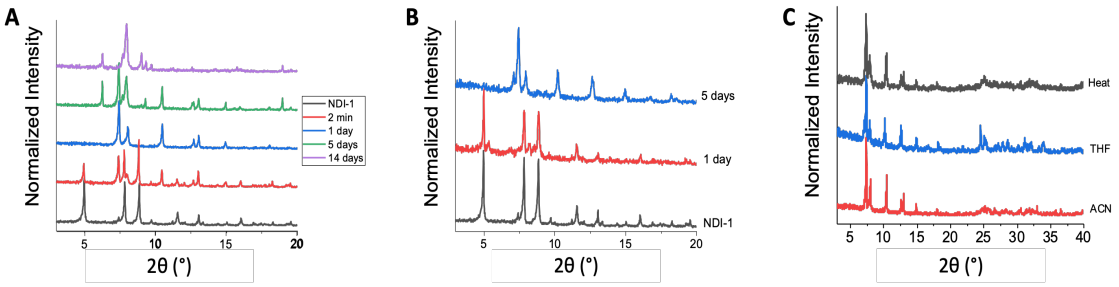

Figure 5.13 Temporal evolution of the PXRD pattern when **1** is dispersed in (A) MeCN and (B) THF. (C) PXRD data for **7** obtained from **1** through different solvent and thermal treatments.

HIPC **7** is further transformed to another material, **8**, when left in acetonitrile for more than two weeks (see Figure 13A). Again, the crystal structure could not be obtained, but, EA suggests a formula of [(NDIC2)Pb$_3$I$_8$]•MeCN. Although the structure is unknown, it is worth noting that several previous structures incorporating inorganic anions of empirical formula Pb$_3$I$_8^{2-}$ have been reported; these contain ribbons of edge-sharing or edge- and face-sharing PbI$_6$ octahedra.[342, 359-361] Finally, heating compound **1** to 130 °C also leads to formation of **7** (Figure 13C), presumably through loss of DMF and accompanied by formation of (NDIC2)I$_2$.

Crystal Structure of (NDIC$_2$)Pb$_2$I$_6$•2H$_2$O (5). As indicated in the previous section, the single crystal structure of **5** was determined (see Figure 14A). The linear chains of face-sharing PbI$_6$ octahedra present in the structure are similar to those in **4** and a variety of

other previously reported structures. Each ammonium moiety of the NDIC2 dications is engaged in hydrogen bonds to an iodide (resulting in NDIC2 bridges between adjacent chains) and a water molecule (Figure 14B). There is no π-stacking between NDI moieties, but there are close iodide-NDI contacts (see the following section).

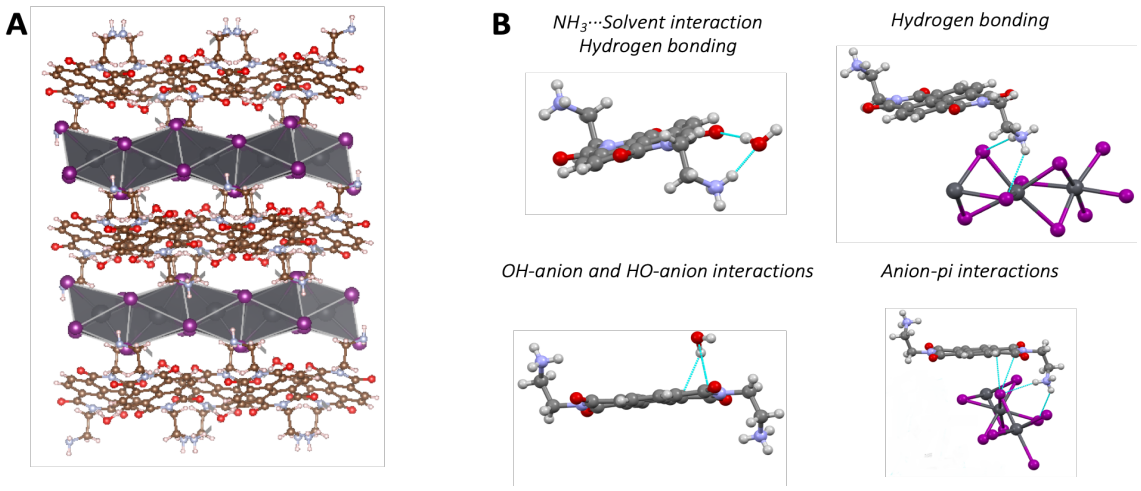

Figure 5.14 (A) View of the crystal structure of **5**, $(NDIC_2)Pb_2I_6•2H_2O$. (B) Cation-cation and cation-inorganic interactions present in **5**.

Optical Properties of NDIC2-Based HIPCs. Diffuse reflectance spectra of **1** and **4-8** are shown in Figure 15A.[69] Spectra were not obtained for **2** and **3** due to the small quantities obtained, but **2** has a similar red color to **1**, **4**, and **5**, while **3** is yellow-orange. The red color and long-wavelength absorption onsets for **1**, **2**, and **4-8** suggests a mixed organic-inorganic origin, since isolated NDI *N,N'*-dialkyl NDIs absorb at ca. 380 nm,[362] while [(piperidinium)PbI_3] (which contains similar chains to **4** and **5**) exhibits an absorption maximum of ca. 400 nm.[363] Accordingly, we attribute the long-wavelength absorption of the red materials to charge transfer (CT) from the inorganic portion – the highest-lying states from which are presumably predominantly iodide based – to the NDI. CT of this type has previously been suggested to account for the similar spectrum of [(**III**)$_4Pb_3I_{10}$],[333] while

inorganic-to-cation CT has been invoked in other HIPCs in which the cations have comparable or more less cathodic reduction potentials than NDIs, for example, in the cases of methylviologen and tropylium materials.[355, 363] Indeed, visible-region CT bands between "free" iodide ions and NDIs are also seen in solution (see ref. 72 and Figure 15B), and presumably account for the spectrum reported for the iodide salt of **III**$^{+}$.[333]

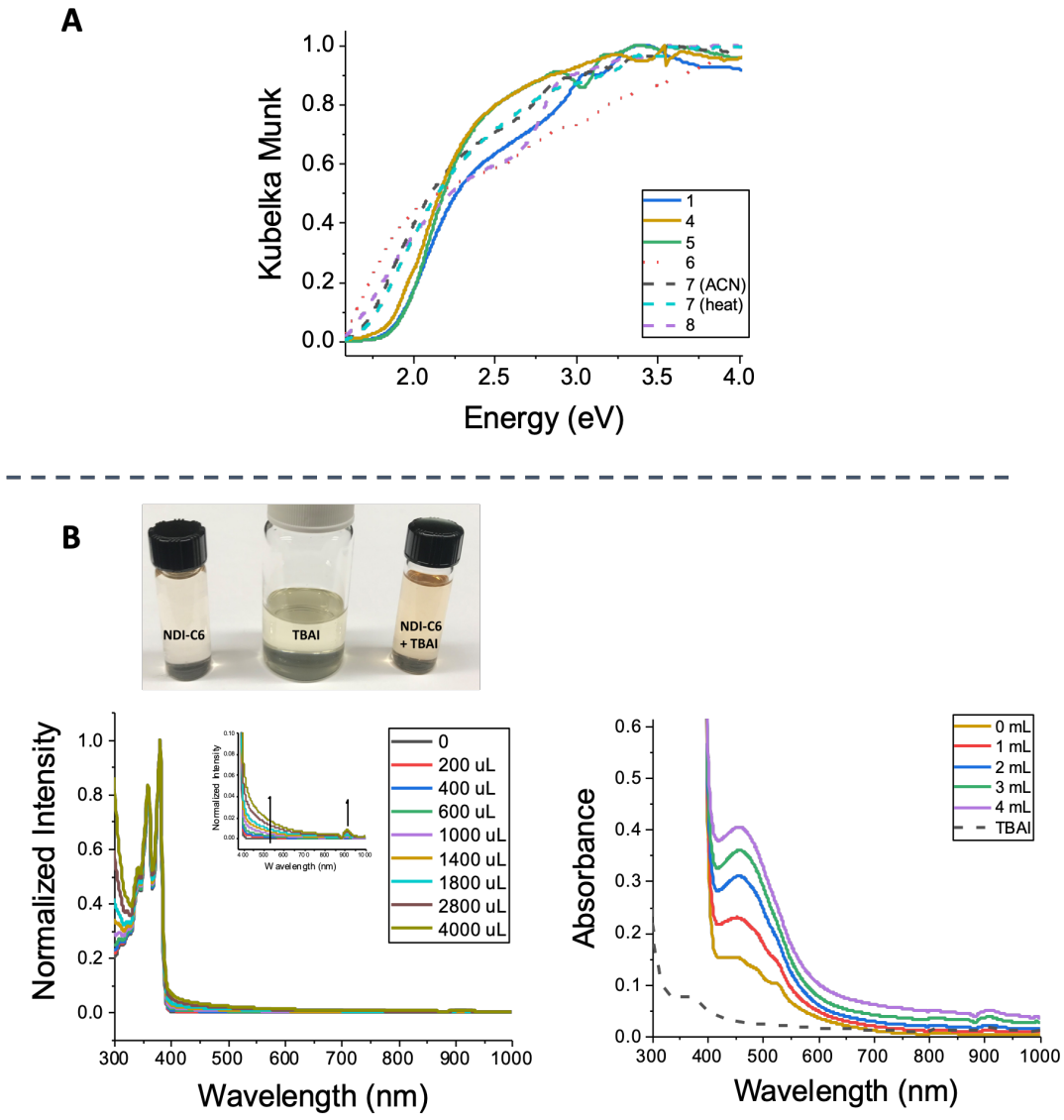

Figure 5.15 (A) Diffuse reflectance spectra of HIPCs **1** and **4-8**. (B) UV-vis spectra of a simple naphthalene diimide, *N,N′*-dihexyl-naphthalene-1,8:4,5-bis(dicarboximide) (synthesized according to the literature[364]), in CH_2Cl_2 with incremental addition of tetrabutylammonium iodide (TBAI) for (left) addition of portions of 0.1 M of

TBAI solution to a 0.1 mM solution of NDI and for (right) addition of a 1 M solution of TBAI to 10 mM NDI. Bottom: photographs of solutions. Note that in the right figure a structured feature is seen in the absence of iodide at similar wavelength to the feature that grows on iodide addition and that is assigned to CT; the structured feature is likely attributable to NDI aggregation. Data showing growth of a similar CT band, but with less complication from aggregation, on addition of TBAI to *N,N'*-bis(2,4,6-trimethylphenyl)naphthalene-1,8:4,5-bis(dicarboximide) in MeCN / $CHCl_3$, are shown in ref.[365]

Consistent with an iodide-to-NDI CT origin for their low-energy absorption onsets, all the red crystals, exhibit close contacts between an iodide and an imide ring (Figure 16), where there are known to be large LUMO coefficients located between the quaternary and CO carbon atoms.[73] Crystals of **3** do not exhibit such short distances between iodides and the NDI cores, consistent with the orange-yellow, rather than red, color of this material. The somewhat lower-energy absorption onsets of **6-9** (for which we do not have structural information) relative to those of **1**/**4**/**5** may reflect destabilization of the highest filled iodide-based orbitals through significantly different structures in the inorganic portion, or stabilization of the lowest-lying empty NDI-based orbitals through π-aggregation.

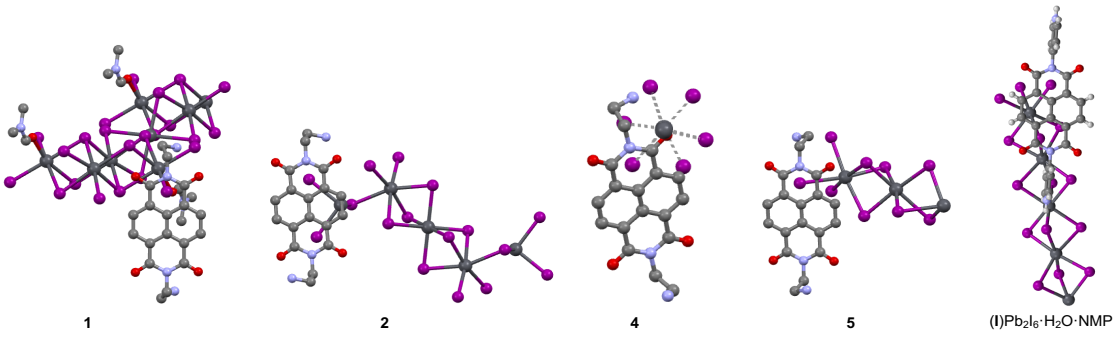

Figure 5.16 Close contacts between iodides and naphthalene diimide cores in the crystal structures of **1** (iodide—ring centroid distance = 3.534 Å), **2** (3.666 Å), **4** (3.519 Å), and **5** (3.580 Å), and in the previously reported structure of (**I**)Pb_2I_6•H_2O•NMP (3.485 Å). The distances are calculated from the crystal structure (I to centroid of the ring).

Electrical Properties of HIPC 1. The conductivity of crystals of **1** was tested using two-point current-voltage (*I-V*) scans (Figure 17A).[366] Although the orientation of the crystals and crystal clusters used was not established, their morphology suggests that the *ab* plane, which contains the iodoplumbate ribbons, is parallel to the substrate, and it is, therefore, this plane in which the conductivity was measured. The linear *I-V* behavior confirms that ohmic contacts have been established. There is also no hysteresis. The conductivity extracted from the *I-V* curves is $5.4 \times 10^{-5} \pm 1.1 \times 10^{-5}$ S m^{-1}. This is comparable to the value reported for (1-methylpiperidinium)PbI_3, which contains 1D chains of face-sharing octahedral similar to those in **4** and **5**,[75] but significantly higher than in layered perovskites of the type $(\beta\text{-Me-PEA})_2MA_{n-1}Pb_nI_{3n+1}$ (β-Me-PEA = β-methylphenethylammonium = 2-phenylpropan-1-ammonium; MA = methylammonium; n = 1-3).[76] Similar conductivities, ranging from ca. 10^{-5} to 10^{-4} S m^{-1}, have been reported for single crystals of $MAPbI_3$.[367, 368]

The photoresponse of the crystals was evaluated by taking *I*−*V* scans under dark and illuminated conditions, using a white LED light source. A slight increase in current with increasing light intensity (Figure 17B) is consistent with photogeneration of charge carriers. The responsivity (*R*), detectivity (*D**), and on/off ratio at 5 V and a light intensity of 14.5 W m^{-2} are calculated bellow. These properties are quite modest compared with those obtained in related materials, such as $MAPbI_3$ nanowires.[369, 370] The first metric used in characterizing the photoresponse was responsivity (*R*), which is defined as

$$R = \frac{I_{light} - I_{dark}}{P * A}$$

where I_{light}, I_{dark}, P, and A are the illuminated current, dark current, incident optical intensity, and active area of the device respectively. It was estimated to be be $2.2 \times 10^{-3} \pm 0.2 \times 10^{-3}$ A W^{-1}.

The second metric used was detectivity (D^*). Assuming that the noise of the device is dominated by the shot noise, detectivity is defined as

$$D^* = \frac{R\sqrt{A}}{\sqrt{2qI_{dark}}}$$

where R and q are the responsivity and electron charge magnitude respectively. It was estimated to be be $4.3 \times 10^7 \pm 1.4 \times 10^7$ Jones.

The third metric used was the on/off ratio, defined as

$$on/off = \frac{I_{light} - I_{dark}}{I_{dark}}$$

and was estimated to be 3.9 ± 0.3.

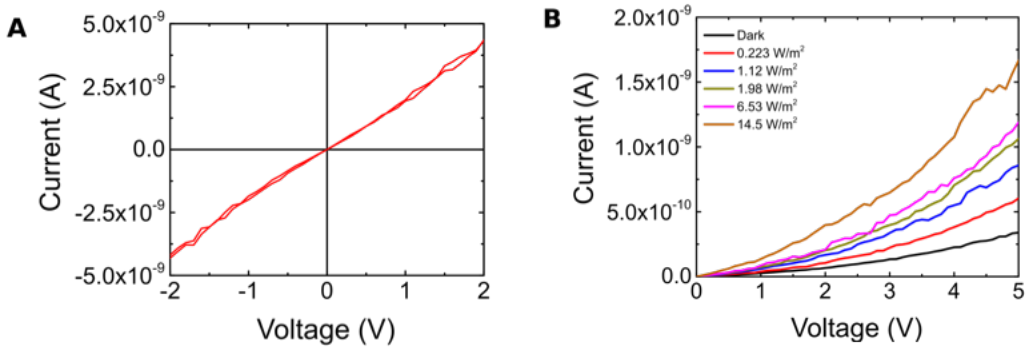

Figure 5.17 (A) Current-Voltage scan of single crystals of **1** (contact separation for this sample was 80 µm, contact width 550 µm, and crystal thickness was 450 µm). Note that the curve is linear, and the double sweep shows no hysteresis. (B) Photoresponse of single crystals **1**, showing an increase in current with increasing light intensity.

5.4 Conclusion

Several previous studies make clear that different products can be obtained from the same organic and lead halide components depending on aspects of the reaction conditions, such as the ratio of reagents,[356] the temperature and/or pressure,[338] or, especially when solvent is incorporated in one of the possible products, the solvent used.[204, 332] In all of the crystallographically determined structures, the solvent acts a hydrogen-bond acceptor, suggesting that use of a non-hydrogen-bond-acceptor solvent might afford a solvent-free structure; unfortunately, it was not possible to identify a suitable solvent in which the starting materials were sufficiently soluble. Moreover, interconversions between different structures,[337] in some cases involving loss or gain of solvent,[338] have also been reported. Nonetheless, the (NDIC2)I_2 / PbI_2 system is particularly rich, yielding eight new HIPCs under a variety of mild reaction conditions, either directly from a 2:1 molar ratio of the reagents or by subsequent treatments of these products. Five of these have been structurally characterized; these exhibit a variety of inorganic 0D or 1D structural motifs and a variety of organic-organic and inorganic-organic approaches attributable to a variety of different interactions. In general, the iodoplumbate portions of the structure consist of face- and/or edge-sharing PbI_6 structure, but that of **1** also incorporates PbI_5(DMF) octahedra, and that of **2** includes unusual highly distorted $PbI_5(\eta^2$-NDI) octahedra. Different solvent or thermal treatments of **1** afforded four additional new materials, demonstrating the lability of structures of this type, one of which, **6**, was stable in water for at least a few months. Many of these materials absorb through much of the visible, the long-wavelength onset being attributed to an inorganic-to-organic CT excitation facilitated by close contacts between iodide donors and the NDI moieties.

CHAPTER 6: UNDERSTANDING OF STRUCTURE OF THE CATION – STRUCTURE OF THE HALOPLUMBATE MATERIAL RELATIONSHIPS: CONTRIBUTIONS FROM THIS THESIS AND FUTURE WORK

If one is to design hybrid haloplumbate materials with desired structures and properties, it is critical to understand how the structure of the cation determines the structure of the hybrid organic inorganic perovskite and how that, in turn, determines the electronic structure, and other properties such as stability. While we are only starting to understand the structure of the cation – structure of the haloplumbate material relationship, the guidelines presented in this thesis can help design new materials. In chapters 2-5, a range of new 1D and 2D iodoplumbate structures were described. In Chapter 2.1, it was showed that, for a series of compounds, the offset of the inorganic layers is related to the strength of cation-cation interaction. In Chapter 2.2, it was demonstrated that, for a series of compounds, the Pb−I−Pb bond angle can be tuned by changing the width of the cation. In Chapter 3, the first cation engineering that favors the formation of 1D face-sharing iodoplumbate material was demonstrated. In Chapter 4, the first 3×3 2D HOIPs with Pb/I is reported. It was showed in this chapter that the NMR chemical shift of ^{207}Pb correlates with the distortion from the octahedra. In Chapter 5, the structural diversity in a NDI-based iodoplumbate system is reported.

In this chapter, the wider implications of these findings are discussed, along with suggestions for future work. Here, several already proposed categorizations are described, while new classifications are suggested that can help classify the published iodoplumbate materials. Based on the results presented in this thesis, some cation

engineering projects to expand the families of haloplumbate materials are proposed. In particular, a few ideas to facilitate design guidelines for relationships between cation structure and the optical properties of the resulting haloplumbates are presented.

6.1 Cation structure – haloplumbate structure relationships

6.1.1 Role of the cation-cation and cation-inorganic interaction strength

As mentioned previously for 2D HOIPs, as the head of the cation, the ammonium, points toward the inorganic layer, the tail can rearrange differently from one cation to another depending on the balance of steric and electronic interactions between the organic cation and the iodides and between neighboring organic cations, and of distortions within the inorganic framework. While the relative importance of each of these variables is unclear, one can see that, when using a series of similar compounds, a vast diversity of families can be obtained. In Chapter 2-4, it has been suggested that one of the key parameters that has a structure directing role in perovskite and perovskitoids is the interaction between adjacent cations or between the inorganic layer and the organic cation. Similar suggestions have been made in the literature.

In Chapter 2.1, it was reported that within a couple of series of 2D A_2PbI_4 compounds, changes that are expected to increase the strength of cation-cation interactions seem to lead to a progression in the stacking of 2D structures from RP-like (Ruddlesden-Popper), to or towards DJ-like (Dion Jacobsn), and finally back to RP. A weak interaction between two cations or between the cation and the inorganic layer allows the synthesis of a 2D RP structure. A medium interaction allows the synthesis of an intermediate structure (nRP or MnDJ), whereas a strong interaction again affords a RP structure. Literature data for the simplest cations that can be used in 2D HOIPs, the

alkylammonium cations, follow this trend as the chain length, and, therefore, total strength of cation-cation van der Waals interaction, increases. This relationship between the inorganic layer offset and interaction strength can also be applied to other series of cations. For example Y-PEA (4-Y-phenylethylammonium; Y = H, F, Cl, Br), where the cation-cation interaction is a close contact between the organic halogen atoms in neighboring layers, and Y-PMA (4-Y-phenylmethylammonium; Y = H, F, Cl, Br, I)[6], where there is a close contact between the cation halogen and the inorganic iodide. If this pattern holds more generally, one could potentially synthesize a 2D perovskite with a new cation and, depending on the structure obtained, increase or decrease the cation-cation interactions via the substituents to tune the structure. However, it is worth pointing out that this is an empirical observation and the mechanism by which the cation-cation interactions affect the offset of the layers is not obvious and perhaps not general for all families of cations. At least for some families of compounds, this pattern does *not* hold, perhaps due to the competing influence of multiple interactions, for example, in the series incorporating the cations Y-EA (Y-ethylammonium; Y = I, Br, Cl),[7] NH_3-$(CH_2)_n$-NH_3[8-10] (n = 2-6) and I-$(CH_2)_n$-NH_3 (n = 2-6)[11].

6.1.2 Role of cation-cation interactions

In 2D perovskites, as in their 3D counterparts, the "head" of the cation, the charged moiety, acts as a hydrogen-bond donor (HBD) with the halides of the inorganic layer.[12,13] Cations bearing multiple HBD groups have proven to be an important class of material to obtain uncommon structure types.[2, 14-20] For example, cation-cation or cation-inorganic HB interactions seem to be one of the principal factor that help one obtain corrugated structures. For most of the corrugated iodoplumbate compounds in the literature, dications possessing a primary ammonium and a substituted nitrogen

substituent are typically used (see Fig. 1A-E). It is thought that the primary ammonium of the cation allows the formation of the 2D layer, while the second substituted nitrogen-bearing group interacts with the iodide of the inorganic layer in a way to favor corrugation over planar 2D structure. As seen before, not all dications form 2D corrugated HOIPs: cations with two primary ammonium or rigid cations seem to form 2D planar structures over corrugated ones.

Two other corrugated structures have been reported using a monocation bearing a substituent that could play a similar role. In (2,2-(ethylenedioxy)bis-(ethylammonium))PbX_4 where X = Br, I, the authors believe that the intracation interaction is important; the driving force for the corrugated 2×2 structure might be the hydrogen bonding interaction between the head's N–H and the tail's hydrogen bonding acceptor (HBA) substituent (oxygen of ether) (see Fig. 1F).[14] When this interaction was not observed (X = Cl), the usual (100) structure was obtained. The role of the halide remains unclear. The first use of a nitro-substituted cation was reported in Chapter 4 and enabled the synthesis of a corrugated 3×3 2D HOIP structure, (4-nitrophenylethylammonium)$_2PbI_4$. Multiple cation-cation and cation-inorganic interactions were observed in this crystal structure. It was hypothesized that ONO···I interaction contributed to the formation of this structure (see Fig. 1G).

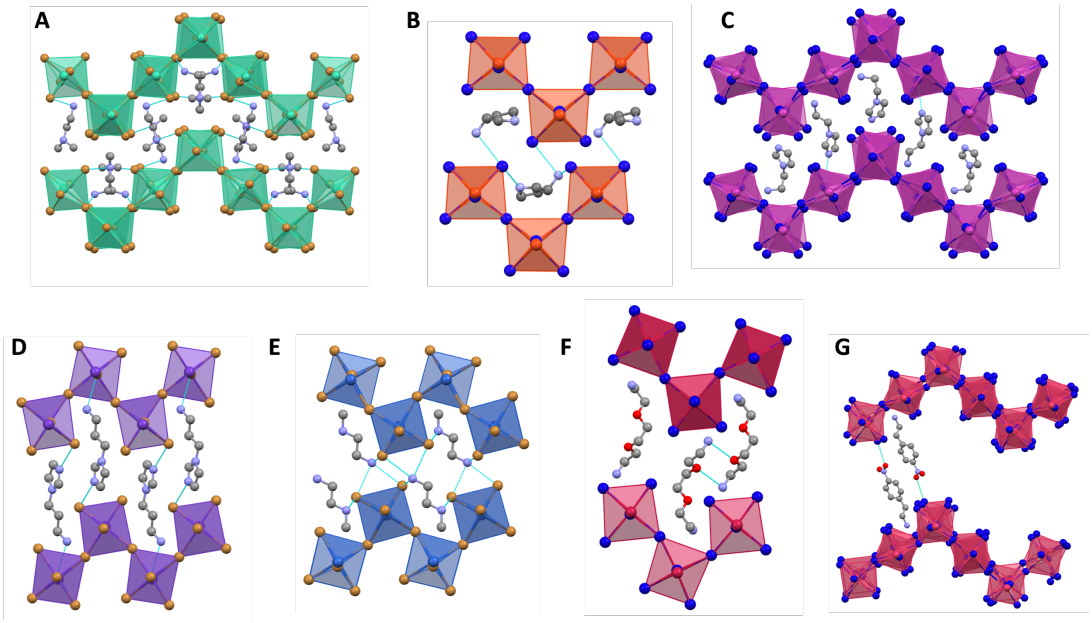

Figure 6.1. Crystal structures of the corrugated 2D HOIPs (A) (*N*,*N*-dimethylethane-1,2-diyl bis(ammonium))$PbBr_4$,[21] (B) (1-(2-ammonioethyl)-1H-imidazol-3-ium)PbI_4,[22] (C) (2-(2-ammonioethyl)isothiouronium)PbI_4,[16] (D) (3-(3-ammoniopropyl)imidazolium)$PbBr_4$,[15] (E) (*N*-methylethan-1,2-diyl diammonium)$PbBr_4$[23] and (F) (2,2-(ethylenedioxy)bis-(ethylammonium))PbI_4,[14] (G) (4-nitrophenylethylammonium)$_2PbI_4$ (see Chapter 4)[4]. The turquoise line highlights the discussed interaction.

In certain cases, hydrogen bonding interactions can also favor other types of structures. As discussed in Chapter 3, a HBA group on the cation can help favor the formation of 1D face-sharing iodoplumbate perovskitoids (FSIP, $APbI_3$) rather than 2D A_2PbI_4 HOIPs. Different phenylethylammonium cations with weak, medium and strong HBA substituents were tested; 10 examples of 1D FSIP compounds were obtained when medium-to-strong HBAs were used, whereas cations with comparable steric demands, but weak to no HBAs, formed 2D HOIPs. It is the first report that shows the ability to predict the tendency to form a FSIP rather than a 2D perovskite.

Many other types of substituents have been added on the tail of the cation to induce cation-cation or cation-inorganic interactions (see Fig. 2). In most cases, the goal was to study the influence of these substituents on the structure of the HOIP. A carboxylic acid moiety was used in (3-Carboxypropylammonium)$_2PbI_4$; the structure exhibits

hydrogen bonding interaction of the carboxylic acid in a polymeric fashion.[24] Nitrile functional group in ((cyanoethylammonium)$_2$PbI$_4$, lead to cation dimer formation through H-bonds between cyano groups and the ammonium heads.[25] Disulfide substituents on (cystamine)PbI$_4$, have been added on the tail of the cation enabling both polymeric SS···SS interactions and SS···I interactions.[26]

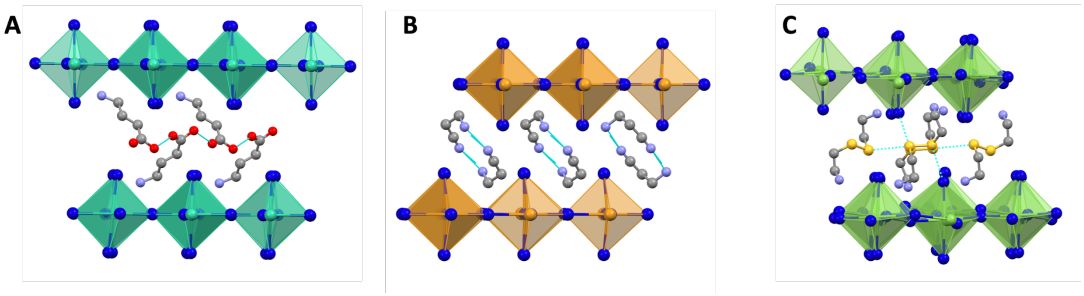

Figure 6.2. Effect of cation substituents on the structure of 2D HOIPs. (A) The carboxylic acid in (3-carboxypropylammonium)$_2$PbI$_4$ hydrogen bond in a polymeric fashion.[24] (B) The nitrile in (cyanoethylammonium)$_2$PbI$_4$ form cation dimers through H-bonds.[7] (C) The disulfide in (cystamine)PbI$_4$ form both polymeric SS···SS interactions and SS···I interactions.[26]

Halogen substituents have also been used in multiple instances. In some cases, they can interact with the halide of the inorganic layer; e.g. (Y-PMA)$_2$PbI$_4$ (Y = F, Cl, Br, I) or the (Y-EA)$_2$PbI$_4$ (Y = Cl, Br, I) series (see Fig. 3A-B).[6, 7] In the Y-PMA series (Chapter 2.1), instead of obtaining a bilayer of organic cations, the cations were embedded with each other, leading to distortions of the inorganic layers. In some cases there appear to be halogen bonding interactions between the iodides (halogen bond acceptors) and the organic halo substituents (halogen bond donors). In other cases, the halogens on adjacent cations can interact with each other; e.g. (3,5-dY-PEA)$_2$PbI$_4$ (Y = F, Cl, Br) (see Fig. 3C, Chapter 2.2) or (4Y-PEA)$_2$PbI$_4$ (Y = F, Cl, Br). It is still not well understood what dictates cases in which the halogen substituent of the cation will interact with the inorganic sheet or the halogen substituent of another cation, but the

steric bulk and flexibility of the cations are factors that have been hypothesized to be important.

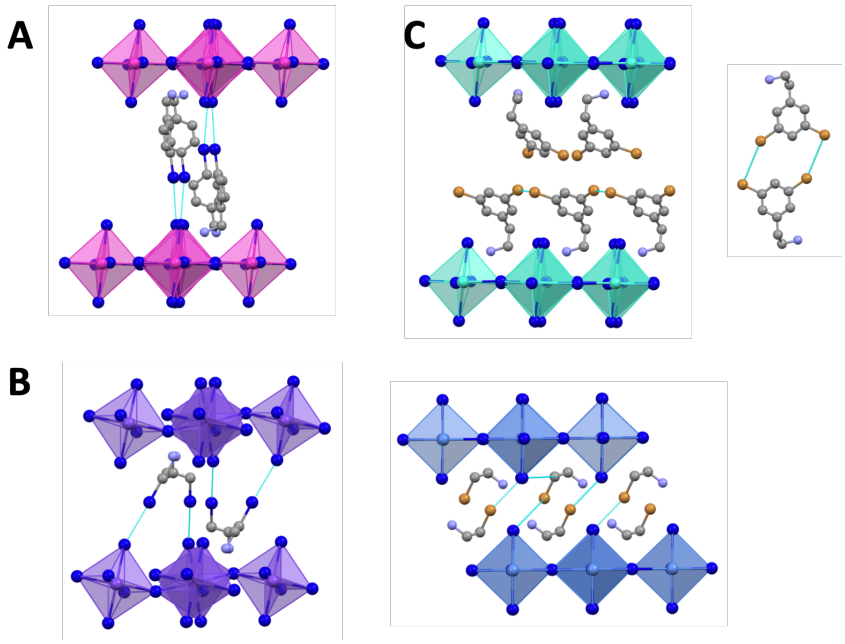

Figure 6.3. Effect of halogen substitution on the cation. Halogen bonding interaction between Y and the iodide of the inorganic layer (A) $(I\text{-}PMA)_2PbI_4$ where the interaction leads to interdigitated cations,[6] (B) $(I\text{-}EA)_2PbI_4$ and $(Br\text{-}EA)_2PbI_4$ where the interaction leads to different degree of distortion of the inorganic plane.[7] (C) $(dBr\text{-}PEA)_2PbI_4$ where there are Br···Br interactions within a layer of cations leading to a polymeric chain, while Br···Br dimers are formed by pairs of cations in adjacent layers.

Each isothiourea-based cation used so far in a Pb/I system have produced unusual structures. With 2-methylisothiouronium, a linear 1D compound is obtained. Its crystal structure reveals two important types of close contact between the organic and inorganic portions of the material: NH···Br and S···Br. 2-Phenylethylisothiourea (1D) and 2-(aminoethyl)isothiourea (2D) cations are used to obtain corrugated HOIPs. Close contacts found in their crystal structures include NH···Br and CH(α-S)···Br approaches. The difference in interactions (S···Br vs CH(α-S)···Br) could help explain the corrugation obtained. More HOIPs using isothiourea will have to be synthesized to confirm or refute this hypothesis.

6.2 Different strategies to tune the exciton energy of the 2D HOIPs

For A_2PbI_4 or A'PbI_4 2D HOIPs, undistorted Pb-I-Pb bond angles of 180° can be targeted when a lower band gap material (red crystals instead of orange) is desired. Different strategies have been used to tune this Pb-I-Pb bond angle. First, the Pb-I-Pb bond angle seems to often approach 180° when a cation with two hydrogen bonding donor groups that will interact with iodides of the same semi-cubooctahedral "pocket" of the inorganic layer in a symmetric fashion is used. While not discussed in the original publication, the surprisingly low band gap leading to the red color of (benzo[*d*]imidazolium)$_2PbI_4$ could be due to the fact that both NH group of the imizadole form hydrogen bonding interactions with the iodide of the inorganic layer, leading to no distortion in the Pb-I-Pb angle (180°).[27] The same rationale can be used for the rigid and divalent (2,2′-biimidazolium)PbI_4 or (Benzo[1,2-*d*:4,5-*d*′]diimidazolium)PbI_4, where the unprotonated N-H hydrogen bonds with the Pb/I layer, leading to red crystals, probably due to the minimally distorted Pb-I-Pb bond angle (173.69° and 180° respectively).[28]

Another strategy is to use a rigid cation with two HBD groups that will interact with both inorganic layers. (*N,N*-Dimethylbenzene-1,4-diammonium)PbI_4, employing a rigid dication, shows again unusual low distortion Pb–I–Pb bond angle (176.64°), close to ideal, and low band gap.[29] The rigid 3- and 4-(aminomethyl)pyridinium cations give a 2D HOIP with a low band gap and low distortion of the Pb-I-Pb bond angle .[30]

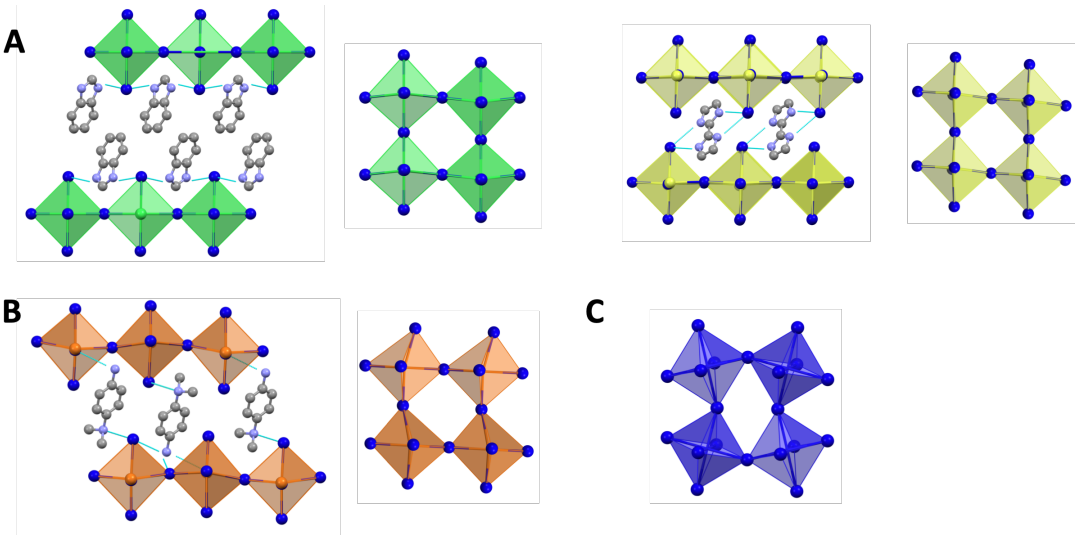

Figure 6.4. Strategies to obtain undistorted Pb-I-Pb planes (Pb-I-Pb angle close to 180°). (A) Symmetrical cation with two HBD groups that interact with the same semi-cubooctahedral "pocket" of the inorganic layer: (benzo[*d*]imidazolium)PbI_4 (left)[27] and (2,2′-biimidazolium)PbI_4 (right)[28]. (B) Rigid cation with two HBD groups that will interact with both inorganic layers: (*N*,*N*-dimethylbenzene-1,4-diammonium)PbI_4.[29] (C) Distorted structure of $(PEA)_2PbI_4$ as reference.

The second strategy to lower band gap of 2D HOIP material (red crystals instead of orange) reported so far is to decrease the interlayer distance. In most cases, RP structures have larger interlayer distance due to the bilayer of organic cations, when compared with analogue DJ structures using a bifunctional cation. X. Li *et al.* suggested that increasing the rigidity of the cation – comparing analogous cycloalkyl and arylakyl cations – helps to reduce the interlayer distance between the inorganic layers which reduced the optical gap.[30, 31]

Another way to decrease the interlayer distance is by having a substituent on the tail that can interact with the inorganic layer. Indeed, in some cases, it can help bring the inorganic layers closer. For example, with hydroxyethylammonium, $HO(CH_2)_2NH_3^+$, the two inorganic layers are quite close to each other, which was hypothesized by Mercier *et al*. to reduce the quantum confinement and lead to an unusually red exciton band.[19]

The third strategy, reported in Chapter 2.2, is to vary the width of the cation. It was showed that, at least for some limited series of compounds, the width of the cation influences the distortion of the inorganic sheet through Pb−I−Pb bond angle variation, which leads to a variation of the exciton energy. Using this strategy, the exciton band energy could be varied by 100 meV.

6.3 Expanding the cation structure – haloplumbate structure relationship

In Chapter 2.1, a series of compounds with the general formula $(4Y\text{-}PMA)_2PbI_4$ was presented, where a close contact between the substituent of the cation (Y = F, Cl, Br, I) and the inorganic sheet was present. It was previously rationalized that different strategies that are used to obtain unusually red exciton band, among those, using a symmetrical rigid cation to obtain close-to-ideal Pb-I-Pb bond angle. As a follow up study, it would be possible to try to use the symmetrical and rigid 3,5-dY-aniline (where Y = F, Cl, Br, I) as the A-site cation. Removing the flexible $-CH_2$ substituent might lead to a red-shift of the exciton band compared to those presented in Chapter 2.1. Again, the cross-section size will be incrementally increased to try to push the limit of the exciton band energy.

Only few crystals incorporating two different cations have been reported in the literature. One can only imagine the structural diversity that these structures could have. It could be interesting to see if it could be possible to mix cations that are known to form a corrugated structure, like the one presented in Chapter 4.1, with ones that form planar structure. By careful selection of the cation, new types of corrugation might be obtained. For example, 4-nitrophenylethylammonium (4N-PEA) and 4-iodophenylethylammonium (4I-PEA) as the two cations. 4N-PEA was shown (Chapter

4) to form a 3x3 corrugated structure that interacts with the iodide of the inorganic layer. If a cation bearing an iodine substituent (which might be expected to interact more strongly with a nitro group than an inorganic iodide ion) is incorporated in the structure, the type of corrugation might change.

As it was mentioned in Chapter 4.2, it seems difficult, if not impossible, to form 2D perovskites when complex cations, such as naphthalenediimides and cyanine, are used. Complex cations have been shown, in some cases, to add their intrinsic properties to the Pb/I materials they are incorporated in. One way to add complex cations into 2D perovskite might be to use the strategy suggested by W. T. M. Van Gompel *et al,* who incorporated a neutral molecule, tetracyanoquinodimethane, in (4-(pyren-1-yl)butan-1-ammonium)$_2$PbI$_4$ due to the donor-acceptor interaction between tetracyanoquinodimethane and the pyrene moiety of the cation (the crystal structure of the complex is not available). Naphthalene and naphthalene diimide (NDI) are known to co-crystallize together in an electron donor-acceptor fashion. In the donor-acceptor complex, the distance between the naphthalene plane and the naphthalene diimide plane is about 3.3 Å. In (3-naphthyl-propylammonium)$_2$PbI$_4$, the distance between the plane of two naphthalene cations is about 8.2 Å. This means that it may be possible to incorporate a neutral NDI derivative into a naphthalene-derivative lead iodide 2D perovskite.

6.4 Towards cation structure – iodoplumbate property relationships

In Chapter 2.2, it was demonstrated that, at least for some limited series of compounds (dY-PEA and 3Y-PEA where Y = F, Cl, Br, Me), the width of the cation influences the distortion of the inorganic sheet through Pb−I−Pb bond angle variation. As expected,

this led to a variation of the exciton energy. Using this method, the band gap was tuned by 100 meV. In this study, commercially available cations or easy-to-synthesize cations were used. It would be interesting to examine the applicability of this relationship between cation width and exciton energy in other families of cations; for example, as the cation's width is further increased (Y = I, CH_2CH_3, $CH_2CH_2CH_3$) or in cases where the cation is unsymmetrical (3Y,5Z-PEA). This would help confirm the generality and/or limitations of this structural guideline.

As mentioned in Chapter 3.1, in most cases, lowering the dimensionality of the Pb/I material leads to increased stability to moisture and heat.[32, 33] Because of this, 1D $APbI_3$ perovskitoid compounds have been used as a capping layer for three-dimensional (3D) perovskite films in perovskite solar cells.[34-37] Chapter 3.1 introduced the first cation engineering rationale for obtaining 1D face-sharing iodoplumbate compounds. In light of these findings, it would be interesting to know what structural feature of the cation might help improve the stability of the perovskite. This can be studied using Machine Learning methodology coupled with PXRD experiments.

ANNEXE A: A PHOTO-CROSSLINKABLE BIS-TRIARYLAMINE SIDE-CHAIN POLYMER AS A HOLE-TRANSPORT MATERIAL FOR STABLE PEROVSKITE SOLAR CELLS

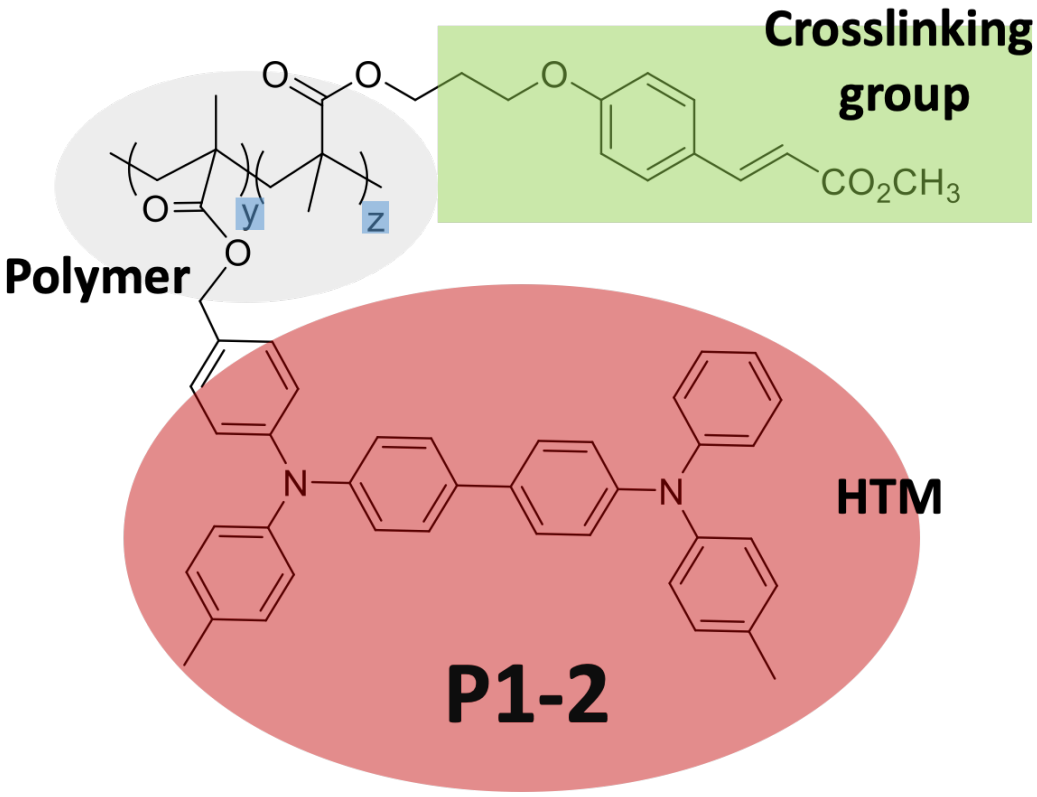

This project was accomplished with the collaboration of Kelly Schutt, Yadong Zhang, Jongchul Lim, Jonathan H. Warby, Yen-Hung Lin, Stephen Barlow, Henry J. Snaith, and Seth R. Marder. Kelly Schutt, in Professor Henry Snaith group, from the Clarendon Laboratory at the University of Oxford, helped with the solar cell characterization and performed most of the half-cell characterization. Yadong Zhang provided the studied HTM. Jongchul Lim, in Professor Henry Snaith group, from the Clarendon Laboratory at the University of Oxford, helped with the conductivity measurement. Jonathan H. Warby, in Professor Henry Snaith group, from the Clarendon Laboratory at the

University of Oxford, helped set up the oven for the long-term stability measurements. Yen-Hung Lin, in Professor Henry Snaith group, from the Clarendon Laboratory at the University of Oxford, provided training on the reference cells. Stephen Barlow helped with the data analysis and he helped to write the manuscript. The content of this chapter was published in Sustainable Energy and Fuels in Sept 2019 (DOI: 10.1039/C9SE00513G). Kelly Schutt and I are co-author on this publication. All authors contributed to the redaction of the manuscript. This work was supported by NSERC (ES. D. Scholarship for MHT), the AFOSR (FA9550-18-1-0499), the Marshall Aid Commemoration Commission, and EPSRC UK.

A.1 Introduction

The efficiency of lead-halide perovskite solar cells (PSCs) has improved significantly since their debut in the literature in 2009.[1, 2, 4-6] A transition to polycrystalline thin films,[3, 371] improvements in film quality,[372-374] organic and metal contacts,[375, 376] doping of charge extraction layers,[377, 378] and band-gap tuning[254, 301] have all contributed to the achievement of power conversion efficiency (PCE) values greater than 20%. Nevertheless, the stability of these solar cells must be improved for commercialization of this technology,[379, 380] and often the most efficient cells are not the most stable.[381] Among ways to achieve improved stability, one can use mixed-cation perovskites[382,383] or a quasi two-dimensional perovskite,[9, 11-13, 15, 16] and modify the chemical structure of the hole-[384-387] and electron-transport materials[388-390] (HTMs and ETMs, respectively) and of the dopants used to enhance their conductivity.

HTMs play a crucial role in PSCs by reducing the charge recombination that occurs at direct perovskite:hole-collecting electrode interfaces. Organic molecules and polymers, as well as various inorganic materials, can be used as HTMs in PSCs.[391] The development of crosslinkable HTMs and ETMs for multilayer organic electronic devices, such as light-emitting diodes (OLEDs), was motivated by the need to avoid possible dissolution of the first layer during solution deposition of subsequent layers. Once crosslinked (thermally, photochemically, or by acid), the material becomes insoluble, allowing the subsequent layer to be easily processed on top of it and protecting the layer underneath. Crosslinking offers similar advantages for the HTMs of "p-i-n" PSCs, potentially allowing the lead-halide perovskite to be solution-processed without damage to the HTM layer. Easily processed and insolubilized HTMs are

also ideal candidates for tandem cells, where many more layers are required to be sequentially processed. A few crosslinkable HTMs and ETMs have been reported to show promise in PSCs applications. Thermal crosslinking has been achieved using HTMs with two or more styrene[392-394] or other vinyl moieties,[395] or by reacting styrene-functionalized HTMs with oligo(thiol) derivatives.[396] While respectable photo and thermal stability, and performance have been achieved with those materials, the high temperature and crosslinking time needed alkene polymerization, and the multiple ways in which the thiols used in the ene/thiol approach can react, are not optimal for multilayer printable electronics.

Lithium bis(trifluoromethanesulfonyl)imide (Li-TFSI), in combination with oxygen exposure, has been the frequently used dopant for HTMs in PSCs, and is typically used in conjunction with 4-*tert*-butylpyridine (*t*BP), which helps prevent phase segregation.[397] Unfortunately, the use of both Li-TFSI and *t*BP have been shown to degrade performance in long term stability tests, since Li-TFSI is hygroscopic and *t*BP is volatile.[380, 398] While alternative dopants have not been as heavily investigated, F_4-TCNQ is commonly utilized in so-called positive-intrinsic-negative (p-i-n) PSCs, but has been found to migrate into adjacent layers in device stacks due to its relatively high diffusivity, and is also highly volatile.[399, 400] A dopant-free HTM or one in which dopant diffusion is minimized is clearly desirable for long-term stability. Crosslinking could potentially also help in this regard.

Here the use of a photo-crosslinkable HTM, **P1-2** (Fig. 1A), in PSCs is reported. The impact of a crosslinked copolymer of acrylate monomers with bis(triarylamine) and cinnamate side groups[401] on the stability of PSCs is investigated. By careful optimization of p-i-n PSCs, a stable, dopant-free HTM

PSC with comparable performance to state-of-the-art p-i-n cells employing F_4-TCNQ-doped poly(4-butyl-triphenylamine-4',4"-diyl) (PolyTPD, Fig. 1B) as the HTM is achieved.

A.2 Experimental Procedures

Synthesis. P1-2 was synthesized according to the literature.[401]

CL1-2. **P1-2** was crosslinked under a UV-lamp at 356 nm for 4 min after the annealing step.

UV−Vis absorption spectroscopy. Absorbance spectra were measured with a Cary 5000 UV−vis/NIR spectrometer. For liquid measurement, the samples were dissolved in anhydrous and degassed toluene. For solid-state measurement, the samples were prepared by spincoating the HTM on glass substrates.

Fluorescence spectroscopy. Fluorescence spectra were measured with a Horiba Jobin Yvon Fluorolog 3-2i spectrometer.

Cyclic voltammetry (CV). Cyclic voltammetry experiments were performed using a BAS potentiostat with a glassy carbon working electrode, platinum counter electrode and an Ag wire reference electrode at a scan rate of 100 mV s^{-1}. Anhydrous and degassed dichloromethane solutions containing 0.1 M of tetrabutylammonium hexafluorophosphate as electrolyte was used to dissolve **1** (10^{-3} M). Ferrocene was used as the reference.

Current−voltage measurements. The *JV* curves were measured (2400 Series SourceMeter, Keithley Instruments) under simulated AM 1.5 sunlight at 100 mW cm^{-2} irradiance generated by an Abet Class AAB sun 2000 simulator, with the intensity calibrated with an NREL calibrated KG 5 filtered Si reference cell. The forward *J–V* scans were measured from forward bias to short circuit and the backward scans were

from short circuit to forward bias, both at a scan rate of 380 mV s^{-1}. A stabilization time of 5 s at forward bias of 0 V under illumination was done prior to scanning.

Scanning electron microscope. SEM images were measured using a FEI Sirion scanning electron microscope at an acceleration voltage of 5 kV.

Powder X-ray diffraction. XRD spectra were measured using a Panalytical X'pert powder diffractometer with Cu anode X-ray source.

Conductivity. Conductivity data were acquired with a custom built 4 point probe system with Au contact pins connected to a Keithly 2636 SourceMeter. To prepare the substrates, X nm of gold was evaporated on clean glass substrates and the HTM was spincoated from a toluene solution.

Profilometry. Film thicknesses were measured with a Veeco Dektak 150 surface profilometer.

AFM. Atomic force microscopy images were acquired with an Asylum MFP3D (Asylum Research and Oxford Instruments Co.) in AC (tapping) mode. Asylum Research Econo-LTESP-Au silicon tips were used for topography measurements.

Substrate preparation. Fluorine doped tin oxide (FTO) (Pilkington TEC 7) or indium tin oxides (ITO) (Shenzhen Display, < 10 ohm cm^{-2}) coated glass substrates were used in this experiment. FTO or ITO substrates were etched at specific regions using a 2 M HCl and zinc powder. Substrates were then cleaned with water, then sequentially sonicated for 5 min in acetone, isopropyl alcohol and water, and dried with a compressed nitrogen gun. Next, the substrates were treated for 5 min in oxygen plasma.

F_4-TCNQ-doped PolyTPD. 0.2 mg of F_4-TCNQ and 1 mg of PolyTPD were added to 1 mL of toluene. The solution was stirred for 12 h prior to deposition. The filtered solution was spincoated at 2000 rpm, 2000 rpm s^{-1} for 20 s and dried at 130 °C for 10 min. PFN (9,9-bis(3-(*N,N*-dimethylamino)propyl)fluorene-2,7-diyl)-*alt*-(9,9-dioctylfluoren-2,7-diyl) devices were made by spin coating 0.1 mg mL^{-1} PFN in methanol onto the annealed PolyTPD substrate at 3000 rpm for 30 s.

F_4-TCNQ-doped P1-2. For undoped films, 1 mg of **P1-2** was added to 1 mL of toluene. The solution was stirred for 12 h prior to deposition. The filtered solution was spincoated at 2000 rpm, 2000 rpm s^{-1} for 20 s and dried at 130 °C for 10 min. For doped films, a solution of 0.5 mg mL^{-1} of F_4-TCNQ in toluene was added to **P1-2** solution in toluene (2 mg mL^{-1}) at the mol% desired and toluene was added to achieve a 1 mg mL^{-1} solution of **P1-2**.

$Cs_{0.05}(FA_{0.85}MA_{0.15})_{0.95}Pb(I_{0.9}Br_{0.1})_3$ perovskite (FAMACs). The precursor solution was prepared by dissolving formamidinium iodide (FAI; Dyesol), methylammonium iodide (MAI; Dyesol), cesium iodide (CsI; Sigma Aldrich), lead iodide (PbI_2; TCI) and lead bromide ($PbBr_2$; Alfa Aesar) in anhydrous *N,N*-dimethylformamide (DMF; Sigma-Aldrich) and dimethylsulfoxide (DMSO; Sigma-Aldrich) in a ratio 4:1 in a nitrogen-filled glovebox to obtain a stoichiometric 1.3 M solution. The solution was then stirred overnight at room temperature and filtered using a 0.44 μm filter. 150 μL of the precursor perovskite solution was spin-coated in a drybox at 1000 rpm for 10 s and then 6000 rpm for 35 s with a ramp of 2000 rpm s^{-1}. After 35 s, 400 μL of toluene (Sigma) was quickly added on the spinning substrates. The films were dried on a hot plate at a temperature of 100 °C for 60 min.

$FA_{0.83}Cs_{0.17}PbI_{0.83}Br_{0.17}$ perovskite (FACs). A 1.45 M solution was stirred at 70 °C for 15 min immediately prior to use. 64.0 mg CsI, 103.8 mg $PbBr_2$, 207.0 mg FAI, and 538.2 mg PbI_2 were added to 800 μL DMF and 200 μL DMSO. The solution was then stirred overnight at room temperature. 150 μL of the precursor perovskite solution was spin-coated in a drybox at 1000 rpm for 10 s and then 6000 rpm for 35 s with a ramp of 2000 rpm s^{-1}. After 30 s, 400 μL of toluene (Sigma) was quickly added on the spinning substrates. The films were dried on a hot plate at a temperature of 100 °C for 60 min.

Electron-transport material. PCBM (PCBM = phenyl-C_{61}-butyric acid methyl ester) (20 mg mL^{-1} in 3:1 chlorobenzene/dichlorobenzene) and BCP (BCP = bathocuproine) (0.5 mg mL^{-1} in isopropanol) were stirred overnight prior to deposition. They were then sequentially dynamically deposited by spin coating. First, PCBM was deposited at 2000 rpm for 20 s, followed by annealing for 5 min at 100 °C. Second, BCP was deposited at 5000 rpm for 20 s followed by annealing at 100 °C for 1 min.

Electrode evaporation. An 100 nm silver or 80 nm gold electrode was thermally evaporated under vacuum.

PL data treatment. Each normalized PL decay was fitted to a stretched exponential function following the method of Stranks *et al*.:[402]

$$I(t) = exp\left[-\left(\frac{t - t_0}{\tau}\right)^{\beta}\right]$$

with I(t) the PL intensity at time t, t_0 an offset correction (constrained such that $0 \leq t0 \leq 10$), τ the characteristic lifetime and β the stretching exponent. The use of a stretched exponential function to fit PL data from perovskite films is well established in the

literature, in lieu of a true analytical model.[254, 403] The stretching of the exponential has been interpreted as resulting from a distribution of monomolecular (trap-assisted) non-radiative decay rates within the material.[404] The mean relaxation time, <τ>, given by Equation 4:

$$\langle \tau \rangle = \frac{\tau}{\beta} \Gamma\left(\frac{1}{\beta}\right)$$

where Γ(z) is the gamma function:

$$\Gamma(z) = \int_0^\infty x^{z-1} e^{-x} dx$$

Tandem perovskite/HTM/perovskite structures. FTO substrates were cleaned as above. FACs perovskite was spin coated, then annealed at 100 °C as previously described. PolyTPD (10 mg/ml) and **P1-2** (10 mg/ml) were filtered through a 0.22 um PTFE syringe filter, then spin-coated on top of the perovskite (2k rpm, 20 s) and annealed at 130 °C for 10 mins for layer thicknesses of approximately 68 and 50 nm, respectively. **P1-2** was then crosslinked as above. For the top layer of perovskite, $MAPbI_3$ was prepared in acetonitrile by adding PbI_2 (1.466 g) and methylammonium iodide (0.477 g) to acetonitrile (6 ml), and then bubbling the solution with methylamine for about 5 min until the solution turned from black and opaque to colorless and transparent (see ref 6 for details). Solution was dynamically dispensed onto substrates spinning at 2000 rpm for 35 s. Substrates were then annealed at 100 °C for 10 minutes. Absorption spectra were collected with a Varian Cary 1050 UV Vis spectrophotometer before thermally evaporating 80 nm of Au to improve contrast for the SEM cross section. Cross sectional images were acquired with an FEI Quanta 600 scanning electron microscope at 10 kV acceleration voltage.

A.3 Results and Discussion

Synthesis and characterization of the HTM

HTMs for PSCs often contain the bis(diarylamino)biphenyl moiety. For example, the widely used spiro-OMeTAD consists of two such moieties linked by a bridging carbon atom. More recently, polymeric materials containing the same moiety, such as PolyTPD and PTAA (poly(2,4,6-trimethyltriphenylamine-4',4"-diyl)), have shown great potential as HTMs in so-called "inverted" (i.e., p-i-n) PSCs,[405-407] where the HTM is the first layer deposited. Cells using PolyTPD have achieved a record of 19.1% PCE.[378] The same bis(diarylamino)biphenyl motif has also been widely used in OLEDs and some of us have previously reported a series of papers[401, 408-411] in which random copolymers of monomers with bis(diarylamino)biphenyl functionalization and monomers with cinnamate side chains have been used as solution-processible materials that can subsequently be insolubilized through brief UV irradiation to induce a 2+2 cycloaddition of the cinnamate groups. This approach is modular in that the properties of the polymer can be adjusted through varying the HTM:crosslinker ratio, the ionization energy (IE) of the polymer can be varied through the substitution pattern of the HTM monomer, and other polymer properties can be varied through the choice of the polymer backbone. We chose one of these previously reported polymers – **P1-2**, the copolymer of a bis(diarylamino)biphenyl-acrylate monomer (**1**) and a cinnamate-acrylate monomer (**2**)[401] (Fig. 1A) – as a candidate HTM for investigation in PSCs.

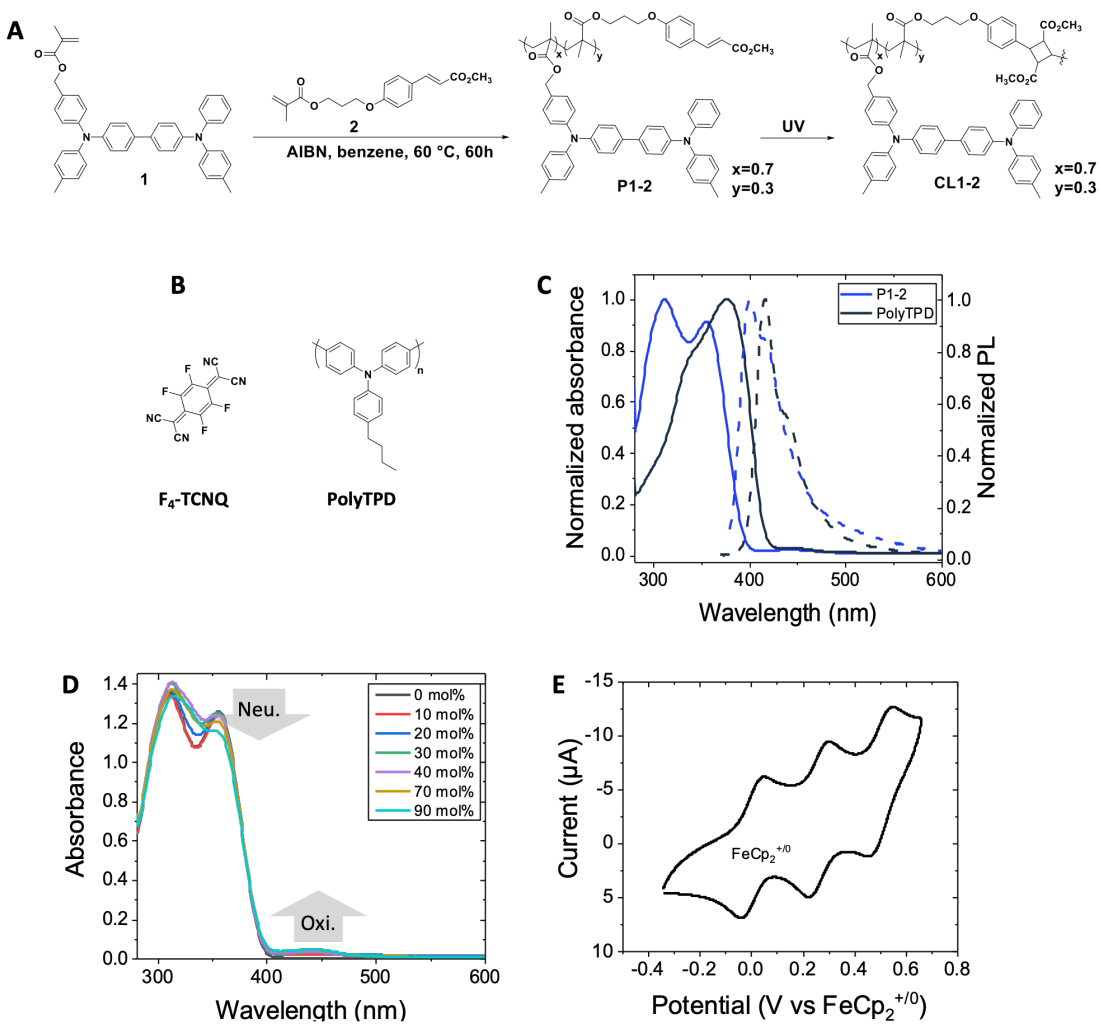

Figure A.1 (A) Synthesis of copolymer **P1-2** from the bis(triarylamine) **1** and the cinnamate **2**. The crosslinked material **CL1-2** can be obtained after illumination with UV light. (B) Chemical structure of PolyTPD and F_4-TCNQ, the dopant usually used to dope triarylamine-based HTMs. (C) Comparison of the absorbance (solid line) and photoluminescence (dashed line) spectra of **P1-2** and PolyTPD in toluene (with 20 mol% F_4-TCNQ per triarylamine unit). (D) UV-vis spectrum showing the doping in toluene solution of **P1-2** with F_4-TCNQ (where Neut. and Ox. indicate signals attributable to the neutral and oxidized bis(diarylamino)biphenyl units, respectively, and *x* mol% is relative to the number of triarylamine units, i.e. corresponds 2*x* molar equivalents per 100 moles of monomer). Cyclic voltammetry of **1** in dichloromethane (10^{-3} M) with 0.1 M Bu_4NPF_6 and ferrocene as reference (10^{-3} M).

Monomers **1** and **2** and copolymer **P1-2** were synthesized as previously described.[401] Films of the polymer were insolubilized using a short illumination time at 356 nm, which does not significantly degrade the HTM unit of the polymer. From the point of view of PSC fabrication, this facile photocrosslinking is potentially advantageous over alternative thermal crosslinker approaches that require high temperatures >150 °C since the process can be done at ambient

temperature on plastic substrates. Moreover, for n-i-p structures, the low power UV-lamp used would not degrade the underlying perovskite layer, whereas the temperatures required for many thermal crosslinking reactions would.

P1-2 has a slightly higher energy onset of optical absorption than PolyTPD (Fig. 1C, Table 1), which is potentially advantageous in allowing more of the solar spectrum to reach the active layer, potentially reducing parasitic absorption and maximizing current density. Electrochemical measurements on the monomer **1** in CH_2Cl_2/0.1 M Bu_4NPF_6 indicate a reversible oxidation at +0.26 V vs $FeCp_2^{+/0}$ (see Fig. 1E), from which an IE of 5.1 eV is estimated, similar to that of PolyTPD (Table 1). Addition of F_4-TCNQ to solutions of either PolyTPD or **P1-2** leads to only moderate changes in the optical spectra, suggesting inefficient doping with this oxidant. This is further illustrated by Fig. 1D, where the effects of successive dopant addition are shown for the case of **P1-2**. The low yield of oxidized HTM in each case is expected given the redox potential of F_4TCNQ (+0.15 V in the CH_2Cl_2/0.1 M Bu_4NPF_6).[412,54]

Table A.1 Key properties of the hole-transport materials.

	PolyTPD	**P1-2**
$\lambda_{max,\ abs}$[a] (nm)	377 (338)	313 (356)
$\lambda_{max,\ PL}$[a,b] (nm)	417 (441)	400 (416)
IE[c] (eV)	5.2[h]	5.1[i]
EA[d] (eV)	2.1	1.8
$E_{opt,\ gap}$[e] (eV)	3.06	3.23
σ[f] (S m^{-1})	0.010 ± 0.001	0.0141 ± 0.0007[j]
T_g[g] (°C)	230	137

a The spectra were measured in toluene. b Measured at 0.1 absorbance. c Estimated according to IE (eV) = 4.8 + E1,½ (V), where the E1,½ is relative to FeCp2+/0. d Electron affinity estimated from EA = IE – Eopt, gap. e Optical gap calculated using the crossing of normalized absorbance and fluorescence spectra. f Measured by 4-point probe of the undoped films. g According to literature: PolyTPD,55 P1-2 (prior to crosslinking).45. h From ref. 55. i Estimated from E1/2 of monomer 1. j Measured on the crosslinked film CL1-2.

Characterization of HTM films and perovskite growth

Atomic force microscopy of thin films of **CL1-2** and PolyTPD on glass substrates showed similar homogeneity and smoothness (see Fig. 2A-B). Perovskite films crystallized on top of the two HTM films on FTO substrates also appeared similar by scanning electron microscopy (SEM), although we observed a larger distribution of bright color grains on the **CL1-2** film than on PolyTPD (Fig. 2C-E); it is unclear what the cause of this observation is, or whether it has any device consequence, although excess PbI_2 has been found to be beneficial in previous PSC studies.[56,57] The powder X-ray diffraction (PXRD) of the perovskite films on top of the two different HTMs are also similar, indicating comparable perovskite growth on both material when FTO is used as the substrate (see Fig. 2F).

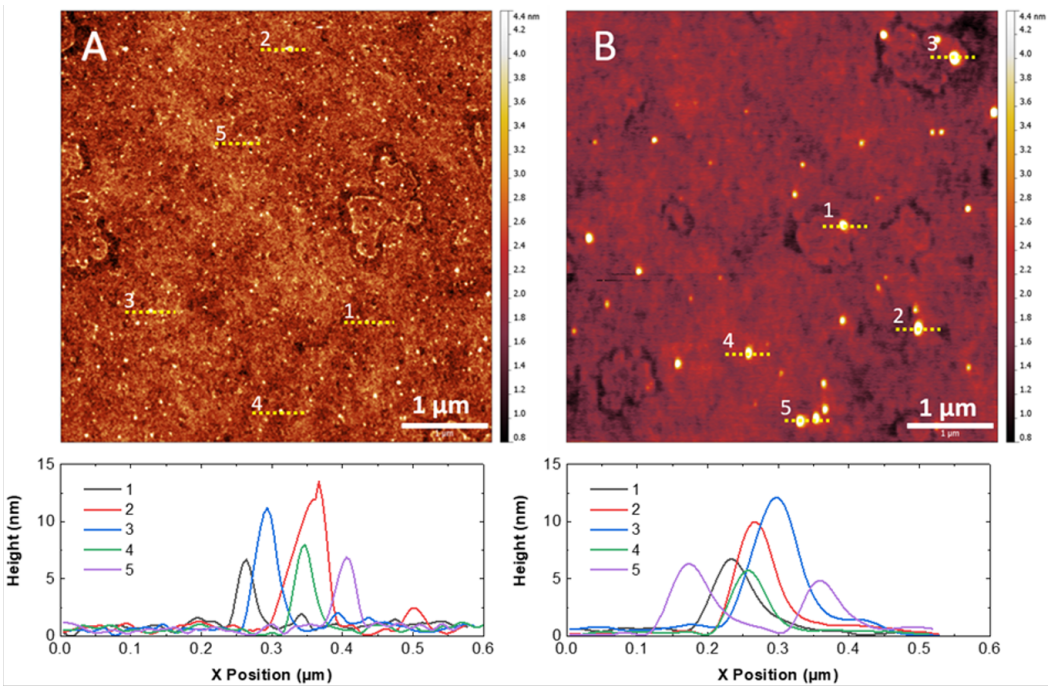

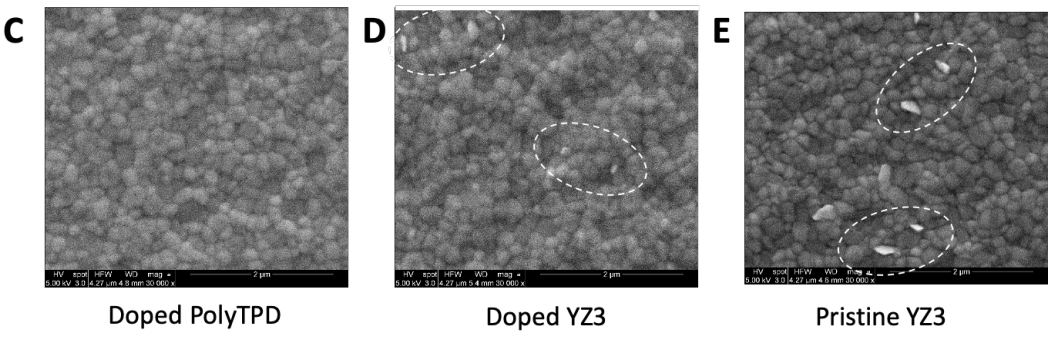

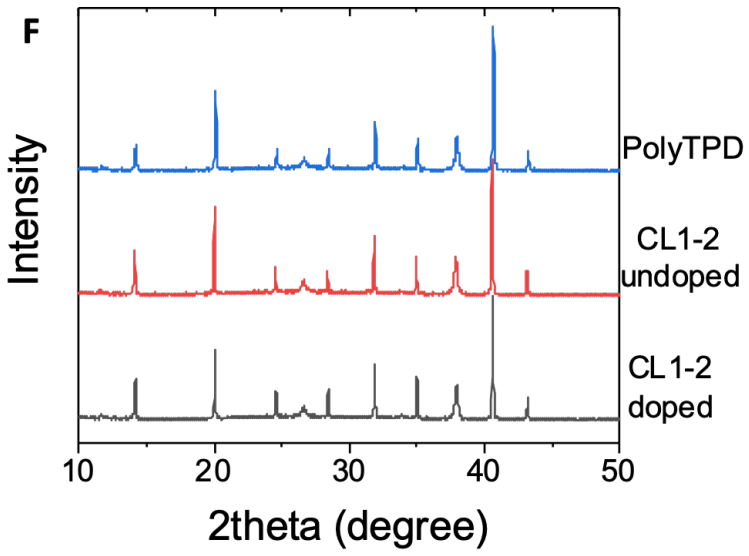

Figure A.2 AFM images of (A) PolyTPD and (B) **CL1-2** spincoated on glass. Height profiles of surface aggregates are shown below. SEM images of the FAMACs perovskite film crystallized on top of FTO/HTM layer, where HTM is (C) doped PolyTPD, (D) pristine **CL1-2** and (E) doped **CL1-2**. The circled bright

particles are assumed to be PbI_2 crystals. (F) PXRD of the FAMACs perovskite spincoated on PolyTPD, and doped and undoped **CL1-2** films on FTO.

The conductivity of the HTMs was characterized using four-point probe measurements with and without F_4-TCNQ. Slightly lower conductivity was measured for pristine PolyTPD compared to pristine **CL1-2** (see Fig. 3) after annealing at 130 °C. In both cases, doping the HTM with F_4-TCNQ p-dopant increased the conductivity of the HTM by similar amounts; however, as discussed in the following section, PSC device performance was comparable for undoped and doped **CL1-2,** while the performance increased upon doping of PolyTPD (see device data later). Although the active layers of the PSCs fabricated in this work (see below) are annealed at only 100 °C, some perovskite materials necessitate high annealing temperature (e.g., often >200 °C for inorganic $CsPbX_3$ perovskites).[413, 414] Accordingly, we also investigated the effect of higher temperatures on both doped **CL1-2** and doped uncrosslinked **P1-2**. After annealing at 180 °C, the doped **CL1-2** conductivity was found to be higher than that of doped uncrosslinked **P1-2**, which is consistent with crosslinking perhaps helping to retain the volatile F_4-TCNQ within the film. When films were further annealed at 250 °C, the conductivity of **CL1-2** actually increased, while the integrity of the PolyTPD film was damaged, and the conductivity of PolyTPD decreased dramatically, perhaps due to film damage occurring above the T_g of the latter polymer. This enhanced dopant retention of doped **CL1-2** may, therefore, make it a suitable HTM for PSCs in which subsequently deposited layers require high annealing temperatures.

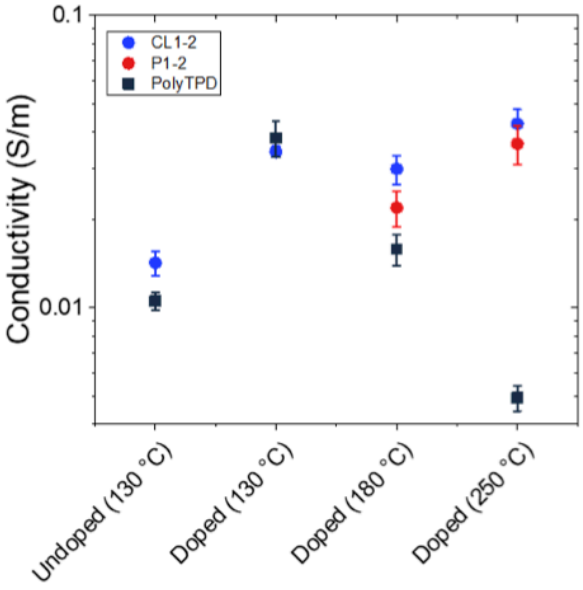

Figure A.3 4-point probe conductivity measurement of PolyTPD and **P1-2/CL1-2**. Films are 10 nm thick. The samples are first annealed 130 °C, which correspond to the processing temperature in the solar cells, and further annealed at the indicated temperature for 10 min. The HTMs are both doped with 20 mol% F_4-TCNQ in solution prior to film deposition.

Finally, to investigate the charge transfer at the perovskite and the HTM interface, we performed steady-state photoluminescence (PL) measurements (Fig. 4). The doped **CL1-2** showed similar PL quantum yield quenching compared to that of PolyTPD, indicating comparable hole-extraction capability of both HTMs at the perovskite/HTM interface, but different PL lifetimes (see below).

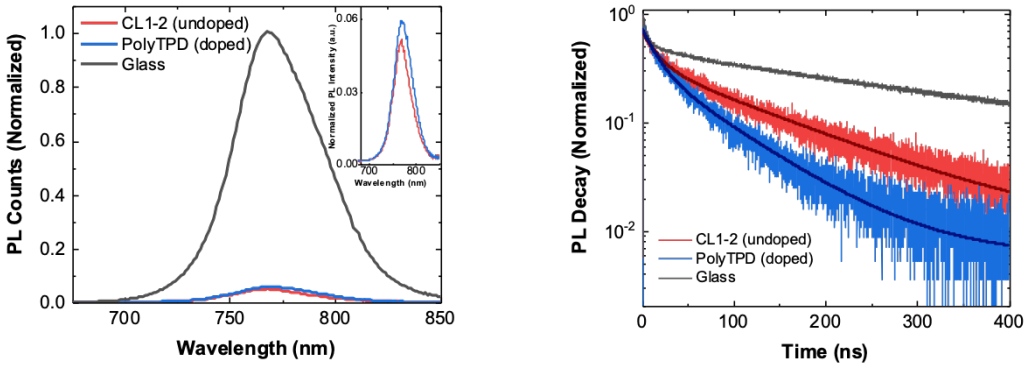

Figure A.4 Top: Photoluminescence (PL) of the FAMACs perovskite spincoated on the HTM films and on clean glass, showing similar levels of steady state photoluminescence (PL) quenching for both FTO/**CL1-2**/perovskite and FTO/PolyTPD/perovskite. The PL maximum for the PolyTPD sample is slightly red-shifted (770 nm) relative to the **CL1-2** and the perovskite-on-glass sample (both 768 nm), which may indicate more

band-bending due to shallow-trap formation in the PolyTPD case.[7,8] Bottom: Time-resolved PL of the FAMACs perovskite spincoated on the HTM (doped PolyTPD, undoped **CL1-2**) films and on glass. Fitting as a biexponential decay

$$Y = A_1 \exp\left(\frac{-t}{\tau_1}\right) + A_1 \exp\left(\frac{-t}{\tau_2}\right) + y_0$$

where τ_1 is the lifetime for fast, trap-assisted processes (Shockley-Read-Hall recombination), τ_2 is the lifetime for slower bimolecular recombination, and A_1 and A_2 are the relative amplitudes,[9] gave lifetimes τ_1 = 16.1 ns and τ_2 = 127.5 ns for the **CL-2** sample, while the perovskite film on doped PolyTPD exhibits lifetimes of τ_1 = 15.7 ns and a reduced τ_2 lifetime of 74.5 ns. In contrast, the perovskite on glass, where bulk recombination processes dominate, exhibits a much longer τ_2 lifetime of 324.2 ns.

Device fabrication and characterization

The photovoltaic performance of **CL1-2** and PolyTPD as HTMs in PSCs was compared using the architecture: FTO/HTM/$Cs_{0.05}(FA_{0.85}MA_{0.15})_{0.95}Pb(I_{0.9}Br_{0.1})_3$/PCBM/BCP/Ag (or Cr/Au for thermal stability tests), where FTO = fluorine-doped tin oxide, MA = methylammonium, FA = formamidinium, PCBM = phenyl-C_{61}-butyric acid methyl ester, and BCP = bathocuproine. The two HTM layers had approximately the same thickness (~6-8 nm as determined by profilometry). Both pristine and doped **CL1-2** showed similar performance to PolyTPD. The current-density–voltage (J–V) characteristics were measured under a simulated AM 1.5G (100 mW cm^{-2}) sunlight (see Fig. 5, Fig. S1 and Table S1).

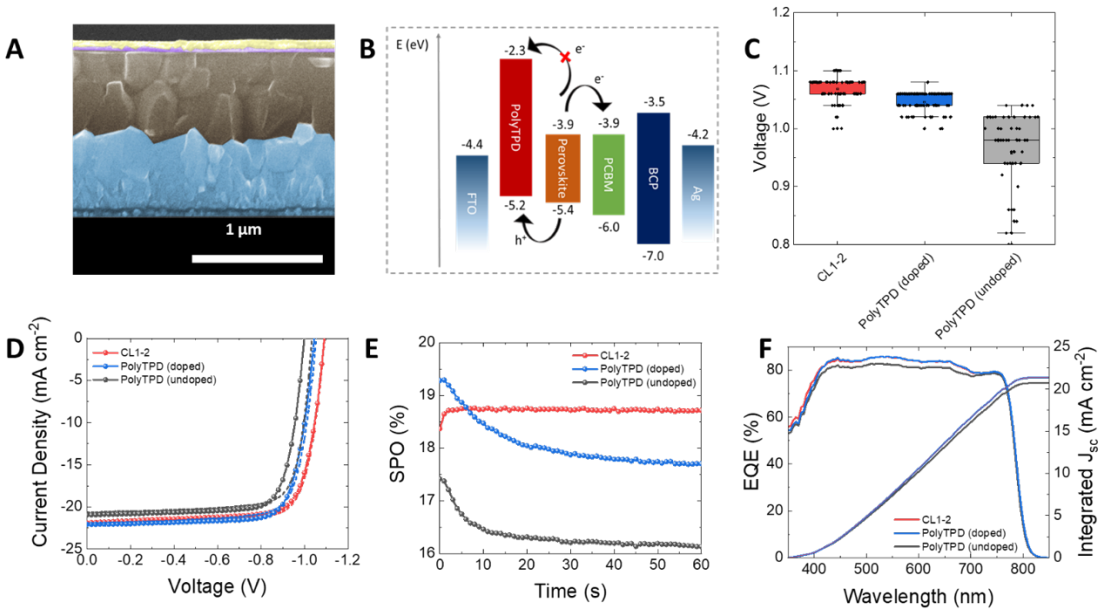

Figure A.5 (A) SEM device cross section with FTO (blue), **CL1-2**, $Cs_{0.05}(FA_{0.85}MA_{0.15})_{0.95}Pb(I_{0.9}Br_{0.1})_3$ (gray), PCBM and BCP (purple), and Ag electrode (yellow). (B) Schematic representation of the inverted "p-i-n" PSCs. (C) Comparison of V_{oc} for undoped **CL1-2**, doped PolyTPD, and undoped PolyTPD. (D) J-V characteristics for champion devices employing undoped **CL1-2**, doped PolyTPD, and undoped PolyTPD collected under AM 1.5G simulated sunlight. (E) Steady-state power output. (F) External quantum efficiency (EQE).

Only a slight improvement was noticed when **CL1-2** was doped using F_4-TCNQ (see Fig. S2 and Table S2), while a significant improvement was obtained for PolyTPD devices. The devices using undoped **CL1-2** in its optimal condition (see Fig. S3-4 and Table S3-4 for optimization of **CL1-2** concentration and annealing temperature), shows a PCE of (16±2)%, which is similar to the control device with doped PolyTPD ((16±2)%; Table S1†). Fig. 6 shows the low hysteresis present in the cells presented here. The SPO provides a more complete view of solar cell performance under operating conditions and avoids the ambiguities associated with JV hysteresis. **CL1-2** achieves 18.7% SPO, matching its scanned efficiency, while PolyTPD achieves 17.7%. The performance of the cells over time is consistent with the trend seen on the J-V curves. Despite the longer wavelength onset of absorption seen for PolyTPD, all devices gave similar external quantum efficiency (EQE) spectra, which is

consistent with the similar J_{sc} measured in the J-V scans. Moreover, PSCs made with $FA_{0.83}Cs_{0.17}PbI_{0.83}Br_{0.17}$ also showed comparable performance with **CL1-2** and PolyTPD (see Fig. S5 and Table S5), showing that this HTM also performs well with this more stable double-cation perovskite.

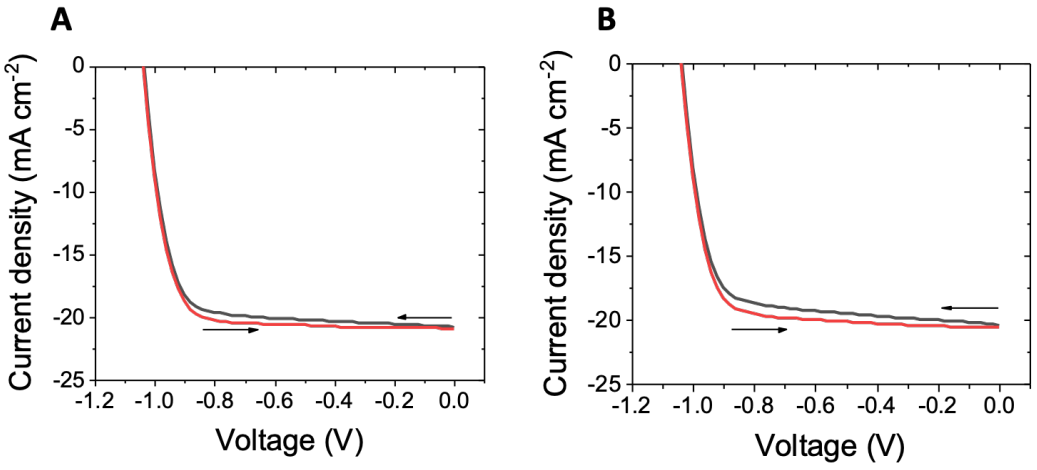

Figure A.6 Comparison of hysteresis in the J-V curves of FAMACs PSCs with (A) **CL1-2** and (B) PolyTPD HTMs.

One way that the solar-cell performance of cells with PolyTPD and **CL1-2** HTMs differ is that the latter exhibit somewhat larger V_{oc} values (Fig. 5C). It has previously been shown that Lewis base-containing HTMs or small molecules can passivate the surface traps and electronic disorder at the surface of the perovskite layer;[387, 415-417] in the present case coordination of the multiple ester moieties present in **CL1-2** to the perovskite surface might act in a similar way, thus reducing recombination and increasing V_{oc} (Fig. 5C). PL lifetime experiments on films of perovskite in contact with undoped **CL1-2** or doped PolyTPD (Fig. 4) are consistent, the former exhibiting longer lifetimes associated with bimolecular recombination. Correlations between PL decay and V_{OC} have been reported in the literature.[63-65] In addition, several previous studies have found esters can play a useful role in perovskite growth and/or passivation: poly(methyl methacrylate)

has been codeposited with the active layer of n-i-p cells,[66] and used an interlayer between perovskite and HTM in both n-i-p[67] and p-i-n[68] cells.

Perovskite growth using more planar substrates

While no major differences were noticed on the perovskite film on top of FTO/HTMs by SEM and PXRD, a major difference in the perovskite growth is noticeable when glass or tin-doped indium oxide (ITO), both of which are considerably smoother substrates than FTO, are used as the substrate. ITO has achieved slightly higher transmittance in the visible spectrum and can offer somewhat lower resistivity than FTO, making it attractive when maximum current density and fill factor are desired.[69,70] The **CL1-2** film displays slightly more hydrophilic surface, with a water contact angle, θ, of (82±3)°, than the PolyTPD film (θ = 93±6)°, which could explain why it is easier to spin-coat perovskite on smooth **CL1-2** films on glass or ITO, while it is not possible or difficult for PolyTPD films on glass and ITO. Stronger perovskite-HTM interactions could also be the cause for the improved wettability of **CL1-2** relative to PolyTPD. Indeed, the esters and ether on **CL1-2** could possibly hydrogen bond with the cations of the perovskite to facilitate its deposition, or the carbonyl group could form an intermediate adduct with PbI_2,[418] and hypotheses such as this will be probed in the future. While PolyTPD can be treated with UV Ozone to improve its wettability, sufficient treatment time to ensure full perovskite film coverage of the substrate substantially degrades photovoltaic device performance.[71] In order to make PSCs on ITO using PolyTPD, we tested a polyelectrolyte that has previously been used to improve the wettability and performance of PTAA in p-i-n PSCs, as shown in Fig. 7 and Table S6.[65,72] We find that (9,9-bis(3-(*N,N*-dimethylamino)propyl)fluorene-2,7-

diyl)-*alt*-(9,9-dioctylfluoren-2,7-diyl) (PFN) treatment on PolyTPD degrades fill factor and the SPO of the PolyTPD devices.

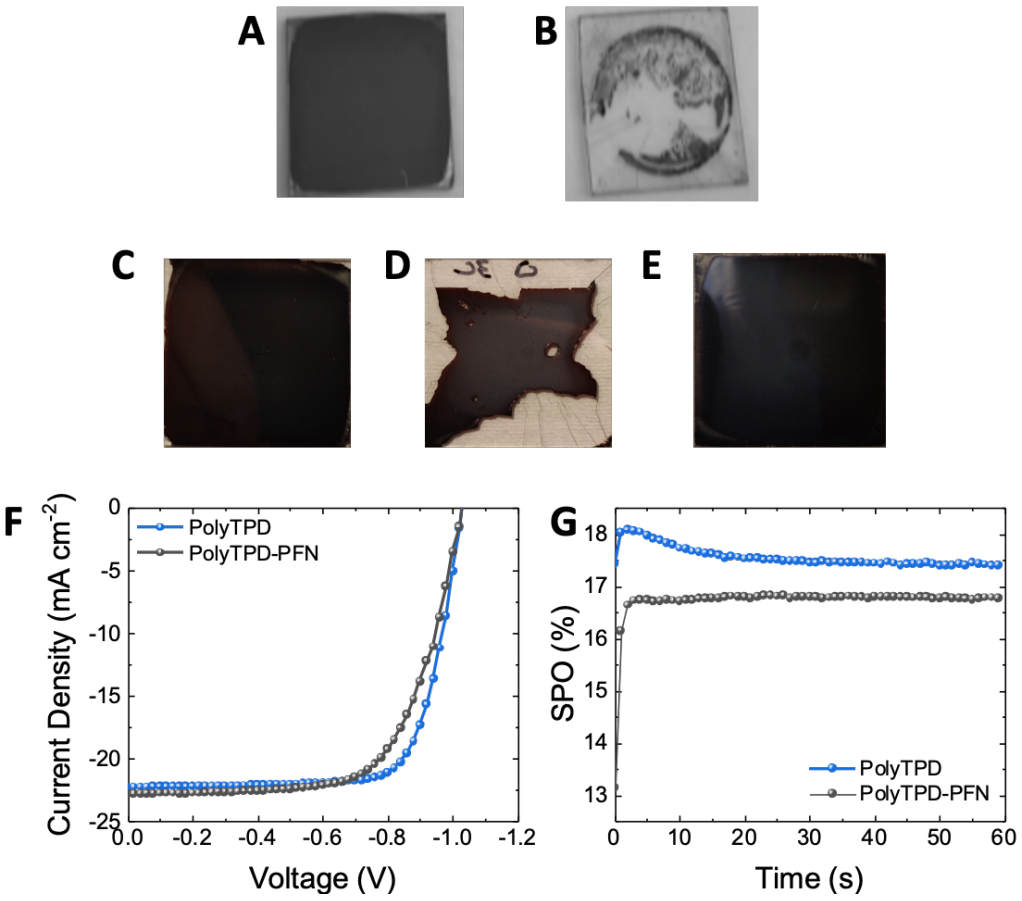

Figure A.7 A) Perovskite on Glass/**CL1-2 B)** Perovskite on Glass/PolyTPD **C)** Perovskite on ITO/**CL1-2** D) Perovskite on ITO/PolyTPD E) Perovskite on ITO/PFN/PolyTPD on ITO. The perovskite is FACs. F) JV-curves of champion devices with and without PFN G) Stabilized power output of champion devices

Another consequence of the improved growth of perovskites on **CL1-2** on a smooth substrate relative to that on PolyTPD is shown in Fig. 8. Here we show that a layer of $MAPbI_3$ can be successively coated onto **CL1-2** deposited onto $FA_{0.83}Cs_{0.17}Pb(I_{0.90}Br_{0.10})_3$ (itself grown on FTO), whereas it does not coat an analogous structure using a PolyTPD interlayer. This result suggests cross-linked organic semiconductors may help facilitate solution processing of tandem solar cells, where the crosslinking approach could potentially be extended to allow for a recombination layer that is itself a multilayer composed of sequentially

deposited and crosslinked materials with separate hole- and electron-transport functions and potentially with and without dopants. Although multilayer recombination layers of this kind have been fabricated using organic semiconductors,[73] they generally require vacuum evaporation to avoid the deposition of one layer leading to dissolution of another. An alternative solution-processed approach involves the use of PEDOT:PSS and ITO nanoparticles,[74] but the former may lead to incorporation of traces of water in the device, and both can impair transmission.

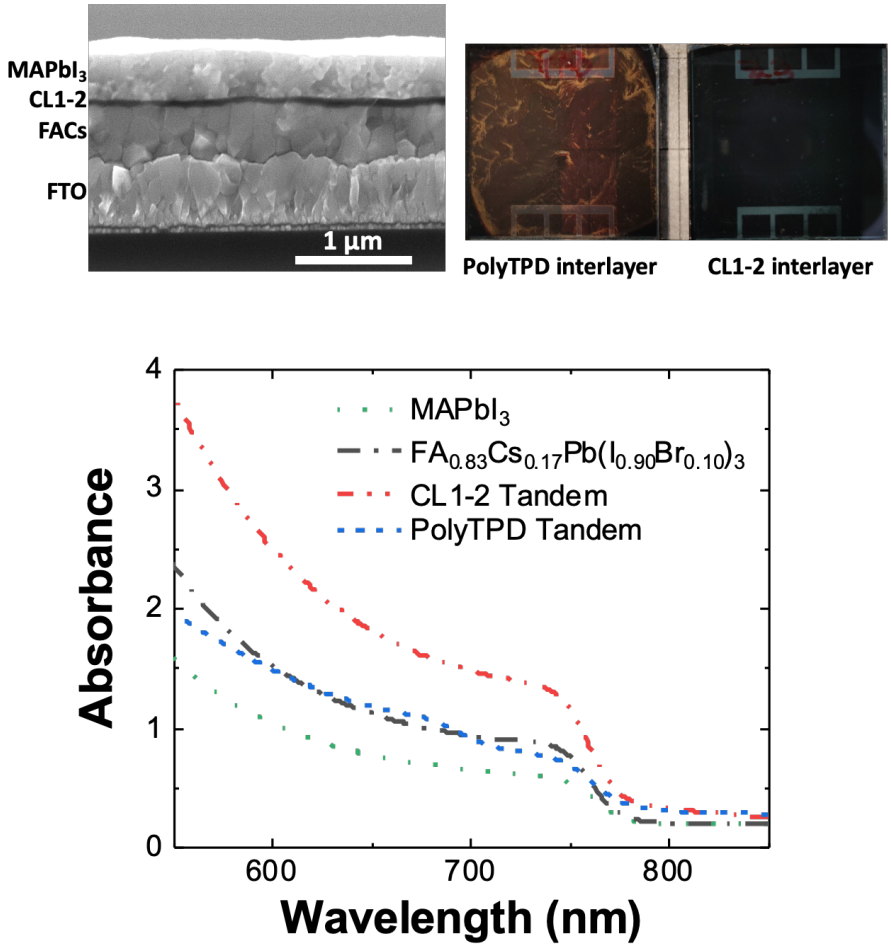

Figure A.8 Top left: SEM cross section showing a "tandem" structure FTO/FACs/**CL1-2**/$MAPbI_3$ (FACs = $FA_{0.83}Cs_{0.17}Pb(I_{0.90}Br_{0.10})_3$). Top right: photographs from the top of structures such as those shown left with PolyTPD and **CL1-2** interlayers, indicating a poorer coverage of $MAPbI_3$ when using PolyTPD. Bottom: absorption spectra of the films shown in the center, compared to those of films of the two perovskite materials deposited separately. These data show use of **CL1-2** leads to a structure that is much more strongly absorbing than FACs alone due to successful deposition of $MAPbI_3$, whereas use of PolyTPD does not.

Device stability studies

The photo- and thermal-stability of the $Cs_{0.05}(FA_{0.85}MA_{0.15})_{0.95}Pb(I_{0.9}Br_{0.1})_3$ PSCs incorporating **CL1-2** and PolyTPD were studied without encapsulation in a N_2-filled glovebox. The devices were periodically removed to ambient atmosphere for measurements under an AM 1.5G solar simulator, where the stabilized power output was measured after 50 s. Fig. 10A shows the stability in an oven at 85 °C; **CL1-2** showed similar stability to PolyTPD devices. Remarkably, the devices show an improvement in performance over the first 1000 hours of aging, and retain greater than their initial efficiency until after 3000 h, which to the best of our knowledge is the longest 85 °C thermal stability timescale reported in the literature (see Fig. 9 for picture of the device after 3000 h of aging).[397, 419-421]

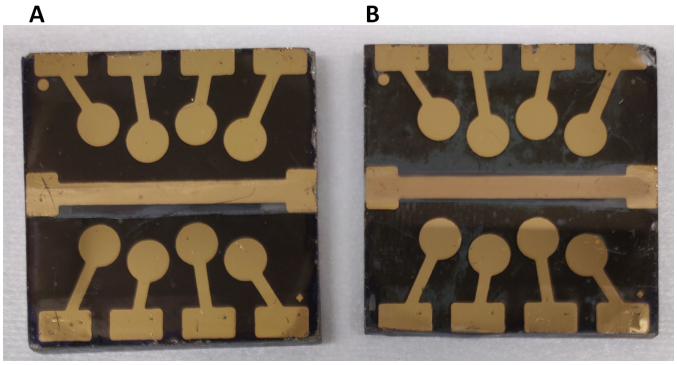

Figure A.9 **CL1-2** (A) and PolyTPD (B) devices after aging experiment.

Photostability was studied under a high intensity LED array (365 nm LED, equivalent to 12 suns UV component of the AM 1.5G spectrum). Initially, a drop in SPO is seen for the PolyTPD devices, while the **CL1-2** devices stayed approximately at the same initial SPO (Fig. 10B). The current density decreased at

a greater extent for PolyTPD devices (Fig. 10C). In order to study this instability, we measured the photoluminescence quantum efficiency (PLQE) over time of the perovskite film crystallized on top of the HTM layer on FTO. We observe a 70% drop in PolyTPD PLQE after stabilization (2 min), while the **CL1-2** doped and pristine PLQE retained 81% and 87% of their initial PLQE respectively (Fig. 10D and Table S7).

A.4 Conclusion

In summary, a description of the first use of a photo-crosslinked HTM in PSCs is presented. The crosslinkable acrylate copolymer with bis(triarylamine) and cinnamate side chains presented here is promising since it has similar performance to PolyTPD, a widely used HTM, combined with outstanding 85 °C thermal stability and improved PSC UV photo stability. Solar cells using **CL1-2** match the state-of-the-art HTM PolyTPD in terms of both performance and stability under 85 °C. Also, the multiple advantages of **CL1-2** over PolyTPD are presented: **CL1-2** does not need to be doped, while PolyTPD does; highly reproducible photovoltaic performance across multiple batches of devices are achieved; the HTM is transparent in the visible region, while PolyTPD is not; and the perovskite is easier to process on top of the **CL1-2** HTM, which together suggest that the crosslinkable polymeric **CL1-2** is a promising candidate for single junction and tandem solar cells.

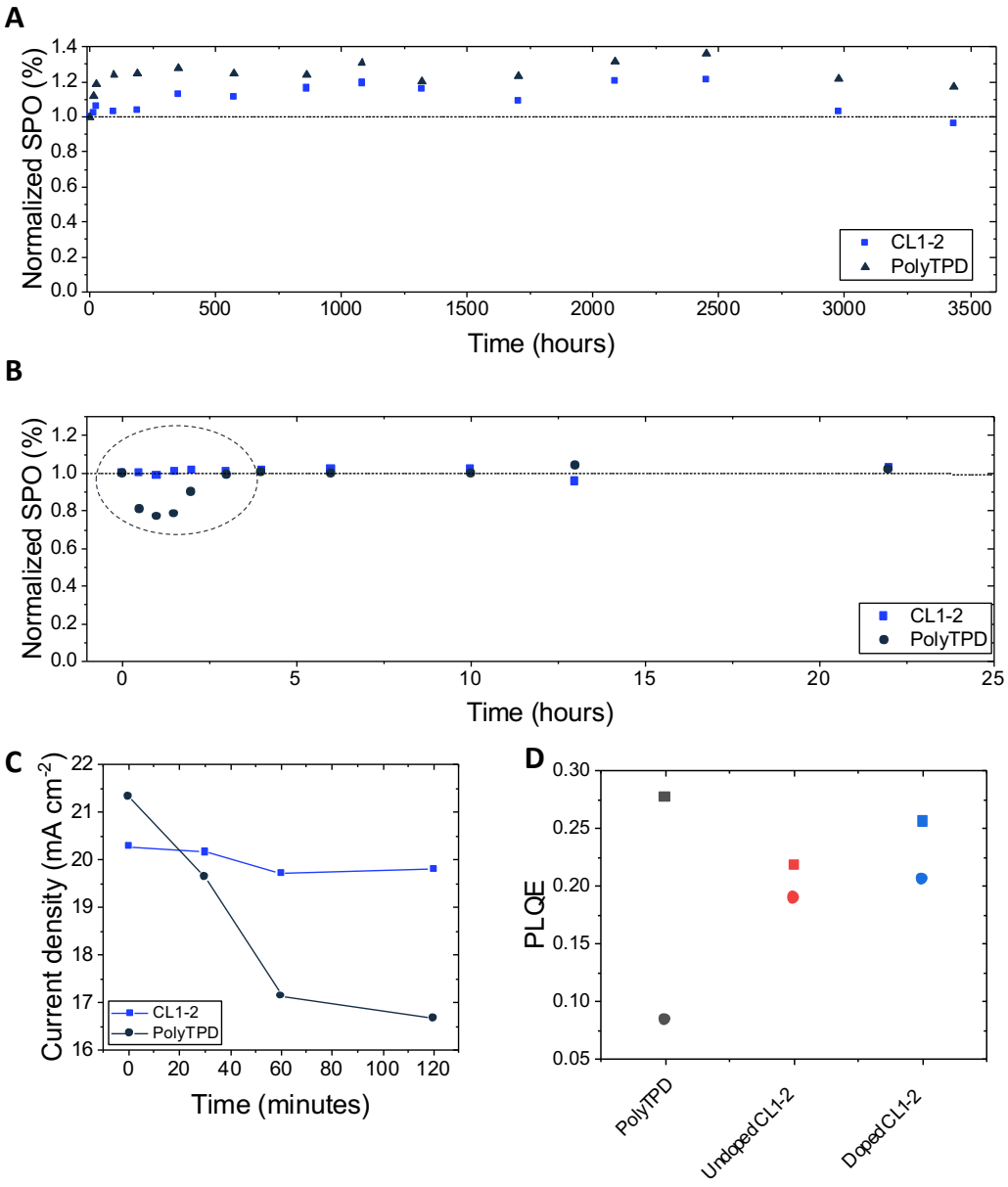

Figure A.10 Normalized stabilized power output (SPO) over 50 s after (A) aging the devices at 85 °C in an oven inside a N_2-filled glovebox without encapsulation, (B) aging the devices with a UV LED light inside a N_2-filled glovebox without encapsulation. The devices were periodically removed to atmosphere for measurements. Both HTMs are doped with F_4-TCNQ. (C) Evolution of the current density of **CL1-2** and PolyTPD devices when aged under UV LED light (same experiments as B). (D) Initial (square) and stabilized (circle) PLQE of the half devices (FTO/HTM/perovskite). See Fig. S6 and S7 for plots showing the temporal evolution of key solar-cell parameters for the experiments shown in A and B.

A.5 Supplemental information

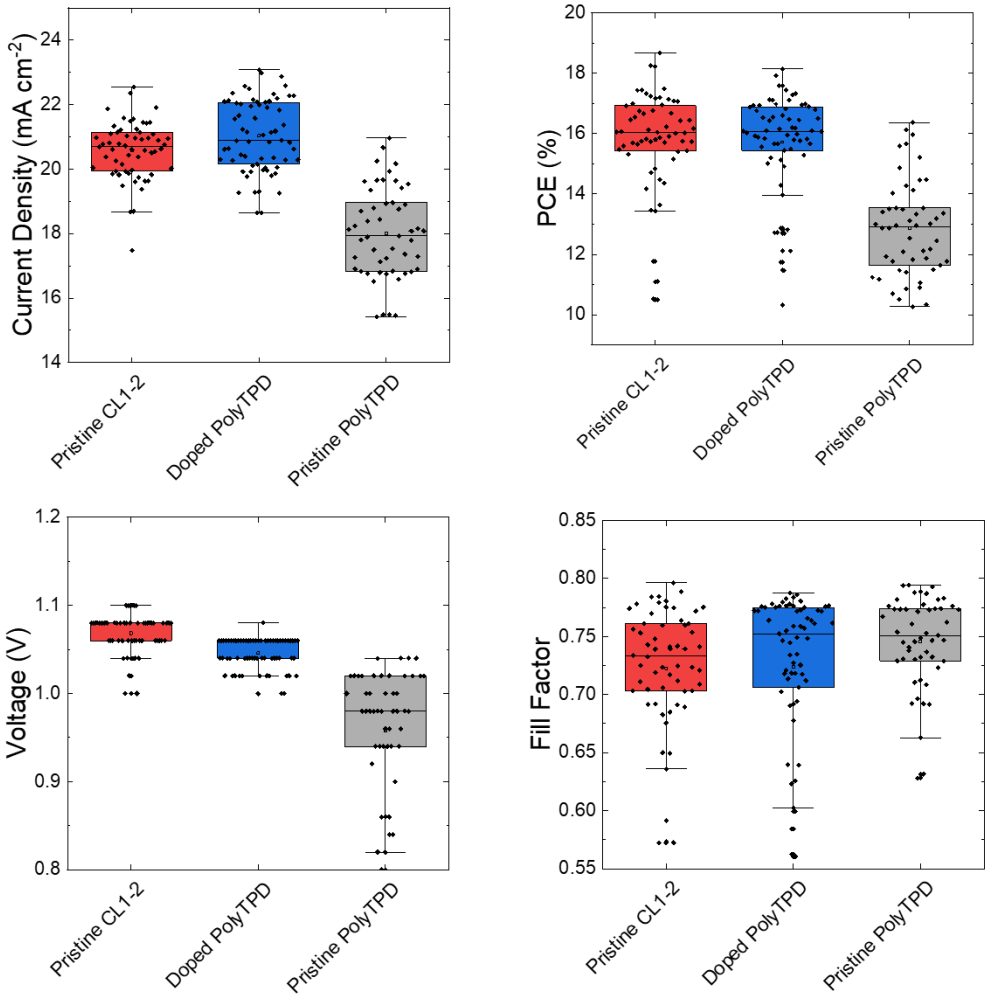

Fig. S1 Comparing the photovoltaic performance of FAMACs devices with pristine **CL1-2** and doped/undoped PolyTPD as HTM (1 mg mL^{-1}). Box-plot of devices prepared in 2 batches showing the comparison of the PV parameters (from J-V curves) of devices made using **CL1-2** and PolyTPD.

Table S2 Statistics for 48 individual FAMACs devices.

		J_{sc} (mA cm^{-2})	V_{OC} (V)	FF	PCE (%)
Pristine **CL1-2**	Average	20.6 ± 0.9	1.07 ± 0.02	0.72 ± 0.05	16 ± 2
	Maximum	22.6	1.10	0.80	18.7
Pristine PolyTPD	Average	18.0 ± 1.4	0.96 ± 0.08	0.72 ± 0.07	13 ± 2
	Maximum	21.0	1.04	0.79	16.4
Doped PolyTPD	Average	21.0 ± 1.1	1.05 ± 0.02	0.74 ± 0.04	16 ± 2
	Maximum	23.1	1.08	0.79	18.1

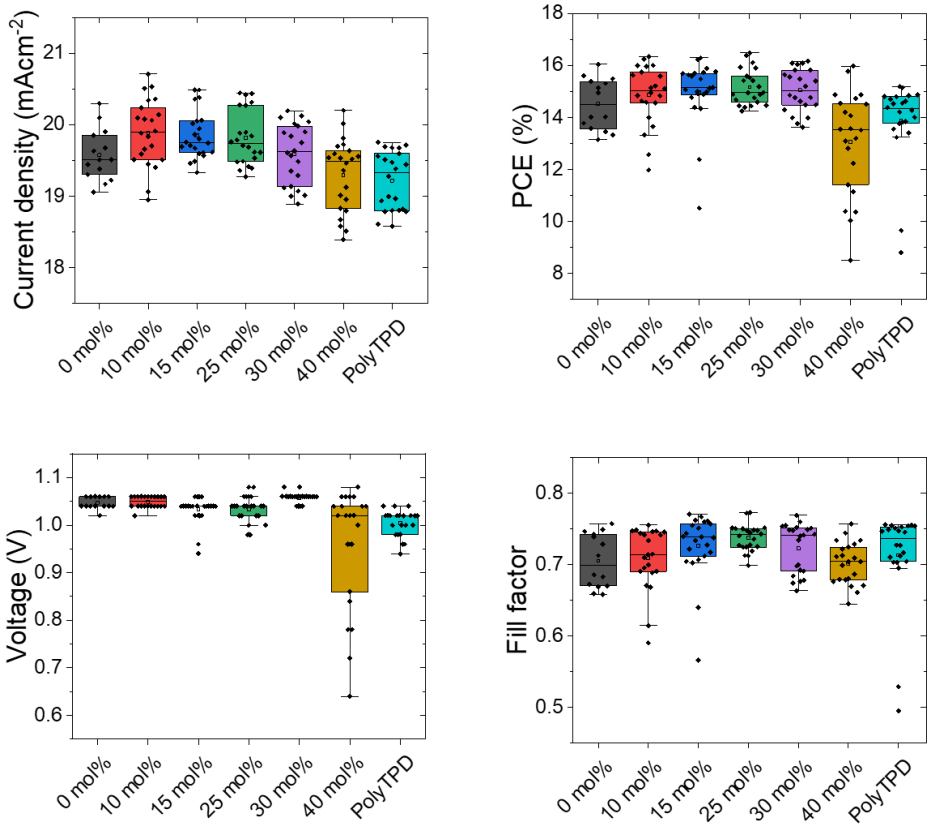

Fig. S2 Comparing the photovoltaic performance of FAMACs devices with different F_4-TCNQ concentration. Box-plot of 22 individual devices prepared in 2 batches showing the comparison of the PV parameters (from J-V curves) of devices comprising either PolyTPD or **CL1-2** at different dopant concentration. Note that these devices are not directly comparable to those in Figure S7 and Table S1 since the experiments shown here were conducted using unoptimized HTM thicknesses (HTM concentration = 2 mg mL^{-1}), whereas those in Figure S7 are optimized HTM concentration = 1 mg mL^{-1}).

Table S2 Statistical for individual FAMACs devices made to optimize the dopant concentration when **CL1-2** is used as HTM (HTM concentration = 2 mg mL^{-1}).

		J_{sc} (mA cm^{-2})	V_{OC} (V)	FF	PCE (%)
CL1-2 Undoped	Average	19.6 ± 0.4	1.05 ± 0.01	0.71 ± 0.04	15 ± 1
	Maximum	20.3	1.06	0.76	16.0
CL1-2 25 mol% F_4-TCNQ	Average	19.8 ± 0.4	1.03 ± 0.03	0.74 ± 0.02	15.2 ± 0.7
	Maximum	20.4	1.08	0.77	16.5
CL1-2 40 mol% F_4-TCNQ	Average	19.3 ± 0.5	1.0 ± 0.1	0.70 ± 0.03	13 ± 2
	Maximum	20.2	1.08	0.76	16.0
PolyTPD Doped	Average	19.2 ± 0.4	1.00 ± 0.03	0.71 ± 0.07	14 ± 2
	Maximum	19.8	1.04	0.76	15.2

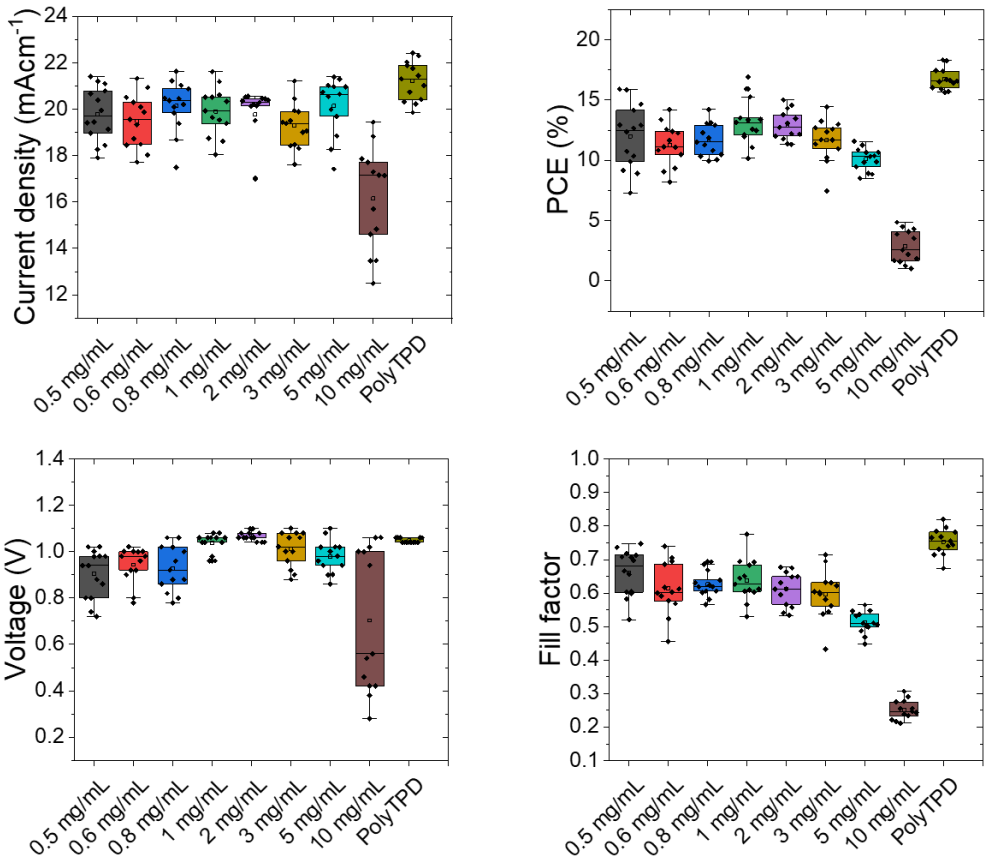

Fig. S3 Comparing the photovoltaic performance of FAMACs devices with different **P1-2** concentration used to cast 20 mol% doped **CL1-2** films. Box-plot of 14 individual devices prepared in 2 batches showing the comparison of the PV parameters (from J-V curves) of devices comprising either PolyTPD or **CL1-2** at different concentration as HTM.

Table S3 Statistics for 14 individual FAMACs devices made to optimize the concentration of **P1-2** used to cast 20 mol% doped **CL1-2** films.

		J_{sc} (mA cm^{-2})	V_{OC} (V)	FF	PCE (%)
0.5 mg mL^{-1} **P1-2**	Average	19.8 ± 1.2	0.90 ± 0.1	0.66 ± 0.07	12 ± 3
	Maximum	21.4	1.02	0.74	15.8
1 mg mL^{-1} **P1-2**	Average	19.9 ± 1.0	1.04 ± 0.04	0.64 ± 0.06	13 ± 2
	Maximum	21.6	1.08	0.78	16.9
3 mg mL^{-1} **P1-2**	Average	19.3 ± 0.9	1.01 ± 0.08	0.60 ± 0.07	12 ± 2
	Maximum	21.2	1.10	0.71	14.4
PolyTPD	Average	21.2 ± 0.9	1.05 ± 0.01	0.75 ± 0.04	16 ± 0.8
	Maximum	22.4	1.06	0.82	18.3

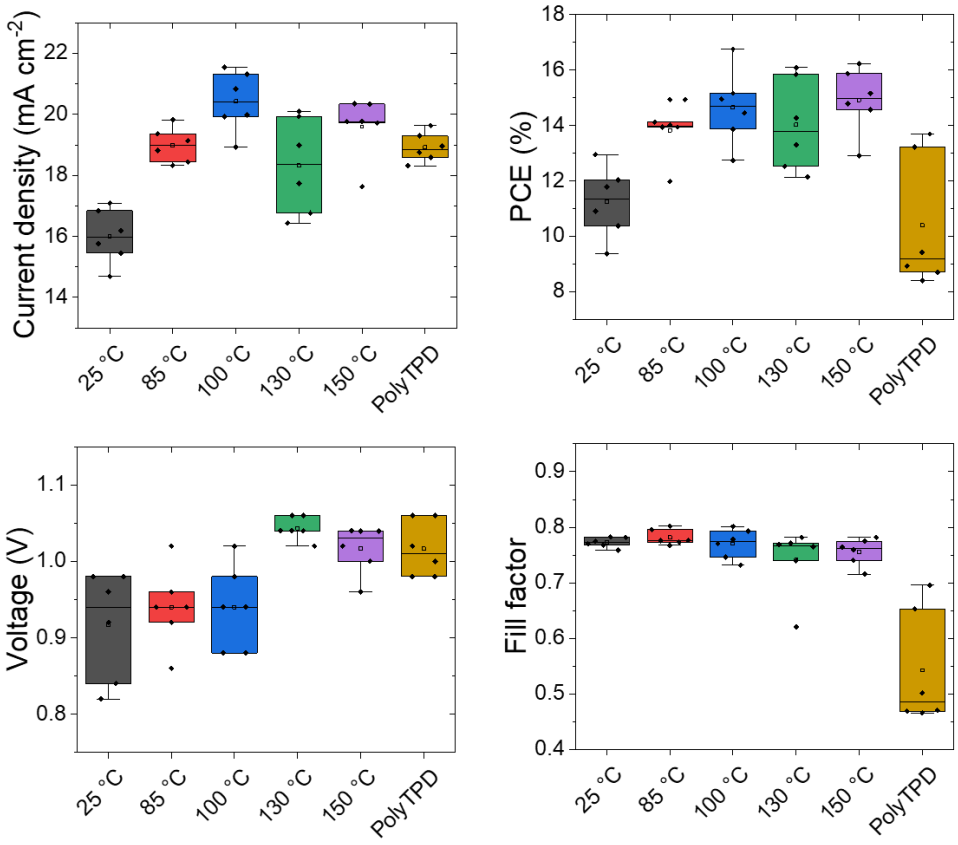

Fig. S4 Comparing the photovoltaic performance of FAMACs devices with different annealing temperature of **CL1-2**. Box-plot of 14 individual devices prepared in 1 batch showing the comparison of the PV parameters (from J-V curves) of devices comprising either PolyTPD or **CL1-2**, where **CL1-2** is annealed at different temperature.

Table S4 Overview statistical analysis of 14 individual FAMACs devices made to optimize the annealing temperature of **CL1-2**.

		J_{sc} (mA cm^{-2})	V_{OC} (V)	FF	PCE (%)
25 °C	Average	16.0 ± 0.9	0.92 ± 0.07	0.77 ± 0.01	11.2 ± 1.3
	Maximum	17.1	0.98	0.78	13.0
100 °C	Average	20.4 ± 1.0	0.94 ± 0.06	0.77 ± 0.03	14.7 ± 1.3
	Maximum	21.5	1.02	0.80	16.8
150 °C	Average	19.6 ± 1.0	1.02 ± 0.03	0.76 ± 0.02	14.9 ± 1.2
	Maximum	20.4	1.04	0.78	16.2
PolyTPD	Average	18.9 ± 0.5	1.02 ± 0.04	0.5 ± 0.1	10 ± 2
	Maximum	19.6	1.06	0.7	13.7

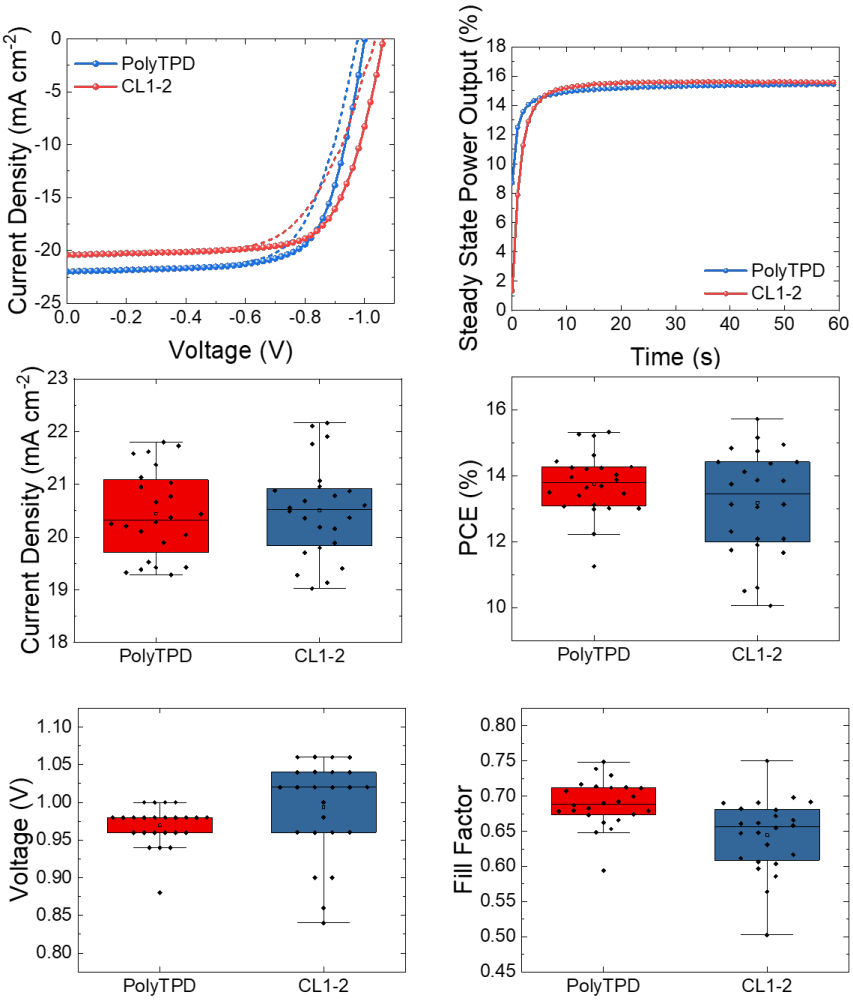

Fig. S5 Comparing the photovoltaic performance of FACs devices with different HTMs. Box-plot of 9 individual devices prepared in 1 batch showing the comparison of the PV parameters (from J-V curves) of devices comprising either PolyTPD or **CL1-2**.

Table S5 Statistics from 9 individual FACs devices.

		J_{sc} (mA cm^{-2})	V_{OC} (V)	FF	PCE (%)
CL1-2	Average	20.5 ± 0.9	0.99 ± 0.06	0.64 ± 0.03	13 ± 2
	Maximum	22.2	1.06	0.75	15.7
PolyTPD	Average	20.4 ± 0.8	0.97 ± 0.03	0.69 ± 0.03	13.8 ± 0.9
	Maximum	21.8	1.00	0.75	15.3

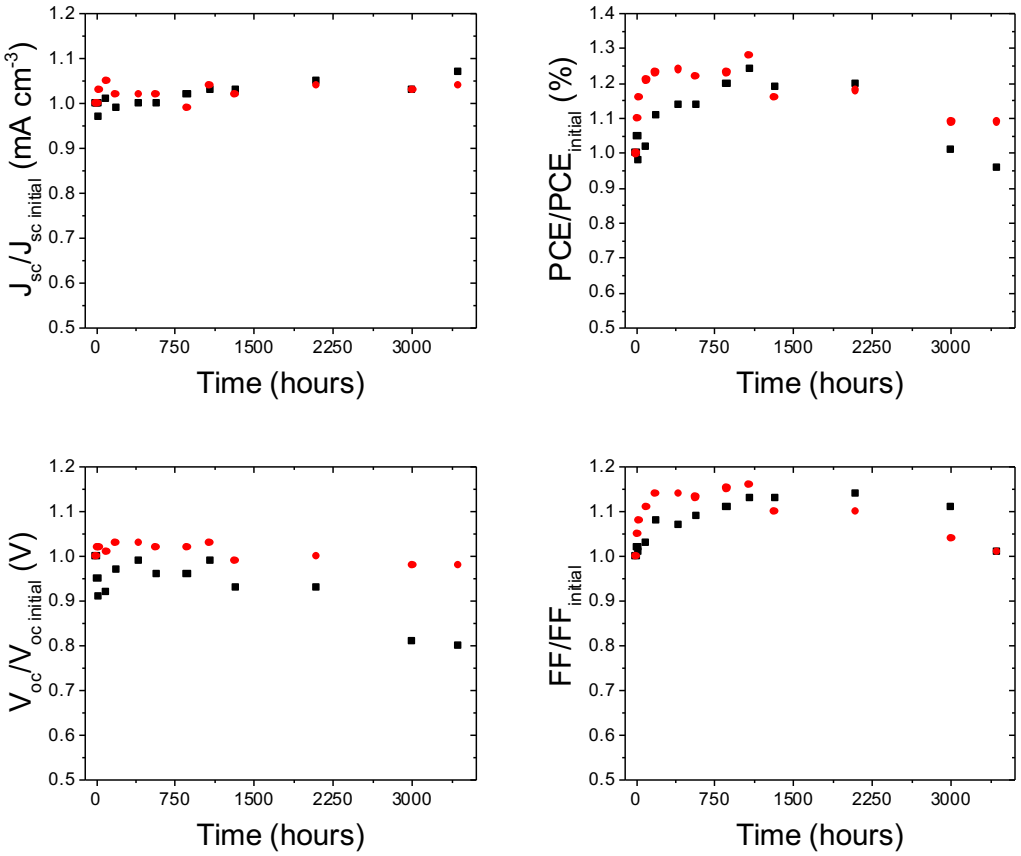

Fig. S6 Temporal evolution of photovoltaic parameters for $Cs_{0.05}(FA_{0.85}MA_{0.15})_{0.95}Pb(I_{0.9}Br_{0.1})_3$ PSCs devices at 85 °C in an oven inside a N_2-filled glovebox without encapsulation (from the same experiment as the stabilized power output data shown in Fig. 5A). Red dots for PolyTPD and black square for **CL1-2** as HTM.

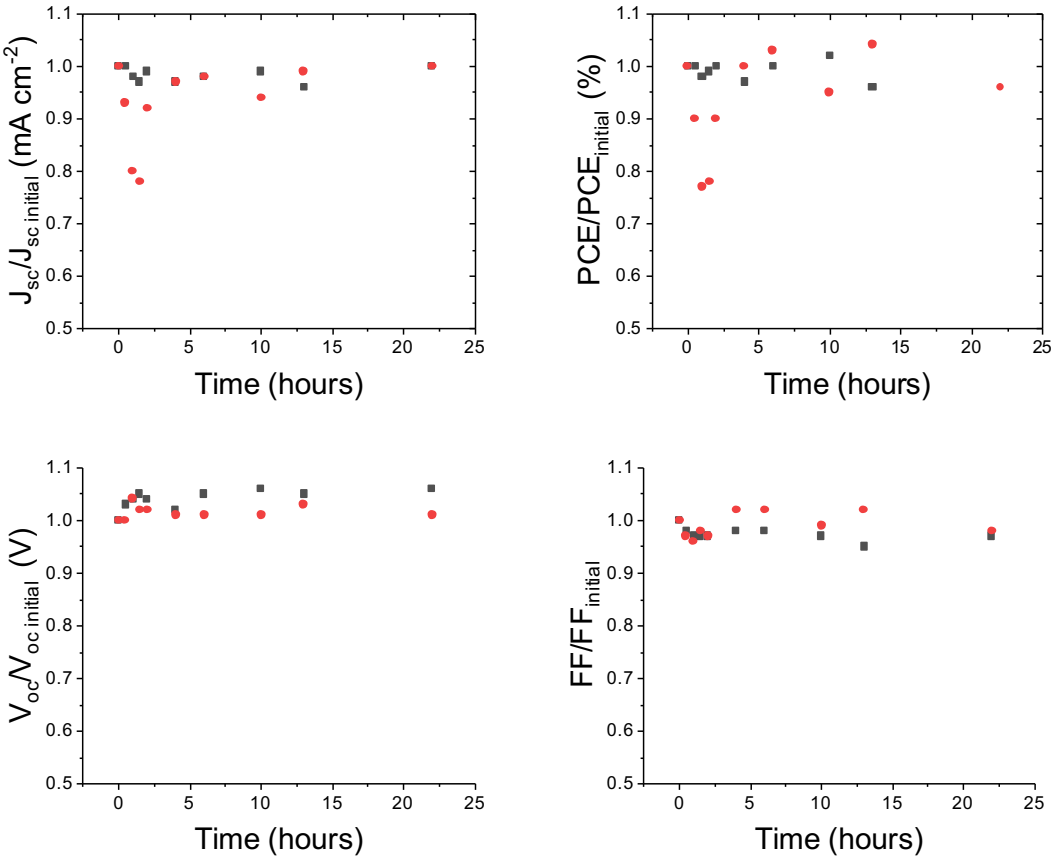

Fig. S7 Temporal evolution of photovoltaic parameters for $Cs_{0.05}(FA_{0.85}MA_{0.15})_{0.95}Pb(I_{0.9}Br_{0.1})_3$ PSCs devices under a UV LED light inside a N_2-filled glovebox without encapsulation (from the same experiment as the stabilized power output and J data shown in Fig. 5B and C). Red dots for PolyTPD and black square for **CL1-2** as HTM.

ANNEXE B: POLYMERIC BIS(DI-*P*-ANISYLAMINO)FLUORENE HOLE-TRANSPORT MATERIALS FOR STABLE N-I-P PEROVSKITE SOLAR CELLS

This project was accomplished with the collaboration of Kelly Schutt, Yadong Zhang, Stephen Barlow, Henry J. Snaith, and Seth R. Marder. Kelly Schutt, in Professor Henry Snaith group, from the Clarendon Laboratory at the University of Oxford, helped with the solar cell characterization and performed most of the half-cell characterization. Yadong Zhang provided the Mo-dopant. Stephen Barlow helped with the data analysis and he helped to write the manuscript. The content of this chapter is unpublished. This work was supported by NSERC (ES. D. Scholarship for MHT), the AFOSR (FA9550-18-1-0499), the Marshall Aid Commemoration Commission, and EPSRC UK.

B.1 Introduction

Proper choice of hole-transport materials (HTM) is key factor for efficient and stable lead-halide perovskite solar cells (PSCs). HTMs are necessary to minimize the charge recombination that would occur at direct perovskite:hole-collecting electrode interfaces. Organic molecules, polymers, metallomacrocycles, and inorganic materials can be used as HTMs in PSCs.[391] One of the widely used HTM in high performance PSCs is spiro-OMeTAD (2,2′,7,7′-tetrakis(di-*p*-anisylamino)-9,9′-spirobi[9*H*-fluorene]). Favorable attributes include its ionization energy (IE), which is well-matched with that of the perovskite absorber layer, easy solution processability, good conductivity (when appropriately doped), electrochemical stability, and high glass-transition temperature. Nevertheless, many studies show that the use of spiro-OMeTAD (with additive/dopants) can limit the stability of PSCs.[422] Crystallization of,[423] photo-oxidation of,[424] and diffusion of electrode metal into[425] spiro-OMeTAD all lead to degradation of the PSC performance. Some of these drawbacks may potentially be addressed by using a polymeric material with similar electronic characteristics to spiro-OMeTAD. Here a polymeric HTM, **P1**, designed to have electronic properties similar to spiro-OMeTAD, and its incorporation in n-i-p PSCs (see Fig. 1) is reported. The polymeric approach was also hypothesized to lead to denser film that could better protect the perovskite underneath and prevent moisture, dopant and electrode metal diffusion.

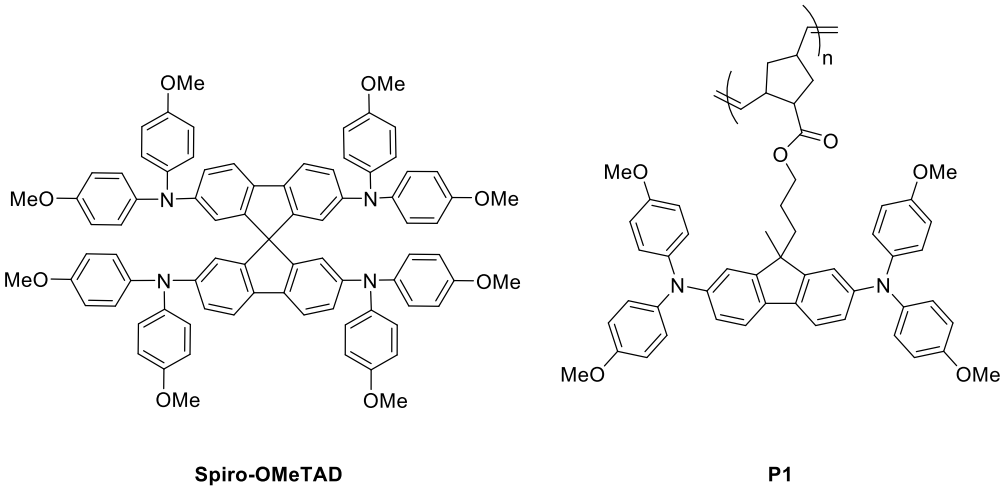

Figure B.1 Structure of the widely used spiro-OMeTAD and the HTM, **P1**, presented here.

B.2 Experimental Procedures

Synthesis

Molybdenum tris(1-(trifluoroacetyl)-2-(trifluoromethyl)ethane-1,2-dithiolene) (Mo(tfd-$COCF_3)_3$) was synthesized according to the literature.[426] 5-Norbornyl Acid Chloride was synthesized according to the literature.[427] Tert-butyl(3-(2,7-diiodo-9-methyl-9H-fluoren-9-yl)propoxy)dimethylsilane was obtained from Girindus and purified by column chromatography (8% ethyl acetate in hexane) prior to the synthesis. Other chemicals were purchased and used without further purification.

9-(3-((tert-butyldimethylsilyl)oxy)propyl)-N2,N2,N7,N7-tetrakis(4-methoxyphenyl)-9-methyl-9H-fluorene-2,7-diamine (1): ^{t}BuOK (1.23 g, 11.21 mmol), (3-(2,7-diiodo-9-methyl-9H-fluoren-9-yl)propoxy) tert-butyldimethylsilane (1 g, 1.78 mmol), and bis(4-methoxyphenyl)amine (2.04 g, 8.9 mmol) were added in a 2 neck round bottom flask. 18 mL of toluene was added, and the solution was deoxygenized. ^{t}Bu$_3$P (0.04 g, 0.178 mmol) and $Pd(OAc)_2$ (0.02 mg, 0.089 mmol) were then added in the solution and heated at 140 °C for 48 h under N_2. The mixture was filtered over celite and washed in DCM. The filtrate was partitioned between water and CH_2Cl_2 and the organic layer was washed with saturated NaCl solution, dried over Na_2SO_4, and evaporated in vacuo. The residue was purified by column chromatography (10% Ethyl acetate in hexane) to obtain a beige oil (714 mg, 54%). ^{1}H NMR ($CDCl_3$, 400 MHz): 7.47 (d, J = 8.2 Hz, 2H), 7.01 (m, 10H), 6.88 (m, 8H), 6.81 (m, 2H), 3.78 (s, 12H), 3.36 (t, J = 6.7 Hz, 2H), 1.82 (m, 2H), 1.30 (s, 3H), 0.90 (s, 3H), 0.83 (s, 9H), 0.04 (s, 6H). ^{13}C{^{1}H} NMR ($CDCl_3$, 100 MHz): δ 155.83, 152.77, 147.61, 141.40, 133.56, 125.92, 120.54, 119.51, 115.92, 114.61, 6.05, 54.81, 50.01, 36.54, 28.15,

26.29, 25.46, 17.90, -5.93. HRMS-ESI (m/z): calcd for $C_{55}H_{54}O_5N_2$ $(M+H)^+$, 806.4078; found, 806.4094. Anal. Calcd for $C_{55}H_{54}O_5N_2$: C, 75.89; H, 7.42; N, 3.47. Found: C, 75.60; H, 7.25; N, 3.42.

3-(2,7-bis(bis(4-methoxyphenyl)amino)-9-methyl-9H-fluoren-9-yl)propan-1-ol (2): **1** (1 g, 1.23 mmol) was dissolved in THF (0.5 mL) and a solution of tetra-n-butylammonium fluoride (1.0 M in THF, 2 mL). The mixture was stirred at room temperature while the reaction was followed by TLC. Upon the disappearance of the protected alcohol, the solution was filtered on a silica gel plug with celite on top. And wash with a 1:1 hexane ethyl acetate solution. The filtrate was poured into a separatory funnel containing 15 mL of water. The product was extracted with dichloromethane (3 x 5 mL). The organic layers were combined and the solvent was removed under reduced pressure. A flash chromatography column was also performed (silica gel, 3-100% ethyl acetate in hexane gradient). The solvent was removed using a rotary evaporator to yield 0.668 g (100%) of a beige powder. ^{1}H NMR ($CDCl_3$, 400 MHz): δ 7.51 (d, J = 8.3Hz, 2H), 7.05 (dt, J = 3.7, 9.0 Hz, 7H), 7.03 (d, J = 2.2 Hz, 2H), 6.90 (dt, J = 2.4, 9.0 Hz, 8H), 6.82 (dd, J = 2.2, 8.3 Hz, 2H), 3.80 (s, 12H), 2.29 (m, 2H), 1.83 (m, 2H), 1.31 (s, 3H), 0.92 (m, 2H). ^{13}C{^{1}H} NMR ($CDCl_3$, 100 MHz): δ 155.8, 152.8, 147.6, 141.4, 133.6, 125.9, 120.4, 119.5, 115.9, 114.6. HRMS-ESI (m/z): calcd for $C_{45}H_{44}O_5N_2$ $(M+H)^+$, 692.3245; found, 692.3231. Anal. Calcd for $C_{45}H_{44}O_5N_2$: C, 78.01; H, 6.40; N, 4.04. Found: C, 75.75; H, 6.42; N, 3.75.

3-(2,7-bis(bis(4-methoxyphenyl)amino)-9-methyl-9H-fluoren-9-yl)propyl (1R,4R)-bicyclo[2.2.1]hept-5-ene-2-carboxylate (**M1**): To a solution of **2** (275 mg, 0.395 mmol) and pyridine (0.1 mL) in 1 mL of dry DCM, a solution of 5-norbornyl acid chloride (150

mg, 0.961 mmol) in 1 mL of dry DCM was added dropwise under an atmosphere of argon. The reaction mixture was stirred overnight at room temperature. After completion by TLC, 10 mL of water was added to the solution and the solution was extracted 3x using DCM. The crude product was purified via flash chromatography using hexanes/EtOAc (9:1 v/v) to yield a beige powder as a mixture of the endo and exo stereoisomers (263 mg, 82%). ^{1}H NMR (Acetone, 700 MHz): δ 7.52 (d, *J* = 8.2 Hz, 2H), 7.05 (m, 10H), 6.90 (m, 8H), 6.83 (dd, *J* = 1.4, 8.2Hz, 2H), 6.10-5.80 (m, 2H), 3.80 (s, 12H), 3.08 (s, 1H), 2.92 (m, 1H), 3.08 (m, 3H), 1.85 (m, 3H), 1.32 (m, 7H), 1.02 (m, 2H). ^{13}C{^{1}H} NMR (Acetone, 175 MHz): δ 174.4, 156.7, 153.3, 153.3, 148.6, 148.6, 142.3, 142.2, 138.2, 134.4, 133.3, 126.8, 126.7, 121.6, 121.5, 120.5, 116.9, 116.7, 115.5, 64.7, 55.7, 50.8, 50.1, 46.4, 43.8, 43.2, 42.3, 37.4, 27.1, 25.0. HRMS-ESI (m/z): calcd for $C_{53}H_{52}O_6N_2$ $(M+H)^+$, 812.3820; found, 812.3797. Anal. Calcd for $C_{53}H_{52}O_6N_2$: C, 78.30; H, 6.45; N, 3.45. Found: C, 77.81; H, 6.46; N, 3.27.

P1: **M1** was dissolved in anhydrous and degazed dichloromethane. Grubbs 2nd generation was added in one scoop to the stirring solution. The solution was stirred at room temperature under nitrogen for 6 h before ethyl vinyl ether was added and stirred for 1 h. The polymer was precipitated in MeOH and recrystallized twice from DCM and MeOH.

Characterization Techniques

Nuclear magnetic resonance (NMR). NMR measurements were conducted with a Bruker Advance IIIHD 500 and a Bruker Advance IIIHD 700 spectrometer operating at 500 MHz and 700 MHz.

Elemental analysis (EA). Elemental analyses for C, H, and N were performed at the Elemental Analysis Service Atlantic Microlab, GA, USA.

Gel permeation chromatography (GPC). Molecular weight and molecular weight distribution were measured by GPC equipped with a Wyatt Dynamic Light Scattering and Viscosity detectors. The GPC was operated at a flow rate of 1 mL min^{-1} with a concentration of 2 mg mL^{-1} in chloroform with 0.025 % triethylamine as a solvent. Polystyrene was used as reference for calibration.

UV−Vis Absorption Spectroscopy. Absorbance spectra were measured with a Carry 5000 UV−vis/NIR spectrometer. For liquid measurement, the samples were dissolved in anhydrous DCM. For solid-state measurement, the samples were prepared by spincoating the HTM on glass substrates.

Fluorescence Spectroscopy. Fluorescence spectra were measured with a Horiba Jobin Yvon Fluorolog 3-2i spectrometer by dissolving the samples in anhydrous DCM.

Cyclic Voltammetry (CV). Cyclic voltammetry experiments were performed using a BAS potentiostat with a glassy carbon working electrode, platinum counter electrode and an Ag wire reference electrode at a scan rate of 100 mV s^{-1}. Anhydrous and degassed dichloromethane solutions containing 0.1 M of tetrabutylammonium hexafluorophosphate as electrolyte was used to dissolve **1** (10^{-3} M). Ferrocene was used as the reference.

Differential scanning microscopy (DSC). DSC spectra were measured using a TA Instruments Q200 Differential Scanning Calorimeter and run in the range of 25-200 °C, in nitrogen flow at 5 °C min^{-1} heating rate.

Thermogravimetric analysis (TGA). TGA spectra were measured using a Perkin Elmer Pyris 1 Thermogravimetric Analyzer at 10 °C min^{-1} heating rate and at 20 mL min^{-1} air flow rate.

Scanning electron microscope. SEM images were measured using a FEI Sirion scanning electron microscope at an acceleration voltage of 5 kV.

Current−Voltage Measurements. The *JV* curves were measured (2400 Series SourceMeter, Keithley Instruments) under simulated AM 1.5 G sunlight at 100 mW cm^{-2} irradiance generated by an Abet Class AAB sun 2000 simulator, with the intensity calibrated with an NREL calibrated KG 5 filtered Si reference cell. The forward *J–V* scans were measured from forward bias to short circuit and the backward scans were from short circuit to forward bias, both at a scan rate of 380 mV s^{-1}. A stabilization time of 5 s at forward bias of 0 V under illumination was done prior to scanning.

Powder X-ray Diffraction

XRD spectra were measured using a Panalytical X'pert powder diffractometer with Cu anode X-ray source.

Device fabrication

Substrate Preparation. Fluorine doped tin oxide (FTO) (Pilkington TEC 7) or indium tin oxides (ITO) (Shenzhen Display, < 10 ohm cm^{-2}) coated glass substrates were used in this experiment. FTO or ITO substrates were etched at specific regions using a 2 M HCl and zinc powder. Substrates were then cleaned with water, then sequentially sonicated for 5

min in acetone, isopropyl alcohol and water, and dried with a compressed nitrogen gun. Next, the substrates were treated for 5 min in oxygen plasma.

Electrode Evaporation. An 100 nm silver electrode was thermally evaporated under vacuum.

SnO_2 nanocrystal. We selected a planar SnO_2 nanocrystal deposition procedure that gives us lower power conversion efficiency than SnO_2 chemical bath, but allows the fabrication of devices in a shorter time without requiring high heat or high energy. SnO_2 colloidal precursor (15% in H_2O dispersion) was purchased from Alfa Aesar and diluted in DI water to 2.7% concentration before use. The dispersion was spin coated onto plasma cleaned FTO substrates at 4000 rpm for 30 s, and then annealed in ambient conditions at 150 °C for 30 min. The SnO_2 films were treated with UV ozone for 10 min immediately prior to perovskite deposition

$Cs_{0.05}FA_{0.95}Pb(I_{0.83}Br_{0.17})_3$ Perovskite. The precursor solution was prepared by dissolving the precursors in anhydrous *N,N*-dimethylformamide and dimethylsulfoxide in a ratio 4:1 in a nitrogen-filled glovebox to obtain a stoichiometric 1.5 M solution. 150 µL of the precursor perovskite solution was spin-coated in a drybox at 1000 rpm for 10 s and then 6000 rpm for 35 s with a ramp of 2000 rpm s^{-1}. After 35 s, 400 µL of toluene was quickly added on the spinning substrates. The films were dried on a hot plate at a temperature of 100 °C for 10 min.

PEA-I passivation layer. To improve the performance of solar cells, the devices with both P1 and spiro-OMeTAD were further passivated with PEAI by spin coating a solution of 1

mg/mL in IPA at 1000 rpm for 10 s prior to HTM deposition. No additional annealing was performed after depositing PEAI.

Mo(tfd-COCF$_3$)$_3$ Doped P1. A 46 mg mL^{-1} solution of **P1** was prepared in dichlorobenzene in a nitrogen-filled glovebox. The solution was stirred 2 h at 70 °C. Mo(tfd-COCF$_3$)$_3$ in dichlorobenzene (15 mg mL^{-1}) was added accordingly to the molar ratio needed to the polymer solution. Dichlorobenzene was added to adjust the concentration needed. The solution was spin-coated on the perovskite layer at 2500 rpm, 2500 rpm s^{-1} for 45 s in a nitrogen-filled glovebox. The films were dried for 5 minutes at 70 °C.

Li-TFSI Doped P1 or Spiro-OMeTAD. A 85 mg mL^{-1} solution of HTM was prepared in dichlorobenzene in a nitrogen-filled glovebox. The solution was stirred 2h at 70 °C. Li-TFSI in acetonitrile (500 mg mL^{-1}) and tert-butylpyridine were added accordingly to the molar ratio needed to the polymer solution. Dichlorobenzene was added to adjust the concentration needed. The solution was spin-coated on the perovskite layer at 2500 rpm, 2500 rpm s^{-1} for 45 s in a nitrogen-filled glovebox.

B.3 Results and Discussion

Synthesis

Attaching one polymerizable group to the symmetrical spiro-OMeTAD was anticipated to be synthetically complex. However, the role of the spiro-linkage in spiro-OMeTAD is largely to ensure a high glass-transition temperature, which, in a polymer, can be largely compensated for by an appropriate polymer backbone. Furthermore, the electrochemical and optical properties are primarily determined by the two bis(di-*p*-anisylamino)fluorene "arms" of the structure.[428] Thus, we chose to use a bis(di-*p*-anisylamino)fluorene building block, the 9-position of the fluorene providing an ideal site for introduction of a single polymerizable group, as in some of our previous work on bis(diarylamino)fluorene[409] and di(carbazolyl)fluorene[429] side-chain norbornene polymers as hole-transport and host materials for organic light-emitting diodes.

The synthesis of the hole-transporting monomer **M1** was carried out as followed. First, bis(4-methoxyphenyl)amine and protected-hydroxyl-functionalized 2,7-diiodofluorene were converted to **2** using a Buchwald and Hartwig coupling.[430, 431] The silyl ether **2** was deprotected to the hydroxyl-functionalized bis(diarylamino)fluorene **3** using tetra-n-butylammonium fluoride in tetrahydrofuran. The deprotonation of the alcohol with sodium hydride, followed by an esterification reaction with 5-norbornyl acid chloride, gave a mixture of endo/exo monomer **M1**. **P1** was successfully synthesized using the Grubbs 2nd generation initiator (see Fig. 2). The polymer was soluble in a range of organic solvents including THF, chloroform, dichloromethane, and dichlorobenzene. A broadening of the ^{1}H NMR peaks was observed, consistent with the formation of a polymer. Moreover, an

appreciable downfield chemical shift corresponding to the norbornene alkene protons was observed in the ^{1}H NMR spectrum of the polymer.

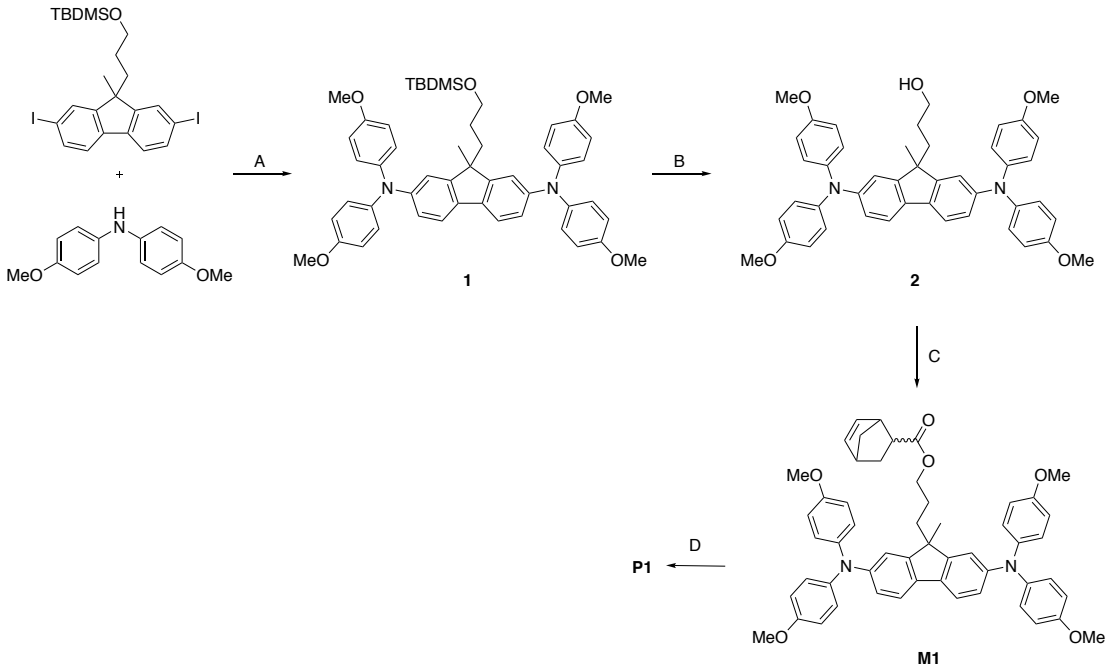

Figure B.2 Synthesis of hole-transporting polymer **P1**. (A) $Pb(OAc)_2$, P^tBu_3, Cs_2CO_3, toluene, (B) $^nBu_4NF$, THF, (C) pyridine, CH_2Cl_2, endo/exo 5-norbornyl acid chloride, (D) 2nd generation Grubbs initiator.

Characterization of HTM

P1 has similar optical properties to spiro-OMeTAD (see Fig. 3B, Table 1). Electrochemical measurements on the monomer M1 in CH_2Cl_2/0.1 M Bu_4NPF_6 indicate two successive reversible oxidations at +0.57 V and +0.87 V vs $FeCp^*_2{}^{+/0}$ (Cp^* = h^5-C_5Me_5; see Fig. 3A), from which a solid-state IE of 4.8 eV can be estimated, similar to that of spiro-OMeTAD.

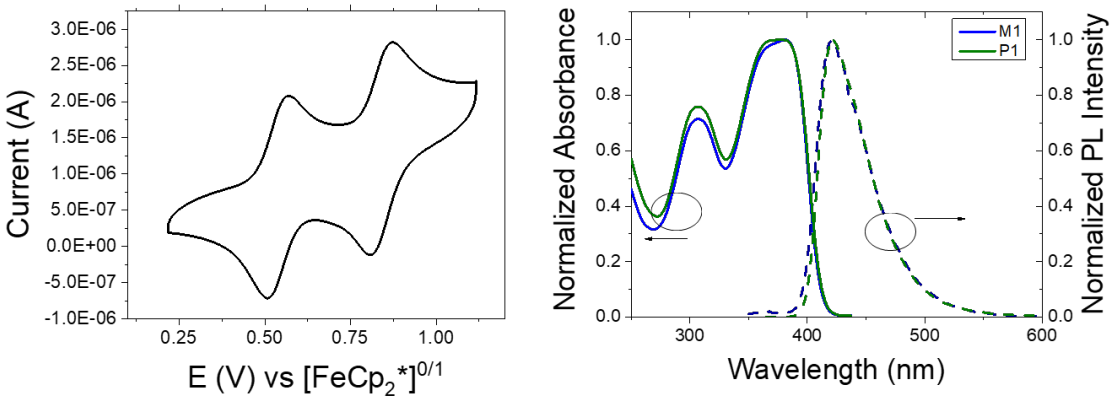

Figure B.3 (A) Cyclic voltammograms of **M1** in CH_2Cl_2 with $TBAPF_6$ (0.1 M) as an electrolyte with $FeCp^{*2+/0}$ where Cp* is C_5Me_5. (B) Normalized UV-vis and photoluminescence spectrum of **M1** and **P1** in anhydrous CH_2Cl_2.

Table B.1 Physical properties of the synthesized materials.

	λ_{abs} (nm) [a]	λ_{fluo} (nm) [a, b]	IE (eV) [c]	EA (eV) [d]	E_g (eV) [e]
M1	307, 366, 381	422	4.8	1.7	3.07
P1	301, 375[f]	422	-	-	3.06
Spiro-OMeTAD	306, 386	423	4.8	1.8	2.98

[a] The spectra were measured in CH_2Cl_2. [b] Measured at 0.1 absorbance. [c] Estimated using the equation IE (eV) = 4.8 + $E_{½}^{+/0}$ (V), where the $E_{½}^{+/0}$ is relative to $FeCp_2^{+/0}$. [d] Estimated from EA = IE – $E_{opt, gap}$. [e] Optical gap calculated using the crossing of normalized absorbance and fluorescence spectra. [f] The differences in maxima reported for **M1** and **P1** are due to minor changes in peak shape; the overall absorption profiles are very similar (see Fig. 3B).

Li-TFSI (50 mol%) and tert-butylpyridine (tBP) (330 mol%) are often used as additives to spiro-OMeTAD and result in p-doping upon exposure to air. Due to the hygroscopic behavior of the Li-TFSI/tBP dopant, other dopants have been tried, including Mo(tfd-$COCF_3$)$_3$, which was used as a dopant for spiro-OMeTAD in n-i-p devices in which no additive was needed, resulting in higher stability.[432] As expected from the similar redox potentials for spiro-OMeTAD and **P1**, optical absorption measurements upon addition of Li-TFSI/tBP or Mo(tfd-$COCF_3$)$_3$ to a solution containing **P1** (see Fig.4) show the growth of new peaks consistent with a bis(diarylamino)fluorene radical cation.

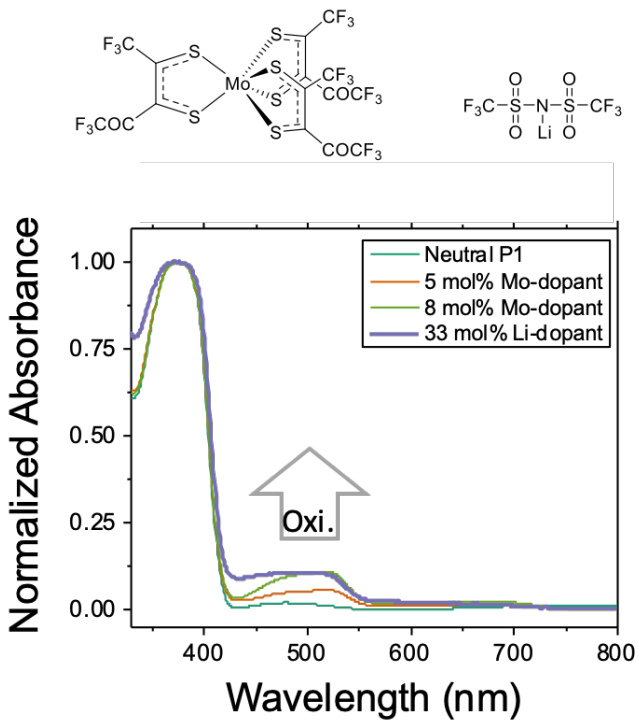

Figure B.4 Chemical structure of Mo(tfd-$COCF_3$)$_3$ and Li-TFSI. Doping of **P1** with Mo(tfd-$COCF_3$)$_3$ (taken at t = 0 h) and Li-TFSI/tBP (taken at t = 24 h) in CH_2Cl_2. The weak absorption seen between 600 and 700 nm for the Mo(tfd-$COCF_3$)$_3$-doped samples is attributable to Mo(tfd-$COCF_3$)$_3$.[433]

Half-devices optical characterization

We aimed to characterize and compare the optical properties of the half devices. The Li-TFSI/tBP doped **P1** and spiro-OMeTAD films spin-coated on top of perovskite film on clean glass showed similar PL quenching (PLQE = 0.02 in each case) compared to that of the bare perovskite film (PLQE = 0.28) suggesting comparable losses due to non-radiative recombination at the perovskite/HTM interface, likely related to their similar structures and optical properties.

Deposition of some molecules with Lewis basic substituents on top of the perovskite has been suggested to passivate defects.[387, 415-417] Several studies, including ours, have found esters can play a useful role in perovskite growth and/or passivation. The added ester

moieties on the polymer could potentially bind to any undercoordinated lead ions at the surface, effectively screening the charge and reducing recombination. Photoluminescence (PL) lifetime experiments on films of perovskite in contact with doped **P1** or spiro-OMeTAD (see Fig. 5) are consistent with this idea; the former exhibit longer lifetimes associated with bimolecular recombination. Moreover, the PL peak of **P1** containing film is blue-shifted compared to the spiro-OMeTAD one, which also suggests that there is passivation of trap states at the interface between the HTM and perovskite layers.

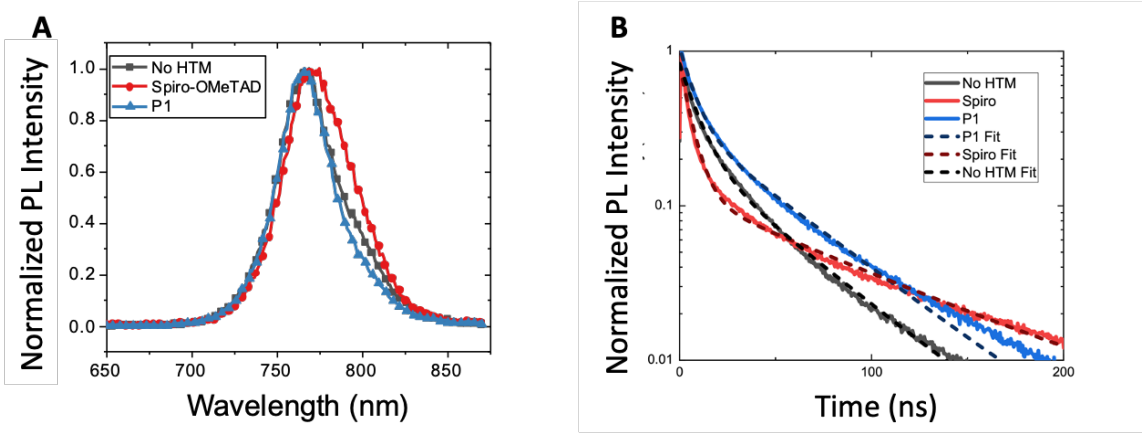

Figure B.5 (A) Photoluminescence of the glass/perovskite/HTM half devices. The PL maximum for the spiro-OMeTAD sample is slightly red-shifted relative to that of the **P1** and the bare perovskite sample, which may indicate more band-bending due to shallow-trap formation in the spiro-OMeTAD case.[7,8] (B) Fitting of the time-resolved PL of the glass/perovskite/HTM half devices.

Half-device stability studies

In addition to possibly passivating the perovskite, it was hypothesized that the polymer could also better protect the perovskite from extrinsic factors (such as moisture or oxygen penetration) compared to the small spiro-OMeTAD molecule.[434, 435] In order to probe if the polymer **P1** could improve the stability of the solar cells, we fabricated half-cells with the architecture FTO/perovskite/HTMs (undoped) and heated them in an aging box

(conditions: 85 °C, 76 mW cm^{-2}, 50% relative humidity). We measured the PXRD of the half-cells over time by periodically moving the films to ambient conditions for the time of measurement (see Fig. 6A-B). After 20 h, the bare perovskite film no longer shows the (110) peak of the 3D perovskite at ~14°, while the **P1**- and spiro-OMeTAD-coated films retained 50% and 25% of the peak intensity respectively, clearly showing the advantage of using a polymeric analogue. We also followed the decomposition of the perovskite by UV-vis spectroscopy (see Fig. 6C-D). After 48h in the aging box, the spiro-OMeTAD containing film turned gray and no longer shows a discernable onset of absorption at the perovskite band gap at ~775 nm, while for the **P1** containing film, we can still observe this feature.

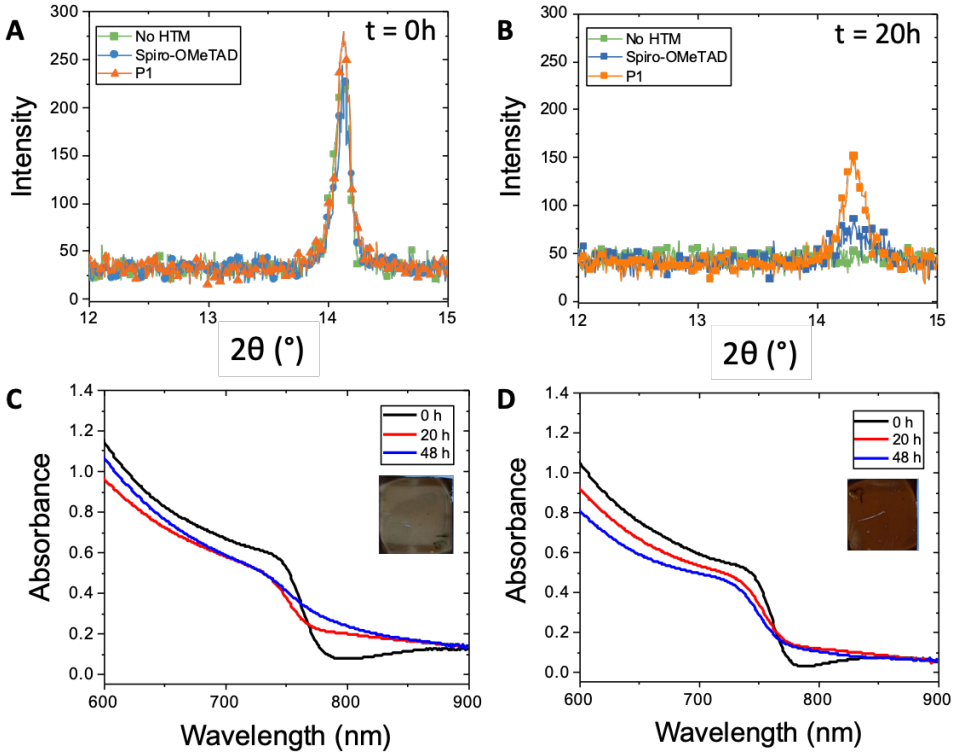

Figure B.6 Stability study of the glass/perovskite/HTM half devices. PXRD of the films without thermal stress (A) and after 20 h in an aging box (conditions: 85 °C, 76 mW cm^{-2}, 50% relative humidity) (B).

Absorbance of time under stress in the aging box for (C) spiro-OMeTAD and (D) **P1** as the HTM. Onset: picture of the film after 48 h in the aging box.

Device fabrication and characterization

We investigated the performance of the new HTM **P1** in n-i-p PSCs using the following architecture; FTO/SnO_2/$FA_{0.85}Cs_{0.15}Pb(I_{0.83}Br_{0.17})_3$/PEA-I/p-doped HTM/Ag, where FTO = fluorine-doped tin oxide, FA = formamidinium, HTM is spiro-OMeTAD or **P1** and PEA-I is phenylethylammonium iodide, a known passivating agent.[66] The devices using p-doped **P1** in its optimal condition (see Supporting Information for optimization of PEA-I, Li-TFSI, **P1** and tBP concentration, Fig. S1-4 and Table S1-4) are reported in Fig. 6 and Table 2. We obtained a champion PCE of 15.5% for Li-TFSI-doped devices, which is similar to that for the control devices with doped spiro-OMeTAD (16.5%) (see Table S2). The current density−voltage (J−V) characteristics of the best performing devices using Li-TFSI-doped spiro-OMeTAD and **P1** recorded under simulated AM1.5, 1 sun irradiance are presented in Fig. 7. As it can be seen from **Error! Reference source not found.**, **P1** and s piro-OMeTAD have similar performance with the averaged performance of **P1** being slightly higher compared to spiro-OMeTAD. The reduced spread in the data also shows improved reproducibility over spiro-OMeTAD, which has previously been shown to form films with poor uniformity and visible "comets" that appear during spin coating.[417] Furthermore, the improved thermal and atmospheric stability of half devices with **P1** suggests that the lifetime power output for devices based on **P1** may be greater than those with spiro-OMeTAD.

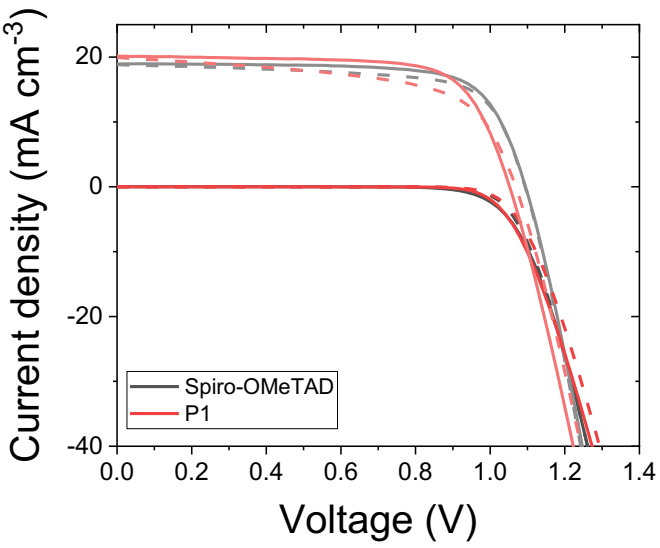

Figure B.7 Comparison of the JV curves of the champion cells obtained for Li-TFSI-doped **P1** and spiro-OMeTAD HTMs under 1 sun and in the dark.

Table B.2 Basic parameters for the champion n-i-p cell prepared with the two HTMs p-doped using Li-TFSI and tBP.

HTM		**PCE (%)**	**J_{sc} (mA cm^{-2})**	**V_{oc} (V)**	**FF**
Spiro-OMeTAD	Average	14 ± 2	18 ± 1	1.06 ± 0.02	0.69 ± 0.03
	Maximum	16.5	19.8	1.10	0.75
P1	Average	14.6 ± 0.9	19.3 ± 0.8	1.05 ± 0.01	0.71 ± 0.02
	Maximum	15.5	20.1	1.06	0.73

Using spiro-OMeTAD ca. 1.5x more material (85 mg mL^{-1} vs. 55 mg mL^{-1} for **P1**) is needed to obtain similar photovoltaic performance. The thickness of an optimal **P1** layer was approximately half that of an optimal spiro-OMeTAD layer (~100 nm vs. 200 nm as determined by profilometry). Both **P1** and spiro-OMeTAD films have visible "comets", as is typical for spiro-OMeTAD films. Careful optimization of Li-TFSI and tBP helps to decrease the density of pinholes (see Fig. 8) and to reach optimal device performance. For **P1**, the optimal Li-TFSI dopant concentration is 25 mol%, while spiro-OMeTAD is 50 mol%, which in both cases corresponding to oxidation of half of the bis(diarylamino)fluorene units. Moreover, PSCs made with **P1** p-doped using Mo(tfd-

$COCF_3)_3$ (see Fig. S5 and Table S5) were fabricated and achieved similar PCE (14.3 ± 0.9%).

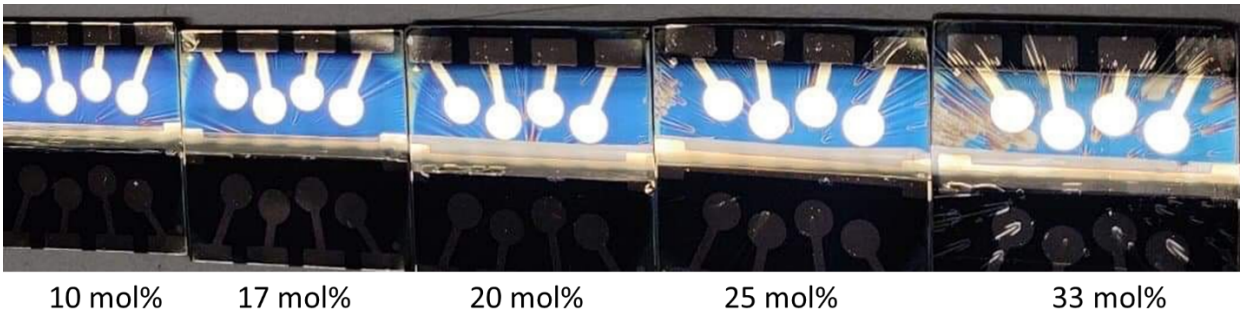

Figure B.8 Optimization of the *t*BP concentration. The lower concentration solution lead to a lower density of pinholes, but poorer photovoltaic performance.

B.4 Conclusion

In summary, a description of the use of a polymeric HTM analogue to spiro-OMeTAD in n-i-p PSCs is reported. n-i-p PSCs using **P1** exhibit PCE as high as 15.5% which is similar to the PSC using the widely used HTM spiro-OMeTAD in the same conditions. Half-device stability under harsh conditions is also significantly improved when using **P1**, suggesting that it is a promising candidate for single junction and tandem solar cells.

B.5 Supporting Information

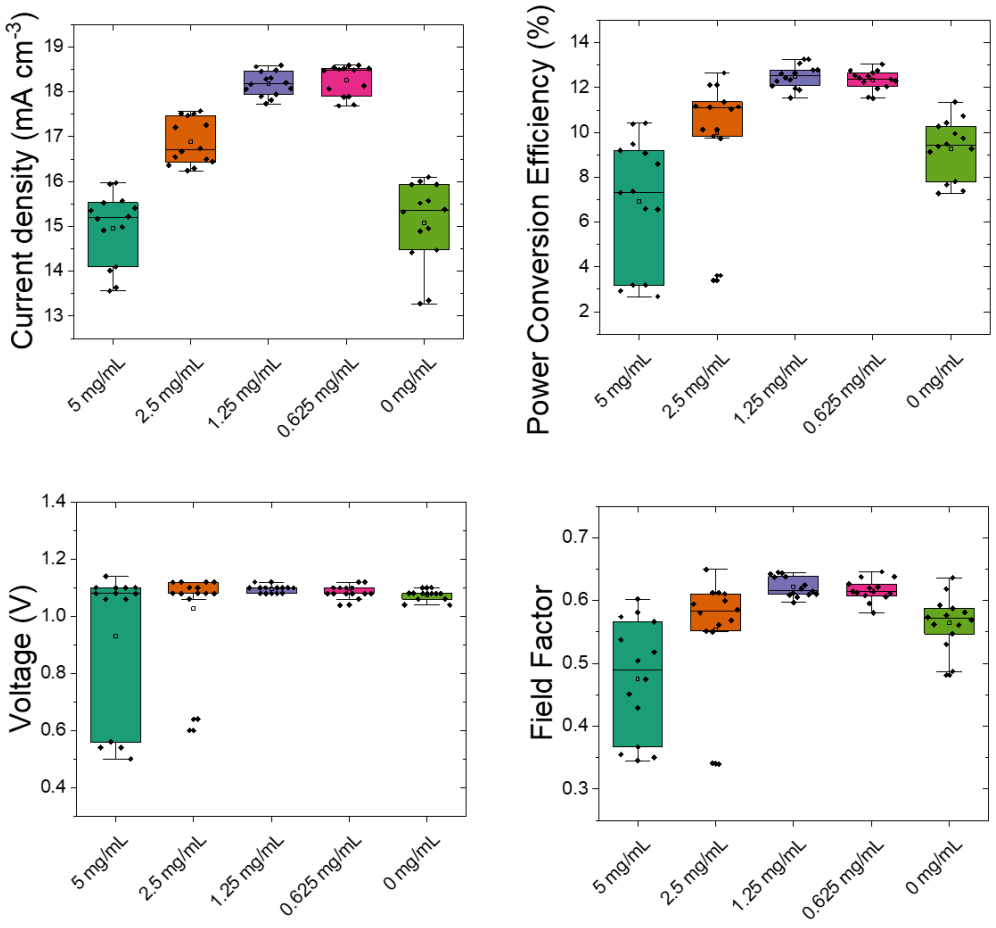

Fig. S1 Comparing the photovoltaic performance of FACs devices with different amount of PEA-I passivator. Box-plot of devices prepared in 1 batch showing the comparison of the PV parameters (from J-V curves) of devices at different PEA-I concentration.

Table S1 Statistics for individual FACs devices made to optimize PEA-I concentration when **P1** is used as HTM (HTM concentration = 55 mg mL^{-1}).

Concentration PEA-I		J_{sc} (mA cm^{-2})	V_{OC} (V)	FF	PCE (%)
-	Average	15.1 ± 0.9	1.07 ± 0.02	0.56 ± 0.04	9 ± 1
	Maximum	16.1	1.1	0.64	11.4
1.25 mg/mL	Average	18.2 ± 0.3	1.10 ± 0.01	0.62 ± 0.01	12.5 ± 0.5
	Maximum	18.6	1.12	0.65	13.3

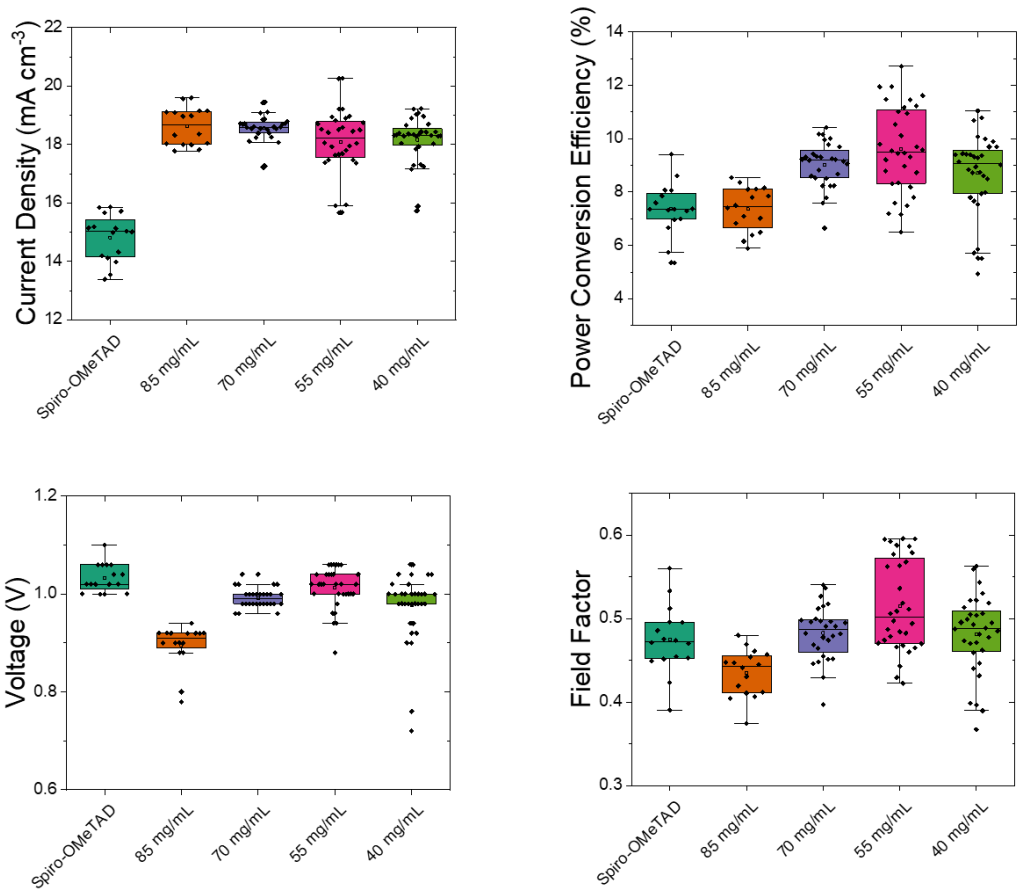

Fig. S2 Comparing the photovoltaic performance of FACs devices with different **P1** concentration used to cast 33 mol% Li-doped, 220 mol% *t*BP **P1** films. Box-plot of 16 individual devices for Spiro-OMeTAD and 32 devices for **P1** prepared in 1 batches showing the comparison of the PV parameters (from J-V curves) of devices comprising either Spiro-OMeTAD or **P1** at different concentration as HTM.

Table S2 Statistics for individual FACs devices made to optimize **P1** concentration used to cast 33 mol% Li-doped, 220 mol% *t*BP **P1** films.

HTM		J_{sc} (mA cm^{-2})	V_{OC} (V)	FF	PCE (%)
Spiro-OMeTAD reference	Average	14.8 ± 0.8	1.03 ± 0.03	0.47 ± 0.04	7.4 ± 1.0
	Maximum	15.9	1.1	0.56	9.40
P1 55 mg/mL	Average	18 ± 1	1.01 ± 0.04	0.51 ± 0.05	10 ± 2
	Maximum	20.3	1.06	0.60	12.71

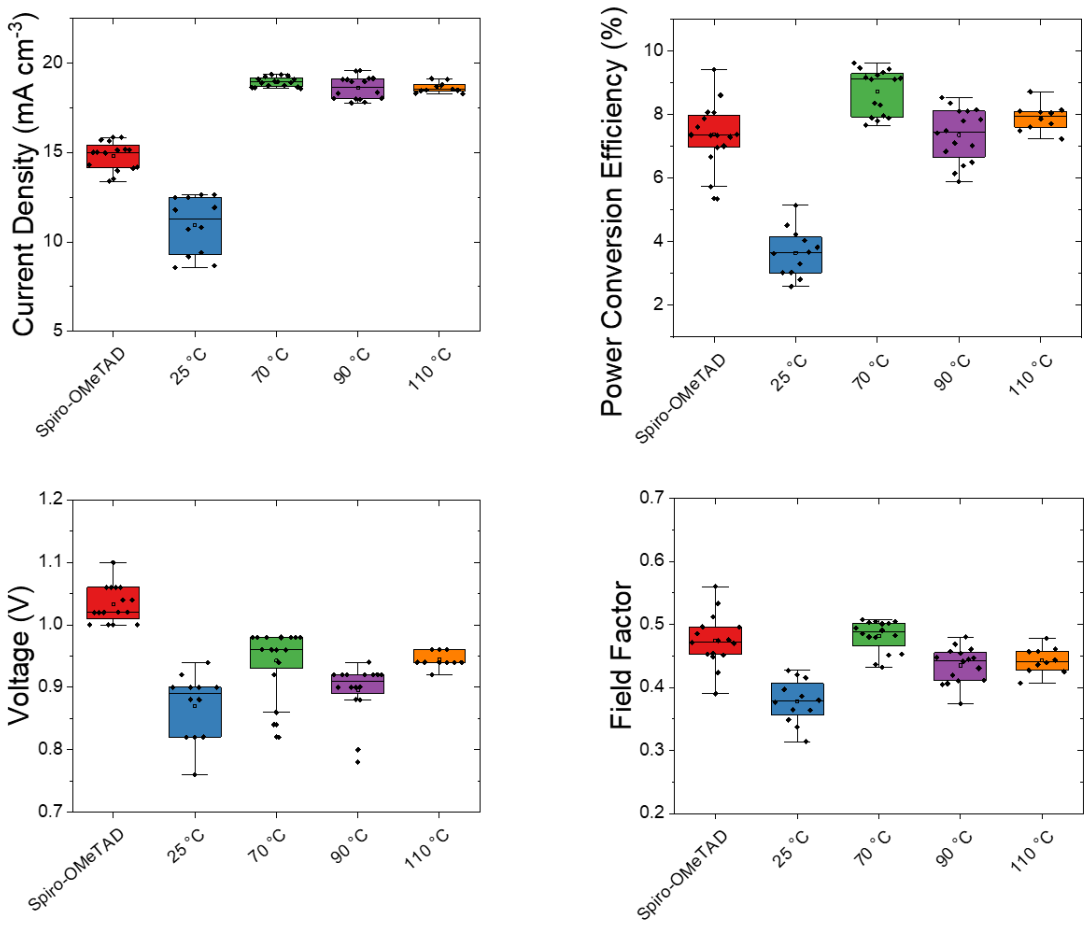

Fig. S3 Comparing the photovoltaic performance of FACs devices with different **P1** solution's temperature used to cast 85 mg/mL, 33 mol% Li-doped, 220 mol% *t*BP **P1** films. Box-plot of 16 individual devices prepared in 1 batches showing the comparison of the PV parameters (from J-V curves) of devices comprising either Spiro-OMeTAD or **P1** spun at different temperature as HTM.

Table S3 Statistics for individual FACs devices made to optimize **P1** temperature deposition used to cast 85 mg/mL, 33 mol% Li-doped, 220 mol% *t*BP **P1** films.

HTM		J_{sc} (mA cm^{-2})	V_{OC} (V)	FF	PCE (%)
Spiro-OMeTAD reference	Average	14.8 ± 0.8	1.03 ± 0.03	0.47 ± 0.04	7.4 ± 1.0
	Maximum	15.9	1.1	0.56	9.41
P1 70 °C	Average	19.0 ± 0.3	0.94 ± 0.05	0.48 ± 0.03	8.7 ± 0.7
	Maximum	19.4	1.0	0.51	9.63

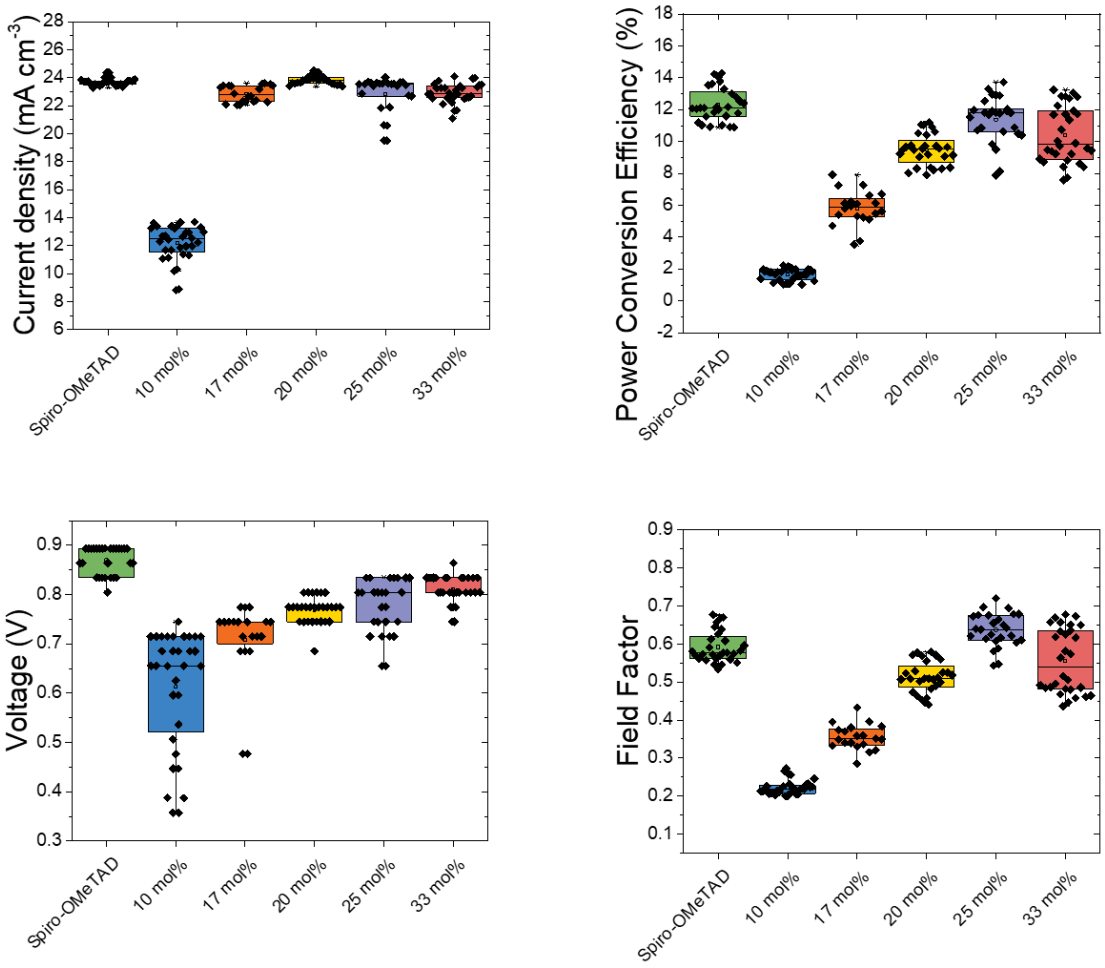

Fig. S4 Comparing the photovoltaic performance of FACs devices with different Li-TFSI concentration used to cast 85 mg/mL, 220 mol% *t*BP **P1** films. Box-plot of 26 individual devices prepared in 1 batches showing the comparison of the PV parameters (from J-V curves) of devices comprising either Spiro-OMeTAD or **P1** at different dopant concentration.

Table S4 Statistics for individual FACs devices made to optimize **P1** Li-TFSI p-dopant concentration when **P1** is used as HTM (HTM concentration = 85 mg/mL, *t*BP concentration = 220 mol%).

HTM		J_{sc} (mA cm^{-2})	V_{OC} (V)	FF	PCE (%)
Spiro-OMeTAD reference	Average	23.7 ± 0.3	0.87 ± 0.03	0.59 ± 0.04	12 ± 1
	Maximum	24.4	0.90	0.68	14.3
P1 25 mol% Li-TFSI	Average	23 ± 1	0.78 ± 0.06	0.64 ± 0.04	11 ± 1
	Maximum	24.0	0.83	0.72	13.7

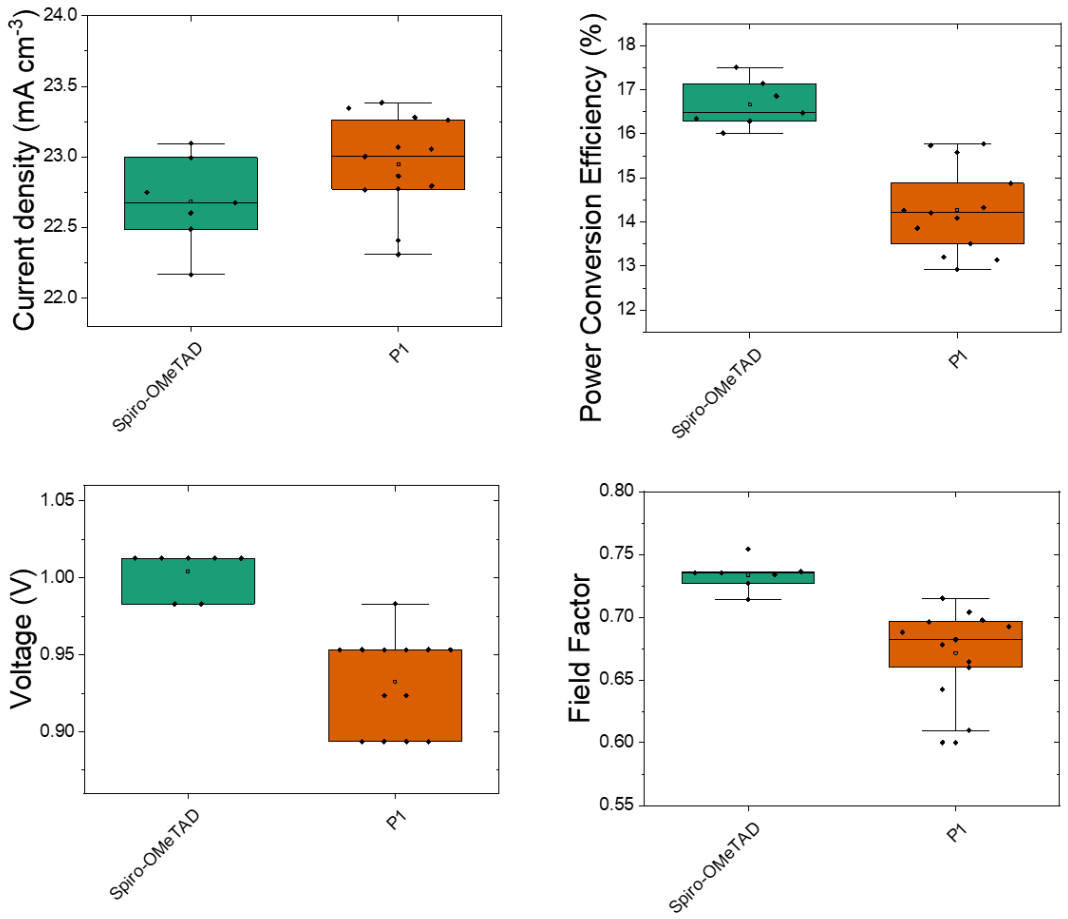

Fig. S5 Comparing the photovoltaic performance of FACs devices with Mo(tfd-$COCF_3$)$_3$ dopant. Box-plot of 13 individual devices prepared in 1 batches showing the comparison of the PV parameters (from J-V curves) of devices comprising either Mo-doped Spiro-OMeTAD or **P1**. Note that the **P1** devices were not fully optimized and this experiment is to present that **P1** devices could be made using another dopant.

Table S5 Statistics for individual FACs devices made with Mo(tfd-$COCF_3$)$_3$ p-dopant when **P1** and Spiro-OMeTAD are used as HTM (HTM concentration = 85 mg/mL).

HTM		J_{sc} (mA cm^{-2})	V_{OC} (V)	FF	PCE (%)
Spiro-OMeTAD Mo-doped	Average	22.7 ± 0.3	1.00 ± 0.01	0.73 ± 0.01	16.7 ± 0.5
	Maximum	23.1	1.01	0.75	17.5
P1 Mo-doped	Average	23.0 ± 0.3	0.93 ± 0.03	0.67 ± 0.04	14.3 ± 0.9
	Maximum	23.4	0.98	0.72	15.8

ANNEXE C: THERMO-CROSSLINKABLE POLYMERIC ELECTRON TRANSPORT MATERIAL ANALOGUE TO PCBM FOR P-I-N PEROVSKITE SOLAR CELLS

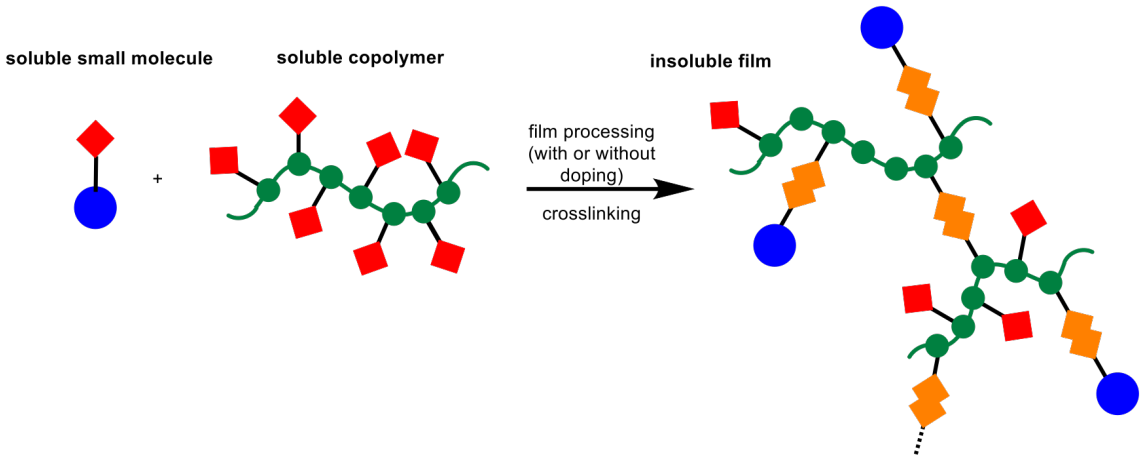

This project was accomplished with the collaboration of Kelly Schutt, Thorsten Schultz, Berthold Wegner, Federico Pulvirenti, Yadong Zhang, Elena Longhi, Raghunath R. Dasari, Xiaojia Jia, Bernard Kippelen, Norbert Koch, Stephen Barlow, Henry J. Snaith, and Seth R. Marder. Kelly Schutt, in Professor Henry Snaith group, from the Clarendon Laboratory at the University of Oxford, helped with the solar cell characterization and performed most of the half-cell characterization. Thorsten Schultz and Berthold Wegner, in the group of Norbert Koch from the Humboldt-Universität zu Berlin, performed the UPS and XPS experiment. Federico Pulvirenti and Yadong Zhang prepared the polymer studied here. Elena Longhi provided the Ir dopant. Raghunath R. Dasari provided the PCBCB. Xiaojia Jia, in Bernard Kippelen group, performed the ellipsometry and conductivity measurement. Stephen Barlow helped with the data analysis and he helped to write the manuscript. The content of this chapter is unpublished in peer review journal. Since this project is the

continuity of Dr Federico Pulvirenti work, the content for the synthesis of the crosslinker and the doping studies (absorption, conductivity, UPS and XPS) are published in his doctoral thesis. This work was supported by NSERC (ES. D. Scholarship for MHT), the AFOSR (FA9550B15B0115 and A9550-18-1-04999), the NSF (DMR-1729737), the Marshall Aid Commemoration Commission, and EPSRC UK.

C.1 Introduction

Hybrid organic-inorganic perovskites have been extensively studied as the absorber layer in solar cells due to their high visible absorption, tunable band gap, and long carrier diffusion length.[1, 254, 436-439] Despite their impressive performance, perovskite solar cells (PSC) still lack long term stability. The diffusion of dopant ions, iodide ions and metal ions originating from the electrodes are all known to be significant degradation pathways.[440-443]

Electron transport materials (ETM) play a crucial role in PSCs by reducing the charge recombination that occurs at direct perovskite:electron-collecting electrode interfaces. Fullerene derivatives work well in PSCs due to the favorable alignment of their electron affinities with the conduction band of perovskite absorbers. The synthesis of an analogue ETM to the widely used PCBM ([6,6]-phenyl-C_{60}-butyric methyl ester) is reported, where the methyl group is replaced by a benzocyclobutene moiety (BCB), a thermally-activated cross-linker which can be insolubilized at a temperature as low as 150 °C to form fullerene oligomers $(PCBCB)_n$. Chemical modification of the ETM with cross-linking substituents, which enables the formation of new bonds between individual molecules or polymer units, is an effective approach to increase the mechanical and thermal stability of the material, as well as its solvent resistance.[444] Two different heat-activated reaction pathways can be achieved using PCBCB to form $(PCBCB)_n$ films that are insoluble in DMF and chlorobenzene;[445] thermally opening of the cyclobutene to form *o*-quinodimethane derivatives, which can then dimerize to form dibenzocyclooctanes, or cycloaddition of quinodimethane intermediates with the fullerene core.[446, 447] It was previously shown by mass spectrometry that some form of dimers of PCBCB are the major product(s) of the

thermally activated ring-opening reaction.[446] $(PCBCB)_n$ was previously used to prevent aggregation of fullerenes in OPVs under thermal aging at 150 °C,[446] and as an ETM in so-called *n-i-p* (negative-intrinsic-positive) perovskite solar cells,[445] reaching stabilized power conversion efficiencies above 17%.[448] The strategy presented here to improve the stability of the perovskite solar cells is to introduce an additive polymeric cross-linker (poly(methyl methacrylate with a pendant BCB group) to increase connectivity between the $(PCBCB)_n$ oligomers.

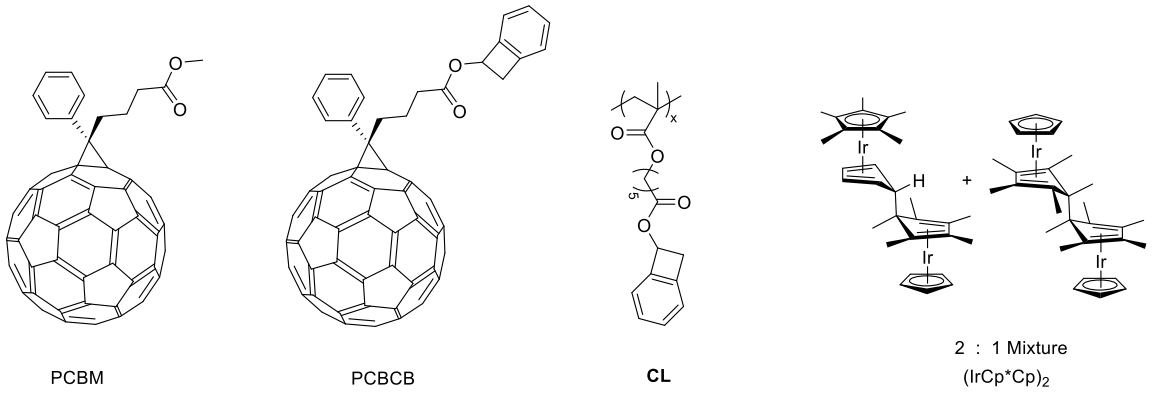

Figure C.1 Molecular structures of the molecules studied here: the ETMs PCBM (reference) and PCBCB, the crosslinker CL and the n-dopant $(IrCp^*Cp)_2$.

The synthesis and characterization of this crosslinker CL (CL = poly(benzocyclobutene methacrylate)) is reported. $(PCBCB)_n$ and that $(PCBCB)_n$·CL could be doped using $(IrCp^*Cp)_2$ n-dopant (see structures in Fig. 1). The effect of the addition of both the n-dopant and the cross-linker were studied on the performance and stability of positive-intrinsic-negative (p-i-n) PSCs.

C.2 Experimental Procedures

Materials Synthesis

PCBCB and $(IrCp^*Cp)_2$ were synthesized as reported previously.[445, 449] Bicyclo[4.2.0]octa-1,3,5-trien-7-ol, **1**, was synthesized in two steps as reported previously.[450]

Bicyclo[4.2.0]octa-1(6),2,4-trien-7-yl 6-bromohexanoate (**2**). To a solution of bicyclo[4.2.0]octa-1,3,5-trien-7-ol (0.65 g, 5.4 mmol) and 6-bromohexanoic acid (1.11 g, 5.7 mmol) in dry dichloromethane (20.0 mL) were added *N,N′*-dicyclohexylcarbodiimide (1.23 g, 6 mmol) and 4-dimethylaminopyridine (0.05 g, 0.4 mmol) at room temperature under stirring. The reaction was carried out at room temperature for 2 h. The reaction mixture was filtered, and the solvent was removed. A yellow oil was obtained (2.45 g, 91%) after column chromatography using $CHCl_3$ and ethanol (100:1) as eluent. ^{1}H NMR (300 MHz, $CDCl_3$): d 7.32 (m, 2H), 7.24 (m, 1H), 7.15 (d, $J_{H\text{-}H}$ = 6 Hz, 1H), 5.92 (dd, $J_{H\text{-}H}$ = 3.0, 1.5 Hz, 1H), 3.66 (dd, $J_{H\text{-}H}$ = 15.0 Hz, 3.0 Hz, 1H), 3.40 (t, $J_{H\text{-}H}$ = 6.0 Hz, 2H), 3.22 (dd, $J_{H\text{-}H}$ = 15.0 Hz, 1.5 Hz, 1H), 2.38 (t, $J_{H\text{-}H}$ = 6 Hz, 2H), 1.88 (p, $J_{H\text{-}H}$ = 9.0 Hz, 2H), 1.69 (p, $J_{H\text{-}H}$ = 6.0 Hz, 2H), 1.49 (m, 2H). ^{13}C{^{1}H} NMR (100.62 MHz, dimethyl sulfoxide-d_6): d 172.88, 144.05, 142.51, 130.00, 127.52, 123.33, 123.30, 71.02, 38.55, 34.97, 33.19, 31.86, 26.99, 23.55. Anal. Calcd. for $C_{14}H_{17}BrO_2$: C, 56.58; H 5.77; found: C, 56.44; H, 5.68. MS (ESI) *m/z* 319.03 [$C_{14}H_{17}O_2BrNa$ $(M+Na)^+$].

Bicyclo[4.2.0]octa-1(6),2,4-trien-7-yl 6-(methacryloyloxy)hexanoate (**3**). To a solution of methacrylic acid (1.05 g, 12.2 mmol) in dry DMF (10.0 mL) at room temperature, potassium carbonate (1.03 g, 18.3 mmol) and a solution of bicyclo[4.2.0]octa-1(6),2,4-trien-7-yl 6-bromohexanoate (0.9 g, 3.1 mmol) in DMF (2.0 mL) were added under

nitrogen. Light exposure of the reaction was minimized by wrapping the flask in aluminum foil. The reaction was monitored by thin layer chromatography. After 72 h the reaction was halted, the product was extracted in ether, and the extracts were washed with water at least three times. The organic residue was dried on Na_2SO_4, and the solvent was removed. A column was performed using a Biotage flash purification system (70% hexanes : 30% ethyl acetate) without exposing the crude to light or heating. The organic phase was collected and the product exacted in water. The solvent was removed under reduced pressure. The product (0.46 g, 50% yield) and the starting material (250 mg, 0.86 mmol) bicyclo[4.2.0]octa-1(6),2,4-trien-7-yl 6-bromohexanoate were isolated. ^{1}H NMR (500 MHz, $CDCl_3$): d 7.32 (td, J_{H-H} = 6.0, 0.5 Hz, 1H), 7.24 (m, 2H), 7.15 (d, J_{H-H} = 6.0 Hz, 1H), 6.09 (m, 1H), 5.92 (dd, J_{H-H} = 3.0, 1.5 Hz, 1H), 5.54 (m, 1H), 4.14 (t, J_{H-H} = 6.0 Hz, 2H), 3.66 (dd, J_{H-H} = 15.0 Hz, 3.0 Hz, 1H diastereotopic), 3.21 (d, J_{H-H} = 15.0 Hz, 1H diastereotopic), 2.38 (t, J_{H-H} = 6 Hz, 2H), 1.93 (s, 3H), 1.71 (m, 4H), 1.44 (m, 2H). ^{13}C(^{1}H) NMR (125.81 MHz, $CDCl_3$): d 173.54, 167.48, 144.26, 142.72, 136.45, 129.98, 127.54, 125.28, 123.53, 123.22, 71.51, 64.46, 38.95, 34.09, 28.33, 25.61, 24.56, 18.34. Anal. Calcd. for $C_{18}H_{22}O_4$: C, 71.50; H 7.33; found: C, 71.46; H, 7.51. MS (ESI) *m/z* 303.15 [$C_{18}H_{23}O_4$ $(M+H)^+$].

Poly(bicyclo[4.2.0]octa-1(6), 2, 4-trien-7-yl-hexanoyl metacrylate) (CL). **3** (0.40 g, 1.32 mmol) and AIBN (2.0 mg, 0.012 mmol) were dissolved in dry benzene (6 ml) under nitrogen. The polymerization mixture was deoxygenated and was then heated up at 60 °C for 7 days without light exposure. The polymer was precipitated into methanol three times. After drying under vacuum, a white polymer was obtained (0.32 g, 80%). ^{1}H NMR (500 MHz, $CDCl_3$): d 7.28 (m, 1H), 7.20 (m, 2H), 7.11 (d, J_{H-H} = 10 Hz, 1H), 5.87 (s, 1H), 3.89

(s, br, 2H), 3.61 (dd, $J_{H\text{-}H}$ = 15.0 Hz, 5.0 Hz, 1H diastereotopic), 3.17 (d, $J_{H\text{-}H}$ = 15.0 Hz, 1H diastereotopic), 2.34 (s, br, 2H), 1.77 (m, br, 2H), 1.65 (m, br, 2H), 1.58 (s, 3H), 1.36 (s, br, 2H), 0.99 (s, br, 2H). $^{13}C\{^{1}H\}$ NMR (125.81 MHz, $CDCl_3$): d 177.45, 173.54, 144.43, 142.81, 130.07, 127.65, 123.69, 123.33, 71.60, 64.87, 54.24, 45.02, 39.05, 34.08, 27.99, 25.70, 24.62, 16.86. Anal. Calcd. for $C_{18}H_{22}O_4$: C, 71.50; H 7.33; found: C, 71.41; H, 7.36. MS (MALDI) 302.53 g/mol. [$C_{18}H_{22}O_4$]. M_w = 580 kg/mol, D = 1.99 (determined via GPC in $CHCl_3$ at 35 °C). T_g = -10 °C, T_d = 210 °C.

Characterization techniques

Nuclear magnetic resonance (NMR). NMR spectra were acquired using a Bruker Avance III 500 MHz spectrometer using $CDCl_3$ as the solvent at 25 °C. The chemical shifts were calibrated using the residual proton signal or the ^{13}C signal of the solvent as an internal reference ($CDCl_3$: 7.26 ppm for ^{1}H NMR, 77.00 ppm for ^{13}C NMR).

Gel Permeation Chromatography (GPC). GPC was performed using a Tosoh EcoSEC HT GPC instrument with RI detector. Experiments were run with chloroform as eluent at 140 °C at a flow rate of 1 mL/min on two sequentially connected 30 × 7.8 mm GMHhr-H(S) HT2 columns (Tosoh Bioscience). The instrument was calibrated vs. polystyrene standards (1,390−1,214,000 g/mol), and data were analyzed using EcoSEC High Temperature GPC Workstation Software. To prepare polymer sample for GPC measurement, the polymer was dissolved in HPLC grade chloroform at a concentration of 1.0 mg/mL and then stirred overnight prior to filtering through a 0.45 mm PTFE filter.

Thermogravimetric analyses (TGA). TGA were measured under nitrogen atmosphere on a Pyris 1 TGA (PerkinElmer) at a heating rate of 15 °C/min from 50-700 °C.

Scanning electron microscope (SEM). SEM images were measured using a FEI Sirion scanning electron microscope at an acceleration voltage of 5 kV.

X-ray Photoelectron Spectroscopy (XPS). XPS measurements for the washing experiments were performed at a JEOL JPS-9030 setup, using monochromatic Al K_a radiation for excitation and a pass energy of 30 eV. The samples were transferred from a glovebox to the UHV system without exposure to air. Depth profiles were recorded using a Kaufmann-type etching ion source, with an Ar pressure of 3×10^{-4} mbar and an ion energy of 300 eV. The sputter rate was determined subsequently with an atomic force microscope.

Ultraviolet Photoelectron Spectroscopy (UPS). UPS measurements were performed using a helium discharge lamp for excitation. Aluminum filters were used to reduce the photon flux and the exposure time was kept to a minimum to minimize charging of the samples. A bias of 10 V was applied for the secondary electron cut-off measurements.

UV-vis-NIR Absorption Spectroscopy. Absorbance spectra were measured with a Lambda 1050 UV-vis-NIR spectrophotometer (PerkinElmer) in a controlled nitrogen atmosphere. The solutions were prepared and sealed in the cuvettes in a glovebox. A baseline spectrum of dichlorobenzene was subtracted from the spectra before further analysis.

Steady state photoluminescence. Steady state photoluminescence was measured using a Horiba Fluorolog-3 with an InGaAs detector.

Time resolved photoluminescence. Time resolved photoluminescence was measured using a time correlated single photon counting (TCSPC) setup (FluoTime 300 PicoQuant

GmbH). Samples were photoexcited with a 507 nm laser head (LDH-P-C-510, PicoQuant GmbH) at frequencies between 0.5 and 2 MHz with a pulse duration of 117 ps and a detection wavelength of 775 nm.

PL data treatment. Each normalized PL decay was fitted to a stretched exponential function following the method of Stranks *et al*.:[402]

$$I(t) = exp\left[-\left(\frac{t - t_0}{\tau}\right)^{\beta}\right]$$

with I(t) the PL intensity at time t, t_0 an offset correction (constrained such that $0 \leq t0 \leq 10$), τ the characteristic lifetime and β the stretching exponent. The use of a stretched exponential function to fit PL data from perovskite films is well established in the literature, in lieu of a true analytical model.[254, 403] The stretching of the exponential has been interpreted as resulting from a distribution of monomolecular (trap-assisted) non-radiative decay rates within the material.[404] The mean relaxation time, $\langle\tau\rangle$, given by Equation 4:

$$\langle\tau\rangle = \frac{\tau}{\beta}\Gamma\left(\frac{1}{\beta}\right)$$

where $\Gamma(z)$ is the gamma function:

$$\Gamma(z) = \int_0^{\infty} x^{z-1}e^{-x}dx$$

Transmission Line Measurements. All films of the electron transporting materials [i.e., PCBM, $(PCBCB)_n$ with and without addition of dopant or crosslinker] had a thickness of 50 nm, measured via ellipsometry. To keep the thickness of the ETM constant, the final

concentration of all fullerene derivative solutions, with and without the addition of *n*-dopant and/or crosslinker, was set to 30 mg mL^{-1}. For doping concentrations > 1 mol%, the concentration of $(IrCp^*Cp)_2$ and PCBCB solutions was fixed to 17 mg/mL in chlorobenzene and 50 mg/mL in dichlorobenzene, respectively; for doping concentrations < 1 mol%, the concentration of $(IrCp^*Cp)_2$ and PCBCB solutions was fixed to 2 mg/mL in chlorobenzene and 31 mg/mL in dichlorobenzene, respectively. 5 mg of crosslinker were dissolved in 1 mL of dichlorobenzene. All solutions were prepared, stirred for at least six hours, and spin-coated at 2000 rpm, 2000 rpm s^{-1}, for 45 s onto detergent/solvent-cleaned glass substrates in a glovebox (<0.5 ppm water and <50 ppm oxygen), using degassed and anhydrous solvents. PCBM films – obtained from 30 mg mL^{-1} solutions in chlorobenzene – were annealed at 70 °C for 10 min, while PCBCB-based films were annealed at 200 °C for 10 min to promote crosslinking, yielding the fullerene insolubilized product $(PCBCB)_n$. All films were immediately transferred without air exposure to a vacuum thermal evaporation system (SPECTROS, K. J. Lesker), for the deposition of silver metal (100 nm).

Current−Voltage (JV) measurements. The *JV* curves were measured (2400 Series SourceMeter, Keithley Instruments) under simulated AM 1.5 sunlight at 100 mW cm^{-2} irradiance generated by an Abet Class AAB sun 2000 simulator, with the intensity calibrated with an NREL calibrated KG 5 filtered Si reference cell. The forward *J–V* scans were measured from forward bias to short circuit and the backward scans were from short circuit to forward bias, both at a scan rate of 380 mV s^{-1}. A stabilization time of 5 s at forward bias of 0 V under illumination was done prior to scanning.

Device preparation

Substrate preparation. Fluorine doped tin oxide (FTO) coated glass substrates (Pilkington TEC 7) were used here. FTO was etched at specific regions using a 2M HCl and zinc powder. Substrates were then cleaned with water, then sequentially sonicated for 5 minutes in water, acetone and isopropyl alcohol, and dried with a compressed nitrogen gun. Next, the substrates were treated for 15 min with UV ozone.

F_4-TCNQ-doped PolyTPD. 0.2 mg of F_4-TCNQ and 1 mg of PolyTPD were added to 1 mL of toluene. The solution was stirred for 12 h prior to deposition. The filtered solution was spincoated at 2000 rpm, 2000 rpm s^{-1} for 20 s and dried at 130 °C for 10 min.

$Cs_{0.05}(FA_{0.85}MA_{0.15})_{0.95}Pb(I_{0.9}Br_{0.1})_3$ perovskite (FAMACs). The precursor solution was prepared by dissolving formamidinium iodide (FAI; Dyesol), methylammonium iodide (MAI; Dyesol), cesium iodide (CsI; Sigma Aldrich), lead iodide (PbI_2; TCI) and lead bromide ($PbBr_2$; Alfa Aesar) in anhydrous *N,N*-dimethylformamide (DMF; Sigma-Aldrich) and dimethylsulfoxide (DMSO; Sigma-Aldrich) in a ratio 4:1 in a nitrogen-filled glovebox to obtain a stoichiometric 1.3 M solution. The solution was then stirred overnight at room temperature and filtered using a 0.44 μm filter. 150 μL of the precursor perovskite solution was spin-coated in a drybox at 1000 rpm for 10 s and then 6000 rpm for 35 s with a ramp of 2000 rpm s^{-1}. After 35 s, 400 μL of toluene (Sigma) was quickly added on the spinning substrates. The films were dried on a hot plate at a temperature of 100 °C for 60 min.

Electron-transport material. PCBM (PCBM = phenyl-C_{61}-butyric acid methyl ester) (20 mg mL^{-1} in 3:1 chlorobenzene/dichlorobenzene) was stirred overnight prior to deposition.

PCBM was deposited by spin coating at 2000 rpm for 20 s, followed by annealing for 5 min at 100 °C.

PCBCB (30 mg mL^{-1} in dichlorobenzene), $(IrCp^*Cp)_2$ (2.4 mg mL^{-1} in chlorobenzene) and CL (12 mg mL^{-1} in dichlorobenzene) were dissolved and stir overnight prior to deposition. The filtered solutions were mixed with dichlorobenzene to obtain the right ratio of PCBCB:crosslinker:$(IrCp^*Cp)_2$ with a final concentration of PCBCB of 20 mg mL^{-1}. The prepared solutions were spin coated at 2000 rpm, 2000 rpm s^{-1} for 20 s and crosslinked on a hotplate at 150°C for 5 minutes in a N_2-filled glovebox.

BCP (BCP = bathocuproine) (0.5 mg mL^{-1} in isopropanol) was stirred overnight prior to deposition. BCP was deposited by spin coating at 5000 rpm for 20 s followed by annealing at 100 °C for 1 min.

Electrode evaporation. An 100 nm silver or 80 nm gold electrode was thermally evaporated under vacuum.

C.3 Results and Discussion

Synthesis and characterization of a new ETM system

PCBCB and $(IrCp^*Cp)_2$ were synthesized as reported previously.[445, 449] The polymeric crosslinker CL was synthesized via polymerization of a methacrylate monomer containing a BCB moiety using the radical initiator azobisisobutyronitrile (AIBN) (see Fig. 2). The polymer had good solubility in chlorobenzene, the solvent used to solubilize the ETM. Gel permeation chromatography against polystyrene standards gave a molecular weight of 580 kg/mol and a dispersity index of 2.

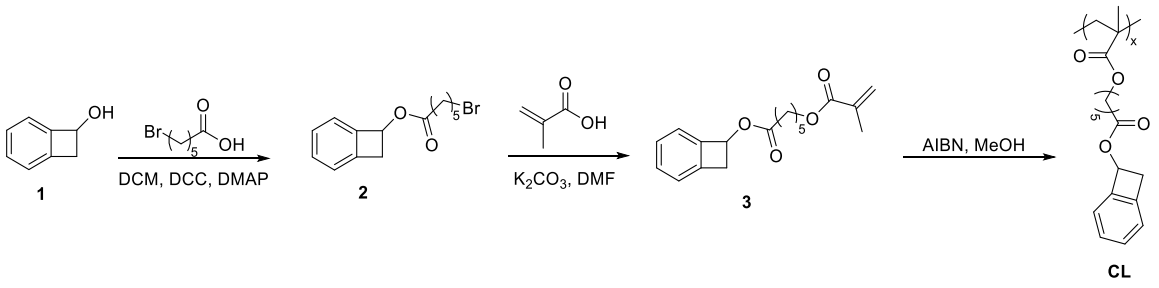

Figure C.2 Synthesis of the crosslinker CL. DCM = dichloromethane, DCC = *N,N′*-dicyclohexylcarbodiimide, DMAP = 4-dimethylaminopyridine, DMF = dimethylformamide, AIBN = azobisisobutyronitrile, MeOH = methanol.

n-Dopants can be used to fill electronic traps and increase the number of charge carriers in an ETM, leading to increased conductivity of the ETM, and to reduce barriers to electron extraction (and injection). Moderately air-stable 19-electron sandwich organometallic dimers, $(MCp^*Cp)_2$ (where Cp* = pentamethylcyclopentadienyl; Cp = cyclopentadienyl, M = Rh,[451] Ir[449]), can n-dope ETMs with electron affinities as small as ca. 2.8 eV, do not form byproducts, and do not require time-consuming thermal activation.[452-454] The fairly large size of the corresponding monomeric cations formed on doping, at least relative to those of species such as alkali-metal ions, may hinder their diffusion in the ETM layer.

$(IrCp^*Cp)_2$ can dope both solutions of PCBCB (see Fig. 3A) and films of $(PCBCB)_n$ (see Fig. 3B), forming fullerene radical anions, $PCBCB^{\bullet-}$, and iridium monomer cations, $(IrCp^*Cp)^+$. As the molar concentration of dopant is increased, the absorption peak corresponding to the neutral acceptor at 330 nm[446] decreases in intensity while the presence of a peak at 1070 nm, corresponding to the fullerene radical anion,[455, 456] becomes more evident (see Fig. 3A). UPS shows how the ionization energy (IE = ϕ + VBO, where ϕ is the work function and VBO is the valence band orbital) of $(PCBCB)_n$ films on FTO decreases by up to 0.6 eV with increasing addition of $(IrCp^*Cp)_2$, suggesting that the number of occupied states increases (see Fig. 3B).

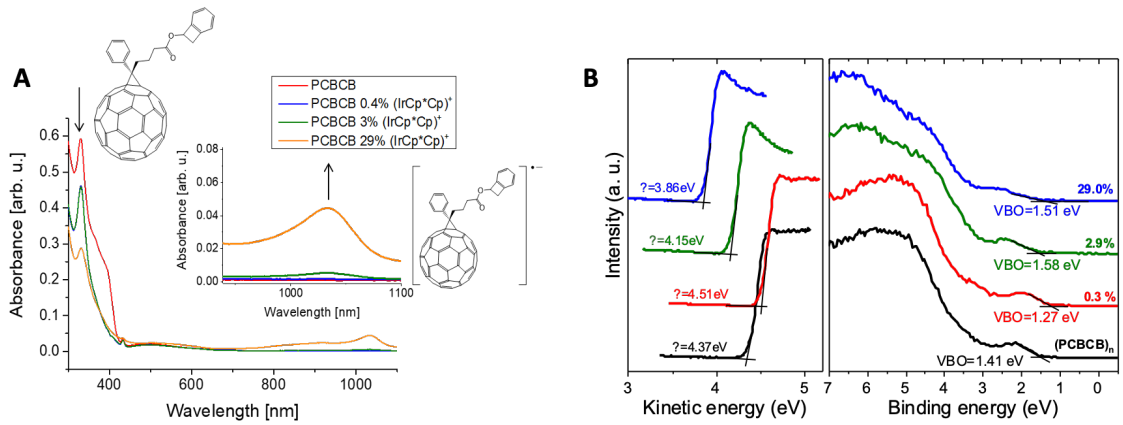

Figure C.3 (A) UV-vis-NIR absorption spectra of solutions of PCBCB as a function of $(IrCp^*Cp)^+$ content (molar percentage). The inset shows the appearance of the PCBCB radical anion at 1070 nm and the disappearance of neutral PCBCB at 330 nm. (B) UPS spectra of neat and doped $(PCBCB)_n$ film with $(IrCp^*Cp)_2$. Dimer content is reported as a function of molar percentage of monomer cations $(IrCp^*Cp)^+$ relative to the host.

Transmission line measurements were performed to quantify the impact of dopant and cross-linker addition on the in-plane electrical conductivity of $(PCBCB)_n$ film. The sheet resistance (R_s) of the ETMs spin-coated on glass with a silver electrode on top was measured to determine their conductivity (σ), their resistivity (ρ), and the resistance at the ETM/Ag contact (R_c) (see Fig. 4 and Table 1-2).

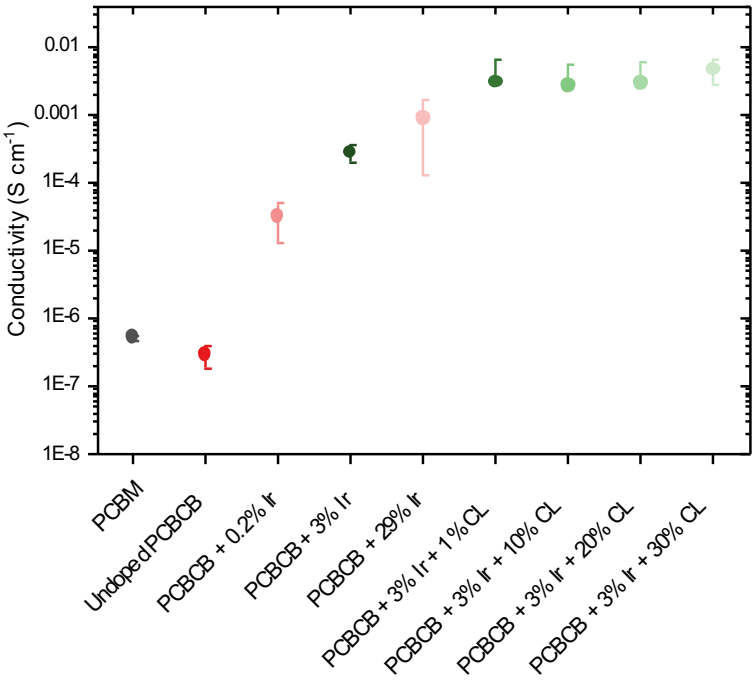

Figure C.4 Conductivity of $(PCBCB)_n$ with silver electrodes as a function of $(IrCp^*Cp)^+$ content (molar percentage) and CL content. The conductivity of PCBM is reported for comparison.

The thermally insolubilized $(PCBCB)_n$ has an in-plane conductivity comparable to that of PCBM. Upon addition of the organometallic dimer, the conductivity of $(PCBCB)_n$ increases by up to four orders-of-magnitude, confirming doping of the ETM by the Ir-dimer (see Fig. 4). To assess the impact of the introduction of CL (1-30 mol%) on the in-plane electrical conductivity, the concentration of $(IrCp^*Cp)^+$ in the $(PCBCB)_n$ films was kept constant at 3 mol%. Upon addition of 1 mol% CL to doped $(PCBCB)_n$ films, the conductivity increases by ten-fold. Surprisingly, the conductivity remains roughly constant with additional CL, up to 30 mol%.

Table C.1 Sheet resistance of $(PCBCB)_n$, resistance at the $(PCBCB)_n$/silver contact and conductivity of $(PCBCB)_n$ as a function of $(IrCp^*Cp)^+$ content (molar percentage). The resistivity and conductivity of PCBM are reported for comparison.

Material	R_s (Ω^{-1})	R_c (Ω)	σ (S cm^{-1})
PCBM	$2.8 \times 10^{12} \pm 4.4 \times 10^{12}$	$8.2 \times 10^{10} \pm 6.9 \times 10^{10}$	$5.6 \times 10^{-7} \pm 5.0 \times 10^{-7}$
$(PCBCB)_n$	$6.7 \times 10^{11} \pm 3.1 \times 10^{11}$	$5.4 \times 10^{9} \pm 3.8 \times 10^{9}$	$3.7 \times 10^{-7} \pm 2.2 \times 10^{-7}$
$(PCBCB)_n$ 0.2% $(IrCp^*Cp)^+$	$5.3 \times 10^{9} \pm 2.9 \times 10^{9}$	$2.9 \times 10^{7} \pm 2.4 \times 10^{7}$	$4.5 \times 10^{-5} \pm 1.9 \times 10^{-5}$
$(PCBCB)_n$ 3% $(IrCp^*Cp)^+$	$1.0 \times 10^{9} \pm 9.4 \times 10^{8}$	$1.6 \times 10^{7} \pm 1.3 \times 10^{7}$	$3.3 \times 10^{-4} \pm 2.3 \times 10^{-4}$
$(PCBCB)_n$ 29% $(IrCp^*Cp)^+$	$1.5 \times 10^{8} \pm 3.7 \times 10^{7}$	$1.4 \times 10^{6} \pm 1.0 \times 10^{6}$	$1.4 \times 10^{-3} \pm 3.8 \times 10^{-4}$

Table C.2 Sheet resistance of doped $(PCBCB)_n$, resistance at the doped $(PCBCB)_n$/silver contact and conductivity as a function of crosslinker concentration. The $(IrCp^*Cp)^+$ concentration was fixed to 3 mol%.

Material	R_s (Ω^{-1})	R_c (Ω)	σ (S cm^{-1})
PCBM	$2.8 \times 10^{12} \pm 4.4 \times 10^{12}$	$8.2 \times 10^{10} \pm 6.9 \times 10^{10}$	$5.6 \times 10^{-7} \pm 5.0 \times 10^{-7}$
$(PCBCB)_n$	$6.7 \times 10^{11} \pm 3.1 \times 10^{11}$	$5.4 \times 10^{9} \pm 3.8 \times 10^{9}$	$3.7 \times 10^{-7} \pm 2.2 \times 10^{-7}$
$(PCBCB)_n$ 3% $(IrCp^*Cp)^+$, 1% crosslinker	$3.7 \times 10^{7} \pm 3.6 \times 10^{6}$	$9.6 \times 10^{5} \pm 4.9 \times 10^{5}$	$5.5 \times 10^{-3} \pm 5.4 \times 10^{-4}$
$(PCBCB)_n$ 3% $(IrCp^*Cp)^+$, 10% crosslinker	$4.3 \times 10^{7} \pm 5.8 \times 10^{6}$	$7.7 \times 10^{5} \pm 1.8 \times 10^{5}$	$4.7 \times 10^{-3} \pm 6.8 \times 10^{-4}$
$(PCBCB)_n$ 3% $(IrCp^*Cp)^+$, 20% crosslinker	$4.3 \times 10^{7} \pm 7.1 \times 10^{6}$	$2.8 \times 10^{5} \pm 2.2 \times 10^{5}$	$4.8 \times 10^{-3} \pm 8.8 \times 10^{-4}$
$(PCBCB)_n$ 3% $(IrCp^*Cp)^+$, 30% crosslinker	$4.4 \times 10^{7} \pm 2.9 \times 10^{7}$	$2.7 \times 10^{6} \pm 6.4 \times 10^{5}$	$5.9 \times 10^{-3} \pm 3.4 \times 10^{-3}$

It has been shown that, in some cases, blending a commodity polymer like poly(methyl methacrylate (PMMA) with an organic semiconductor can help enhance the rheological, mechanical and electrical properties of the latter.[457-459] It can also permit the fabrication of thick films that feature a fine distribution of the dopant:semiconductor complex.[460] By engineering the blend and deposition technique, the conductivity of the blend can increase by nearly an order-of-magnitude relative to that of the pure semiconductor without any doping.[459, 461-465]

We performed XPS to determine the impact of CL addition on the retention of $(IrCpCp^*)^+$ cation in $(PCBCB)_n$ films upon washing (see Fig. 5). We measured the elemental composition of doped $(PCBCB)_n$ films (3 mol%) with and without crosslinker, as prepared and after spin-coating solvents commonly used in device fabrication (chlorobenzene and DMF). Without CL, the iridium elemental contribution – calculated from the area under the Ir 4f peaks – of the $(PCBCB)_n$ films decreases upon washing with chlorobenzene and DMF. When 10 mol% of CL was added in the precursor solution of doped PCBCB, the elemental contribution of iridium remains unchanged after washing with DMF or chlorobenzene, showing a better immobilization of the dopant in the films containing CL.

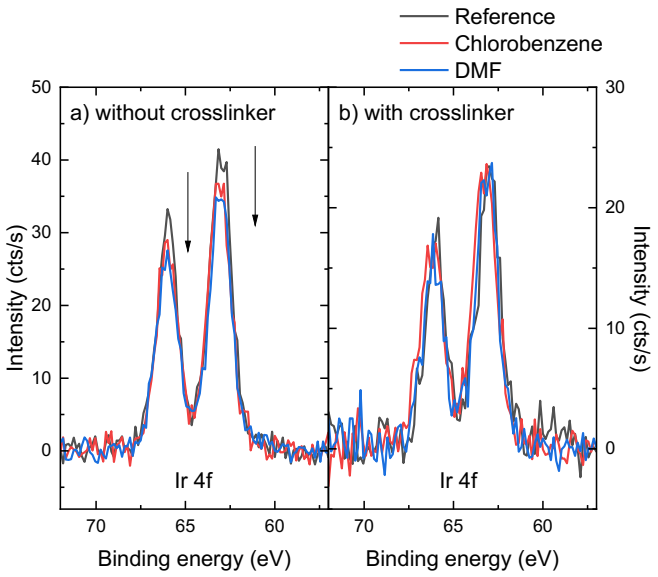

Figure C.5 Iridium elemental contribution in doped $(PCBCB)_n$ films with 3 mol% $(IrCp^*Cp)_2$ without CL (a) and with 10 mol% CL (b) as prepared, and after spin-coating chlorobenzene or DMF onto the film. The elemental contribution of iridium is calculated from the area under the Ir 4f peaks in XPS spectra. The carbon elemental contribution in the same films is constant regardless of washing.

Perovskite solar cells fabrication and characterization

Perovskite solar cells with the *p-i-n* architecture were fabricated to assess the impact of the additive crosslinker on the stability of the devices. The device structure was FTO/F_4-TCNQ-doped PolyTPD/$Cs_{0.05}(FA_{0.85}MA_{0.15})_{0.95}Pb(I_{0.9}Br_{0.1})_3$/ETM/BCP/Ag, where ETM is either PCBM or $(PCBCB)_n$ with and without crosslinker and dopant, FA is formamidinium, MA is methylammonium, PolyTPD is poly(4-butyl-triphenylamine-4',4"-diyl) and BCP is bathocuproine. The selected perovskite is a thermally stable triple cation (FAMACs) lead mixed-halide perovskite, processed from solutions of DMF and dimethylsulfoxide (DMSO). State-of-the-art solar cells with ETM = PCBM were used as the reference. The device performance parameters averaged over 20 solar cells per each type of ETM, as well as the champion cells, are shown in Table 3 (see Fig. S1-2 and Table

S1-2 for optimization of CL concentration and dopant concentrattion). The current density – voltage ($J - V$) curves of the best-performing solar cells are shown in Fig. 6.

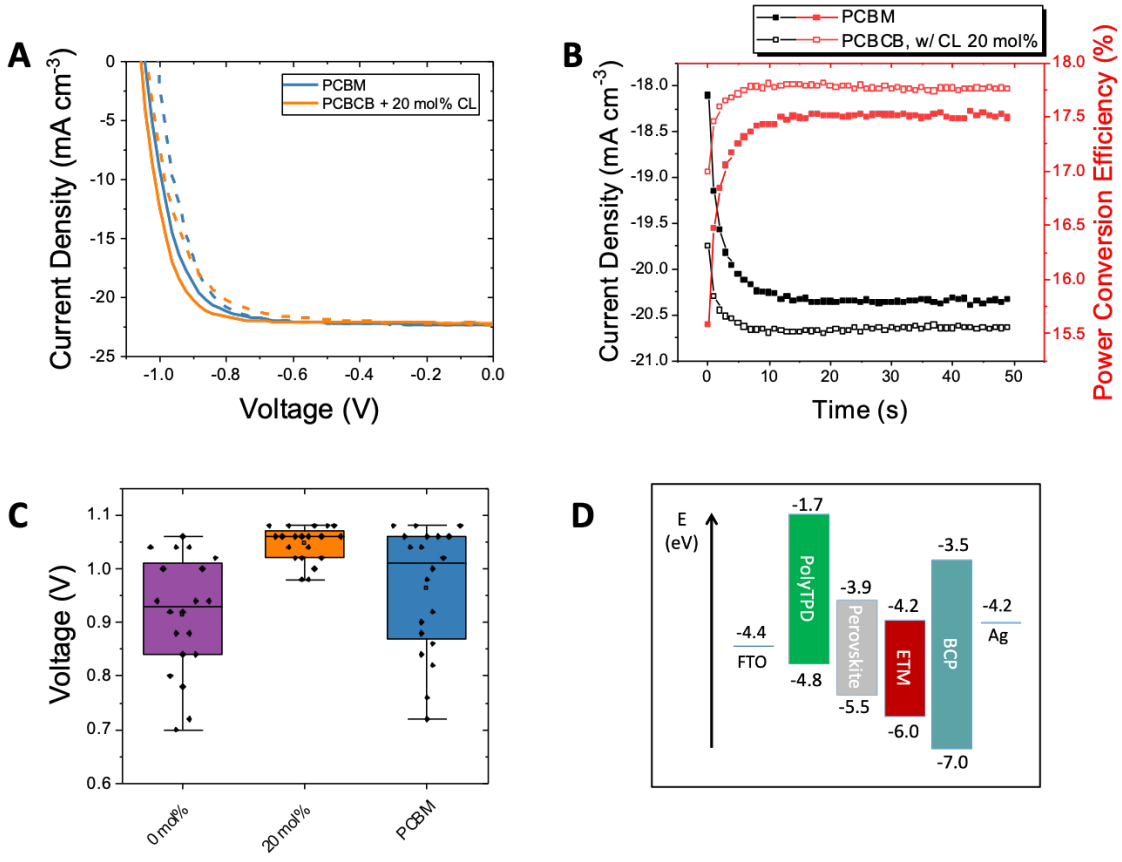

Figure C.6 (A) J-V characteristics for champion devices employing $(PCBCB)_n$ with 20 mol% CL and PCBCB collected under AM 1.5G simulated sunlight. Solid line: forward scan, dotted line: backward scan. (B) Steady-state power output and current density over time. (C) Comparison of V_{oc} for $(PCBCB)_n$, $(PCBCB)_n$ with 20 mol% CL and PCBM. (D) Schematic representation of the inverted "p-i-n" PSCs.

Table C.3 Statistics for 20 individual FAMACs devices.

		J_{sc} (mA cm^{-2})	V_{oc} (V)	FF	PCE (%)
$(PCBCB)_n$	Average	21 ± 2	0.92 ± 0.1	0.65 ± 0.05	12 ± 2
	Maximum	23.20	1.06	0.72	15.35
$(PCBCB)_n$ with 20 mol% CL	Average	21.5 ± 0.8	1.05 ± 0.03	0.68 ± 0.03	16 ± 2
	Maximum	22.87	1.08	0.78	18.54
PCBM	Average	20 ± 2	1.0 ± 0.1	0.70 ± 0.07	14 ± 3
	Maximum	22.39	1.08	0.77	17.64

On average, the V_{oc} increases from 0.92 V to 1.05 V, for PSCs fabricated with $(PCBCB)_n$ and $(PCBCB)_n$·CL, respectively. The increase in V_{oc}, shown in Fig. 4, suggests a reduction of non-radiative recombination at the interface. Moreover, variations in V_{OC} across devices with $(PCBCB)_n$·CL (20 mol%) are smaller compared to those in devices with unmodified $(PCBCB)_n$ or PCBM, showing better reproducibility of the data. Improvement of J_{sc}, V_{oc} and FF on average for $(PCBCB)_n$·CL PSCs leads to an improvement of PCE, which reaches up to 18.54%. The champion cells containing $(PCBCB)_n$·CL exceeded the performance of those using state-of-the-art PCBM as ETM.

While doping PCBM with n-dopant such as N-DMBI-H improves the performance of the PSC using this architecture,[466-470] those made with Ir-doped $(PCBCB)_n$ did not show an improvement over the undoped analogue (see Fig. S1 and Table S1). Nevertheless, in other type of architecture, this type of dopant has been seen to improve the performance of the PSCs.[454, 471] The V_{oc} of the PSCs decreases upon doping of the ETM, probably due to an increase of charge recombination at the perovskite:ETM interface. It was previously showed elsewhere that the improvement in conductivity of the charge transport material doesn't necessarily lead to an improvement of the solar cell performances.[432, 472]

The photoluminescence (PL) properties of the different ETMs on top of the perovskite film on glass are comparable, which is not surprising due to the chemical similarities of the ETMs. The carrier lifetime and PLQE are similar across all ETMs. The PL maximum for the samples without an ETM is slightly red-shifted (779 nm) relative to those with PCBM (770 nm) or $(PCBCB)_n$ (both 767 nm), which may indicate more band-bending due to shallow-trap formation in the bare perovskite case.[7,8] A shift to wider band gap when a

material is added on the perovskite has been suggested to be due to a passivation effect of the perovskite.

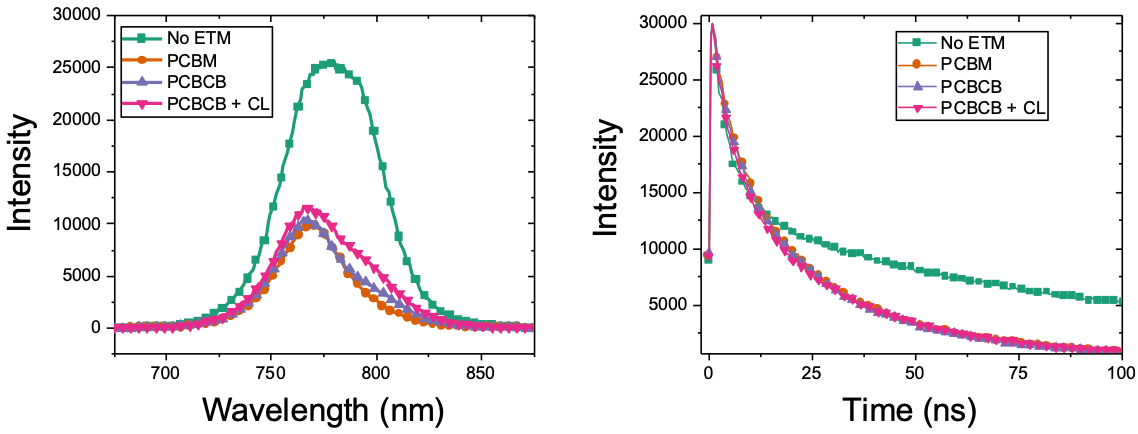

Figure C.7 Steady state photoluminescence (left) and time-resolved PL (right) of half devices on FTO.

Stability of Perovskite Solar Cells

Perovskite solar cells with the *p-i-n* architecture were aged in the dark in inert atmosphere at 85 °C to investigate the dependence of the thermal stability with the choice of ETM (see Fig. 8 for doped ETM and Fig. S3 for undoped analog). The PSCs were brought to atmosphere and room temperature for SPO measurement. The PSCs were stable for more than 3000 hours. After 4500 h, there is a clear distinction between the normalized SPO of PCBM cells and those using $(PCBCB)_n$, with the latter exhibiting better performance. The additive cross-linker also appears to improve the stability of the cells over the oligomeric analogue ($(PCBCB)_n$·CL vs $(PCBCB)_n$).

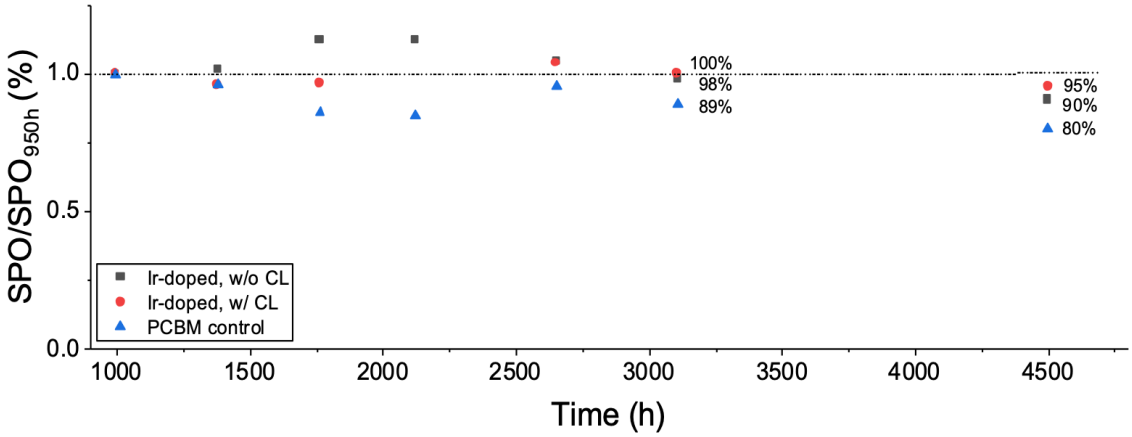

Figure C.8 Stability comparison of non-encapsulated perovskite solar cells (PSCs) fabricated using doped $(PCBCB)_n$, doped $(PCBCB)_n$·CL (20 mol%) and PCBM. An average of four devices per each data point is reported. The SPO is normalized with the SPO after the initial improvement of the PSCs.

C.4 Conclusions

Here the effect of adding a polymeric crosslinking additive to thermally insolubilizable fullerene PCBCB in p-i-n PSCs is reported. It is demonstrated that $(IrCp^*Cp)_2$ can dope a fullerene derivative and that doped insoluble films of $(PCBCB)_n$ oligomers exhibit four orders-of-magnitude higher in-plane conductivity of than the undoped material. Adding an additive crosslinker, CL, inhibits washing of $(IrCp^*Cp)^+$ from the film and does not negatively affect the conductivity of the doped $(PCBCB)_n$.

While the conductivity of the $(PCBCB)_n$ film was improved using the $(IrCp^*Cp)_2$ dopant, the performance of the PSCs decreased with its addition. PCSs made using $(PCBCB)_n$ with CL leads to an improvement in PCE, as well as an improved data reproducibility. The degradation of the perovskite under the ETM is diminished when the crosslinker is added, showing a promising avenue to obtain long term stability solar cells.

C.5 Supporting Information

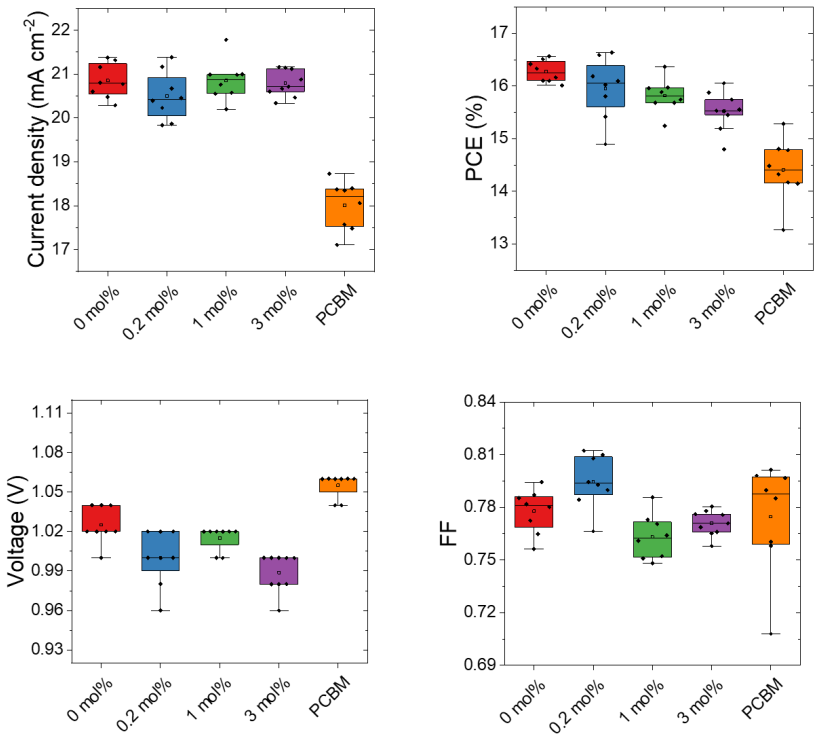

Figure S1 Comparing the photovoltaic performance of FAMACs devices with $(PCBCB)_n$·CL at different concentration of $(IrCp^*Cp)_2$. Box-plot of devices prepared in 1 batch showing the comparison of the PV parameters (from J-V curves) of devices made using $(PCBCB)_n$·CL and PCBM.

Table S1 Statistics for FAMACs devices made to optimize the concentration of dopant used to cast **$(PCBCB)_n$·CL** films (concentration **P1-2:** 20 mg mL^{-1}, concentration of **CL:** 20 mol%).

		J_{sc} (mA cm^{-2})	V_{OC} (V)	FF	PCE (%)
$(PCBCB)_n$·CL	**Average**	20.8 ± 0.4	1.03 ± 0.01	0.78 ± 0.01	16.3 ± 0.2
	Maximum	21.38	1.04	0.79	16.56
$(PCBCB)_n$·CL with $(IrCp^*Cp)_2$ (0.2 mol%)	**Average**	20.5 ± 0.6	1.00 ± 0.02	0.79 ± 0.01	16.0 ± 0.6
	Maximum	21.38	1.02	0.81	16.63
$(PCBCB)_n$·CL with $(IrCp^*Cp)_2$ (1 mol%)	**Average**	20.9 ± 0.5	1.02 ± 0.01	0.76 ± 0.01	15.8 ± 0.3
	Maximum	21.78	1.02	0.79	16.37
$(PCBCB)_n$·CL with $(IrCp^*Cp)_2$ (3 mol%)	**Average**	21.8 ± 0.3	0.99 ± 0.01	0.77 ± 0.01	15.5 ± 0.4
	Maximum	21.16	1.00	0.78	16.05
PCBM	**Average**	18.0 ± 0.6	1.06 ± 0.01	0.77 ± 0.03	14.4 ± 0.6
	Maximum	18.73	1.06	0.80	15.28

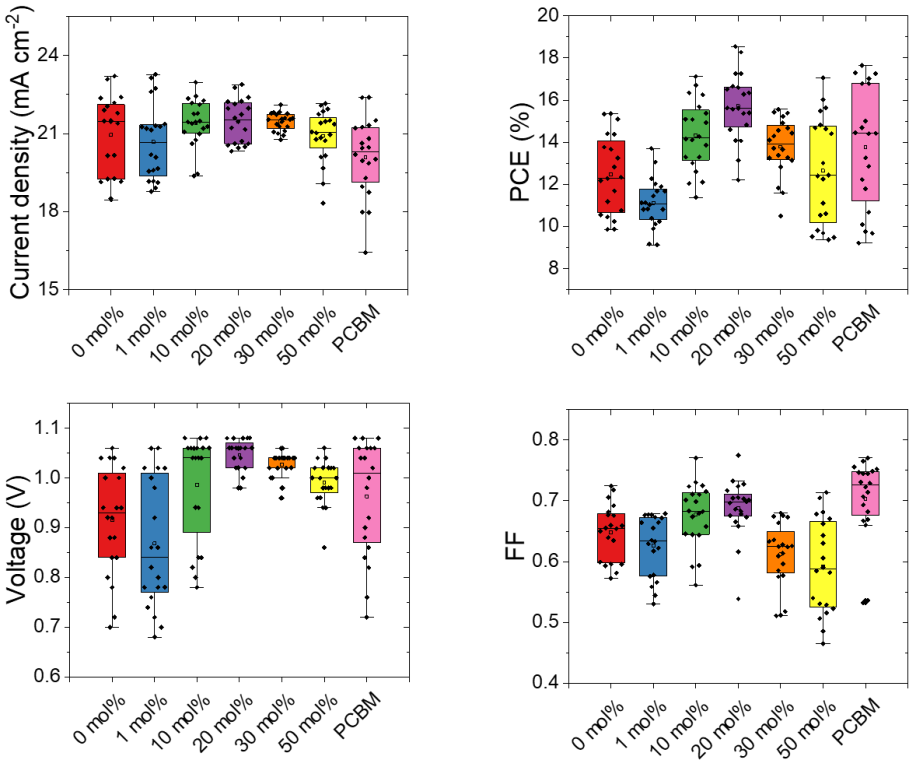

Figure S2 Comparing the photovoltaic performance of FAMACs devices with $(PCBCB)_n$·CL at different concentration of CL. Box-plot of devices prepared in 1 batch showing the comparison of the PV parameters (from J-V curves) of devices made using $(PCBCB)_n$·CL and PCBM.

Table S2 Statistics for FAMACs devices made to optimize the concentration of CL used to cast **$(PCBCB)_n$·CL** films (concentration **P1-2:** 20 mg mL^{-1}).

		J_{sc} (mA cm^{-2})	V_{OC} (V)	FF	PCE (%)
$(PCBCB)_n$	**Average**	21 ± 2	0.9 ± 0.1	0.65 ± 0.05	12 ± 2
	Maximum	23.20	1.06	0.72	15.35
$(PCBCB)_n$·CL (1 mol%)	**Average**	21 ± 1	0.9 ± 0.1	0.63 ± 0.05	11 ± 1
	Maximum	23.27	1.06	0.68	13.70
$(PCBCB)_n$·CL (10 mol%)	**Average**	21.4 ± 0.9	1.0 ± 0.1	0.67 ± 0.05	14 ± 2
	Maximum	22.96	1.08	0.77	17.12
$(PCBCB)_n$·CL (20 mol%)	**Average**	21.5 ± 0.8	1.05 ± 0.03	0.69 ± 0.05	16 ± 2
	Maximum	22.87	1.08	0.78	18.54
$(PCBCB)_n$·CL (30 mol%)	**Average**	21.4 ± 0.3	1.03 ± 0.03	0.61 ± 0.05	14 ± 1
	Maximum	22.10	1.06	0.68	15.57
$(PCBCB)_n$·CL (50mol%)	**Average**	21 ± 1	0.99 ± 0.05	0.59 ± 0.08	13 ± 3
	Maximum	22.14	1.06	0.71	17.06
PCBM	**Average**	20 ± 2	1.0 ± 0.1	0.70 ± 0.07	14 ± 3
	Maximum	22.39	1.08	0.77	17.65

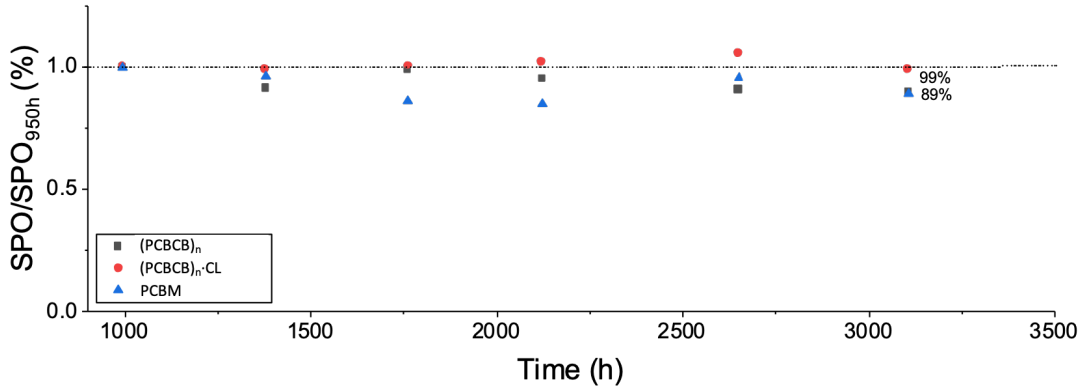

Figure S3. Stability comparison of non-encapsulated perovskite solar cells (PSCs) fabricated using undoped $(PCBCB)_n$, $(PCBCB)_n$·CL (20 mol%) and PCBM. An average of four devices per each data point is reported. The SPO is normalized with the SPO after the initial improvement of the PSCs.

REFERENCES

1. Kojima, A.; Teshima, K.; Shirai, Y.; Miyasaka, T., Organometal Halide Perovskites as Visible-Light Sensitizers for Photovoltaic Cells. *Journal of the American Chemical Society* **2009,** *131*, 6050.

2. Zhou, H.; Chen, Q.; Li, G.; Luo, S.; Song, T.-b.; Duan, H.-S.; Hong, Z.; You, J.; Liu, Y.; Yang, Y., Interface engineering of highly efficient perovskite solar cells. *Science* **2014,** *345*, 542.

3. Lee, M. M.; Teuscher, J.; Miyasaka, T.; Murakami, T. N.; Snaith, H. J., Efficient Hybrid Solar Cells Based on Meso-Superstructured Organometal Halide Perovskites. *Science* **2012,** *338*, 643.

4. Arora, N.; Dar, M. I.; Hinderhofer, A.; Pellet, N.; Schreiber, F.; Zakeeruddin, S. M.; Grätzel, M., Perovskite solar cells with CuSCN hole extraction layers yield stabilized efficiencies greater than 20%. *Science* **2017,** *358*, 768.

5. Yang, W. S.; Park, B.-W.; Jung, E. H.; Jeon, N. J.; Kim, Y. C.; Lee, D. U.; Shin, S. S.; Seo, J.; Kim, E. K.; Noh, J. H.; Seok, S. I., Iodide management in formamidinium-lead-halide–based perovskite layers for efficient solar cells. *Science* **2017,** *356*, 1376.

6. Stoumpos, C. C.; Kanatzidis, M. G., Halide Perovskites: Poor Man's High-Performance Semiconductors. *Advanced Materials* **2016,** *28*, 5778.

7. Chin, X. Y.; Cortecchia, D.; Yin, J.; Bruno, A.; Soci, C., Lead iodide perovskite light-emitting field-effect transistor. *Nature Communications* **2015,** *6*, 7383.

8. Zhou, B.; Jiang, M.; Dong, H.; Zheng, W.; Huang, Y.; Han, J.; Pan, A.; Zhang, L., High-Temperature Upconverted Single-Mode Lasing in 3D Fully Inorganic Perovskite Microcubic Cavity. *ACS Photonics* **2019,** *6*, 793.

9. Smith, I. C.; Hoke, E. T.; Solis-Ibarra, D.; McGehee, M. D.; Karunadasa, H. I., A Layered Hybrid Perovskite Solar-Cell Absorber with Enhanced Moisture Stability. *Angewandte Chemie* **2014,** *53*, 11232.

10. Yan, J.; Qiu, W.; Wu, G.; Heremans, P.; Chen, H., Recent progress in 2D/quasi-2D layered metal halide perovskites for solar cells. *Journal of Materials Chemistry A* **2018,** *6*, 11063.

11. Chen, Y.; Sun, Y.; Peng, J.; Zhang, W.; Su, X.; Zheng, K.; Pullerits, T.; Liang, Z., Tailoring Organic Cation of 2D Air-Stable Organometal Halide Perovskites for Highly Efficient Planar Solar Cells. *Advanced Energy Materials* **2017,** *7*, 1700162.

12. Cao, D. H.; Stoumpos, C. C.; Farha, O. K.; Hupp, J. T.; Kanatzidis, M. G., 2D Homologous Perovskites as Light-Absorbing Materials for Solar Cell Applications. *Journal of the American Chemical Society* **2015,** *137*, 7843.

13. Ma, C.; Shen, D.; Ng, T.-W.; Lo, M.-F.; Lee, C.-S., 2D Perovskites with Short Interlayer Distance for High-Performance Solar Cell Application. *Advanced Materials* **2018,** *30*, 1800710.

14. Lai, H.; Kan, B.; Liu, T.; Zheng, N.; Xie, Z.; Zhou, T.; Wan, X.; Zhang, X.; Liu, Y.; Chen, Y., Two-Dimensional Ruddlesden–Popper Perovskite with Nanorod-like Morphology for Solar Cells with Efficiency Exceeding 15%. *Journal of the American Chemical Society* **2018,** *140*, 11639.

15. Tsai, H.; Nie, W.; Blancon, J.-C.; Stoumpos, C. C.; Asadpour, R.; Harutyunyan, B.; Neukirch, A. J.; Verduzco, R.; Crochet, J. J.; Tretiak, S.; Pedesseau, L.; Even, J.; Alam, M. A.; Gupta, G.; Lou, J.; Ajayan, P. M.; Bedzyk, M. J.; Kanatzidis, M. G.; Mohite, A. D., High-efficiency two-dimensional Ruddlesden–Popper perovskite solar cells. *Nature* **2016,** *536*, 312.

16. Mao, L.; Ke, W.; Pedesseau, L.; Wu, Y.; Katan, C.; Even, J.; Wasielewski, M. R.; Stoumpos, C. C.; Kanatzidis, M. G., Hybrid Dion–Jacobson 2D Lead Iodide Perovskites. *Journal of the American Chemical Society* **2018,** *140*, 3775.

17. Stoumpos, C. C.; Cao, D. H.; Clark, D. J.; Young, J.; Rondinelli, J. M.; Jang, J. I.; Hupp, J. T.; Kanatzidis, M. G., Ruddlesden–Popper Hybrid Lead Iodide Perovskite 2D Homologous Semiconductors. *Chemistry of Materials* **2016,** *28*, 2852.

18. Ahmad, S.; Fu, P.; Yu, S.; Yang, Q.; Liu, X.; Wang, X.; Wang, X.; Guo, X.; Li, C., Dion-Jacobson Phase 2D Layered Perovskites for Solar Cells with Ultrahigh Stability. *Joule* **2019,** *3*, 794.

19. Yuan, M.; Quan, L. N.; Comin, R.; Walters, G.; Sabatini, R.; Voznyy, O.; Hoogland, S.; Zhao, Y.; Beauregard, E. M.; Kanjanaboos, P.; Lu, Z.; Kim, D. H.; Sargent, E. H., Perovskite energy funnels for efficient light-emitting diodes. *Nature Nanotechnology* **2016,** *11*, 872.

20. Tsai, H.; Nie, W.; Blancon, J.-C.; Stoumpos, C. C.; Soe, C. M. M.; Yoo, J.; Crochet, J.; Tretiak, S.; Even, J.; Sadhanala, A.; Azzellino, G.; Brenes, R.; Ajayan, P. M.; Bulović, V.; Stranks, S. D.; Friend, R. H.; Kanatzidis, M. G.; Mohite, A. D., Stable Light-Emitting Diodes Using Phase-Pure Ruddlesden–Popper Layered Perovskites. *Advanced Materials* **2018,** *30*, 1704217.

21. Chung, I.; Lee, B.; He, J.; Chang, R. P. H.; Kanatzidis, M. G., All-solid-state dye-sensitized solar cells with high efficiency. *Nature* **2012,** *485*, 486.

22. Lee, M. M.; Teuscher, J.; Miyasaka, T.; Murakami, T. N.; Snaith, H. J., Efficient Hybrid Solar Cells Based on Meso-Superstructured Organometal Halide Perovskites. **2012,** *338*, 643.

23. Kim, H.-S.; Lee, C.-R.; Im, J.-H.; Lee, K.-B.; Moehl, T.; Marchioro, A.; Moon, S.-J.; Humphry-Baker, R.; Yum, J.-H.; Moser, J. E.; Grätzel, M.; Park, N.-G., Lead iodide perovskite sensitized all-solid-state submicron thin film mesoscopic solar cell with efficiency exceeding 9%. *Scientific reports* **2012,** *2*, 591.

24. Papavassiliou, G. C., Three- and low-dimensional inorganic semiconductors. *Progress in Solid State Chemistry* **1997,** *25*, 125.

25. Saparov, B.; Mitzi, D. B., Organic–Inorganic Perovskites: Structural Versatility for Functional Materials Design. *Chemical Reviews* **2016,** *116*, 4558.

26. Seth, C.; Khushalani, D., Non-Perovskite Hybrid Material, Imidazolium Lead Iodide, with Enhanced Stability. *ChemNanoMat* **2019,** *5*, 85.

27. Chung, I.; Song, J.-H.; Im, J.; Androulakis, J.; Malliakas, C. D.; Li, H.; Freeman, A. J.; Kenney, J. T.; Kanatzidis, M. G., CsSnI3: Semiconductor or Metal? High Electrical Conductivity and Strong Near-Infrared Photoluminescence from a Single Material. High Hole Mobility and Phase-Transitions. *Journal of the American Chemical Society* **2012,** *134*, 8579.

28. Yusoff, A. R. b. M.; Nazeeruddin, M. K., Low-Dimensional Perovskites: From Synthesis to Stability in Perovskite Solar Cells. *Advanced Energy Materials* **2018,** *8*, 1702073.

29. Min, X.; Pengchen, Z.; Gu, S.; Jia, Z., Research progress of low-dimensional perovskites: synthesis, properties and optoelectronic applications. *Journal of Semiconductors* **2017,** *38*, 011004.

30. Katan, C.; Mercier, N.; Even, J., Quantum and Dielectric Confinement Effects in Lower-Dimensional Hybrid Perovskite Semiconductors. *Chemical Reviews* **2019,** *119*, 3140.

31. Mao, L.; Stoumpos, C. C.; Kanatzidis, M. G., Two-Dimensional Hybrid Halide Perovskites: Principles and Promises. *Journal of the American Chemical Society* **2019,** *141*, 1171.

32. Grancini, G.; Nazeeruddin, M. K., Dimensional tailoring of hybrid perovskites for photovoltaics. *Nature Reviews Materials* **2019,** *4*, 4.

33. Hong, K.; Le, Q. V.; Kim, S. Y.; Jang, H. W., Low-dimensional halide perovskites: review and issues. *Journal of Materials Chemistry C* **2018,** *6*, 2189.

34. Smith, M. D.; Crace, E. J.; Jaffe, A.; Karunadasa, H. I., The Diversity of Layered Halide Perovskites. *Annual Review of Materials Research* **2018,** *48*, 111.

35. Mitzi, D. B., Synthesis, Structure, and Properties of Organic-Inorganic Perovskites and Related Materials. *Progress in Inorganic Chemistry* **1999**, 1.

36. Wu, L.-M.; Wu, X.-T.; Chen, L., Structural overview and structure–property relationships of iodoplumbate and iodobismuthate. *Coordination Chemistry Reviews* **2009,** *253*, 2787.

37. Cheng, Z.; Lin, J., Layered organic–inorganic hybrid perovskites: structure, optical properties, film preparation, patterning and templating engineering. *CrystEngComm* **2010,** *12*, 2646.

38. Mercier, N.; Louvain, N.; Bi, W., Structural diversity and retro-crystal engineering analysis of iodometalate hybrids. *CrystEngComm* **2009,** *11*, 720.

39. Mitzi, D. B., Templating and structural engineering in organic–inorganic perovskites. *Journal of the Chemical Society, Dalton Transactions* **2001**, 1.

40. Huang, S.; Huang, P.; Wang, L.; Han, J.; Chen, Y.; Zhong, H., Halogenated-Methylammonium Based 3D Halide Perovskites. *Advanced Materials* **2019,** *31*, 1903830.

41. Kieslich, G.; Sun, S.; Cheetham, A. K., Solid-state principles applied to organic–inorganic perovskites: new tricks for an old dog. *Chemical Science* **2014,** *5*, 4712.

42. Kieslich, G.; Sun, S.; Cheetham, A. K., An extended Tolerance Factor approach for organic–inorganic perovskites. *Chemical Science* **2015,** *6*, 3430.

43. Zhang, Y.; Grancini, G.; Fei, Z.; Shirzadi, E.; Liu, X.; Oveisi, E.; Tirani, F. F.; Scopelliti, R.; Feng, Y.; Nazeeruddin, M. K.; Dyson, P. J., Auto-passivation of crystal defects in hybrid imidazolium/methylammonium lead iodide films by fumigation with methylamine affords high efficiency perovskite solar cells. *Nano Energy* **2019,** *58*, 105.

44. Cheng, N.; Li, W.; Zhang, M.; Wu, H.; Sun, S.; Zhao, Z.; Xiao, Z.; Sun, Z.; Zi, W.; Fang, L., Enhance the performance and stability of methylammonium lead iodide perovskite solar cells with guanidinium thiocyanate additive. *Current Applied Physics* **2019,** *19*, 25.

45. Jodlowski, A. D.; Roldán-Carmona, C.; Grancini, G.; Salado, M.; Ralaiarisoa, M.; Ahmad, S.; Koch, N.; Camacho, L.; de Miguel, G.; Nazeeruddin, M. K., Large guanidinium cation mixed with methylammonium in lead iodide perovskites for 19% efficient solar cells. *Nature Energy* **2017,** *2*, 972.

46. Pering, S. R.; Deng, W.; Troughton, J. R.; Kubiak, P. S.; Ghosh, D.; Niemann, R. G.; Brivio, F.; Jeffrey, F. E.; Walker, A. B.; Islam, M. S.; Watson, T. M.; Raithby, P. R.; Johnson, A. L.; Lewis, S. E.; Cameron, P. J., Azetidinium lead iodide for perovskite solar cells. *Journal of Materials Chemistry A* **2017,** *5*, 20658.

47. D'Annibale, A.; Panetta, R.; Tarquini, O.; Colapietro, M.; Quaranta, S.; Cassetta, A.; Barba, L.; Chita, G.; Latini, A., Synthesis, physico-chemical characterization and structure of the elusive hydroxylammonium lead iodide perovskite NH3OHPbI3. *Dalton Transactions* **2019,** *48*, 5397.

48. Campbell, E. V.; Dick, B.; Rheingold, A. L.; Zhang, C.; Liu, X.; Vardeny, Z. V.; Miller, J. S., Structures of a Complex Hydrazinium Lead Iodide, (N2H5)15Pb3I21,

Possessing [Pb2I9]5−, [PbI6]4−, and I− Ions and α- and β-(N2H5)PbI3. *Chemistry – A European Journal* **2018,** *24*, 222.

49. Zheng, C.; Rubel, O., Aziridinium Lead Iodide: A Stable, Low-Band-Gap Hybrid Halide Perovskite for Photovoltaics. *The Journal of Physical Chemistry Letters* **2018,** *9*, 874.

50. Lichtenberg, F.; Herrnberger, A.; Wiedenmann, K.; Mannhart, J., Synthesis of perovskite-related layered $A_nB_nO_{3n+2}$ = ABOX type niobates and titanates and study of their structural, electric and magnetic properties. *Progress in Solid State Chemistry* **2001,** *29*, 1.

51. Lichtenberg, F.; Herrnberger, A.; Wiedenmann, K., Synthesis, structural, magnetic and transport properties of layered perovskite-related titanates, niobates and tantalates of the type $A_nB_nO_{3n+2}$, $A'A_{k-1}B_kO_{3k+1}$ and $A_mB_{m-1}O_{3m}$. *Progress in Solid State Chemistry* **2008,** *36*, 253.

52. Sourisseau, S.; Louvain, N.; Bi, W.; Mercier, N.; Rondeau, D.; Boucher, F.; Buzaré, J.-Y.; Legein, C., Reduced Band Gap Hybrid Perovskites Resulting from Combined Hydrogen and Halogen Bonding at the Organic−Inorganic Interface. *Chemistry of Materials* **2007,** *19*, 600.

53. Traore, B.; Pedesseau, L.; Assam, L.; Che, X.; Blancon, J.-C.; Tsai, H.; Nie, W.; Stoumpos, C. C.; Kanatzidis, M. G.; Tretiak, S.; Mohite, A. D.; Even, J.; Kepenekian, M.; Katan, C., Composite Nature of Layered Hybrid Perovskites: Assessment on Quantum and Dielectric Confinements and Band Alignment. *ACS Nano* **2018,** *12*, 3321.

54. Knutson, J. L.; Martin, J. D.; Mitzi, D. B., Tuning the Band Gap in Hybrid Tin Iodide Perovskite Semiconductors Using Structural Templating. *Inorganic Chemistry* **2005,** *44*, 4699.

55. Lemmerer, A.; Billing, D. G., Synthesis, characterization and phase transitions of the inorganic–organic layered perovskite-type hybrids [(CnH2n+1NH3)2PbI4], n = 7, 8, 9 and 10. *Dalton Transactions* **2012,** *41*, 1146.

56. Billing, D. G.; Lemmerer, A., Synthesis, characterization and phase transitions in the inorganic-organic layered perovskite-type hybrids [(CnH2n + 1NH3)2PbI4], n = 4, 5 and 6. *Acta Crystallographica Section B* **2007,** *63*, 735.

57. Billing, D. G.; Lemmerer, A., Synthesis, characterization and phase transitions of the inorganic–organic layered perovskite-type hybrids [(CnH2n+1NH3)2PbI4] (n = 12, 14, 16 and 18). *New Journal of Chemistry* **2008,** *32*, 1736.

58. Liu, G.; Gong, J.; Kong, L.; Schaller, R. D.; Hu, Q.; Liu, Z.; Yan, S.; Yang, W.; Stoumpos, C. C.; Kanatzidis, M. G.; Mao, H.-k.; Xu, T., Isothermal pressure-derived metastable states in 2D hybrid perovskites showing enduring bandgap narrowing. *Proceedings of the National Academy of Sciences* **2018,** *115*, 8076.

59. Umeyama, D.; Lin, Y.; Karunadasa, H. I., Red-to-Black Piezochromism in a Compressible Pb–I–SCN Layered Perovskite. *Chemistry of Materials* **2016,** *28*, 3241.

60. Smith, M. D.; Connor, B. A.; Karunadasa, H. I., Tuning the Luminescence of Layered Halide Perovskites. *Chemical Reviews* **2019,** *119*, 3104.

61. Cortecchia, D.; Yin, J.; Petrozza, A.; Soci, C., White light emission in low-dimensional perovskites. *Journal of Materials Chemistry C* **2019,** *7*, 4956.

62. Sheikh, T.; Shinde, A.; Mahamuni, S.; Nag, A., Possible Dual Bandgap in (C4H9NH3)2PbI4 2D Layered Perovskite: Single-Crystal and Exfoliated Few-Layer. *ACS Energy Letters* **2018,** *3*, 2940.

63. Du, K.-z.; Tu, Q.; Zhang, X.; Han, Q.; Liu, J.; Zauscher, S.; Mitzi, D. B., Two-Dimensional Lead(II) Halide-Based Hybrid Perovskites Templated by Acene Alkylamines: Crystal Structures, Optical Properties, and Piezoelectricity. *Inorganic Chemistry* **2017,** *56*, 9291.

64. Lemmerer, A.; Billing, D. G., Lead halide inorganic–organic hybrids incorporating diammonium cations. *CrystEngComm* **2012,** *14*, 1954.

65. Mousdis, G. A.; Papavassiliou, G. C.; Raptopoulou, C. P.; Terzis, A., Preparation and characterization of [H3N(CH2)6NH3]PbI4 and similar compounds with a layered perovskite structure. *Journal of Materials Chemistry* **2000,** *10*, 515.

66. Lee, D. S.; Yun, J. S.; Kim, J.; Soufiani, A. M.; Chen, S.; Cho, Y.; Deng, X.; Seidel, J.; Lim, S.; Huang, S.; Ho-Baillie, A. W. Y., Passivation of Grain Boundaries by Phenethylammonium in Formamidinium-Methylammonium Lead Halide Perovskite Solar Cells. *ACS Energy Letters* **2018,** *3*, 647.

67. Rayner, M. K.; Billing, D. G., Poly[1,4-bis-(ammonio-meth-yl)cyclo-hexane [di-μ-iodido-diiodido-plumbate(II)]]. *Acta crystallographica. Section E, Structure reports online* **2010,** *66*, m660.

68. Hautzinger, M. P.; Dai, J.; Ji, Y.; Fu, Y.; Chen, J.; Guzei, I. A.; Wright, J. C.; Li, Y.; Jin, S., Two-Dimensional Lead Halide Perovskites Templated by a Conjugated Asymmetric Diammonium. *Inorganic Chemistry* **2017,** *56*, 14991.

69. Billing, D. G.; Lemmerer, A., Synthesis and crystal structures of inorganic–organic hybrids incorporating an aromatic amine with a chiral functional group. *CrystEngComm* **2006,** *8*, 686.

70. Yang, C.-K.; Chen, W.-N.; Ding, Y.-T.; Wang, J.; Rao, Y.; Liao, W.-Q.; Tang, Y.-Y.; Li, P.-F.; Wang, Z.-X.; Xiong, R.-G., The First 2D Homochiral Lead Iodide Perovskite Ferroelectrics: [R- and S-1-(4-Chlorophenyl)ethylammonium]2PbI4. *Advanced Materials* **2019,** *31*, 1808088.

71. Meadows, M. K.; Roesner, E. K.; Lynch, V. M.; James, T. D.; Anslyn, E. V., CCDC 1557307: Experimental Crystal Structure Determination.

72. Hu, J.; Oswald, I. W. H.; Stuard, S. J.; Nahid, M. M.; Zhou, N.; Williams, O. F.; Guo, Z.; Yan, L.; Hu, H.; Chen, Z.; Xiao, X.; Lin, Y.; Huang, J.; Moran, A. M.; Ade, H.; Neilson, J. R.; You, W., CCDC 1893384: Experimental Crystal Structure Determination. *CSD Communication*.

73. Straus, D. B.; Iotov, N.; Gau, M. R.; Zhao, Q.; Carroll, P. J.; Kagan, C. R., Longer Cations Increase Energetic Disorder in Excitonic 2D Hybrid Perovskites. *The Journal of Physical Chemistry Letters* **2019,** *10*, 1198.

74. Liu, Z.; Yu, W.-T.; Tao, X.-T.; Jiang, M.-H.; Yang, J.-X.; Wang, L., CCDC 249243: Experimental Crystal Structure Determination.

75. Dai, H.; Liu, Z.; Fan, J., Crystal structure of bis(4-bromophenylaminium) tetraiodoplumbate(II), (BrC6H4NH3)2PbI4. *Zeitschrift für Kristallographie - New Crystal Structures* **2014,** *224*, 149.

76. Kamminga, M. E.; Fang, H.-H.; Filip, M. R.; Giustino, F.; Baas, J.; Blake, G. R.; Loi, M. A.; Palstra, T. T. M., Confinement Effects in Low-Dimensional Lead Iodide Perovskite Hybrids. *Chemistry of Materials* **2016,** *28*, 4554.

77. Van Gompel, W. T. M.; Herckens, R.; Van Hecke, K.; Ruttens, B.; D'Haen, J.; Lutsen, L.; Vanderzande, D., Towards 2D layered hybrid perovskites with enhanced functionality: introducing charge-transfer complexes via self-assembly. *Chemical Communications* **2019,** *55*, 2481.

78. Passarelli, J. V.; Fairfield, D. J.; Sather, N. A.; Hendricks, M. P.; Sai, H.; Stern, C. L.; Stupp, S. I., Enhanced Out-of-Plane Conductivity and Photovoltaic Performance in n = 1 Layered Perovskites through Organic Cation Design. *Journal of the American Chemical Society* **2018,** *140*, 7313.

79. Lermer, C.; Senocrate, A.; Moudrakovski, I.; Seewald, T.; Hatz, A.-K.; Mayer, P.; Pielnhofer, F.; Jaser, J. A.; Schmidt-Mende, L.; Maier, J.; Lotsch, B. V., Completing the Picture of 2-(Aminomethylpyridinium) Lead Hybrid Perovskites: Insights into Structure, Conductivity Behavior, and Optical Properties. *Chemistry of Materials* **2018,** *30*, 6289.

80. Febriansyah, B.; Koh, T. M.; Lekina, Y.; Jamaludin, N. F.; Bruno, A.; Ganguly, R.; Shen, Z. X.; Mhaisalkar, S. G.; England, J., Improved Photovoltaic Efficiency and Amplified Photocurrent Generation in Mesoporous n = 1 Two-Dimensional Lead–Iodide Perovskite Solar Cells. *Chemistry of Materials* **2019,** *31*, 890.

81. Dammak, H.; Elleuch, S.; Feki, H.; Abid, Y., Synthesis, crystal structure, vibrational spectra, optical properties and theoretical investigation of a two-dimensional self-assembled organic-inorganic hybrid material. *Solid State Sciences* **2016,** *61*, 1.

82. Gao, Y.; Shi, E.; Deng, S.; Shiring, S. B.; Snaider, J. M.; Liang, C.; Yuan, B.; Song, R.; Janke, S. M.; Liebman-Peláez, A.; Yoo, P.; Zeller, M.; Boudouris, B. W.; Liao, P.; Zhu, C.; Blum, V.; Yu, Y.; Savoie, B. M.; Huang, L.; Dou, L., Molecular engineering of organic–inorganic hybrid perovskites quantum wells. *Nature Chemistry* **2019,** *11*, 1151.

83. Jana, M. K.; Liu, C.; Lidin, S.; Dirkes, D. J.; You, W.; Blum, V.; Mitzi, D. B., Resolving Rotational Stacking Disorder and Electronic Level Alignment in a 2D Oligothiophene-Based Lead Iodide Perovskite. *Chemistry of Materials* **2019,** *31*, 8523.

84. Lermer, C.; Harm, S. P.; Birkhold, S. T.; Jaser, J. A.; Kutz, C. M.; Mayer, P.; Schmidt-Mende, L.; Lotsch, B. V., Benzimidazolium Lead Halide Perovskites: Effects of Anion Substitution and Dimensionality on the Bandgap. *Zeitschrift für anorganische und allgemeine Chemie* **2016,** *642*, 1369.

85. Tang, Z.; Guan, J.; Guloy, A. M., Synthesis and crystal structure of new organic-based layered perovskites with 2,2′-biimidazolium cations. *Journal of Materials Chemistry* **2001,** *11*, 479.

86. Zimmermann, I.; Aghazada, S.; Nazeeruddin, M. K., Lead and HTM Free Stable Two-Dimensional Tin Perovskites with Suitable Band Gap for Solar Cell Applications. *Angewandte Chemie International Edition* **2019,** *58*, 1072.

87. Louvain, N.; Frison, G.; Dittmer, J.; Legein, C.; Mercier, N., Noncovalent Chalcogen Bonds and Disulfide Conformational Change in the Cystamine-Based Hybrid Perovskite [H3N(CH2)2SS(CH2)2NH3]PbIII4. *European Journal of Inorganic Chemistry* **2014,** *2014*, 364.

88. Billing, D. G.; Lemmerer, A., Inorganic–organic hybrid materials incorporating primary cyclic ammonium cations: The lead iodide series. *CrystEngComm* **2007,** *9*, 236.

89. Lemmerer, A.; Billing, D. G., Effect of heteroatoms in the inorganic–organic layered perovskite-type hybrids [(ZCnH2nNH3)2PbI4], n = 2, 3, 4, 5, 6; Z = OH, Br and I; and [(H3NC2H4S2C2H4NH3)PbI4]. *CrystEngComm* **2010,** *12*, 1290.

90. Mercier, N., (HO2C(CH2)3NH3)2(CH3NH3)Pb2I7: a predicted non-centrosymmetrical structure built up from carboxylic acid supramolecular synthons and bilayer perovskite sheets. *CrystEngComm* **2005,** *7*, 429.

91. Oswald, I. W. H.; Koegel, A. A.; Neilson, J. R., General Synthesis Principles for Ruddlesden–Popper Hybrid Perovskite Halides from a Dynamic Equilibrium. *Chemistry of Materials* **2018,** *30*, 8606.

92. Mitzi, D. B., Synthesis, Crystal Structure, and Optical and Thermal Properties of (C4H9NH3)2MI4 (M = Ge, Sn, Pb). *Chemistry of Materials* **1996,** *8*, 791.

93. Papavassiliou, G.; Mousdis, G.; Raptopoulou, C.; Terzis, A., Some New Luminescent Compounds Based on 4-Methylbenzylamine and Lead Halides. *Zeitschrift Fur Naturforschung Section B-a Journal of Chemical Sciences* **2000,** *55*, 536.

94. Liu, G.-N.; Shi, J.-R.; Han, X.-J.; Zhang, X.; Li, K.; Li, J.; Zhang, T.; Liu, Q.-S.; Zhang, Z.-W.; Li, C., A comparison study of aliphatic and aromatic structure directing agents influencing the crystal and electronic structures, and properties of iodoplumbate hybrids: water induced structure conversion and visible light photocatalytic properties. *Dalton Transactions* **2015,** *44*, 12561.

95. Yu, T.; Zhang, L.; Shen, J.; Fu, Y.; Fu, Y., Hydrogen bonds and steric effects induced structural modulation of three layered iodoplumbate hybrids from nonperovskite to perovskite structure. *Dalton Transactions* **2014,** *43*, 13115.

96. Li, T.; Dunlap-Shohl, W. A.; Reinheimer, E. W.; Le Magueres, P.; Mitzi, D. B., Melting temperature suppression of layered hybrid lead halide perovskites via organic ammonium cation branching. *Chemical Science* **2019,** *10*, 1168.

97. Sha, T.-T.; Xiong, Y.-A.; Pan, Q.; Chen, X.-G.; Song, X.-J.; Yao, J.; Miao, S.-R.; Jing, Z.-Y.; Feng, Z.-J.; You, Y.-M.; Xiong, R.-G., Fluorinated 2D Lead Iodide Perovskite Ferroelectrics. *Advanced Materials* **2019,** *31*, 1901843.

98. Li, X.; Ke, W.; Traoré, B.; Guo, P.; Hadar, I.; Kepenekian, M.; Even, J.; Katan, C.; Stoumpos, C. C.; Schaller, R. D.; Kanatzidis, M. G., Two-Dimensional Dion–Jacobson Hybrid Lead Iodide Perovskites with Aromatic Diammonium Cations. *Journal of the American Chemical Society* **2019,** *141*, 12880.

99. Venkatesan, N. R.; Mahdi, A.; Barraza, B.; Wu, G.; Chabinyc, M. L.; Seshadri, R., Enhanced yield-mobility products in hybrid halide Ruddlesden–Popper compounds with aromatic ammonium spacers. *Dalton Transactions* **2019,** *48*, 14019.

100. Billing, D. G.; Lemmerer, A., Poly[bis[2-(1-cyclohexenyl)ethylammonium] di-[mu]-iodo-diodoplumbate(II)]. *Acta Crystallographica Section C* **2006,** *62*, m269.

101. Daub, M.; Haber, C.; Hillebrecht, H., Synthesis, Crystal Structures, Optical Properties, and Phase Transitions of the Layered Guanidinium-Based Hybrid Perovskites [C(NH2)3]2MI4; M = Sn, Pb. *European Journal of Inorganic Chemistry* **2017,** *2017*, 1120.

102. Li, X.; Guo, P.; Kepenekian, M.; Hadar, I.; Katan, C.; Even, J.; Stoumpos, C. C.; Schaller, R. D.; Kanatzidis, M. G., Small Cyclic Diammonium Cation Templated (110)-Oriented 2D Halide (X = I, Br, Cl) Perovskites with White-Light Emission. *Chemistry of Materials* **2019,** *31*, 3582.

103. Dohner, E. R.; Jaffe, A.; Bradshaw, L. R.; Karunadasa, H. I., Intrinsic White-Light Emission from Layered Hybrid Perovskites. *Journal of the American Chemical Society* **2014,** *136*, 13154.

104. Guan, J.; Tang, Z.; M. Guloy, A., α-[NH3(CH2)5NH3]SnI4: a new layered perovskite structure. *Chemical Communications* **1999**, 1833.

105. Tremblay, M.-H.; Thouin, F.; Leisen, J.; Bacsa, J.; Srimath Kandada, A. R.; Hoffman, J. M.; Kanatzidis, M. G.; Mohite, A. D.; Silva, C.; Barlow, S.; Marder, S. R., $(4NPEA)_2PbI_4$ (4NPEA = 4-Nitrophenylethylammonium): Structural, NMR, and Optical Properties of a 3 × 3 Corrugated 2D Hybrid Perovskite. *Journal of the American Chemical Society* **2019,** *141*, 4521.

106. Mao, L.; Guo, P.; Kepenekian, M.; Hadar, I.; Katan, C.; Even, J.; Schaller, R. D.; Stoumpos, C. C.; Kanatzidis, M. G., Structural Diversity in White-Light-Emitting Hybrid Lead Bromide Perovskites. *Journal of the American Chemical Society* **2018,** *140*, 13078.

107. Dohner, E. R.; Hoke, E. T.; Karunadasa, H. I., Self-Assembly of Broadband White-Light Emitters. *Journal of the American Chemical Society* **2014,** *136*, 1718.

108. Li, Y. Y.; Lin, C. K.; Zheng, G. L.; Cheng, Z. Y.; You, H.; Wang, W. D.; Lin, J., Novel 〈110〉 -Oriented Organic−Inorganic Perovskite Compound Stabilized by N-(3-Aminopropyl)imidazole with Improved Optical Properties. *Chemistry of Materials* **2006,** *18*, 3463.

109. Gautier, R.; Massuyeau, F.; Galnon, G.; Paris, M., Lead Halide Post-Perovskite-Type Chains for High-Efficiency White-Light Emission. *Advanced Materials* **2019,** *31*, 1807383.

110. Haris, M. P. U.; Bakthavatsalam, R.; Shaikh, S.; Kore, B. P.; Moghe, D.; Gonnade, R. G.; Sarma, D. D.; Kabra, D.; Kundu, J., Synthetic Control on Structure/Dimensionality and Photophysical Properties of Low Dimensional Organic Lead Bromide Perovskite. *Inorganic Chemistry* **2018,** *57*, 13443.

111. Guo, Y.-Y.; McNulty, J. A.; Mica, N. A.; Samuel, I. D. W.; Slawin, A. M. Z.; Bühl, M.; Lightfoot, P., Structure-directing effects in (110)-layered hybrid perovskites containing two distinct organic moieties. *Chemical Communications* **2019,** *55*, 9935.

112. Li, Y.; Zheng, G.; Lin, J., Synthesis, Structure, and Optical Properties of a Contorted <110>-Oriented Layered Hybrid Perovskite: C3H11SN3PbBr4. *European Journal of Inorganic Chemistry* **2008,** *2008*, 1689.

113. Mao, L.; Wu, Y.; Stoumpos, C. C.; Wasielewski, M. R.; Kanatzidis, M. G., White-Light Emission and Structural Distortion in New Corrugated Two-Dimensional Lead Bromide Perovskites. *Journal of the American Chemical Society* **2017,** *139*, 5210.

114. Nazarenko, O.; Kotyrba, M. R.; Wörle, M.; Cuervo-Reyes, E.; Yakunin, S.; Kovalenko, M. V., Luminescent and Photoconductive Layered Lead Halide Perovskite Compounds Comprising Mixtures of Cesium and Guanidinium Cations. *Inorganic Chemistry* **2017,** *56*, 11552.

115. Xu, Z.; Mitzi, D. B., SnI42--Based Hybrid Perovskites Templated by Multiple Organic Cations: Combining Organic Functionalities through Noncovalent Interactions. *Chemistry of Materials* **2003,** *15*, 3632.

116. Soe, C. M. M.; Stoumpos, C. C.; Kepenekian, M.; Traoré, B.; Tsai, H.; Nie, W.; Wang, B.; Katan, C.; Seshadri, R.; Mohite, A. D.; Even, J.; Marks, T. J.; Kanatzidis, M. G., New Type of 2D Perovskites with Alternating Cations in the Interlayer Space, (C(NH2)3)(CH3NH3)nPbnI3n+1: Structure, Properties, and Photovoltaic Performance. *Journal of the American Chemical Society* **2017,** *139*, 16297.

117. Mitzi, D. B.; Medeiros, D. R.; Malenfant, P. R. L., Intercalated Organic−Inorganic Perovskites Stabilized by Fluoroaryl−Aryl Interactions. *Inorganic Chemistry* **2002,** *41*, 2134.

118. Smith, M. D.; Pedesseau, L.; Kepenekian, M.; Smith, I. C.; Katan, C.; Even, J.; Karunadasa, H. I., Decreasing the electronic confinement in layered perovskites through intercalation. *Chemical Science* **2017,** *8*, 1960.

119. Dolzhenko, Y. I.; Inabe, T.; Maruyama, Y., In Situ X-Ray Observation on the Intercalation of Weak Interaction Molecules into Perovskite-Type Layered Crystals (C9H19NH3)2PbI4 and (C10H21NH3)2CdCl4. *Bulletin of the Chemical Society of Japan* **1986,** *59*, 563.

120. Zhang, Z.-J.; Guo, G.-C.; Xu, G.; Fu, M.-L.; Zou, J.-P.; Huang, J.-S., [(H2en)7(C2O4)2] n (Pb4I18) n ·4nH2O, a New Type of Perovskite Co-templated by Both Organic Cations and Anions. *Inorganic Chemistry* **2006,** *45*, 10028.

121. Daub, M.; Hillebrecht, H., First representatives of (210)-oriented perovskite variants−Synthesis, crystal structures and properties of the new 2D hybrid perovskites A[HC(NH2)2]PbI4; A=[C(NH2)3], [HSC(NH2)2]. *Zeitschrift für Kristallographie - Crystalline Materials* **2018,** *233*, 555.

122. Nazarenko, O.; Kotyrba, M. R.; Yakunin, S.; Aebli, M.; Rainò, G.; Benin, B. M.; Wörle, M.; Kovalenko, M. V., Guanidinium-Formamidinium Lead Iodide: A Layered

Perovskite-Related Compound with Red Luminescence at Room Temperature. *Journal of the American Chemical Society* **2018,** *140*, 3850.

123. ZhenTao, J.; Yanhuan, H.; Hui, W.; Xiuxiu, Z.; Jiaojiao, Y.; Mingli, L.; Zhenhong, W., Two bilayer organic-inorganic hybrid perovskite compounds exhibiting reversible phase transition and dielectric anomalies. *Journal of Solid State Chemistry* **2020,** *282*, 121104.

124. Calabrese, J.; Jones, N. L.; Harlow, R. L.; Herron, N.; Thorn, D. L.; Wang, Y., Preparation and characterization of layered lead halide compounds. *Journal of the American Chemical Society* **1991,** *113*, 2328.

125. Li, X.; Hoffman, J.; Ke, W.; Chen, M.; Tsai, H.; Nie, W.; Mohite, A. D.; Kepenekian, M.; Katan, C.; Even, J.; Wasielewski, M. R.; Stoumpos, C. C.; Kanatzidis, M. G., Two-Dimensional Halide Perovskites Incorporating Straight Chain Symmetric Diammonium Ions, (NH3CmH2mNH3)(CH3NH3)n−1PbnI3n+1 (m = 4–9; n = 1–4). *Journal of the American Chemical Society* **2018,** *140*, 12226.

126. Han, S.; Liu, X.; Liu, Y.; Xu, Z.; Li, Y.; Hong, M.; Luo, J.; Sun, Z., High-Temperature Antiferroelectric of Lead Iodide Hybrid Perovskites. *Journal of the American Chemical Society* **2019,** *141*, 12470.

127. Fu, Y.; Jiang, X.; Li, X.; Traore, B.; Spanopoulos, I.; Katan, C.; Even, J.; Kanatzidis, M. G.; Harel, E., Cation Engineering in Two-Dimensional Ruddlesden–Popper Lead Iodide Perovskites with Mixed Large A-Site Cations in the Cages. *Journal of the American Chemical Society* **2020,** *142*, 4008.

128. Stoumpos, C. C.; Soe, C. M. M.; Tsai, H.; Nie, W.; Blancon, J.-C.; Cao, D. H.; Liu, F.; Traoré, B.; Katan, C.; Even, J.; Mohite, A. D.; Kanatzidis, M. G., High Members of the 2D Ruddlesden-Popper Halide Perovskites: Synthesis, Optical Properties, and Solar Cells of (CH3(CH2)3NH3)2(CH3NH3)4Pb5I16. *Chem* **2017,** *2*, 427.

129. Soe, C. M. M.; Nagabhushana, G. P.; Shivaramaiah, R.; Tsai, H.; Nie, W.; Blancon, J.-C.; Melkonyan, F.; Cao, D. H.; Traoré, B.; Pedesseau, L.; Kepenekian, M.; Katan, C.; Even, J.; Marks, T. J.; Navrotsky, A.; Mohite, A. D.; Stoumpos, C. C.; Kanatzidis, M. G., Structural and thermodynamic limits of layer thickness in 2D halide perovskites. *Proceedings of the National Academy of Sciences* **2019,** *116*, 58.

130. Smith, I. C.; Hoke, E. T.; Solis-Ibarra, D.; McGehee, M. D.; Karunadasa, H. I., A Layered Hybrid Perovskite Solar-Cell Absorber with Enhanced Moisture Stability. *Angewandte Chemie International Edition* **2014,** *53*, 11232.

131. Zhu, X.-H.; Mercier, N.; Riou, A.; Blanchard, P.; Frère, P., $(C_4H_3SCH_2NH_3)_2(CH_3NH_3)Pb_2I_7$: non-centrosymmetrical crystal structure of a bilayer hybrid perovskite. *Chemical Communications* **2002**, 2160.

132. Spanopoulos, I.; Hadar, I.; Ke, W.; Tu, Q.; Chen, M.; Tsai, H.; He, Y.; Shekhawat, G.; Dravid, V. P.; Wasielewski, M. R.; Mohite, A. D.; Stoumpos, C. C.; Kanatzidis, M. G., Uniaxial Expansion of the 2D Ruddlesden–Popper Perovskite Family for Improved Environmental Stability. *Journal of the American Chemical Society* **2019,** *141*, 5518.

133. Hao, Y.; Qiu, Z.; Zhang, X.; Wei, Z.; Yao, J.; Cai, H., Series of 2D multilayered perovskites constructed by slicing the 3D [(CH3NH3)PbI3] with 4-fluorobenzylamine. *Inorganic Chemistry Communications* **2018,** *97*, 134.

134. Fu, D.; Yuan, J.; Wu, S.; Yao, Y.; Zhang, X.; Zhang, X.-M., A two-dimensional bilayered Dion–Jacobson-type perovskite hybrid with a narrow bandgap for broadband photodetection. *Inorganic Chemistry Frontiers* **2020**.

135. Slavney, A. H.; Smaha, R. W.; Smith, I. C.; Jaffe, A.; Umeyama, D.; Karunadasa, H. I., Chemical Approaches to Addressing the Instability and Toxicity of Lead–Halide Perovskite Absorbers. *Inorganic Chemistry* **2017,** *56*, 46.

136. Huang, P.-J.; Taniguchi, K.; Miyasaka, H., Bulk Photovoltaic Effect in a Pair of Chiral–Polar Layered Perovskite-Type Lead Iodides Altered by Chirality of Organic Cations. *Journal of the American Chemical Society* **2019,** *141*, 14520.

137. Hoffman, J. M.; Che, X.; Sidhik, S.; Li, X.; Hadar, I.; Blancon, J.-C.; Yamaguchi, H.; Kepenekian, M.; Katan, C.; Even, J.; Stoumpos, C. C.; Mohite, A. D.; Kanatzidis, M. G., From 2D to 1D Electronic Dimensionality in Halide Perovskites with Stepped and Flat Layers Using Propylammonium as a Spacer. *Journal of the American Chemical Society* **2019,** *141*, 10661.

138. Biswas, A.; Bakthavatsalam, R.; Shaikh, S. R.; Shinde, A.; Lohar, A.; Jena, S.; Gonnade, R. G.; Kundu, J., Efficient Broad-Band Emission from Contorted Purely Corner-Shared One Dimensional (1D) Organic Lead Halide Perovskite. *Chemistry of Materials* **2019,** *31*, 2253.

139. Wang, S.; Mitzi, D. B.; Feild, C. A.; Guloy, A., Synthesis and Characterization of [NH2C(I):NH2]3MI5 (M = Sn, Pb): Stereochemical Activity in Divalent Tin and Lead Halides Containing Single .ltbbrac.110.rtbbrac. Perovskite Sheets. *Journal of the American Chemical Society* **1995,** *117*, 5297.

140. A. Mousdis, G.; Gionis, V.; C. Papavassiliou, G.; P. Raptopoulou, C.; Terzis, A., Preparation, structure and optical properties of [CHSC(□NH)NH]PbI, [CHSC(□NH)NH]PbBrand [CHSC(□NH)NH]PbCl·CHSC(□NH)NHCl. *Journal of Materials Chemistry* **1998,** *8*, 2259.

141. Papavassiliou, G. C.; Mousdis, G. A.; Raptopoulou, C. P.; Terzis, A., Preparation and characterization of [C6H5CH2NH3]2PbI 4, [C6H5CH2CH2SC(NH2) 2]3PbI5 and [C10H7CH2NH3]PbI3 organic-inorganic hybrid compounds. *Zeitschrift fur Naturforschung - Section B Journal of Chemical Sciences* **1999,** *54*, 1405.

142. Safdari, M.; Fischer, A.; Xu, B.; Kloo, L.; Gardner, J. M., Structure and function relationships in alkylammonium lead(ii) iodide solar cells. *Journal of Materials Chemistry A* **2015,** *3*, 9201.

143. Chen, B.-G., Polymeric haloplumbates(II) templated by ethoxycarbonylmethyl viologen: Structure and enchanced thermochromism behavior. *Inorganic and Nano-Metal Chemistry* **2017,** *47*, 1220.

144. Duan, H.-B.; Yu, S.-S.; Liu, S.-X.; Zhang, H., An inorganic–organic hybrid crystal with a two-step dielectric response and thermochromic luminescence. *Dalton Transactions* **2017,** *46*, 2220.

145. Kollek, T.; Gruber, D.; Gehring, J.; Zimmermann, E.; Schmidt-Mende, L.; Polarz, S., Porous and Shape-Anisotropic Single Crystals of the Semiconductor Perovskite CH3NH3PbI3 from a Single-Source Precursor. *Angewandte Chemie International Edition* **2015,** *54*, 1341.

146. Zhang, L.; Zheng, W.; Li, S.; Han, J.; Jiang, W.; Jia, D., Iodoplumbates from 1D chain to 2D layer: Syntheses, crystal structures, and photocatalytic properties of organic hybrid lead iodides with diammonium structural templating. *Inorganica Chimica Acta* **2019,** *484*, 104.

147. Kollek, T.; Fischer, C.; Göttker-Schnetmann, I.; Polarz, S., Microwave Induced Crystallization of the Hybrid Perovskite CH3NH3PbI3 from a Supramolecular Single-Source Precursor. *Chemistry of Materials* **2016,** *28*, 4134.

148. Arora, Y.; Seth, C.; Khushalani, D., Crafting Inorganic Materials for Use in Energy Capture and Storage. *Langmuir* **2018**.

149. Duan, H.-B.; Zhao, H.-R.; Ren, X.-M.; Zhou, H.; Tian, Z.-F.; Jin, W.-Q., Inorganic–organic hybrid compounds based on face-sharing octahedral [PbI3]∞ chains: self-assemblies, crystal structures, and ferroelectric, photoluminescence properties. *Dalton Transactions* **2011,** *40*, 1672.

150. Weber, O. J.; Marshall, K. L.; Dyson, L. M.; Weller, M. T., Structural diversity in hybrid organic-inorganic lead iodide materials. *Acta Crystallographica Section B* **2015,** *71*, 668.

151. Krautscheid, H.; Vielsack, F.; Klaassen, N., Polymere Iodoplumbate – Synthese und Kristallstrukturen von (Pr3N–C2H4–NPr3)[Pb6I14(dmf)2] · 4DMF, (Pr3N–C2H4–NPr3)[Pb(dmf)6][Pb5I14] · DMF und (Me3N–C2H4–NMe3)2[Pb2I7]I. *Zeitschrift für anorganische und allgemeine Chemie* **1998,** *624*, 807.

152. Mishra, S.; Jeanneau, E.; Daniele, S.; Ledoux, G.; Swamy, P. N., Solid- and Solution Phase Transformations in Novel Hybrid Iodoplumbate Derivatives Templated by Solvated Yttrium Complexes. *Inorganic Chemistry* **2008,** *47*, 9333.

153. Krautscheid, H.; Lode, C.; Vielsack, F.; Vollmer, H., Synthesis and crystal structures of iodoplumbate chains, ribbons and rods with new structural types. *Journal of the Chemical Society, Dalton Transactions* **2001**, 1099.

154. Kaltzoglou, A.; Stoumpos, C. C.; Kontos, A. G.; Manolis, G. K.; Papadopoulos, K.; Papadokostaki, K. G.; Psycharis, V.; Tang, C. C.; Jung, Y.-K.; Walsh, A.; Kanatzidis, M. G.; Falaras, P., Trimethylsulfonium Lead Triiodide: An Air-Stable Hybrid Halide Perovskite. *Inorganic Chemistry* **2017,** *56*, 6302.

155. Zhang, W., CCDC 1905762: Experimental Crystal Structure Determination. *CSD Communication* **2019**.

156. Huang, Z.-J.; Cheng, H.-J.; Dai, M.; Ni, C.-Y.; Li, H.-X.; Hou, K.-P.; Ren, Z.-G.; Lang, J.-P., Solvothermal syntheses and crystal structures of one 1D and two 3D [PbxIy]-based coordination polymers. *Inorganic Chemistry Communications* **2013,** *31*, 33.

157. Maughan, A. E.; Kurzman, J. A.; Neilson, J. R., Hybrid Inorganic–Organic Materials with an Optoelectronically Active Aromatic Cation: (C7H7)2SnI6 and C7H7PbI3. *Inorganic Chemistry* **2015,** *54*, 370.

158. Eppel, S.; Fridman, N.; Frey, G., Amide-Templated Iodoplumbates: Extending Lead-Iodide Based Hybrid Semiconductors. *Crystal Growth & Design* **2015,** *15*, 4363.

159. Wang, G.-E.; Yao, M.-S.; Cai, M.-L.; Xiu, J.-W.; Li, Y.-Z.; Xu, G.; Guo, G.-C., Constructing semiconductive crystalline microporous materials by Coulomb interactions. *Journal of Materials Chemistry A* **2017,** *5*, 18409.

160. Fan, L.-Q.; Chen, L.; Wu, L.-M., catena-Poly[tris(2,2'-bipyridine)nickel(II) [hexa-[mu]-iodo-diplumbate(II)]]. *Acta Crystallographica Section E* **2006,** *62*, m3373.

161. Chen, X.-B.; Li, H.-H.; Chen, Z.-R.; Liu, J.-B.; Li, J.-B.; Dong, H.-J.; Wu, Y.-L., Introducing Transition-Metal Complex Together with Conjugated Ligand into Polymeric Iodoplumbate: Structure Characterization, Properties and Theoretical Study of a New Semi-Conductive Hybrid: {[Cu(II)(2,2′-bipy)3][Pb2I6]}n. *Journal of Cluster Science* **2009,** *20*, 611.

162. Zhang, L.; Tang, C.; Zheng, W.; Jiang, W.; Jia, D., Solvothermal Synthesis, Crystal Structures, and Photocatalytic Properties of Iodoplumbate Hybrids with Nickel(II) Complex Templates. *European Journal of Inorganic Chemistry* **2019,** *2019*, 237.

163. Wang, G.-E.; Xu, G.; Li, P.-X.; Wang, S.-H.; Wang, M.-S.; Guo, G.-C.; Huang, J.-S., Diplex single-crystal-to-single-crystal transformation by different inducement. *CrystEngComm* **2013,** *15*, 2579.

164. Wang, G.-E.; Wang, M.-S.; Zhang, M.-J.; Cai, L.-Z.; Liu, B.-W.; Zhang, C.-J.; Guo, G.-C.; Huang, J.-S., Haloplumbate hybrids with organically coordinated halometal complexes as templates and mixed halo atoms: Solvothermal syntheses, crystal structures, and optical properties. *Inorganic Chemistry Communications* **2012,** *23*, 137.

165. Mishra, S.; Jeanneau, E.; Iasco, O.; Ledoux, G.; Luneau, D.; Daniele, S., Heterometallic, Hybrid, Heavy Main-Group Iodometallates Containing Lanthanide Complexes: Template Synthesis, Structures, Thermal, Optical, Luminescent and Magnetic Properties. *European Journal of Inorganic Chemistry* **2012,** *2012*, 2749.

166. Zeb, A.; Sun, Z.; Khan, T.; Asghar, M. A.; Wu, Z.; Li, L.; Ji, C.; Luo, J., [C5H12N]CdCl3: an ABX3 perovskite-type semiconducting switchable dielectric phase transition material. *Inorganic Chemistry Frontiers* **2017,** *4*, 1485.

167. Zeb, A.; Sun, Z.; Khan, A.; Zhang, S.; Khan, T.; Asghar, M. A.; Luo, J., [C6H14N]PbI3: a one-dimensional perovskite-like order–disorder phase transition

material with semiconducting and switchable dielectric attributes. *Inorganic Chemistry Frontiers* **2018,** *5*, 897.

168. Liu, G.; Liu, J.; Sun, Z.; Zhang, Z.; Chang, L.; Wang, J.; Tao, X.; Zhang, Q., Thermally Induced Reversible Double Phase Transitions in an Organic–Inorganic Hybrid Iodoplumbate C4H12NPbI3 with Symmetry Breaking. *Inorganic Chemistry* **2016,** *55*, 8025.

169. Wang, M.-J.; Chen, X.-R.; Tong, Y.-B.; Yuan, G.-J.; Ren, X.-M.; Liu, J.-L., Phase Transition, Dielectrics, Single-Ion Conductance, and Thermochromic Luminescence of a Inorganic–Organic Hybrid of [Triethylpropylammonium][PbI3]. *Inorganic Chemistry* **2017,** *56*, 9525.

170. Ji, C.; Sun, Z.; Zeb, A.; Liu, S.; Zhang, J.; Hong, M.; Luo, J., Bandgap Narrowing of Lead-Free Perovskite-Type Hybrids for Visible-Light-Absorbing Ferroelectric Semiconductors. *The Journal of Physical Chemistry Letters* **2017,** *8*, 2012.

171. Hua, X.-N.; Liao, W.-Q.; Tang, Y.-Y.; Li, P.-F.; Shi, P.-P.; Zhao, D.; Xiong, R.-G., A Room-Temperature Hybrid Lead Iodide Perovskite Ferroelectric. *Journal of the American Chemical Society* **2018,** *140*, 12296.

172. Zhao, H.-R.; Li, D.-P.; Ren, X.-M.; Song, Y.; Jin, W.-Q., Larger Spontaneous Polarization Ferroelectric Inorganic−Organic Hybrids: [PbI3]∞ Chains Directed Organic Cations Aggregation to Kagomé-Shaped Tubular Architecture. *Journal of the American Chemical Society* **2010,** *132*, 18.

173. Liu, J.-J.; Guan, Y.-F.; Jiao, C.; Lin, M.-J.; Huang, C.-C.; Dai, W.-X., A panchromatic hybrid crystal of iodoplumbate nanowires and J-aggregated naphthalene diimides with long-lived charge-separated states. *Dalton Transactions* **2015,** *44*, 5957.

174. Chen, Y.; Yang, Z.; Guo, C.-X.; Ni, C.-Y.; Li, H.-X.; Ren, Z.-G.; Lang, J.-P., Using alcohols as alkylation reagents for 4-cyanopyridinium and N,N′-dialkyl-4,4′-bipyridinium and their one-dimensional iodoplumbates. *CrystEngComm* **2011,** *13*, 243.

175. Wang, C.-H.; Ma, C.-J.; Huang, Z.-P.; Zai, Y.-X.; Yang, Q.; Li, L.; Liang, Y.; Niu, Y.-Y., Bis(imidazole) Cation Templates and Subtle Effect: Syntheses and Characterization of Three New Pb(II) Halide Supramolecular Polymers. *Journal of Cluster Science* **2015,** *26*, 1027.

176. Véron, A. C.; Linden, A.; Leclaire, N. A.; Roedern, E.; Hu, S.; Ren, W.; Rentsch, D.; Nüesch, F. A., One-Dimensional Organic–Inorganic Hybrid Perovskite Incorporating Near-Infrared-Absorbing Cyanine Cations. *The Journal of Physical Chemistry Letters* **2018,** *9*, 2438.

177. Cai, M.; Wang, G.-E.; Yao, M.; Wu, G.; Li, Y.; Xu, G., Semiconductive 1D nanobelt iodoplumbate hybrid with high humidity response. *Inorganic Chemistry Communications* **2018,** *93*, 42.

178. Ma, C.; Liu, M. E. I.; Zhang, W.; Du, H.; Li, Y. A. O.; Wang, C.; Niu, Y., Syntheses and characterization of two novel 1D Pb(II) Halide supramolecular polymers possessing incomplete Cubane subunit directed by π-conjugated Dication templates. *Journal of Chemical Sciences* **2015,** *127*, 1235.

179. Kamminga, M. E.; de Wijs, G. A.; Havenith, R. W. A.; Blake, G. R.; Palstra, T. T. M., The Role of Connectivity on Electronic Properties of Lead Iodide Perovskite-Derived Compounds. *Inorganic Chemistry* **2017,** *56*, 8408.

180. Febriansyah, B.; Koh, T. M.; John, R. A.; Ganguly, R.; Li, Y.; Bruno, A.; Mhaisalkar, S. G.; England, J., Inducing Panchromatic Absorption and Photoconductivity in Polycrystalline Molecular 1D Lead-Iodide Perovskites through π-Stacked Viologens. *Chemistry of Materials* **2018,** *30*, 5827.

181. Selivanov, N. I.; Murashkina, A. A.; Kevorkyants, R.; Emeline, A. V.; Bahnemann, D. W., Pyridinium lead tribromide and pyridinium lead triiodide: quasi-one-dimensional perovskites with an optically active aromatic π-system. *Dalton Transactions* **2018,** *47*, 16313.

182. Contreras, J. G.; Seguel, G. V.; Ungerer, B.; Maier, W. F.; Hollander, F. J., Triiodolead(II) complexes. structure and Raman spectra. *Journal of Molecular Structure* **1983,** *102*, 295.

183. Li, H.-H.; Chen, Z.-R.; Cheng, L.-C.; Wang, Y.-J.; Feng, M.; Wang, M., Hybrid Polymeric Iodoplumbates Constructed from Morpholine and Its Derivatives: Structures and Properties. *Dalton Transactions* **2010,** *39*, 11000.

184. Tang, Z.; Guloy, A. M., A Methylviologen Lead(II) Iodide: Novel [PbI3-]∞ Chains with Mixed Octahedral and Trigonal Prismatic Coordination. *Journal of the American Chemical Society* **1999,** *121*, 452.

185. Arora, Y.; Seth, C.; Khushalani, D., Crafting Inorganic Materials for Use in Energy Capture and Storage. *Langmuir* **2019,** *35*, 9101.

186. Wei, W.; Gao, H.; Lei, X.; Feng, G.; Li, W., Synthesis and mechanical properties of a new 1D hybrid organic-inorganic lead iodide. *Inorganic Chemistry Communications* **2017,** *85*, 45.

187. Yan, Z. S.; Long, J. Y.; Gong, Y.; Hua Lin, J., Three in situ-synthesized novel inorganic–organic hybrid materials based on metal (M = Bi, Pb) iodide and organoamine using one-pot reactions: structures, band gaps and optoelectronic properties. *New Journal of Chemistry* **2018,** *42*, 699.

188. Xu, G.; He, X., catena-Poly[1,1'-dimethyl-4,4'-(ethane-1,2-di-yl)dipyridinium [lead(II)-tri-μ-iodido-lead(II)-tri-μ-iodido]]. *Acta crystallographica. Section E, Structure reports online* **2011,** *67*, m847.

189. Zhao, J.-J.; Wang, Y.-N.; Jia, H.-L.; Yu, J.-H.; Xu, J.-Q., Crystal Structures of Three Organically Modified Metal Halides. *Journal of Cluster Science* **2014,** *25*, 571.

190. Du, H.; Fu, W.; Zhang, S.; Li, L.; Wang, H.; Yue, Z.; Zhang, W.; Niu, Y.; Zhu, Y., Six cation-templated halometal complexes and C–H activation of alkylene-bridged azoles. *Journal of Coordination Chemistry* **2014,** *67*, 807.

191. Glavcheva, Z.; Umezawa, H.; Okada, S.; Nakanishi, H., New pyridinium–metal iodide complexes toward nonlinear optical materials. *Materials Letters* **2004,** *58*, 2466.

192. Billing, D. G.; Lemmerer, A., catena-Poly[bis(tert-butylammonium) [plumbate(II)-tri-[mu]-iodo] iodide dihydrate]. *Acta Crystallographica Section C* **2006,** *62*, m264.

193. M, G.; H, F., Crystal structure of pyridinium triiodoplumbate(II), C5H6NPbI3. *Zeitschrift für Kristallographie - New Crystal Structures* **1997,** *212*, 235.

194. Usoltsev, A. N.; Adonin, S. A.; Abramov, P. A.; Korolkov, I. V.; Yushina, I. V.; Antonova, O. V.; Sokolov, M. N.; Fedin, V. P., Polymeric hybrid iodoplumbates and iodobismuthates containing mono- and bisalkylated derivatives of 1,2-bis(4-pyridyl)ethylene: Structural and optical features. *Inorganica Chimica Acta* **2017,** *462*, 323.

195. Chai, W.-X.; Lin, J.; Song, L.; Qin, L.-S.; Shi, H.-S.; Guo, J.-Y.; Shu, K.-Y., Three iodometalate organic-inorganic hybrid materials based on methylene blue cation:

Syntheses, structures, properties and DFT calculations. *Solid State Sciences* **2012,** *14*, 1226.

196. Peng, Y.; Albero, J.; Álvarez, E.; García, H., Hybrid benzidinium lead iodide perovskites with a 1D structure as photoinduced electron transfer photocatalysts. *Sustainable Energy & Fuels* **2019,** *3*, 2356.

197. She, Y.-J.; Zhao, S.-P.; Tian, Z.-F.; Ren, X.-M., Inorganic–organic hybrid with one-dimensional face-sharing iodoplumbate chain showing novel dielectric anomaly and semiconductor emission. *Inorganic Chemistry Communications* **2014,** *46*, 29.

198. Stoumpos, C. C.; Malliakas, C. D.; Kanatzidis, M. G., Semiconducting Tin and Lead Iodide Perovskites with Organic Cations: Phase Transitions, High Mobilities, and Near-Infrared Photoluminescent Properties. *Inorganic Chemistry* **2013,** *52*, 9019.

199. Barman, S.; Venkataraman, N. V.; Vasudevan, S.; Seshadri, R., Phase Transitions in the Anchored Organic Bilayers of Long-Chain Alkylammonium Lead Iodides (CnH2n+1NH3)2PbI4; n = 12, 16, 18. *The Journal of Physical Chemistry B* **2003,** *107*, 1875.

200. Billing, D. G.; Lemmerer, A., Synthesis, characterization and phase transitions in the inorganic-organic layered perovskite-type hybrids $[(C_nH_{2n+1}NH_3)_2PbI_4]$, n = 4, 5 and 6. *Acta Crystallographica Section B* **2007,** *63*, 735.

201. Krautscheid, H.; Vielsack, F., [Pb18I44]8−–An Iodoplumbate with an Unusual Structure. *Angewandte Chemie International Edition in English* **1995,** *34*, 2035.

202. Mercier, N.; Barres, A.-L.; Giffard, M.; Rau, I.; Kajzar, F.; Sahraoui, B., Conglomerate-to-True-Racemate Reversible Solid-State Transition in Crystals of an Organic Disulfide-Based Iodoplumbate. *Angewandte Chemie International Edition* **2006,** *45*, 2100.

203. Louvain, N.; Bi, W.; Mercier, N.; Buzaré, J.-Y.; Legein, C.; Corbel, G., PbnI4n+2(2n+2)− ribbons (n = 3, 5) as dimensional reductions of 2D perovskite layers in cystamine cation based hybrids, also incorporating iodine molecules or reversible guest water molecules. *Dalton Transactions* **2007**, 965.

204. Liu, J.-J.; Chen, Y.; Lin, M.-J.; Huang, C.-C.; Dai, W.-X., Two-semiconductive-component hybrid coordination polymers with controllable photo-induced electron-transfer properties. *Dalton Transactions* **2016,** *45*, 6339.

205. Tingting, Y.; Liu, B.; Yan, J.; Fang, Y.; Chen, M.; Kiang Chong, W.; Jiang, S.; Kuo, J.-L.; Fang, J.; Pei, L.; Wei, S.-H.; Loh, K.; Sum, T. C.; White, T.; Xiang Shen, Z., Pressure-Engineered Structural and Optical Properties of Two-Dimensional (C4H9NH3)2PbI4 Perovskite Exfoliated nm-Thin Flakes. *Journal of the American Chemical Society* **2018,** *141*, 6.

206. Lee, Y.; Mitzi, D. B.; Barnes, P. W.; Vogt, T., Pressure-induced phase transitions and templating effect in three-dimensional organic-inorganic hybrid perovskites. *Physical Review B* **2003,** *68*, 020103.

207. Szafrański, M.; Katrusiak, A., Mechanism of Pressure-Induced Phase Transitions, Amorphization, and Absorption-Edge Shift in Photovoltaic Methylammonium Lead Iodide. *The Journal of Physical Chemistry Letters* **2016,** *7*, 3458.

208. Wang, Y.; Lü, X.; Yang, W.; Wen, T.; Yang, L.; Ren, X.; Wang, L.; Lin, Z.; Zhao, Y., Pressure-Induced Phase Transformation, Reversible Amorphization, and Anomalous Visible Light Response in Organolead Bromide Perovskite. *Journal of the American Chemical Society* **2015,** *137*, 11144.

209. Jaffe, A.; Lin, Y.; Mao, W. L.; Karunadasa, H. I., Pressure-Induced Metallization of the Halide Perovskite (CH3NH3)PbI3. *Journal of the American Chemical Society* **2017,** *139*, 4330.

210. Kitazawa, N., Optical Absorption and Photoluminescence Properties of Pb(I, Br)-Based Two-Dimensional Layered Perovskite. *Japanese Journal of Applied Physics* **1997,** *36*, 2272.

211. Kitazawa, N., Excitons in two-dimensional layered perovskite compounds: (C6H5C2H4NH3)2Pb(Br,I)4 and (C6H5C2H4NH3)2Pb(Cl,Br)4. *Materials Science and Engineering: B* **1997,** *49*, 233.

212. Mitzi, D. B.; Dimitrakopoulos, C. D.; Rosner, J.; Medeiros, D. R.; Xu, Z.; Noyan, C., Hybrid Field-Effect Transistor Based on a Low-Temperature Melt-Processed Channel Layer. *Advanced Materials* **2002,** *14*, 1772.

213. Audebert, P.; Clavier, G.; Alain-Rizzo, V.; Deleporte, E.; Zhang, S.; Lauret, J.-S.; Lanty, G.; Boissière, C., Synthesis of New Perovskite Luminescent Nanoparticles in the Visible Range. *Chemistry of Materials* **2009,** *21*, 210.

214. Cheng, Z. Y.; Wang, H. F.; Quan, Z. W.; Lin, C. K.; Lin, J.; Han, Y. C., Layered organic–inorganic perovskite-type hybrid materials fabricated by spray pyrolysis route. *Journal of Crystal Growth* **2005,** *285*, 352.

215. Mitzi, D. B., A Layered Solution Crystal Growth Technique and the Crystal Structure of (C6H5C2H4NH3)2PbCl4. *Journal of Solid State Chemistry* **1999,** *145*, 694.

216. Liang, K.; Mitzi, D. B.; Prikas, M. T., Synthesis and Characterization of Organic−Inorganic Perovskite Thin Films Prepared Using a Versatile Two-Step Dipping Technique. *Chemistry of Materials* **1998,** *10*, 403.

217. Takeoka, Y.; Fukasawa, M.; Matsui, T.; Kikuchi, K.; Rikukawa, M.; Sanui, K., Intercalated formation of two-dimensional and multi-layered perovskites in organic thin films. *Chemical Communications* **2005**, 378.

218. Arora, N.; Dar, M. I.; Hinderhofer, A.; Pellet, N.; Schreiber, F.; Zakeeruddin, S. M.; Grätzel, M., Perovskite solar cells with CuSCN hole extraction layers yield stabilized efficiencies greater than 20%. **2017,** *358*, 768.

219. Dou, L.; Wong, A. B.; Yu, Y.; Lai, M.; Kornienko, N.; Eaton, S. W.; Fu, A.; Bischak, C. G.; Ma, J.; Ding, T.; Ginsberg, N. S.; Lin-Wang Wang; Alivisatos, A. P.; Yang, P., Atomically thin two-dimensional organic-inorganic hybrid perovskites. *Science* **2015,** *349*, 1518.

220. Tian, H.; Zhao, L.; Wang, X.; Yeh, Y.-W.; Yao, N.; Rand, B. P.; Ren, T.-L., Extremely low operating current resistive memory based on exfoliated 2D perovskite single crystals for neuromorphic computing. *ACS Nano* **2017,** *11*, 12247.

221. Blancon, J.-C.; Tsai, H.; Nie, W.; Stoumpos, C. C.; Pedesseau, L.; Katan, C.; Kepenekian, M.; Soe, C. M. M.; Appavoo, K.; Sfeir, M. Y.; Tretiak, S.; Ajayan, P. M.; Kanatzidis, M. G.; Even, J.; Crochet, J. J.; Mohite, A. D., Extremely efficient internal exciton dissociation through edge states in layered 2D perovskites. *Science* **2017,** *355*, 1288.

222. Wang, J.; Su, R.; Xing, J.; Bao, D.; Diederichs, C.; Liu, S.; Liew, T. C. H.; Chen, Z.; Xiong, Q., Room Temperature Coherently Coupled Exciton-Polaritons in Two-Dimensional Organic-Inorganic Perovskite. *ACS Nano* **2018,** *12*, 8382.

223. Tu, Q.; Spanopoulos, I.; Yasaei, P.; Stoumpos, C. C.; Kanatzidis, M. G.; Shekhawat, G. S.; Dravid, V. P., Stretching and Breaking of Ultrathin 2D Hybrid Organic-Inorganic Perovskites. *ACS Nano* **2018,** *12*, 10347.

224. Thouin, F.; Valverde-Chávez, D. A.; Quarti, C.; Cortecchia, D.; Bargigia, I.; Beljonne, D.; Petrozza, A.; Silva, C.; Kandada, A. R. S., Phonon coherences reveal the polaronic character of excitons in two-dimensional lead halide perovskites. *Nature Materials* **2019,** *18*, 349.

225. Wei, W.-J.; Jiang, X.-X.; Dong, L.-Y.; Liu, W.-W.; Han, X.-B.; Qin, Y.; Li, K.; Li, W.; Lin, Z.-S.; Bu, X.-H.; Lu, P.-X., Regulating Second-Harmonic Generation by van der Waals Interactions in Two-dimensional Lead Halide Perovskite Nanosheets. *Journal of the American Chemical Society*

PagesAhead of Print

Journal

2019

CODEN:JACSAT

ISSN:0002-7863

2019, *DOI:10.1021/jacs.9b01874*.

226. Xu, Z.; Mitzi, D. B.; Dimitrakopoulos, C. D.; Maxcy, K. R., Semiconducting Perovskites (2-XC6H4C2H4NH3)2SnI4 (X = F, Cl, Br): Steric Interaction between the Organic and Inorganic Layers. *Inorganic Chemistry* **2003,** *42*, 2031.

227. Yao, Z.; Zhou, Y.; Yin, X.; Li, X.; Han, J.; Tai, M.; Zhou, Y.; Li, J.; Hao, F.; Lin, H., Role of alkyl chain length in diaminoalkane linked 2D Ruddlesden–Popper halide perovskites. *CrystEngComm* **2018,** *20*, 6704.

228. Mercier, N.; Poiroux, S.; Riou, A.; Batail, P., Unique Hydrogen Bonding Correlating with a Reduced Band Gap and Phase Transition in the Hybrid Perovskites $(HO(CH_2)_2NH_3)_2PbX_4$ (X = I, Br). *Inorganic Chemistry* **2004,** *43*, 8361.

229. Li, J.; Yan, K.; Chen, J.; Zhang, Y.; Yang, W.; Lian, X.; Wu, G.; Chen, H., Hydrogen bond enables highly efficient and stable two-dimensional perovskite solar cells based on 4-pyridine-ethylamine. *Organic Electronics* **2019,** *67*, 122.

230. Lee, J. H.; Lee, J.-H.; Kong, E.-H.; Jang, H. M., The nature of hydrogen-bonding interaction in the prototypic hybrid halide perovskite, tetragonal CH3NH3PbI3. *Scientific reports* **2016,** *6*, 21687.

231. El-Mellouhi, F.; Bentria, E. T.; Marzouk, A.; Rashkeev, S. N.; Kais, S.; Alharbi, F. H., Hydrogen bonding: a mechanism for tuning electronic and optical properties of hybrid organic–inorganic frameworks. *Npj Computational Materials* **2016,** *2*, 16035.

232. Papavassilioua, G. C.; Mousdisa, G. A.; Raptopouloub, C. P.; Terzisb, A., Preparation and Characterization of $[C_6H_5CH_2NH_3]_2PbI_4$, $[C_6H_5CH_2CH_2SC(NH_2)_2]_3PbI_5$ and $[C_{10}H_7CH_2NH_3]PbI_3$ Organic-Inorganic Hybrid Compounds. *Z. Naturforsch* **1999,** *54 b*, 1405.

233. YYY, The thermal stability of Y = H, F, Cl, and Br derivatives was also investigated using thermogravimetric analysis: all four materials only lose weight above ca. 320 °C (see Figure S7). *The thermal stability of Y = H, F, Cl, and Br derivatives was also investigated using thermogravimetric analysis of solid samples: all four materials only lose weight above ca. 320 °C (see Figure S7).*

234. Smith, M. D.; Jaffe, A.; Dohner, E. R.; Lindenberg, A. M.; Karunadasa, H. I., Structural origins of broadband emission from layered Pb–Br hybrid perovskites. *Chemical Science* **2017,** *8*, 4497.

235. Gómez, V.; Fuhr, O.; Ruben, M., Structural diversity in substituted-pyridinium iodo- and bromoplumbates: a matter of halide and temperature. *CrystEngComm* **2016,** *18*, 8207.

236. Straus, D. B.; Iotov, N.; Gau, M. R.; Zhao, Q.; Carroll, P. J.; Kagan, C. R., Longer Cations Increase Energetic Disorder in Excitonic 2D Hybrid Perovskites. *J. Phys. Chem. Lett.* **2019,** *10*, 1198.

237. R. Scott Rowland, R. T., Intermolecular Nonbonded Contact Distances in Organic Crystal Structures: Comparison with Distances Expected from van der Waals Radii. *J. Phys. Chem.* **1996,** *100*, 7384.

238. Bondi, A., van der Waals Volumes and Radii. *The Journal of Physical Chemistry* **1964,** *68*, 441.

239. Cavallo, G.; Metrangolo, P.; Milani, R.; Pilati, T.; Priimagi, A.; Resnati, G.; Terraneo, G., The Halogen Bond. *Chemical Reviews* **2016,** *116*, 2478.

240. Mitzi, D. B., Synthesis, Crystal Structure, and Optical and Thermal Properties of (C4H9NH3)2MI4 (M = Ge, Sn, Pb). *Chemistry of Materials* **1996,** *8*, 791.

241. Billing, D. G.; Lemmerer, A., Synthesis, characterization and phase transitions of the inorganic–organic layered perovskite-type hybrids [(CnH2n+1NH3)2PbI4] (n = 12, 14, 16 and 18). *New J. Chem., ,,* **2008,** *32*, 1736.

242. Safdari, M.; Fischer, A.; Xu, B.; Kloo, L.; Gardner, J. M., Structure and function relationships in alkylammonium lead(II) iodide solar cells. *J. Mater. Chem. A* **2015,** *3*, 9201.

243. Im, J.-H.; Chung, J.; Kim, S.-J.; Park, N.-G., Synthesis, structure, and photovoltaic property of a nanocrystalline 2H perovskite-type novel sensitizer (CH3CH2NH3)PbI3. *Nanoscale Research Letters* **2012,** *7*, 353.

244. Billing, D. G.; Lemmerer, A., Synthesis, characterization and phase transitions in the inorganic–organic layered perovskite-type hybrids [(CnH2n + 1NH3)2PbI4], n = 4, 5 and 6. *Acta Crystallographica Section B* **2007,** *63*, 735.

245. Momma, K.; Izumi, F., VESTA: A Three-Dimensional Visualization System for Electronic and Structural Analysis. *Journal of Applied Crystallography* **2008,** *41*, 653.

246. Robinson, K.; Gibbs, G. V.; Ribbe, P. H., Quadratic Elongation: A Quantitative Measure of Distortion in Coordination Polyhedra. *Science* **1971,** *172*, 567.

247. Robinson, K.; Gibbs, G. V.; Ribbe, P. H., Quadratic Elongation: A Quantitative Measure of Distortion in Coordination Polyhedra. **1971,** *172*, 567.

248. XXX, *In all cases, the PL lifetime was < 1.5 ns and the PL quantum yield was < 1%, which is consistent with other n=1 2D HOIPs (see ref. XXX).* .

249. Tanaka, K.; Takahashi, T.; Ban, T.; Kondo, T.; Uchida, K.; Miura, N., Comparative study on the excitons in lead-halide-based perovskite-type crystals CH3NH3PbBr3 CH3NH3PbI3. *Solid State Communications* **2003,** *127*, 619.

250. Noh, J. H.; Im, S. H.; Heo, J. H.; Mandal, T. N.; Seok, S. I., Chemical Management for Colorful, Efficient, and Stable Inorganic–Organic Hybrid Nanostructured Solar Cells. *Nano Letters* **2013,** *13*, 1764.

251. Xing, J.; Yan, F.; Zhao, Y.; Chen, S.; Yu, H.; Zhang, Q.; Zeng, R.; Demir, H. V.; Sun, X.; Huan, A.; Xiong, Q., High-Efficiency Light-Emitting Diodes of Organometal Halide Perovskite Amorphous Nanoparticles. *ACS Nano* **2016,** *10*, 6623.

252. Filip, M. R.; Eperon, G. E.; Snaith, H. J.; Giustino, F., Steric engineering of metal-halide perovskites with tunable optical band gaps. *Nature Communications* **2014,** *5*, 5757.

253. Borriello, I.; Cantele, G.; Ninno, D., Ab initio investigation of hybrid organic-inorganic perovskites based on tin halides. *Physical Review B* **2008,** *77*, 235214.

254. Eperon, G. E.; Stranks, S. D.; Menelaou, C.; Johnston, M. B.; Herz, L. M.; Snaith, H. J., Formamidinium lead trihalide: a broadly tunable perovskite for efficient planar heterojunction solar cells. *Energy & Environmental Science* **2014,** *7*, 982.

255. Stoumpos, C. C.; Kanatzidis, M. G., The Renaissance of Halide Perovskites and Their Evolution as Emerging Semiconductors. *Accounts of Chemical Research* **2015,** *48*, 2791.

256. Meloni, S.; Palermo, G.; Ashari-Astani, N.; Grätzel, M.; Rothlisberger, U., Valence and conduction band tuning in halide perovskites for solar cell applications. *Journal of Materials Chemistry A* **2016,** *4*, 15997.

257. Prasanna, R.; Gold-Parker, A.; Leijtens, T.; Conings, B.; Babayigit, A.; Boyen, H.-G.; Toney, M. F.; McGehee, M. D., Band Gap Tuning via Lattice Contraction and Octahedral Tilting in Perovskite Materials for Photovoltaics. *Journal of the American Chemical Society* **2017,** *139*, 11117.

258. Dolomanov, O. V.; Bourhis, L. J.; Gildea, R. J.; Howard, J. A. K.; Puschmann, H., OLEX2: a complete structure solution, refinement and analysis program. *Journal of Applied Crystallography* **2009,** *42*, 339.

259. Sheldrick, G., SHELXT - Integrated space-group and crystal-structure determination. *Acta Crystallographica Section A* **2015,** *71*, 3.

260. Sheldrick, G., Crystal structure refinement with SHELXL. *Acta Crystallographica Section C* **2015,** *71*, 3.

261. Tremblay, M.-H.; Bacsa, J.; Zhao, B.; Pulvirenti, F.; Barlow, S.; Marder, S. R., Structures of (4-Y-C6H4CH2NH3)2PbI4 {Y = H, F, Cl, Br, I}: Tuning of Hybrid Organic

Inorganic Perovskite Structures from Ruddlesden–Popper to Dion–Jacobson Limits. *Chemistry of Materials* **2019,** *31*, 6145.

262. Hu, J.; Oswald, I. W. H.; Stuard, S. J.; Nahid, M. M.; Zhou, N.; Williams, O. S.; Gui, Z.; Yan, L.; Hu, H.; Chen, Z.; Xiao, X.; Lin, Y.; Huang, J.; Moran, A. M.; Ade, H.; Neilson, J. R.; You, W., CCDC 1893383: Experimental Crystal Structure Determination. *CSD Communication* **2019**.

263. Wang, G.-E.; Sun, C.; Wang, M.-S.; Guo, G.-C., Semiconducting crystalline inorganic–organic hybrid metal halide nanochains. *Nanoscale* **2020,** *12*, 4771.

264. Yuan, Z.; Zhou, C.; Tian, Y.; Shu, Y.; Messier, J.; Wang, J. C.; van de Burgt, L. J.; Kountouriotis, K.; Xin, Y.; Holt, E.; Schanze, K.; Clark, R.; Siegrist, T.; Ma, B., One-dimensional organic lead halide perovskites with efficient bluish white-light emission. *Nature Communications* **2017,** *8*, 14051.

265. Zhang, H.; Yu, S.-S.; Duan, H.-B., A hybrid crystal with high dielectric constant and relaxation dielectric behavior. *Inorganic Chemistry Communications* **2018,** *93*, 1.

266. Matsuishi, K.; Kubo, Y.; Ichikawa, T.; Onari, S., Optical Absorption, Photoluminescence and Photoconductivity of Organic-Inorganic One-Dimensional Semiconductors C5H10NH2PbI3 and [NH2C(I)=NH2]3PbI5. *AIP Conference Proceedings* **2005,** *772*, 1075.

267. Koutselas, I. B.; Mitzi, D. B.; Papavassiliou, G. C.; Papaioannou, G. J.; Krautscheid, H., Optical and related properties of natural one-dimensional semiconductors based on PbI and SnI units. *Synthetic Metals* **1997,** *86*, 2171.

268. Wang, C.-H.; Du, H.-J.; Li, Y.; Niu, Y.-Y.; Hou, H.-W., Crystal structures and photocatalytic properties of two novel iodoplumbate hybrids templated by multivalent organic cations. *New Journal of Chemistry* **2015,** *39*, 7372.

269. Zeb, A.; Sun, Z.; Khan, A.; Zhang, S.; Khan, T.; Asghar, M. A.; Luo, J., [C6H14N]PbI3: a one-dimensional perovskite-like order–disorder phase transition material with semiconducting and switchable dielectric attributes. *Inorg. Chem. Front.* **2018,** *5*, 897.

270. Li, T.; Zeidell, A. M.; Findik, G.; Dunlap-Shohl, W. A.; Euvrard, J.; Gundogdu, K.; Jurchescu, O. D.; Mitzi, D. B., Phase-Pure Hybrid Layered Lead Iodide Perovskite Films Based on a Two-Step Melt-Processing Approach. *Chem. Mater.* **2019,** *31*, 4267.

271. Marchal, N.; Van Gompel, W.; Gélvez-Rueda, M. C.; Vandewal, K.; Van Hecke, K.; Boyen, H.-G.; Conings, B.; Herckens, R.; Maheshwari, S.; Lutsen, L.; Quarti, C.; Grozema, F. C.; Vanderzande, D.; Beljonne, D., Lead-Halide Perovskites Meet Donor–Acceptor Charge-Transfer Complexes. *Chemistry of Materials* **2019,** *31*, 6880.

272. Nagami, A.; Okamura, K.; Ishihara, T., Optical properties of a quantum wire crystal, C5H10NH2PbI3. *Physica B: Condensed Matter* **1996,** *227*, 346.

273. Seth, C.; Jana, D.; Jindal, V.; Khushalani, D.; Ghosh, S., One-Dimensional Behavior of Imidazolium Lead Iodide. *The Journal of Physical Chemistry C* **2019,** *123*, 16449.

274. Gao, L.; Spanopoulos, I.; Ke, W.; Huang, S.; Hadar, I.; Chen, L.; Li, X.; Yang, G.; Kanatzidis, M. G., Improved Environmental Stability and Solar Cell Efficiency of (MA,FA)PbI3 Perovskite Using a Wide-Band-Gap 1D Thiazolium Lead Iodide Capping Layer Strategy. *ACS Energy Letters* **2019,** *4*, 1763.

275. Pham, N. D.; Yang, Y.; Hoang, M. T.; Wang, T.; Tiong, V. T.; Wilson, G. J.; Wang, H., 1D Pyrrolidinium Lead Iodide for Efficient and Stable Perovskite Solar Cells. *Energy Technology* **2020,** *8*, 1900918.

276. Bi, D.; Gao, P.; Scopelliti, R.; Oveisi, E.; Luo, J.; Grätzel, M.; Hagfeldt, A.; Nazeeruddin, M. K., High-Performance Perovskite Solar Cells with Enhanced Environmental Stability Based on Amphiphile-Modified CH3NH3PbI3. *Advanced Materials* **2016,** *28*, 2910.

277. Elsenety, M. M.; Antoniadou, M.; Balis, N.; Kaltzoglou, A.; Sygellou, L.; Stergiou, A.; Tagmatarchis, N.; Falaras, P., Stability Improvement and Performance Reproducibility Enhancement of Perovskite Solar Cells Following (FA/MA/Cs)PbI3–xBrx/(CH3)3SPbI3 Dimensionality Engineering. *ACS Applied Energy Materials* **2020,** *3*, 2465.

278. Safdari, M.; Phuyal, D.; Philippe, B.; Svensson, P. H.; Butorin, S. M.; Kvashnina, K. O.; Rensmo, H.; Kloo, L.; Gardner, J. M., Impact of synthetic routes on the structural and physical properties of butyl-1,4-diammonium lead iodide semiconductors. *Journal of Materials Chemistry A* **2017,** *5*, 11730.

279. Gao, P.; Bin Mohd Yusoff, A. R.; Nazeeruddin, M. K., Dimensionality engineering of hybrid halide perovskite light absorbers. *Nature Communications* **2018,** *9*, 5028.

280. Hu, J.; Oswald, I. W. H.; Stuard, S. J.; Nahid, M. M.; Zhou, N.; Williams, O. S.; Gui, Z.; Yan, L.; Hu, H.; Chen, Z.; Xiao, X.; Lin, Y.; Huang, J.; Moran, A. M.; Ade, H.; Neilson, J. R.; You, W., *CSD Communication* **2019**.

281. Discekici, E. H.; Treat, N. J.; Poelma, S. O.; Mattson, K. M.; Hudson, Z. M.; Luo, Y.; Hawker, C. J.; de Alaniz, J. R., A highly reducing metal-free photoredox catalyst: design and application in radical dehalogenations. *Chemical Communications* **2015,** *51*, 11705.

282. Boyington, A. J.; Seath, C. P.; Zearfoss, A. M.; Xu, Z.; Jui, N. T., Catalytic Strategy for Regioselective Arylethylamine Synthesis. *Journal of the American Chemical Society* **2019,** *141*, 4147.

283. Li, S.; Cai, L.; Ji, H.; Yang, L.; Li, G., Pd(II)-catalysed meta-C–H functionalizations of benzoic acid derivatives. *Nature Communications* **2016,** *7*, 10443.

284. Liu, M.-C.; Lin, T.-S.; Penketh, P.; Sartorelli, A. C., Synthesis and Antitumor Activity of 4- and 5-Substituted Derivatives of Isoquinoline-1-carboxaldehyde Thiosemicarbazone. *Journal of Medicinal Chemistry* **1995,** *38*, 4234.

285. Mukherjee, A.; Srimani, D.; Chakraborty, S.; Ben-David, Y.; Milstein, D., Selective Hydrogenation of Nitriles to Primary Amines Catalyzed by a Cobalt Pincer Complex. *Journal of the American Chemical Society* **2015,** *137*, 8888.

286. Pensa, A. V.; Cinelli, M. A.; Li, H.; Chreifi, G.; Mukherjee, P.; Roman, L. J.; Martásek, P.; Poulos, T. L.; Silverman, R. B., Hydrophilic, Potent, and Selective 7-Substituted 2-Aminoquinolines as Improved Human Neuronal Nitric Oxide Synthase Inhibitors. *Journal of Medicinal Chemistry* **2017,** *60*, 7146.

287. Fontán, N.; García-Domínguez, P.; Álvarez, R.; de Lera, Á. R., Novel symmetrical ureas as modulators of protein arginine methyl transferases. *Bioorganic & Medicinal Chemistry* **2013,** *21*, 2056.

288. Kresse, G.; Furthmüller, J., Efficiency of ab-initio total energy calculations for metals and semiconductors using a plane-wave basis set. *Computational Materials Science* **1996,** *6*, 15.

289. Kresse, G.; Joubert, D., From ultrasoft pseudopotentials to the projector augmented-wave method. *Physical Review B* **1999,** *59*, 1758.

290. Perdew, J. P.; Burke, K.; Ernzerhof, M., Generalized Gradient Approximation Made Simple. *Physical Review Letters* **1996,** *77*, 3865.

291. Grimme, S.; Antony, J.; Ehrlich, S.; Krieg, H., A consistent and accurate ab initio parametrization of density functional dispersion correction (DFT-D) for the 94 elements H-Pu. *The Journal of Chemical Physics* **2010,** *132*, 154104.

292. Beck, H.; Gehrmann, C.; Egger, D. A., Structure and binding in halide perovskites: Analysis of static and dynamic effects from dispersion-corrected density functional theory. *APL Materials* **2019,** *7*, 021108.

293. Krukau, A. V.; Vydrov, O. A.; Izmaylov, A. F.; Scuseria, G. E., Influence of the exchange screening parameter on the performance of screened hybrid functionals. *The Journal of Chemical Physics* **2006,** *125*, 224106.

294. Heyd, J.; Scuseria, G. E.; Ernzerhof, M., Hybrid functionals based on a screened Coulomb potential. *The Journal of Chemical Physics* **2003,** *118*, 8207.

295. Steiner, S.; Khmelevskyi, S.; Marsmann, M.; Kresse, G., Calculation of the magnetic anisotropy with projected-augmented-wave methodology and the case study of disordered Fe 1− x Co x alloys. *Physical Review B* **2016,** *93*, 224425.

296. Li, T.; Dunlap-Shohl, W. A.; Han, Q.; Mitzi, D. B., Melt Processing of Hybrid Organic–Inorganic Lead Iodide Layered Perovskites. *Chemistry of Materials* **2017,** *29*, 6200.

297. Smith, I. C.; Smith, M. D.; Jaffe, A.; Lin, Y.; Karunadasa, H. I., Between the Sheets: Postsynthetic Transformations in Hybrid Perovskites. *Chemistry of Materials* **2017,** *29*, 1868.

298. Beaton, H.; Hamley, P.; Nicholls, D. J.; Tinker, A. C.; Wallace, A. V., 3,4-Dihydro-1-isoquinolinamines: A novel class of nitric oxide synthase inhibitors with a range of isoform selectivity and potency. *Bioorganic & Medicinal Chemistry Letters* **2001,** *11*, 1023.

299. Zhou, C.; Lin, H.; Tian, Y.; Yuan, Z.; Clark, R.; Chen, B.; van de Burgt, L. J.; Wang, J. C.; Zhou, Y.; Hanson, K.; Meisner, Q. J.; Neu, J.; Besara, T.; Siegrist, T.; Lambers, E.; Djurovich, P.; Ma, B., Luminescent zero-dimensional organic metal halide hybrids with near-unity quantum efficiency. *Chemical Science* **2018,** *9*, 586.

300. Mokhnache, O.; Boughzala, H., Crystal structure of a new hybrid compound based on an iodido-plumbate(II) anionic motif. *Acta crystallographica. Section E, Crystallographic communications* **2016,** *72*, 56.

301. Amat, A.; Mosconi, E.; Ronca, E.; Quarti, C.; Umari, P.; Nazeeruddin, M. K.; Grätzel, M.; De Angelis, F., Cation-Induced Band-Gap Tuning in Organohalide Perovskites: Interplay of Spin–Orbit Coupling and Octahedra Tilting. *Nano Letters* **2014,** *14*, 3608.

302. Tsai, H.; Nie, W.; Blancon, J.-C.; Stoumpos, C. C.; Asadpour, R.; Harutyunyan, B.; Neukirch, A. J.; Verduzco, R.; Crochet, J. J.; Tretiak, S.; Pedesseau, L.; Even, J.; Alam, M. A.; Gupta, G.; Lou, J.; Ajayan, P. M.; Bedzyk, M. J.; Kanatzidis, M. G.; Mohite, A. D., High-efficiency two-dimensional Ruddlesden–Popper perovskite solar cells. *Nature* **2016,** *536*, 312.

303. Blancon, J. C.; Tsai, H.; Nie, W.; Stoumpos, C. C.; Pedesseau, L.; Katan, C.; Kepenekian, M.; Soe, C. M. M.; Appavoo, K.; Sfeir, M. Y.; Tretiak, S.; Ajayan, P. M.; Kanatzidis, M. G.; Even, J.; Crochet, J. J.; Mohite, A. D., Extremely efficient internal exciton dissociation through edge states in layered 2D perovskites. *Science* **2017,** *355*, 1288.

304. Lin, H.; Zhou, C.; Tian, Y.; Besara, T.; Neu, J.; Siegrist, T.; Zhou, Y.; Bullock, J.; Schanze, K. S.; Ming, W.; Du, M.-H.; Ma, B., Bulk assembly of organic metal halide nanotubes. *Chemical Science* **2017,** *8*, 8400.

305. Zhou, C.; Lin, H.; Lee, S.; Chaaban, M.; Ma, B., Organic–inorganic metal halide hybrids beyond perovskites. *Materials Research Letters* **2018,** *6*, 552.

306. Macrae, C. F.; Edgington, P. R.; McCabe, P.; Pidcock, E.; Shields, G. P.; Taylor, R.; Towler, M.; van de Streek, J., Mercury: Visualization and Analysis of Crystal Structures. *J. Appl. Crystallogr.* **2006,** *39*, 453.

307. Dolomanov, O. V.; Bourhis, L. J.; Gildea, R. J.; Howard, J. A. K.; Puschmann, H., OLEX2: A Complete Structure Solution, Refinement and Analysis Program. *J. Appl. Crystallogr.* **2009,** *42*, 339.

308. Sheldrick, G., SHELXT - Integrated Space-Group and Crystal-Structure Determination. *Acta Crystallogr. A* **2015,** *71*, 3.

309. Sheldrick, G., Crystal Structure Refinement with SHELXL. *Acta Crystallogr. C* **2015,** *71*, 3.

310. Daszkiewicz, M., Importance of O···N interaction between nitro groups in crystals. *CrystEngComm* **2013,** *15*, 10427.

311. Mitzi, D. B., Organic−Inorganic Perovskites Containing Trivalent Metal Halide Layers: The Templating Influence of the Organic Cation Layer. *Inorganic Chemistry* **2000,** *39*, 6107.

312. Ueda, T. S., K.; Ohki, H.; Okuda, T., *Z. Naturforsch* **1996,** *51a*, 4.

313. Vanderhart, D. L.; Earl, W. L.; Garroway, A. N., Resolution in 13C NMR of organic solids using high-power proton decoupling and magic-angle sample spinning. *Journal of Magnetic Resonance (1969)* **1981,** *44*, 361.

314. Robinson, K.; Gibbs, G. V.; Ribbe, P. H., Quadratic Elongation: A Quantitative Measure of Distortion in Coordination Polyhedra. *Science* **1971,** *172*, 567.

315. Herzfeld, J.; Berger, A. E., Sideband intensities in NMR spectra of samples spinning at the magic angle. *The Journal of Chemical Physics* **1980,** *73*, 6021.

316. Arakcheeva, A.; Chernyshov, D.; Spina, M.; Forró, L.; Horvath, E., CH 3 NH 3 PbI 3 : precise structural consequences of water absorption at ambient conditions. *Acta Crystallographica Section B Structural Science, Crystal Engineering and Materials* **2016,** *72*.

317. van Gorkom, L. C. M.; Hook, J. M.; Logan, M. B.; Hanna, J. V.; Wasylishen, R. E., Solid-state lead-207 NMR of lead(II) nitrate: Localized heating effects at high magic angle spinning speeds. *Magnetic Resonance in Chemistry* **1995,** *33*, 791.

318. Neutzner, S.; Thouin, F.; Cortecchia, D.; Petrozza, A.; Silva, C.; Srimath Kandada, A. R., Exciton-polaron spectral structures in two-dimensional hybrid lead-halide perovskites. *Physical Review Materials* **2018,** *2*, 064605.

319. Thouin, F.; Neutzner, S.; Cortecchia, D.; Dragomir, V. A.; Soci, C.; Salim, T.; Lam, Y. M.; Leonelli, R.; Petrozza, A.; Kandada, A. R. S.; Silva, C., Stable biexcitons in two-dimensional metal-halide perovskites with strong dynamic lattice disorder. *Physical Review Materials* **2018,** *2*, 034001.

320. Smith, M. D.; Jaffe, A.; Dohner, E. R.; Lindenberg, A. M.; Karunadasa, H. I., Structural origins of broadband emission from layered Pb–Br hybrid perovskites. *Chemical Science* **2017,** *8*, 4497.

321. Stranks, S. D.; Burlakov, V. M.; Leijtens, T.; Ball, J. M.; Goriely, A.; Snaith, H. J., Recombination Kinetics in Organic-Inorganic Perovskites: Excitons, Free Charge, and Subgap States. *Physical Review Applied* **2014,** *2*, 034007.

322. Baumann, A.; Väth, S.; Rieder, P.; Heiber, M. C.; Tvingstedt, K.; Dyakonov, V., Identification of Trap States in Perovskite Solar Cells. *The Journal of Physical Chemistry Letters* **2015,** *6*, 2350.

323. Zhou, C.; Lin, H.; Lee, S.; Chaaban, M.; Ma, B., Organic–inorganic metal halide hybrids beyond perovskites. *Mater. Res. Lett.* **2018,** *6*, 552.

324. Mao, L.; Stoumpos, C. C.; Kanatzidis, M. G., Two-Dimensional Hybrid Halide Perovskites: Principles and Promises. *J. Am. Chem. Soc.* **2019,** *141*, 1171.

325. Mao, L.; Guo, P.; Kepenekian, M.; Hadar, I.; Katan, C.; Even, J.; Schaller, R. D.; Stoumpos, C. C.; Kanatzidis, M. G., Structural Diversity in White-Light-Emitting Hybrid Lead Bromide Perovskites. *J. Am. Chem. Soc.* **2018,** *140*, 13078.

326. Amat, A.; Mosconi, E.; Ronca, E.; Quarti, C.; Umari, P.; Nazeeruddin, M. K.; Grätzel, M.; De Angelis, F., Cation-Induced Band-Gap Tuning in Organohalide Perovskites: Interplay of Spin–Orbit Coupling and Octahedra Tilting. *Nano Lett.* **2014,** *14*, 3608.

327. Mao, L.; Ke, W.; Pedesseau, L.; Wu, Y.; Katan, C.; Even, J.; Wasielewski, M. R.; Stoumpos, C. C.; Kanatzidis, M. G., Hybrid Dion–Jacobson 2D Lead Iodide Perovskites. *J. Am. Chem. Soc.* **2018,** *140*, 3775.

328. Du, K.-z.; Tu, Q.; Zhang, X.; Han, Q.; Liu, J.; Zauscher, S.; Mitzi, D. B., Two-Dimensional Lead(II) Halide-Based Hybrid Perovskites Templated by Acene Alkylamines: Crystal Structures, Optical Properties, and Piezoelectricity. *Inorg. Chem.* **2017,** *56*, 9291.

329. Mokhnache, O.; Boughzala, H., Crystal structure of a new hybrid compound based on an iodidoplumbate(II) anionic motif. *Acta Crystallogr. E* **2016,** *72*, 56.

330. Wang, S.; Mitzi, D. B.; Feild, C. A.; Guloy, A., Synthesis and Characterization of [NH2C(I):NH2]3MI5 (M = Sn, Pb): Stereochemical Activity in Divalent Tin and Lead Halides Containing Single .ltbbrac.110.rtbbrac. Perovskite Sheets. *J. Am. Chem. Soc.* **1995,** *117*, 5297.

331. Mitzi, D. B., Templating and structural engineering in organic–inorganic perovskites. *J. Chem. Soc., Dalton Trans.* **2001**, 1.

332. Liu, J.-J.; Guan, Y.-F.; Jiao, C.; Lin, M.-J.; Huang, C.-C.; Dai, W.-X., A panchromatic hybrid crystal of iodoplumbate nanowires and J-aggregated naphthalene diimides with long-lived charge-separated states. *Dalton Trans.* **2015,** *44*, 5957.

333. Li, X.; Yang, J.; Song, Z.; Chen, R.; Ma, L.; Li, H.; Jia, J.; Meng, J.; Li, X.; Yi, M.; Sun, X., Naphthalene Diimide Ammonium Directed Single-Crystalline Perovskites with "Atypical" Ambipolar Charge Transport Signatures in Two-Dimensional Limit. *ACS Appl. Energy Mater.* **2018,** *1*, 4467.

334. Avinash, M. B.; Verheggen, E.; Schmuck, C.; Govindaraju, T., Self-Cleaning Functional Molecular Materials. *Angew. Chem. Int. Ed.* **2012,** *51*, 10324.

335. Licchelli, M.; Linati, L.; Orbelli Biroli, A.; Perani, E.; Poggi, A.; Sacchi, D., Metal-Induced Assembling/Disassembling of Fluorescent Naphthalenediimide Derivatives Signalled by Excimer Emission. *Chem. Eur. J.* **2002,** *8*, 5161.

336. Blank, H.; Delavignette, P.; Amelinckx, S., Dislocations and wide stacking faults in wurtzite type crystals: Zinc sulfide and aluminium nitride. *physica status solidi (b)* **1962,** *2*, 1660.

337. Mao, L.; Wu, Y.; Stoumpos, C. C.; Wasielewski, M. R.; Kanatzidis, M. G., White-Light Emission and Structural Distortion in New Corrugated Two-Dimensional Lead Bromide Perovskites. *J. Am. Chem. Soc.* **2017,** *139*, 5210.

338. Louvain, N.; Bi, W.; Mercier, N.; Buzaré, J.-Y.; Legein, C.; Corbel, G., PbnI4n+2(2n+2)− ribbons (n = 3, 5) as dimensional reductions of 2D perovskite layers in cystamine cation based hybrids, also incorporating iodine molecules or reversible guest water molecules. *Dalton Trans.* **2007**.

339. XXX, *No thermal transitions were observed when the material was scanned from -90 to 125 °C under nitrogen atmosphere (Figure S6).*

340. Krautscheid, H.; Vielsack, F.; Klaassen, N., Polymere Iodoplumbate – Synthese und Kristallstrukturen von (Pr3N–C2H4–NPr3)[Pb6I14(dmf)2] · 4DMF, (Pr3N–C2H4–NPr3)[Pb(dmf)6][Pb5I14] · DMF und (Me3N–C2H4–NMe3)2[Pb2I7]I. *Z. Anorg. Allg. Chem.* **1998,** *624*, 807.

341. Krautscheid, H.; Lekieffre, J.-F.; Besinger, J., Iodoplumbate mit polymeren Anionen – Synthese und Kristallstrukturen von [Na3(OCMe2)12][Pb4I11(OCMe2)], (Ph4P)2[Pb5I12] und (Ph4P)4[Pb15I34(dmf)6]. *Z. Anorg. Allg. Chem.* **1996,** *622*, 1781.

342. Cao, J.; Jing, X.; Yan, J.; Hu, C.; Chen, R.; Yin, J.; Li, J.; Zheng, N., Identifying the Molecular Structures of Intermediates for Optimizing the Fabrication of High-Quality Perovskite Films. *J. Am. Chem. Soc.* **2016,** *138*, 9919.

343. Li, L.; Zhao, D.; Liu, Z.; Zhang, D.; Hu, Z.; Li, K.; Yang, J., Crystal structure of the lead-containing organic-inorganic hybrid: (C18H26N2)3[Pb4I14(DMSO)2].2DMSO. *Acta Crystallogr. E* **2018,** *74*, 1878.

344. Zhang, L.; Tang, C.; Zheng, W.; Jiang, W.; Jia, D., Solvothermal Synthesis, Crystal Structures, and Photocatalytic Properties of Iodoplumbate Hybrids with Nickel(II) Complex Templates. *Eur. J. Inorg. Chem.* **2019,** *2019*, 237.

345. Lermer, C.; Harm, S. P.; Birkhold, S. T.; Jaser, J. A.; Kutz, C. M.; Mayer, P.; Schmidt-Mende, L.; Lotsch, B. V., Benzimidazolium Lead Halide Perovskites: Effects of Anion Substitution and Dimensionality on the Bandgap. *Z. Anorg. Allg. Chem.* **2016,** *642*, 1369.

346. Hao, Y.; Qiu, Z.; Zhang, X.; Wei, Z.; Yao, J.; Cai, H., Series of 2D multilayered perovskites constructed by slicing the 3D [(CH3NH3)PbI3] with 4-fluorobenzylamine. *Inorg. Chem. Commun.* **2018,** *97*, 134.

347. Cai, M.; Wang, G.-E.; Yao, M.; Wu, G.; Li, Y.; Xu, G., Semiconductive 1D nanobelt iodoplumbate hybrid with high humidity response. *Inorg. Chem. Commun.* **2018,** *93*, 42.

348. Petrov, A. A.; Sokolova, I. P.; Belich, N. A.; Peters, G. S.; Dorovatovskii, P. V.; Zubavichus, Y. V.; Khrustalev, V. N.; Petrov, A. V.; Grätzel, M.; Goodilin, E. A.; Tarasov, A. B., Crystal Structure of DMF-Intermediate Phases Uncovers the Link Between CH3NH3PbI3 Morphology and Precursor Stoichiometry. *Journal of Physical Chemistry C* **2017,** *121*, 20739.

349. Li, H.-H.; Chen, Z.-R.; Cheng, L.-C.; Wang, Y.-J.; Feng, M.; Wang, M., Hybrid Polymeric Iodoplumbates Constructed from Morpholine and Its Derivatives: Structures and Properties. *Dalton Trans.* **2010,** *39*, 11000.

350. Harrowfield, J. M.; Maghaminia, S.; Soudi, A. A., Polyhapto-Aromatic Interactions in Lead(II) Coordination. *Inorg. Chem.* **2004,** *43*, 1810.

351. Payehghadr, M.; Yousefi, S.; Morsali, A., Thermal, structural and solution studies of a new lead(II) coordination polymer with η4 Pb–C interactions. *Journal of Organometallic Chemistry* **2008,** *693*, 2514.

352. Chen, B.-G., Polymeric haloplumbates(II) templated by ethoxycarbonylmethyl viologen: Structure and enchanced thermochromism behavior. *Inorg. Nano-Met. Chem.* **2017,** *47*, 1220.

353. Véron, A. C.; Linden, A.; Leclaire, N. A.; Roedern, E.; Hu, S.; Ren, W.; Rentsch, D.; Nüesch, F. A., One-Dimensional Organic–Inorganic Hybrid Perovskite Incorporating Near-Infrared-Absorbing Cyanine Cations. *J. Phys. Chem. Lett.* **2018,** *9*, 2438.

354. Wang, C.-H.; Ma, C.-J.; Huang, Z.-P.; Zai, Y.-X.; Yang, Q.; Li, L.; Liang, Y.; Niu, Y.-Y., Bis(imidazole) Cation Templates and Subtle Effect: Syntheses and Characterization of Three New Pb(II) Halide Supramolecular Polymers. *J. Clust. Sci.* **2015,** *26*, 1027.

355. Maughan, A. E.; Kurzman, J. A.; Neilson, J. R., Hybrid Inorganic–Organic Materials with an Optoelectronically Active Aromatic Cation: (C7H7)2SnI6 and C7H7PbI3. *Inorg. Chem.* **2015,** *54*, 370.

356. Krautscheid, H.; Vielsack, F., [Pb18I44]8- - An Iodoplumbate with an Unusual Structure. *Angew. Chem. Int. Ed. Engl.* **1995,** *34*, 2035.

357. Chakravarthy, V.; M. Guloy, A., Synthesis and structure of a new layered organic–inorganic compound containing unique chains of PbI2. *Chem. Commun.* **1997**, 697.

358. Safdari, M.; Fischer, A.; Xu, B.; Kloo, L.; Gardner, J. M., Structure and function relationships in alkylammonium lead(ii) iodide solar cells. *J. Mater. Chem. A* **2015,** *3*, 9201.

359. Tershansy, M. A.; Goforth, A. M.; Peterson, L.; Burns, M. C.; Smith, M. D.; zur Loye, H.-C., Syntheses and crystal structures of new chain-containing iodometallate

compounds: [H1,10-phen](H2O)1.41[AgI2], [H1,10-phen](H2O)1.42[CuI2]; [Co(tpy)2][Bi2I8], [Fe(tpy)2][Bi2I8]; [Co(1,10-phen)3][Pb3I8]·H2O, and [Fe(1,10-phen)3][Pb3I8]·0.5(H2O). *Solid State Sciences* **2007,** *9*, 895.

360. Miyamae, H.; Nishikawa, H.; Hagimoto, K.; Hihara, G.; Nagata, M., Crystal Structures of Compounds Obtained from Lead(II) Iodide-Hexamethylenetetramine System, [C6H13N4]2[Pb3I8(C6H12N4)2] and [C6H13N4][PbI3M3]. *Chemistry Letters* **1988,** *17*, 1907.

361. Vijaya Prakash, G.; Pradeesh, K.; Ratnani, R.; Saraswat, K.; Light, M. E.; Baumberg, J. J., Structural and optical studies of local disorder sensitivity in natural organic–inorganic self-assembled semiconductors. *J. Phys. D Appl. Phys.* **2009,** *42*, 185405.

362. Nowak-Król, A.; Shoyama, K.; Stolte, M.; Würthner, F., Naphthalene and perylene diimides – better alternatives to fullerenes for organic electronics? *Chem. Commun.* **2018,** *54*, 13763.

363. Fujisawa, J.-i.; Tajima, N.; Tamaki, K.; Shimomura, M., Electronic Interactions between Inorganic Nanowires and Organic Electron Acceptors: Drastic Changes in Optical Response and Molecular Vibration. *J. Phys. Chem. C* **2007,** *111*, 1146.

364. Ofir, Y.; Zelichenok, A.; Yitzchaik, S., 1,4;5,8-naphthalene-tetracarboxylic diimide derivatives as model compounds for molecular layer epitaxy. *Journal of Materials Chemistry* **2006,** *16*, 2142.

365. Dawson, R. E.; Hennig, A.; Weimann, D. P.; Emery, D.; Ravikumar, V.; Montenegro, J.; Takeuchi, T.; Gabutti, S.; Mayor, M.; Mareda, J.; Schalley, C. A.; Matile, S., Experimental evidence for the functional relevance of anion–π interactions. *Nature Chemistry* **2010,** *2*, 533.

366. xxxx, *Most crystals were measured in the plane of the long axis, with the shorter dimension of the crystal perpendicular to the electrical contacts.* **xxxx**.

367. Peng, W.; Yin, J.; Ho, K.-T.; Ouellette, O.; De Bastiani, M.; Murali, B.; El Tall, O.; Shen, C.; Miao, X.; Pan, J.; Alarousu, E.; He, J.-H.; Ooi, B. S.; Mohammed, O. F.; Sargent, E.; Bakr, O. M., Ultralow Self-Doping in Two-dimensional Hybrid Perovskite Single Crystals. *Nano Letters* **2017,** *17*, 4759.

368. Stoumpos, C. C.; Malliakas, C. D.; Kanatzidis, M. G., Semiconducting Tin and Lead Iodide Perovskites with Organic Cations: Phase Transitions, High Mobilities, and Near-Infrared Photoluminescent Properties. *Inorg. Chem.* **2013,** *52*, 9019.

369. Gao, L.; Zeng, K.; Guo, J.; Ge, C.; Du, J.; Zhao, Y.; Chen, C.; Deng, H.; He, Y.; Song, H.; Niu, G.; Tang, J., Passivated Single-Crystalline CH3NH3PbI3 Nanowire Photodetector with High Detectivity and Polarization Sensitivity. *Nano Letters* **2016,** *16*, 7446.

370. Deng, H.; Yang, X.; Dong, D.; Li, B.; Yang, D.; Yuan, S.; Qiao, K.; Cheng, Y.-B.; Tang, J.; Song, H., Flexible and Semitransparent Organolead Triiodide Perovskite Network Photodetector Arrays with High Stability. *Nano Letters* **2015,** *15*, 7963.

371. Ball, J. M.; Lee, M. M.; Hey, A.; Snaith, H. J., Low-temperature processed meso-superstructured to thin-film perovskite solar cells. *Energy & Environmental Science* **2013,** *6*, 1739.

372. Baltakesmez, A.; Biber, M.; Tüzemen, S., Improved perovskite film quality and solar cell performances using dual single solution coating. *Journal of Applied Physics* **2017,** *122*, 085502.

373. Saliba, M.; Correa-Baena, J.-P.; Grätzel, M.; Hagfeldt, A.; Abate, A., Perovskite Solar Cells: From the Atomic Level to Film Quality and Device Performance. *Angewandte Chemie* **2018,** *57*, 2554.

374. Huang, F.; Li, M.; Siffalovic, P.; Cao, G.; Tian, J., From scalable solution fabrication of perovskite films towards commercialization of solar cells. *Energy & Environmental Science* **2019,** *12*, 518.

375. You, J.; Meng, L.; Song, T.-B.; Guo, T.-F.; Yang, Y.; Chang, W.-H.; Hong, Z.; Chen, H.; Zhou, H.; Chen, Q.; Liu, Y.; De Marco, N.; Yang, Y., Improved air stability of perovskite solar cells via solution-processed metal oxide transport layers. *Nature Nanotechnology* **2015,** *11*, 75.

376. Kaltenbrunner, M.; Adam, G.; Głowacki, E. D.; Drack, M.; Schwödiauer, R.; Leonat, L.; Apaydin, D. H.; Groiss, H.; Scharber, M. C.; White, M. S.; Sariciftci, N. S.; Bauer, S., Flexible high power-per-weight perovskite solar cells with chromium oxide–metal contacts for improved stability in air. *Nature Materials* **2015,** *14*, 1032.

377. Giordano, F.; Abate, A.; Correa Baena, J. P.; Saliba, M.; Matsui, T.; Im, S. H.; Zakeeruddin, S. M.; Nazeeruddin, M. K.; Hagfeldt, A.; Graetzel, M., Enhanced electronic properties in mesoporous TiO2 via lithium doping for high-efficiency perovskite solar cells. *Nature Communications* **2016,** *7*, 10379.

378. Wang, J. T.-W.; Wang, Z.; Pathak, S.; Zhang, W.; deQuilettes, D. W.; Wisnivesky-Rocca-Rivarola, F.; Huang, J.; Nayak, P. K.; Patel, J. B.; Mohd Yusof, H. A.; Vaynzof, Y.; Zhu, R.; Ramirez, I.; Zhang, J.; Ducati, C.; Grovenor, C.; Johnston, M. B.; Ginger, D. S.; Nicholas, R. J.; Snaith, H. J., Efficient perovskite solar cells by metal ion doping. *Energy & Environmental Science* **2016,** *9*, 2892.

379. Park, N.-G.; Grätzel, M.; Miyasaka, T.; Zhu, K.; Emery, K., Towards stable and commercially available perovskite solar cells. *Nature Energy* **2016,** *1*, 16152.

380. Niu, G.; Guo, X.; Wang, L., Review of recent progress in chemical stability of perovskite solar cells. *Journal of Materials Chemistry A* **2015,** *3*, 8970.

381. Jiang, Q.; Zhao, Y.; Zhang, X.; Yang, X.; Chen, Y.; Chu, Z.; Ye, Q.; Li, X.; Yin, Z.; You, J., Surface passivation of perovskite film for efficient solar cells. *Nature Photonics* **2019**.

382. Saliba, M.; Matsui, T.; Seo, J.-Y.; Domanski, K.; Correa-Baena, J.-P.; Nazeeruddin, M. K.; Zakeeruddin, S. M.; Tress, W.; Abate, A.; Hagfeldt, A.; Grätzel, M., Cesium-containing triple cation perovskite solar cells: improved stability, reproducibility and high efficiency. *Energy & Environmental Science* **2016,** *9*, 1989.

383. McMeekin, D. P.; Sadoughi, G.; Rehman, W.; Eperon, G. E.; Saliba, M.; Hörantner, M. T.; Haghighirad, A.; Sakai, N.; Korte, L.; Rech, B.; Johnston, M. B.; Herz, L. M.; Snaith, H. J., A mixed-cation lead mixed-halide perovskite absorber for tandem solar cells. *Science* **2016,** *351*, 151.

384. Habisreutinger, S. N.; Leijtens, T.; Eperon, G. E.; Stranks, S. D.; Nicholas, R. J.; Snaith, H. J., Carbon Nanotube/Polymer Composites as a Highly Stable Hole Collection Layer in Perovskite Solar Cells. *Nano Letters* **2014,** *14*, 5561.

385. Rakstys, K.; Paek, S.; Gao, P.; Gratia, P.; Marszalek, T.; Grancini, G.; Cho, K. T.; Genevicius, K.; Jankauskas, V.; Pisula, W.; Nazeeruddin, M. K., Molecular engineering of face-on oriented dopant-free hole transporting material for perovskite solar cells with 19% PCE. *Journal of Materials Chemistry A* **2017,** *5*, 7811.

386. Bi, D.; Xu, B.; Gao, P.; Sun, L.; Grätzel, M.; Hagfeldt, A., Facile synthesized organic hole transporting material for perovskite solar cell with efficiency of 19.8%. *Nano Energy* **2016,** *23*, 138.

387. Saliba, M.; Orlandi, S.; Matsui, T.; Aghazada, S.; Cavazzini, M.; Correa-Baena, J.-P.; Gao, P.; Scopelliti, R.; Mosconi, E.; Dahmen, K.-H.; De Angelis, F.; Abate, A.; Hagfeldt, A.; Pozzi, G.; Graetzel, M.; Nazeeruddin, M. K., A molecularly engineered hole-transporting material for efficient perovskite solar cells. *Nature Energy* **2016,** *1*, 15017.

388. Cao, J.; Wu, B.; Chen, R.; Wu, Y.; Hui, Y.; Mao, B.-W.; Zheng, N., Efficient, Hysteresis-Free, and Stable Perovskite Solar Cells with ZnO as Electron-Transport Layer: Effect of Surface Passivation. *Advanced Materials* **2018,** *30*, 1705596.

389. Liu, C.; Wang, K.; Du, P.; Meng, T.; Yu, X.; Cheng, S. Z. D.; Gong, X., High Performance Planar Heterojunction Perovskite Solar Cells with Fullerene Derivatives as the Electron Transport Layer. *ACS Applied Materials & Interfaces* **2015,** *7*, 1153.

390. Zhu, Z.; Bai, Y.; Liu, X.; Chueh, C.-C.; Yang, S.; Jen, A. K.-Y., Enhanced Efficiency and Stability of Inverted Perovskite Solar Cells Using Highly Crystalline SnO2 Nanocrystals as the Robust Electron-Transporting Layer. *Advanced Materials* **2016,** *28*, 6478.

391. Yu, Z.; Sun, L., Recent Progress on Hole-Transporting Materials for Emerging Organometal Halide Perovskite Solar Cells. *Advanced Energy Materials* **2015,** *5*, 1500213.

392. Chiang, T.-Y.; Fan, G.-L.; Jeng, J.-Y.; Chen, K.-C.; Chen, P.; Wen, T.-C.; Guo, T.-F.; Wong, K.-T., Functional p-Type, Polymerized Organic Electrode Interlayer in CH3NH3PbI3 Perovskite/Fullerene Planar Heterojunction Hybrid Solar Cells. *ACS Applied Materials & Interfaces* **2015,** *7*, 24973.

393. Xu, J.; Voznyy, O.; Comin, R.; Gong, X.; Walters, G.; Liu, M.; Kanjanaboos, P.; Lan, X.; Sargent, E. H., Crosslinked Remote-Doped Hole-Extracting Contacts Enhance Stability under Accelerated Lifetime Testing in Perovskite Solar Cells. *Advanced Materials* **2016,** *28*, 2807.

394. Chang, C.-C.; Tao, J.-H.; Tsai, C.-E.; Cheng, Y.-J.; Hsu, C.-S., Cross-linked Triarylamine-Based Hole-Transporting Layer for Solution-Processed PEDOT:PSS-Free Inverted Perovskite Solar Cells. *ACS Applied Materials & Interfaces* **2018,** *10*, 21466.

395. Zhang, Y.; Kou, C.; Zhang, J.; Liu, Y.; Li, W.; Bo, Z.; Shao, M., Crosslinked and dopant free hole transport materials for efficient and stable planar perovskite solar cells. *Journal of Materials Chemistry A* **2019,** *7*, 5522.

396. Li, Z. a.; Zhu, Z.; Chueh, C.-C.; Luo, J.; Jen, A. K.-Y., Facile Thiol-Ene Thermal Crosslinking Reaction Facilitated Hole-Transporting Layer for Highly Efficient and Stable Perovskite Solar Cells. *Advanced Energy Materials* **2016,** *6*, 1601165.

397. Schloemer, T. H.; Christians, J. A.; Luther, J. M.; Sellinger, A., Doping strategies for small molecule organic hole-transport materials: impacts on perovskite solar cell performance and stability. *Chemical Science* **2019,** *10*, 1904.

398. Li, W.; Dong, H.; Wang, L.; Li, N.; Guo, X.; Li, J.; Qiu, Y., Montmorillonite as bifunctional buffer layer material for hybrid perovskite solar cells with protection from corrosion and retarding recombination. *Journal of Materials Chemistry A* **2014,** *2*, 13587.

399. Li, J.; Rochester, C. W.; Jacobs, I. E.; Friedrich, S.; Stroeve, P.; Riede, M.; Moulé, A. J., Measurement of Small Molecular Dopant F4TCNQ and C60F36 Diffusion in Organic Bilayer Architectures. *ACS Applied Materials & Interfaces* **2015,** *7*, 28420.

400. Gao, Z. Q.; Mi, B. X.; Xu, G. Z.; Wan, Y. Q.; Gong, M. L.; Cheah, K. W.; Chen, C. H., An organic p-type dopant with high thermal stability for an organic semiconductor. *Chemical Communications* **2008**, 117.

401. Zhang, Y.-D.; Hreha, R. D.; Jabbour, G. E.; Kippelen, B.; Peyghambarian, N.; Marder, S. R., Photo-crosslinkable polymers as hole-transport materials for organic light-emitting diodes. *Journal of Materials Chemistry* **2002,** *12*, 1703.

402. Stranks, S. D.; Eperon, G. E.; Grancini, G.; Menelaou, C.; Alcocer, M. J. P.; Leijtens, T.; Herz, L. M.; Petrozza, A.; Snaith, H. J., Electron-Hole Diffusion Lengths Exceeding 1 Micrometer in an Organometal Trihalide Perovskite Absorber. *Science* **2013,** *342*, 341.

403. de Quilettes, D. W.; Vorpahl, S. M.; Stranks, S. D.; Nagaoka, H.; Eperon, G. E.; Ziffer, M. E.; Snaith, H. J.; Ginger, D. S., Impact of microstructure on local carrier lifetime in perovskite solar cells. *Science* **2015,** *348*, 683.

404. deQuilettes, D. W.; Koch, S.; Burke, S.; Paranji, R. K.; Shropshire, A. J.; Ziffer, M. E.; Ginger, D. S., Photoluminescence Lifetimes Exceeding 8 μs and Quantum Yields

Exceeding 30% in Hybrid Perovskite Thin Films by Ligand Passivation. *ACS Energy Letters* **2016,** *1*, 438.

405. Jeon, N. J.; Noh, J. H.; Kim, Y. C.; Yang, W. S.; Ryu, S.; Seok, S. I., Solvent engineering for high-performance inorganic–organic hybrid perovskite solar cells. *Nature Materials* **2014,** *13*, 897.

406. Ryu, S.; Noh, J. H.; Jeon, N. J.; Chan Kim, Y.; Yang, W. S.; Seo, J.; Seok, S. I., Voltage output of efficient perovskite solar cells with high open-circuit voltage and fill factor. *Energy & Environmental Science* **2014,** *7*, 2614.

407. Zhao, D.; Sexton, M.; Park, H.-Y.; Baure, G.; Nino, J. C.; So, F., High-Efficiency Solution-Processed Planar Perovskite Solar Cells with a Polymer Hole Transport Layer. *Advanced Energy Materials* **2015,** *5*, 1401855.

408. Domercq, B.; Hreha, R. D.; Zhang, Y.-D.; Haldi, A.; Barlow, S.; Marder, S. R.; Kippelen, B., Organic light-emitting diodes with multiple photocrosslinkable hole-transport layers. *Journal of Polymer Science B* **2003,** *41*, 2726.

409. Hreha, R. D.; Haldi, A.; Domercq, B.; Barlow, S.; Kippelen, B.; Marder, S. R., Synthesis of acrylate and norbornene polymers with pendant 2,7-bis(diarylamino)fluorene hole-transport groups. *Tetrahedron* **2004,** *60*, 7169.

410. Domercq, B.; Hreha, R. D.; Zhang, Y.-D.; Larribeau, N.; Haddock, J. N.; Schultz, C.; Marder, S. R.; Kippelen, B., Photo-Patternable Hole-Transport Polymers for Organic Light-Emitting Diodes. *Chemistry of Materials* **2003,** *15*, 1491.

411. Kimyonok, A.; Domercq, B.; Haldi, A.; Cho, J.-Y.; Carlise, J. R.; Wang, X.-Y.; Hayden, L. E.; Jones, S. C.; Barlow, S.; Marder, S. R.; Kippelen, B.; Weck, M., Norbornene-Based Copolymers with Iridium Complexes and Bis(carbazolyl)fluorene Groups in Their Side-Chains and Their Use in Light-Emitting Diodes. *Chemistry of Materials* **2007,** *19*, 5602.

412. Qi, Y.; Sajoto, T.; Barlow, S.; Kim, E.-G.; Brédas, J.-L.; Marder, S. R.; Kahn, A., Use of a High Electron-Affinity Molybdenum Dithiolene Complex to p-Dope Hole-Transport Layers. *Journal of the American Chemical Society* **2009,** *131*, 12530.

413. Yu, B.; Zhang, H.; Wu, J.; Li, Y.; Li, H.; Li, Y.; Shi, J.; Wu, H.; Li, D.; Luo, Y.; Meng, Q., Solvent-engineering toward CsPb(IxBr1−x)3 films for high-performance inorganic perovskite solar cells. *Journal of Materials Chemistry A* **2018,** *6*, 19810.

414. Ho-Baillie, A.; Zhang, M.; Lau, C. F. J.; Ma, F.-J.; Huang, S., Untapped Potentials of Inorganic Metal Halide Perovskite Solar Cells. *Joule* **2019,** *3*, 938.

415. Zhang, H.; Xue, L.; Han, J.; Fu, Y. Q.; Shen, Y.; Zhang, Z.; Li, Y.; Wang, M., New generation perovskite solar cells with solution-processed amino-substituted perylene diimide derivative as electron-transport layer. *Journal of Materials Chemistry A* **2016,** *4*, 8724.

416. Chaudhary, B.; Kulkarni, A.; Jena, A. K.; Ikegami, M.; Udagawa, Y.; Kunugita, H.; Ema, K.; Miyasaka, T., Poly(4-Vinylpyridine)-Based Interfacial Passivation to Enhance Voltage and Moisture Stability of Lead Halide Perovskite Solar Cells. *ChemSusChem* **2017,** *10*, 2473.

417. Petrus, M. L.; Schutt, K.; Sirtl, M. T.; Hutter, E. M.; Closs, A. C.; Ball, J. M.; Bijleveld, J. C.; Petrozza, A.; Bein, T.; Dingemans, T. J.; Savenije, T. J.; Snaith, H.; Docampo, P., New Generation Hole Transporting Materials for Perovskite Solar Cells: Amide-Based Small-Molecules with Nonconjugated Backbones. *Advanced Energy Materials* **2018,** *8*, 1801605.

418. Bi, D.; Yi, C.; Luo, J.; Décoppet, J.-D.; Zhang, F.; Zakeeruddin, Shaik M.; Li, X.; Hagfeldt, A.; Grätzel, M., Polymer-templated nucleation and crystal growth of perovskite films for solar cells with efficiency greater than 21%. *Nature Energy* **2016,** *1*, 16142.

419. Christians, J. A.; Habisreutinger, S. N.; Berry, J. J.; Luther, J. M., Stability in Perovskite Photovoltaics: A Paradigm for Newfangled Technologies. *ACS Energy Letters* **2018,** *3*, 2136.

420. Arabpour Roghabadi, F.; Alidaei, M.; Mousavi, S. M.; Ashjari, T.; Tehrani, A. S.; Ahmadi, V.; Sadrameli, S. M., Stability progress of perovskite solar cells dependent on the crystalline structure: From 3D ABX3 to 2D Ruddlesden–Popper perovskite absorbers. *Journal of Materials Chemistry A* **2019,** *7*, 5898.

421. Raza, E.; Aziz, F.; Ahmad, Z., Stability of organometal halide perovskite solar cells and role of HTMs: recent developments and future directions. *RSC Advances* **2018,** *8*, 20952.

422. Jena, A. K.; Numata, Y.; Ikegami, M.; Miyasaka, T., Role of spiro-OMeTAD in performance deterioration of perovskite solar cells at high temperature and reuse of the perovskite films to avoid Pb-waste. *Journal of Materials Chemistry A* **2018,** *6*, 2219.

423. Zhao, X.; Kim, H.-S.; Seo, J.-Y.; Park, N.-G., Effect of Selective Contacts on the Thermal Stability of Perovskite Solar Cells. *ACS Applied Materials & Interfaces* **2017,** *9*, 7148.

424. Sanchez, R. S.; Mas-Marza, E., Light-induced effects on Spiro-OMeTAD films and hybrid lead halide perovskite solar cells. *Solar Energy Materials and Solar Cells* **2016,** *158*, 189.

425. Domanski, K.; Correa-Baena, J.-P.; Mine, N.; Nazeeruddin, M. K.; Abate, A.; Saliba, M.; Tress, W.; Hagfeldt, A.; Grätzel, M., Not All That Glitters Is Gold: Metal-Migration-Induced Degradation in Perovskite Solar Cells. *ACS Nano* **2016,** *10*, 6306.

426. Dai, A.; Zhou, Y.; Shu, A. L.; Mohapatra, S. K.; Wang, H.; Fuentes-Hernandez, C.; Zhang, Y.; Barlow, S.; Loo, Y.-L.; Marder, S. R.; Kippelen, B.; Kahn, A., Enhanced Charge-Carrier Injection and Collection Via Lamination of Doped Polymer Layers p-Doped with a Solution-Processible Molybdenum Complex. *Advanced Functional Materials* **2014,** *24*, 2197.

427. Samanta, S.; Fries, K.; Orski, S.; Locklin, J., Formation of Photo-Responsive Surfaces by Surface-Initiated Ring Opening Metathesis Polymerization and Atom Transfer Radical Polymerization: Reversible Optodes for Metal Ion Sensors. In *Smart Coatings III*, American Chemical Society: 2010; Vol. 1050, pp 73.

428. Fantacci, S.; De Angelis, F.; Nazeeruddin, M. K.; Grätzel, M., Electronic and Optical Properties of the Spiro-MeOTAD Hole Conductor in Its Neutral and Oxidized Forms: A DFT/TDDFT Investigation. *The Journal of Physical Chemistry C* **2011,** *115*, 23126.

429. Cho, J.-Y.; Domercq, B.; Barlow, S.; Suponitsky, K. Y.; Li, J.; Timofeeva, T. V.; Jones, S. C.; Hayden, L. E.; Kimyonok, A.; South, C. R.; Weck, M.; Kippelen, B.; Marder, S. R., Synthesis and Characterization of Polymerizable Phosphorescent Platinum(II) Complexes for Solution-Processible Organic Light-Emitting Diodes. *Organometallics* **2007,** *26*, 4816.

430. Baranamo, D.; Mann, G.; Hartwig, J. F., Nickel and palladium catalyzed cross couplings that form carbon-heteroatom and carbon-element bonds. *Current Organic Chemistry* **1997,** *1*, 287.

431. Yang, B. H.; Buchwald, S. L., Palladium-catalyzed amination of aryl halides and sulfonates. *Journal of Organometallic Chemistry* **1999,** *576*, 125.

432. Pellaroque, A.; Noel, N. K.; Habisreutinger, S. N.; Zhang, Y.; Barlow, S.; Marder, S. R.; Snaith, H. J., Efficient and Stable Perovskite Solar Cells Using Molybdenum Tris(dithiolene)s as p-Dopants for Spiro-OMeTAD. *ACS Energy Letters* **2017,** *2*, 2044.

433. Mohapatra, S. K.; Zhang, Y.; Sandhu, B.; Fonari, M. S.; Timofeeva, T. V.; Marder, S. R.; Barlow, S., Synthesis, characterization, and crystal structures of molybdenum complexes of unsymmetrical electron-poor dithiolene ligands. *Polyhedron* **2016,** *116*, 88.

434. Zhao, P.; Kim, B. J.; Jung, H. S., Passivation in perovskite solar cells: A review. *Materials Today Energy* **2018,** *7*, 267.

435. Rajagopal, A.; Yao, K.; Jen, A. K. Y., Toward Perovskite Solar Cell Commercialization: A Perspective and Research Roadmap Based on Interfacial Engineering. *Advanced Materials* **2018,** *30*, 1800455.

436. Sutton, R. J.; Eperon, G. E.; Miranda, L.; Parrott, E. S.; Kamino, B. A.; Patel, J. B.; Hörantner, M. T.; Johnston, M. B.; Haghighirad, A. A.; Moore, D. T.; Snaith, H. J., Bandgap-Tunable Cesium Lead Halide Perovskites with High Thermal Stability for Efficient Solar Cells. *Advanced Energy Materials* **2016,** *6*, 1502458.

437. Xing, G.; Mathews, N.; Sun, S.; Lim, S. S.; Lam, Y. M.; Grätzel, M.; Mhaisalkar, S.; Sum, T. C., Long-Range Balanced Electron- and Hole-Transport Lengths in Organic-Inorganic CH₃NH₃PbI₃. *Science* **2013,** *342*, 344.

438. Stranks, S. D.; Eperon, G. E.; Grancini, G.; Menelaou, C.; Alcocer, M. J. P.; Leijtens, T.; Herz, L. M.; Petrozza, A.; Snaith, H. J., Electron-Hole Diffusion Lengths Exceeding 1 Micrometer in an Organometal Trihalide Perovskite Absorber. *Science* **2013,** *342*, 341.

439. Dong, Q.; Fang, Y.; Shao, Y.; Mulligan, P.; Qiu, J.; Cao, L.; Huang, J., Electron-hole diffusion lengths > 175 μm in solution-grown CH₃NH₃PbI₃ single crystals. *Science* **2015,** *347*, 967.

440. Bi, C.; Wang, Q.; Shao, Y.; Yuan, Y.; Xiao, Z.; Huang, J., Non-wetting surface-driven high-aspect-ratio crystalline grain growth for efficient hybrid perovskite solar cells. *Nature Communications* **2015,** *6*, 7747.

441. Eames, C.; Frost, J. M.; Barnes, P. R. F.; O'Regan, B. C.; Walsh, A.; Islam, M. S., Ionic transport in hybrid lead iodide perovskite solar cells. *Nature Communications* **2015,** *6*, 7497.

442. Kato, Y.; Ono, L. K.; Lee, M. V.; Wang, S.; Raga, S. R.; Qi, Y., Silver Iodide Formation in Methyl Ammonium Lead Iodide Perovskite Solar Cells with Silver Top Electrodes. *Advanced Materials Interfaces* **2015,** *2*, 1500195.

443. Zhang, G.; Hawks, S. A.; Ngo, C.; Schelhas, L. T.; Scholes, D. T.; Kang, H.; Aguirre, J. C.; Tolbert, S. H.; Schwartz, B. J., Extensive Penetration of Evaporated Electrode Metals into Fullerene Films: Intercalated Metal Nanostructures and Influence on Device Architecture. *ACS Applied Materials & Interfaces* **2015,** *7*, 25247.

444. Derue, L.; Dautel, O.; Tournebize, A.; Drees, M.; Pan, H.; Berthumeyrie, S.; Pavageau, B.; Cloutet, E.; Chambon, S.; Hirsch, L.; Rivaton, A.; Hudhomme, P.; Facchetti, A.; Wantz, G., Thermal Stabilisation of Polymer–Fullerene Bulk Heterojunction Morphology for Efficient Photovoltaic Solar Cells. *Advanced Materials* **2014,** *26*, 5831.

445. Wojciechowski, K.; Ramirez, I.; Gorisse, T.; Dautel, O.; Dasari, R.; Sakai, N.; Hardigree, J. M.; Song, S.; Marder, S.; Riede, M.; Wantz, G.; Snaith, H. J., Cross-Linkable Fullerene Derivatives for Solution-Processed n–i–p Perovskite Solar Cells. *ACS Energy Letters* **2016,** *1*, 648.

446. Deb, N.; Dasari, R. R.; Moudgil, K.; Hernandez, J. L.; Marder, S. R.; Sun, Y.; Karim, A.; Bucknall, D. G., Thermo-Cross-Linkable Fullerene for Long-Term Stability of Photovoltaic Devices. *Journal of Materials Chemistry A* **2015,** *3*, 21856.

447. Gügel, A.; Belik, P.; Walter, M.; Kraus, A.; Harth, E.; Wagner, M.; Spickermann, J.; Müllen, K., The Repetitive Diels-Alder Reaction: A New Approach to [60]Fullerene Maindashchain Polymers. *Tetrahedron* **1996,** *52*, 5007.

448. McMeekin, D. P.; Wang, Z.; Rehman, W.; Pulvirenti, F.; Patel, J. B.; Noel, N. K.; Johnston, M. B.; Marder, S. R.; Herz, L. M.; Snaith, H. J., Crystallization Kinetics and Morphology Control of Formamidinium–Cesium Mixed-Cation Lead Mixed-Halide Perovskite via Tunability of the Colloidal Precursor Solution. *Advanced Materials* **2017,** *29*, 1607039.

449. Gusev, O. V.; Peterleitner, M. G.; Ievlev, M. A.; Kal'sin, A. M.; Petrovskii, P. V.; Denisovich, L. I.; Ustynyuk, N. A., Reduction of Iridocenium Salts [Ir(η5-C5Me5)(η5-

L)]+ (L = C5H5, C5Me5, C9H7); Ligand-to-Ligand Dimerisation Induced by Electron Transfer. *Journal of Organometallic Chemistry* **1997,** *531*, 95.

450. Bubb, W.; Sternhell, S., Proton N.M.R. Spectra of 1-Substituted Benzocyclobutenes (Bicyclo[4,2,0]octa-1,3,5-trienes). *Australian Journal of Chemistry* **1976,** *29*, 1685.

451. Gusev, O. V.; Denisovich, L. I.; Peterleitner, M. G.; Rubezhov, A. Z.; Ustynyuk, N. A.; Maitlis, P. M., Electrochemical generation of 19- and 20-electron rhodocenium complexes and their properties. *Journal of Organometallic Chemistry* **1993,** *452*, 219.

452. Mohapatra, S. K.; Fonari, A.; Risko, C.; Yesudas, K.; Moudgil, K.; Delcamp, J. H.; Timofeeva, T. V.; Brédas, J.-L.; Marder, S. R.; Barlow, S., Dimers of Nineteen-Electron Sandwich Compounds: Crystal and Electronic Structures, and Comparison of Reducing Strengths. *Chemistry – A European Journal* **2014,** *20*, 15385.

453. Olthof, S.; Mehraeen, S.; Mohapatra, S. K.; Barlow, S.; Coropceanu, V.; Brédas, J.-L.; Marder, S. R.; Kahn, A., Ultralow Doping in Organic Semiconductors: Evidence of Trap Filling. *Physical Review Letters* **2012,** *109*, 176601.

454. Pulvirenti, F.; Wegner, B.; Noel, N. K.; Mazzotta, G.; Hill, R.; Patel, J. B.; Herz, L. M.; Johnston, M. B.; Riede, M. K.; Snaith, H. J.; Koch, N.; Barlow, S.; Marder, S. R., Modification of the Fluorinated Tin Oxide/Electron-Transporting Material Interface by a Strong Reductant and its Effect on Perovskite Solar Cell Efficiency. *Molecular Systems Design & Engineering* **2018,** *3*, 741.

455. Konarev, D. V.; Drichko, N. V.; Graja, A., Optical Absorption Spectra of Chemically Generated C60 and C70 Anions. *J. Chim. Phys.* **1998,** *95*, 2143.

456. Naab, B. D.; Guo, S.; Olthof, S.; Evans, E. G. B.; Wei, P.; Millhauser, G. L.; Kahn, A.; Barlow, S.; Marder, S. R.; Bao, Z., Mechanistic Study on the Solution-Phase n-Doping of 1,3-Dimethyl-2-aryl-2,3-dihydro-1H-benzoimidazole Derivatives. *Journal of the American Chemical Society* **2013,** *135*, 15018.

457. Lu, G.; Tang, H.; Huan, Y.; Li, S.; Li, L.; Wang, Y.; Yang, X., Enhanced Charge Transportation in Semiconducting Polymer/Insulating Polymer Composites: The Role of an Interpenetrating Bulk Interface. *Advanced Functional Materials* **2010,** *20*, 1714.

458. Ferenczi, T. A. M.; Müller, C.; Bradley, D. D. C.; Smith, P.; Nelson, J.; Stingelin, N., Organic Semiconductor:Insulator Polymer Ternary Blends for Photovoltaics. *Advanced Materials* **2011,** *23*, 4093.

459. Lu, G.; Tang, H.; Qu, Y.; Li, L.; Yang, X., Enhanced Electrical Conductivity of Highly Crystalline Polythiophene/Insulating-Polymer Composite. *Macromolecules* **2007,** *40*, 6579.

460. Kiefer, D.; Yu, L.; Fransson, E.; Gómez, A.; Primetzhofer, D.; Amassian, A.; Campoy-Quiles, M.; Müller, C., A Solution-Doped Polymer Semiconductor:Insulator Blend for Thermoelectrics. *Advanced Science* **2017,** *4*.

461. Kim, F. S.; Jenekhe, S. A., Charge Transport in Poly(3-butylthiophene) Nanowires and Their Nanocomposites with an Insulating Polymer. *Macromolecules* **2012,** *45*, 7514.

462. Sun, J.; Jung, B. J.; Lee, T.; Berger, L.; Huang, J.; Liu, Y.; Reich, D. H.; Katz, H. E., Tunability of Mobility and Conductivity over Large Ranges in Poly(3,3‴-didodecylquaterthiophene)/Insulating Polymer Composites. *ACS Applied Materials & Interfaces* **2009,** *1*, 412.

463. Kubota, Y.; Tominaga, Y., Effect of nitrile groups on conductivity and morphology of NBR/polyether-based electrolyte blends for antistatic materials. *Materials Today Communications* **2015,** *4*, 124.

464. Lu, G.; Bu, L.; Li, S.; Yang, X., Bulk Interpenetration Network of Thermoelectric Polymer in Insulating Supporting Matrix. *Advanced Materials* **2014,** *26*, 2359.

465. Qiu, L.; Lee, W. H.; Wang, X.; Kim, J. S.; Lim, J. A.; Kwak, D.; Lee, S.; Cho, K., Organic Thin-film Transistors Based on Polythiophene Nanowires Embedded in Insulating Polymer. *Advanced Materials* **2009,** *21*, 1349.

466. Bin, Z.; Li, J.; Wang, L.; Duan, L., Efficient n-type dopants with extremely low doping ratios for high performance inverted perovskite solar cells. *Energy & Environmental Science* **2016,** *9*, 3424.

467. Kim, S. S.; Bae, S.; Jo, W. H., Performance enhancement of planar heterojunction perovskite solar cells by n-doping of the electron transporting layer. *Chemical Communications* **2015,** *51*, 17413.

468. Kakavelakis, G.; Maksudov, T.; Konios, D.; Paradisanos, I.; Kioseoglou, G.; Stratakis, E.; Kymakis, E., Efficient and Highly Air Stable Planar Inverted Perovskite Solar Cells with Reduced Graphene Oxide Doped PCBM Electron Transporting Layer. *Advanced Energy Materials* **2017,** *7*, 1602120.

469. Kuang, C.; Tang, G.; Jiu, T.; Yang, H.; Liu, H.; Li, B.; Luo, W.; Li, X.; Zhang, W.; Lu, F.; Fang, J.; Li, Y., Highly Efficient Electron Transport Obtained by Doping PCBM with Graphdiyne in Planar-Heterojunction Perovskite Solar Cells. *Nano Letters* **2015,** *15*, 2756.

470. Yang, Z.; Xie, J.; Arivazhagan, V.; Xiao, K.; Qiang, Y.; Huang, K.; Hu, M.; Cui, C.; Yu, X.; Yang, D., Efficient and highly light stable planar perovskite solar cells with graphene quantum dots doped PCBM electron transport layer. *Nano Energy* **2017,** *40*, 345.

471. Avila, J.; La-Placa, M.-G.; Longhi, E.; Sessolo, M.; Barlow, S.; Marder, S. R.; Bolink, H. J., Ruthenium pentamethylcyclopentadienyl mesitylene dimer: a sublimable n-dopant and electron buffer layer for efficient n–i–p perovskite solar cells. *Journal of Materials Chemistry A* **2019,** *7*, 25796.

472. Tremblay, M.-H.; Schutt, K.; Zhang, Y.; Lim, J.; Lin, Y.-H.; Warby, J. H.; Barlow, S.; Snaith, H. J.; Marder, S. R., A photo-crosslinkable bis-triarylamine side-chain polymer as a hole-transport material for stable perovskite solar cells. *Sustainable Energy & Fuels* **2020,** *4*, 190.